Structural Elucidation of Membrane Proteins Involved in Photosynthesis

by

Shatabdi Roy Chowdhury

A Dissertation Presented in Partial Fulfillment
of the Requirements for the Degree
Doctor of Philosophy

Approved May 2018 by the
Graduate Supervisory Committee:

Petra Fromme, Chair
Alexandra Ros
Kevin Redding

ARIZONA STATE UNIVERSITY

August 2018

ABSTRACT

Over the last century, X-ray crystallography has been established as the most successful technique for unravelling the structure-function relationship in molecules. For integral membrane proteins, growing well-ordered large crystals is a challenge and hence, there is room for improving current methods of macromolecular crystallography and for exploring complimentary techniques. Since protein function is deeply associated with its structural dynamics, static position of atoms in a macromolecule are insufficient to unlock the mechanism.

The availability of X-ray free electron lasers presents an opportunity to study micron-sized crystals that could be triggered (using light, small molecules or physical conditions) to capture macromolecules in action. This method of 'Time-resolved serial crystallography' answers key biological questions by capturing snapshots of conformational changes associated with multi-step reactions. This dissertation describes approaches for studying structures of large membrane protein complexes. Both macro and micro-seeding techniques have been implemented for improving crystal quality and obtaining high-resolution structures. Well-diffracting 15-20 micron crystals of active Photosystem II were used to perform time-resolved studies with fixed-target Roadrunner sample delivery system. By employing continuous diffraction obtained up to 2 A, significant progress can be made towards understanding the process of water oxidation.

Structure of Photosystem I was solved to 2.3 A by X-ray crystallography and to medium resolution of 4.8 A using Cryogenic electron microscopy. Using complimentary techniques to study macromolecules provides an insight into differences among methods in structural biology. This helps in overcoming limitations of one specific technique and contributes in greater knowledge of the molecule under study.

DEDICATION

This thesis is dedicated to my relentless support-system:

my parents, Swagata and Rajkumar,

and my brother, Shauvik.

ACKNOWLEGMENTS

I express deep gratitude towards my PhD advisor, Petra Fromme, for being the best teacher I have ever had. Her fierce belief in my abilities gave me the courage and motivation to learn more, work harder and reach my potential. In her group, Petra cultivated an environment that permitted healthy exchange of scientific ideas that led to opportunities for several successful collaborative projects across the globe.

I owe huge thanks to my supervisory committee members, Alexandra Ros and Kevin Redding. Both of them impacted my doctoral journey by encouraging me to approach problems with objectivity and made time to guide me when situations were less than ideal. I will forever be in debt of their support and commitment towards my accomplishments.

Over the last few years, all skills garnered by me, have been passed on by kind, passionate scientists. Especially, Raimund Fromme, Iosifina Sarrou, Dewight Williams and Ingo Grotjohann have invested their energies to educate me in creative ways and thus, heavily contributed to my scientific capabilities. I'm also grateful to Subramanyam Rajagopal Sir for his mentorship during my Master's research project that taught me valuable lessons in perseverance towards achieving my scientific goals.

The highlight of my time at ASU has been the collaborative experiments at X-ray facilities. The contributions of Henry Chapman (CFEL), Charles Dismukes (Rutgers University), Alke Meents (CFEL) and Marius Schmidt (UWM) (and their teams) to the success of the PSII project cannot be denied. Additionally, all four of them have had a positive influence on my attitude towards complicated interdisciplinary experiments and that has left an everlasting impression on my approach towards science.

Results described in Chapter 3 of this thesis are the work of a large group of researchers who have contributed their time and energy for the success of PSII beam-

times. The following people have had significant impact on my PhD project: Christopher Kupitz, Shibom Basu, Jesse Coe, Natasha Stander, Jose Martin-Garcia, Nadia Zatsepin, Christopher Gisriel, Michael Vaughn, Alexander Schaffer, Jay-how Yang, Zachary Dobson, Natalie Vaughn, Erin Discianno, Alexander Jones, Gihan Ketawala, Chelsie Conrad and James Zook; Their generosity continues to motivate me to help other peers along in their journey.

My parents have unwavering belief in me and that has always given me something to work for. My brother is the primary reason for me taking up doctoral studies and I hope that someday, I can achieve a fraction of his brilliance. Having all three of them beside me, ensured that I never withdrew, despite any fear, hesitation or disappointment.

Through thick and thin, an army of cheerleaders has consistently rooted for my success. My sanity can largely be attributed to my friends who have celebrated all sides of me. Mainly, Tanushree Mitra, Anindita Debnath, Rohini Chatterjee, Nirupa Nagaratnam, Sumedha Polisetti, Surabhi Rao, Amruta Bhate, Miyuki Dwarak, Santosh Murali, Ganesh Subramanyam, Sachi Mahajan, Raghu Narayan Pradeep, Anasuya Paul and Dhenughen Logeswaran have always had my back and I cannot thank them enough for their thoughtfulness over the years.

Fromme lab has been my family away from home and I am proud to be associated with the spectacular research that is being carried out at Center of Advanced Structural Discovery, Biodesign Institute, ASU. I have also been fortunate to be a BioXFEL scholar with National Science Foundation's Science and Technology Center (Agreement no. 1231306). Finally, I would like to acknowledge that a significant portion of my work was supported by Femtosecond nano-crystallography of membrane proteins award (617095583) by National Institute of Health.

TABLE OF CONTENTS

Page

Page

Page

Page

Page

Page

Page

LIST OF TABLES

Table Page

LIST OF FIGURES

Figure Page

Figure Page

Figure Page

Figure Page

Figure Page

CHAPTER 1

INTRODUCTION

1.1 Shapes tell stories: relationship between structure and function

Biomolecules are the architects of life. All biological function depends on the molecular events that are directed, modulated and performed by intricate biological machines that are essentially, proteins, nucleic acids, carbohydrates, lipids or complex combinations of them. The main theme of structural biology is to understand how the function and dynamics are performed by inspecting the 3D arrangement of atoms. Structural similarities have been portrayed by biomolecules performing similar functions. For e.g., proteins with low sequence homology can belong to the same 'class' owing to presence of similar structural motifs and functional properties. Hence, details about the molecular arrangement of biomolecules can contribute to the advances in understanding their roles.

Several techniques have been developed for studying complex molecular structures and among them, X-ray crystallography, electron microscopy and nuclear magnetic resonance have been greatly established. Each of these methods presents the researcher with complimentary approaches towards studying molecules of interest. Knowledge obtained via structural studies has been used for research in rational drug discovery, in understanding biochemical pathways for cellular processes and in biotechnological advances to name a few.

Understanding structures of bio-macromolecules can help us understand how they can be altered to manipulate the function and this has significant implications in various areas of study. This dissertation discusses progress made using structural biology toward understanding the core biological phenomenon of oxygenic photosynthesis.

1.2 Oxygenic Photosynthesis

Photosynthesis is the process by which plants, algae and cyanobacteria convert solar energy into useful chemical energy to drive metabolism. Over the last 2.5-3 billion years, photosynthesis has led to the oxygenation of our planet, enabling evolution of complex higher life. Hence, photosynthesis is a fundamental biological process with significant impact on Earth's ecology. Studying photosynthesis has direct implications in harnessing solar energy as fuel, global warming, agriculture, nanotechnology and research associated with free radicals.

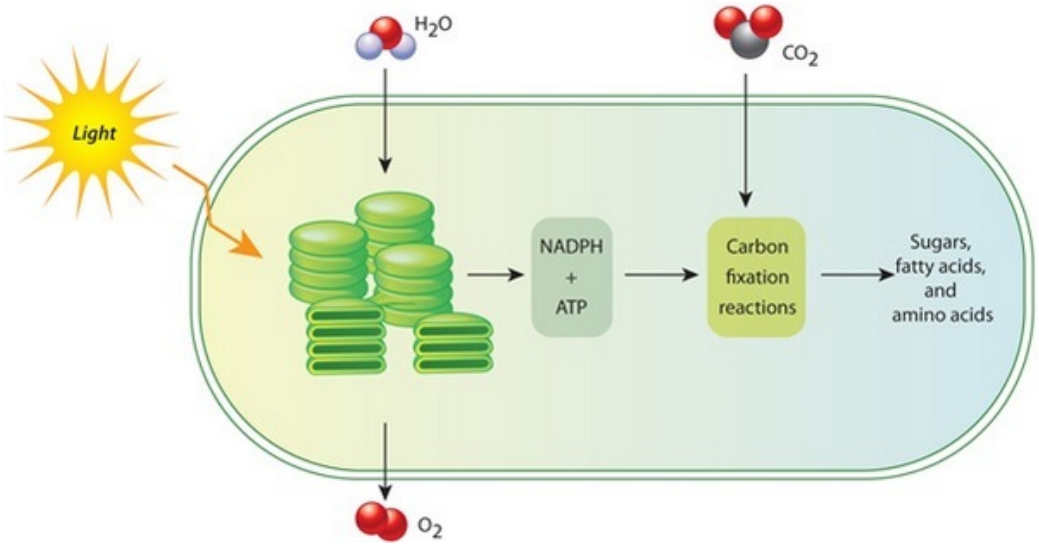

Figure 1.1: **Light and dark reactions in photosynthetic organisms**

Both kinds of reactions occur in the chloroplast. The reactions triggered by light take place in the thylakoid where the oxidation of water releases oxygen, protons and electrons. The energy of the light reactions is harnessed in production of ATP and NADPH, which drive the carbon fixation in the stroma.

Photosynthetic organisms have specialized organelles called chloroplasts that are composed of membrane stacks named 'thylakoids' (depicted in Figure 1.1). The integral membrane proteins in the thylakoid membrane perform the light harvesting and energy conversion processes through a series of redox reactions. These (Photo) Reaction Centers

(RCs) may contain a 4Fe-4S cluster (Type I) or a quinone molecule (Type II) as their terminal electron acceptor. Based on the organism, the light reactions might be oxygenic (involving both Type I and Type II RCs) or anoxygenic (involving either a Type I or II RC). Although, many of the characteristics among all photosynthetic organisms are conserved, billions of years of evolutionary divergence has resulted in differences in metabolic pathways and protein structures. All descriptions involved in this thesis are applicable for oxygenic photosynthesis studied in cyanobacteria, *Thermosynechococcus elongatus (T. elongatus)*.

The major photosynthetic protein complexes and their orientation in the thylakoid membrane are represented in Figure 1.2. The electron transfer reactions initiate at Photosystem II (PSII) which is a Type II RC. Photons captured by an internal chlorophyll system of PSII are used to initiate charge separation at the center of the complex. Subsequently, 4 electrons are extracted in 4 charge-separation steps, oxidizing 2 molecules of water to generate molecular oxygen, 4 protons and 4 electrons at the Oxygen Evolving Complex (OEC) of PSII. The electrons ultimately reduce a mobile Plastoquinone (PQ) twice, which binds 2 protons from the stromal side to form Plastoquinol (PQH_2) and is released into the thylakoid membrane. This PQH_2 serves as a mobile electron and proton carrier and is exchanged with PQ pool in the membrane (Loll et al., 2005).

The PQH_2 eventually diffuses through the membrane and docks at the binding pocket of the cytochrome b_6f complex. Here, the 2 electrons are utilized for reducing 2 molecules of Plastocyanin (PC) or cytochrome c_6. The protons from PQH_2 are released in the lumen of the thylakoid, contributing to the electrochemical gradient across the membrane.

Both cytochrome c_6 (Fe based) and PC (containing Cu) are soluble carriers of single electrons that transfer the electron to Photosystem I (PSI) (Type I RC). The light-induced charge separation event in PSI transfers the electrons from the lumenal side to the stromal

side of the thylakoid membrane to the final electron acceptor, Ferredoxin (Fd). Once reduced, the Fd molecule undocks from PSI, diffuses into the stroma for binding with Ferredoxin: $NADP^+$ reductase (FNR). Upon taking up 2 electrons from Fd molecules, $NADP^+ + H^+$ is reduced to NADPH. Also, the electrochemical gradient generated across the thylakoid membrane is used in the production of ATP from ADP and inorganic phosphate (iP) by the ATP-synthase protein complex.

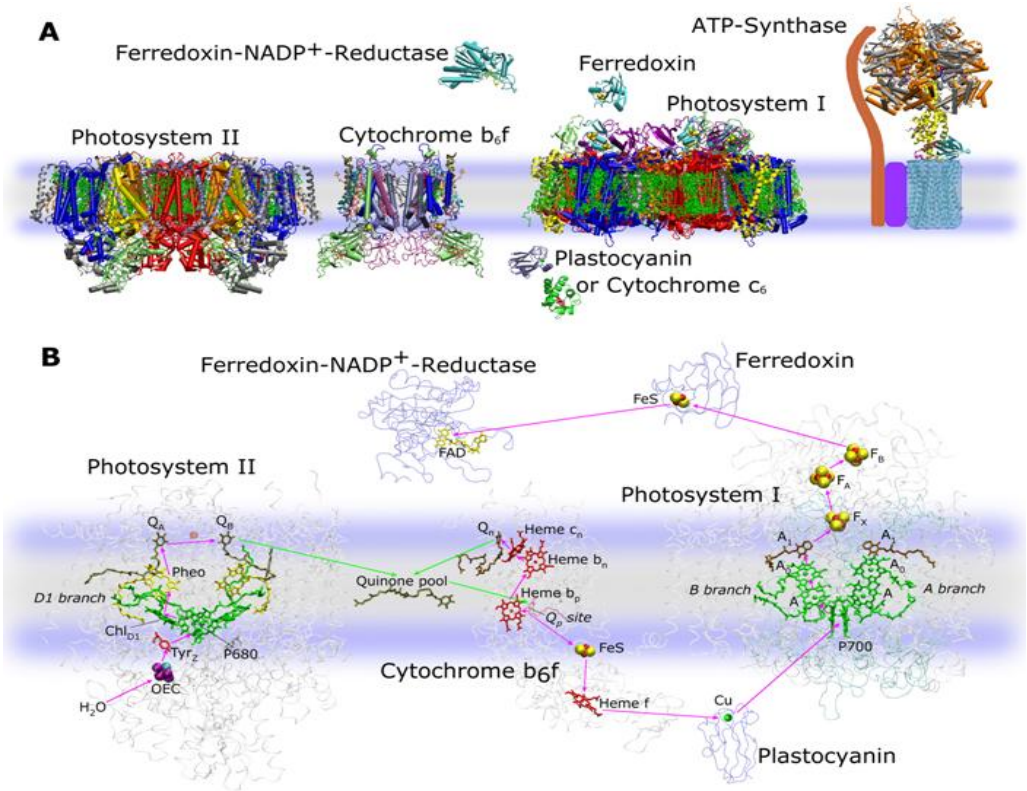

Figure 1.2: **Photosynthetic apparatus**

Image showing structures solved by X-ray crystallography. Shown are (a) the major proteins involved in the light reactions of oxygenic photosynthesis including the electron and proton transport; and (b) their functional components. Membrane orientation depicted is the lumen below and the stroma above. Figure originally from Fromme and Grotjohann (2008)

NADPH, ATP and fixed CO_2 are utilized to drive the dark photosynthetic reactions (Calvin cycle), which eventually stores the energy harnessed from the sun in the form of carbohydrates and other useful molecules. Structure and function of PSII and PSI are described in depth in Chapter 2 and Chapter 4 of this thesis respectively.

1.3 X-ray crystallography of proteins

Since the discovery of diffraction of X-rays by crystals over a century ago, X-ray crystallography has developed into an indispensable tool for structural biologists and material scientists. Over the years, the technique has helped researchers answer key scientific questions, recognizing the method with high success rate and credibility. Because of the immense contributions of crystallography, 2014 was celebrated as the International year of Crystallography by UNESCO and International Union of Crystallography for promoting education and general public awareness across 53 countries. This section will briefly summarize the background of the technique specifically with respect to protein crystallography. Detailed reviews on this well-established technique can be found elsewhere such as Woolfson, 1997 or Rupp, 2010.

1.3.1. History: Impact of 100 years of crystallography

William Conrad Röntgen first discovered X-rays in 1895 and was later awarded the first Nobel Prize in Physics in 1901, but Max von Laue and his co-workers discovered that the interaction of X-rays travelling through a crystal yields diffraction that is dependent on the nature of the crystal. Their pioneering work acquired them the Nobel Prize in Physics in 1914 and laid the foundations for using x-rays to study chemical structures through the use of crystalline material.

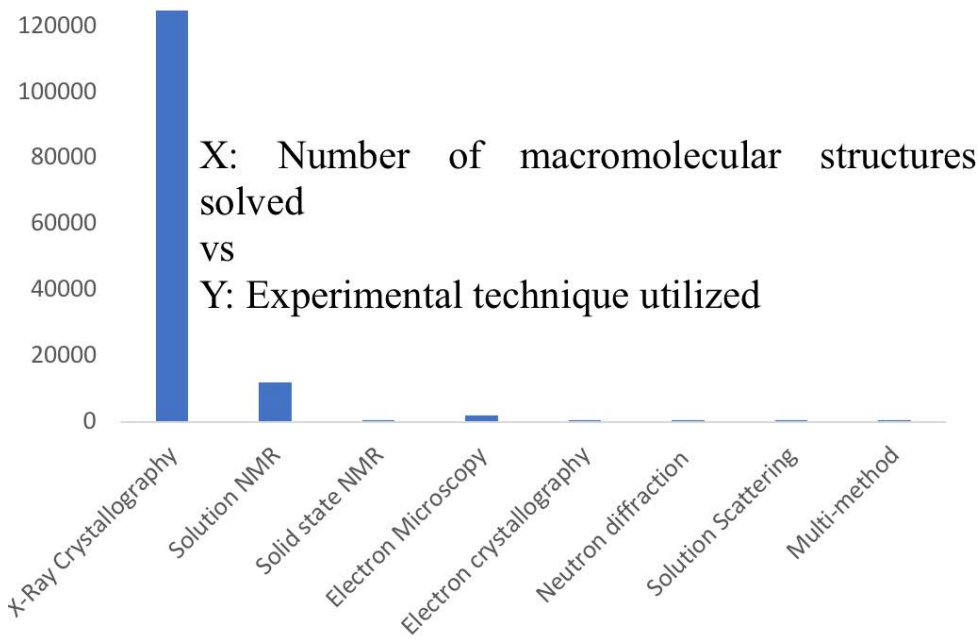

Figure 1.3: **Comparison of total structures solved vs experimental method**

Based on the statistics on RSCB Protein Data Bank on 08 April 2018, 89.5% of all structures were solved by X-Ray crystallography. NMR (8.7%) and EM (1.5%) constituted the majority of the remaining structures.

Subsequently, the father and son duo of William Henry Bragg and William Lawrence Bragg discovered in that X-rays could be used to determine the position of atoms within a crystal and unravel the 3D structure of molecules (Bragg, 1913). This study, which was mainly done on diamonds and salt crystals, was recognized with a Nobel Prize in 1915. Since then, X-ray Crystallography has been employed to understand vital biological structures like cholesterol, penicillin, vitamin B_{12}, insulin, the DNA double-helix, ribosomes, integral membrane G-protein coupled receptors etc. This has led to 28 Nobel recognitions to 45 awardees over the decades in physics, chemistry and physiology or medicine.

The impact of X-ray crystallography on structural biology is highlighted in Figure 1.3 which summarizes all submitted entries for structures of biological molecules based on the technique used for analysis. As seen in the figure, X-ray crystallography is by far the most successfully used technique for structure determination.

1.3.2. Principle of studying crystals using X-rays

Crystallography harnesses the property of coherent scattering of electromagnetic radiation by ordered molecules in a lattice. By definition, crystals are made of translationally repeating copies of the same molecule in a periodic fashion generating a 3D pattern of identical unit cells in a lattice. Due to the translational symmetry inherent in a crystal, a defined phase relationship of the scattered waves occurs and the collective sum of scattered amplitudes leads to constructive and destructive interference. Interference of light by a crystal is dependent on the specific geometry of the lattice planes.

In particular, at specific angles for a defined wavelength of light as a function of lattice geometry, this can result in fully constructive interference, leading to an increased amplitude of the scattered wave that is proportional to the square of the number of planes contributing to it. The bright spots created by this constructive interference are seen as 'Bragg peaks' . Their appearance is explicitly dependent on the parameters as described by the Bragg equation described in Figure 1.7.

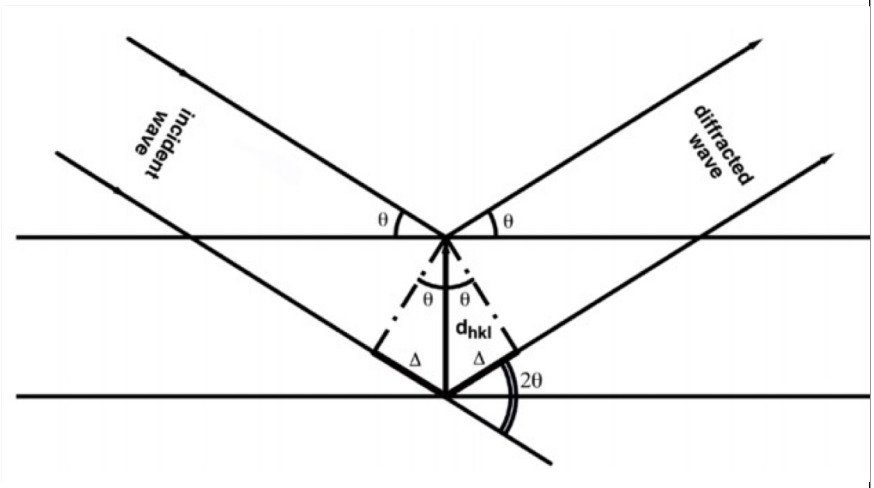

Figure 1.1: **Bragg's representation of the condition for diffraction.**

Image from Lavina et.al., 2014 describes the requirement for constructive interference of light. If d is the spacing between the lattice planes, θ the scattering angle and λ the wavelength of incident radiation, the scattered waves would be in phase only if $2d \sin\theta = n\lambda$ (where n is an integer).

The intensity of the Bragg peaks is dependent on the scattering cross-sections of the atoms constituting the molecule under study and the number of unit cells in the specific direction. Hence, the scattered intensity depends on the size of the crystal (Holton and Frankel, 2010). The integrated intensity is proportional to the crystal volume relative to the unit cell volume i.e. crystal size and scattered intensity are directly correlated. Thus, larger crystals of the same molecules and same crystal packing produce higher intensity Bragg spots than small crystals.

1.3.3. Advances at Third generation synchrotrons

For collecting data at synchrotron sources, the goniometer head (with a mounted crystal) is rotated in the X-ray beam along one or multiple axis for collecting diffraction patterns in different orientations. To ensure that all angles are represented, the crystal of mounted at an angle to the crystal axis or a second rotation set is collected in a different orientation. To reduce overlap of reflections, the rotation is usually performed in small angles (0.1-2°). A data-set typically contains a 100-300 patterns from (usually) a single crystal and since they are collected as a rotational series, their orientation with respect to each other is known.

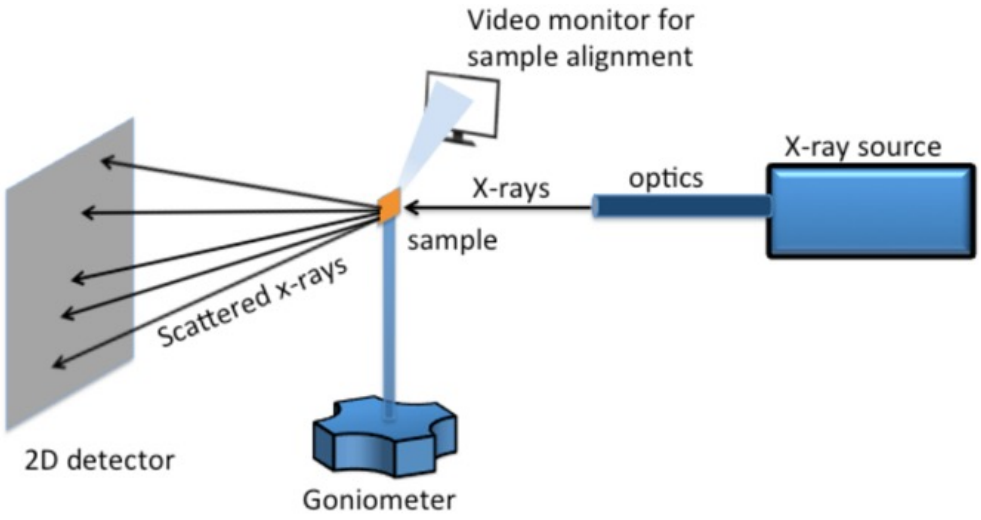

Figure 1.5: **Simplified strategy for data collection for traditional crystallography.**

Crystalline sample is mounted on the goniometer head and frames of diffraction data are collected in the oscillation mode by rotating the crystal until all planes in the crystal have met the Bragg condition. These frames represent diffraction in different orientations and upon integration can yield the amplitude of the structure factors. However the phase is lost and have to be retrieved independently to determine the 3D structure of the molecule under study. Image edited from He et.al., Advances in X-ray Analysis, 2000.

One of the key advances that have greatly contributed to the development of X-ray crystallography is the progress in X-ray sources. Synchrotrons have been used for diffraction studies since 1970s but second generation synchrotrons along with improved data collection strategies brought the time required to collect a complete data-set down from days to hours. Modern third generation synchrotrons feature much higher brilliance (~10^{18} units), small angular diversion of the beam, and a wide range of wavelength tuning-ability. This was largely due to upgrading the design of synchrotron rings and introduction of beam undulators.

Introduction of X-ray optical systems for generating a 'microbeam' have contributed in reducing the focal size (low beam divergence) while maintaining the flux. The full-width-half-maxima (FWHM) of the beam generated may vary between 10-100 μm in diameter, the most recent beamline development at NSLS allows for a 2 um beam focus Particularly note-worthy of the new optical systems are ultra-smooth Kirkpatrick-Baez mirrors (KB-mirrors) that are a double (crossed) mirror system that can generate beam sizes up to 0.16 x 0.21 μm at 20 keV (Eng et al., 1998). The focal length is tunable making the set-up versatile and a key advantage of superior focusing techniques is low background scattering, leading to the ability to collect data from smaller crystals. This improvement of beam brilliance and an increase in available flux permitted structure analysis of 15-20 μm crystals. Note that the size of the crystal required also depends on the unit cell size, essentially the number of unit cells in a crystal and the content of the unit cell as well as the order of the crystals are main determinants for the intensity and intensity of the diffraction patterns.

1.3.4. Radiation damage

X-rays are ionizing and exposure for even a few nanoseconds can damage protein crystals. This destruction may be due to primary damage i.e. caused by photoelectric absorption of X-rays by atoms (leading to photoionization of electrons) or secondary damage caused by the ejected electrons leading to a cascade of formation of radicals that change the electronic structure of the molecules (Garman, 2010). Continued radiation damage eventually disrupts chemical bonds and finally the global crystalline order of the crystal, leading to increases of the mosaicity (discussed in section 1.3.5) and the loss of crystalline order, where the Bragg peaks become broader finally terminating the diffraction ability of the crystal (Meents et al., 2010).

The critical dose for damage depend also on the elements present in a crystal and therefore damage can occur faster at specific sites of the molecule. This is often experienced locally by cofactors, with high-Z metals being more prone to damage (Holton, 2009). Site specific damage is also commonly seen in the reduction of disulfide bonds, decarboxylation of acidic side-chains, and loss of hydroxyls or methylthio groups. Many of these forms of damage have been discussed in Figure 1.6. While third generation microfocus beamlines permit diffraction studies with 20-50 μm crystals X-ray damage is even more imminent with increase in intensity and smaller beam-focus. 'Dose accumulation' affects crystal integrity and leads to decrease in scattered intensities (Holton, 2009). Also, the local damage caused by radiation at specific residues might begin at much lower dose and can go undetected, leading to inaccuracies in the structures determined. Hence, the allowed dose must depend on the biomolecule and if crystals are more susceptible to damage, a lower dose of radiation is necessary.

Radiation based damage also restricts the experiments that can be done at a synchrotron. Redox-active systems are often metallo-proteins and they undergo rapid

photo-reduction with accumulation of X-ray doses. The crystals might continue to diffract, but the structures solved are of damaged metallic centers (Hirata et al., 2014). This is contrary to the purpose of structural elucidation and might lead to erroneous conclusions.

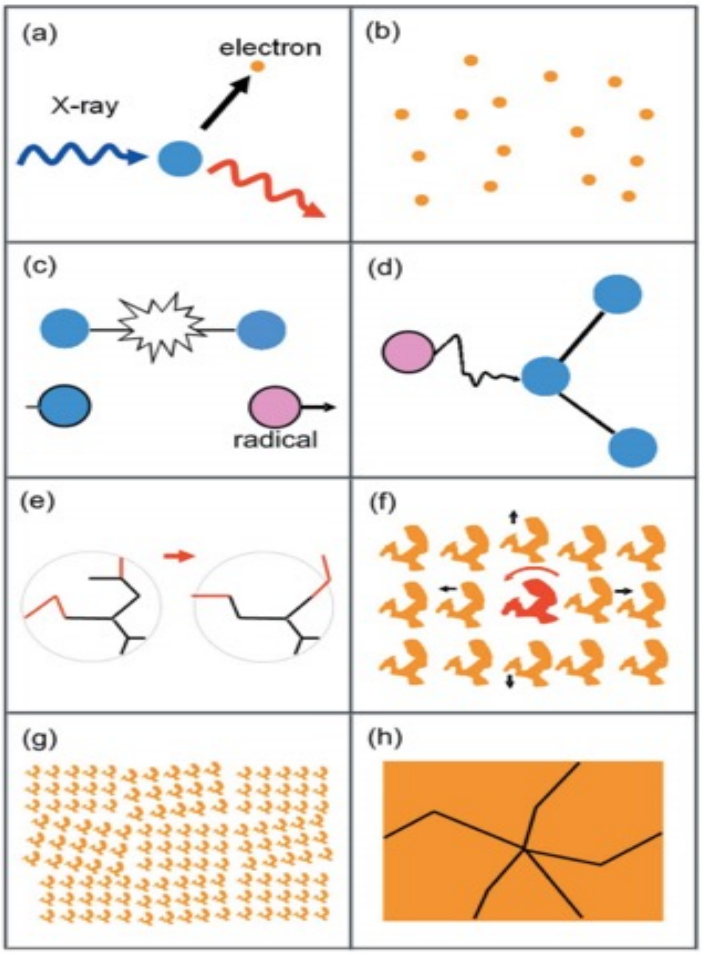

Figure 1.6: **Modes of induction of radiation damage**
The image from Warkentin et.al. 2013 is a depiction of the processes in progression of damage induced in crystals upon exposure to X-rays. a) photoelectric effect causes ejection of electron, b) generation of several low energy electrons, c) bond breakage, d) radicals may attack other parts of the protein leading to a damage cascade, e) conformational changes are induced in side chains / flexible loops due to chemical damage in the structure, f) displacement / reorientation of individual damaged molecules, g) Potential for deformed lattice domains causing increased mosaicity, h) Global plastic damages leading to crystal cracking and loss of diffraction.

To combat the problem of radiation damage, in the early 1990s cryo-cooling was introduced for studying protein crystal structures. The crystals are introduced to highly concentrated cryogenic protectants (e.g. glycerol, sucrose, polyethylene glycol) and flash frozen in liquid nitrogen. The cryogenic agents promote formation of vitreous "ice" upon freezing and retain protein crystal integrity. Data collection proceeds under a stream of liquid nitrogen to maintain the crystals between 70-100 K. This leads in radiation damage to be decreased but not completely diminished (described in Figure 1.7) because the vitreous-solvent matrix slows the diffusion of destructive radicals across the crystal (Henderson, 1995).

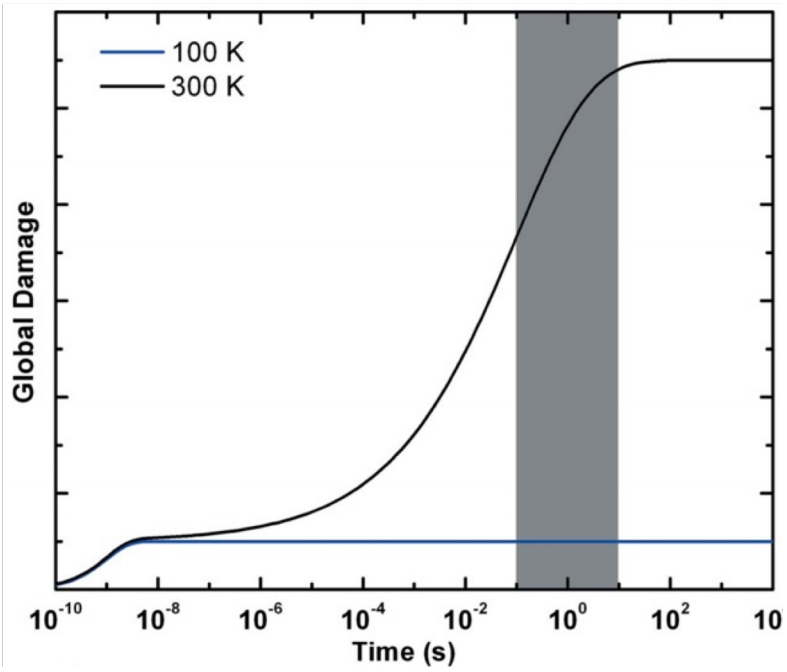

Figure 1.7: **Time scales for damage by X-ray diffraction at cryogenic and room temperatures.**

Image from Warkentin et.al., 2013. Damage (e.g. atomic displacements) inducing processes occur very quickly, and , damage accumulates over time. The damage is reduced by cryo-cooling since free diffusion of radicals is restricted by the frozen mother liquor. The shaded area represents the range of timescales relevant for data collection.

1.3.5. Other limitations of traditional crystallography

A major shortcoming of conventional macromolecular crystallography is the need for large well-ordered crystals due to the damage problem discussed above. Growing large well-ordered crystals is often a challenge, especially for protein complexes, membrane proteins, active enzymes or larger bio-macromolecular structures (like viruses). The amount of sample available is sparse and does not readily form large 3D lattices. While these difficult to crystallize macromolecules can sometimes yield a shower of microcrystals in crystallization screens, expanding that into conditions for large crystal growth often remains a challenge (Mueller et al., 2015). Hence, the ability for collecting usable data from microcrystals would be highly beneficial.

Also, large crystals often contain multiple mosaic blocks and imperfections in their alignment and orientations manifest as inherent growth defects in crystals (Nave, 1998), the larger the crystal is, the higher is the degree of long range disorder. This 'mosaic angular spread' results in broad 'streaks' instead of Bragg spots upon X-ray diffraction and such patterns present challenges for data processing. The effect of mosaicity in large crystals will be discussed further in Chapter 4 with an example from PSI.

For a time, cryo-cooling helped in reducing radiation damage, but with increased beam-intensity at microfocus beamlines, crystals cannot handle prolonged exposure to high dose radiation and only few diffraction patterns can be collected for small crystals before the onset of radiation damage even under cryogenic conditions. Another shortcoming of cryo-protection is that the ideal conditions for a specific cryogen need to be identified and this process is based on trial and error. The sub-optimal use of cryogenic agents can lead to crystal dissolution, increase in mosaicity or cracking. The rate of cooling also needs to be explored , because faster or slower freezing may further increase mosaicity (Nave, 1998) in crystals and has significant impact on the quality of diffraction.

Finally, time resolved crystallography allows for understanding conformational changes associated with the dynamics of the molecule permitting knowledge of the structure-function relationship. At synchrotrons, the duration of the reactions that can be studied is limited to the picosecond time-scale based on the pulse length of Laue exposures (Neutze and Hajdu, 1997; Schotte et al., 2012) (described further in section 1.4.4.). For trapping intermediates in ultra-fast reactions like bond breakage or trans-cis isomerizations that happen in the fs time scale, there is a need for shorter pulses with enough flux to generate interpretable diffraction data.

1.4 Nano-crystallography

In obtaining useful data from X-ray crystallography, the ability to de-convolute the Bragg spots with respect to the background is essential. As discussed in Section 1.3, strategies to increase the intensity of scattered peaks for improved signal to noise ratio are to a) either use a larger crystal, b) prolong the exposure of crystal to X-rays or c) increase the incident photon flux on the sample, or some combination of the three.

1.4.1. Motivation

Crystal growth is often challenging and usually, large crystals have inherent long-range disorder (mosaicity) that restricts the resolution of usable diffraction spots. Preparation of crystals for cryo-protection presents further complications for sample preparation. Also, data collection at cryogenic temperatures may induce structural distortions in the molecules since they are not in their physiological conditions. Exposure of the crystals to incident X-ray beam for even short time-scales of nanoseconds induces global and local damage (explained in Figure 1.10) even at cryogenic temperatures. For traditional crystallography, in order to collect diffraction in all orientations, multiple

frames are collected using the same crystal and over time, dose accumulation leads to insurmountable damage. Furthermore, samples containing high-Z centers are more susceptible to damage and can tolerate lower overall doses of X-rays.

For studying reactions at the molecular level, small crystals permit a more uniform and rapid diffusion of the substrate throughout the crystal, leading to more homogenous transitions of all molecules under study (Schmidt, 2013). The overall brilliance generated at third generation synchrotron sources does not permit the use of weakly diffracting nanocrystals for diffraction-based structural studies. The novel approach of femtosecond nano-crystallography overcomes these shortcomings thereby permitting the study of irreversible, ultra-fast biological reaction dynamics at room temperature.

1.4.2. Diffraction before destruction

As early as in 1980s, it was hypothesized that the duration of the incident X-rays was related to the progression of radiation damage and thus, if data acquisition was sufficiently rapid, it couldenable collection of 'damage-free' diffraction patterns. The effects of ultra-short 5-10 femtosecond (fs) pulses on both single particles and clusters of molecules were calculated by Hajdu and co-workers (Neutze et al., 2000). Their molecular dynamics-based findings predicted that high-intensity femtosecond X-ray pulses are so brief that they pass through the sample before the onset of damage and can yield useful diffraction data describing the term 'diffract before destroy'.

The study analyzed the time-scales of damage in a lysozyme molecule in the gas phase that interacts with an intense X-ray pulse (dose corresponding to $3x10^{12}$ photons (12 keV) per 100 nm diameter spot, making the effective dose to be $3.8x10^{6}$ photons per A^2). The impact of incident photons leads to photo-ionization of the inner atomic electrons. Consequently, these 'positively charged' atoms experience strong repulsive forces leading to a Coulomb explosion of the molecules under study as depicted in Figure 1.8.

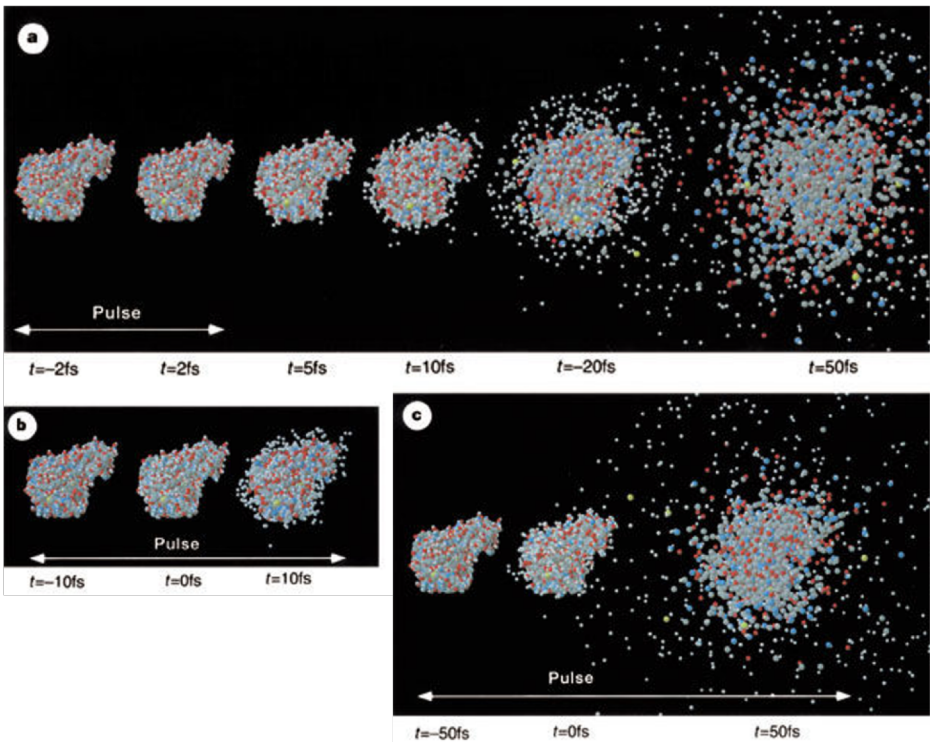

Figure 1.8: **Diffraction before destruction**

Coulomb explosion of T4 lysozyme can be induced by radiation damage. Image from Neutze et.al., 2000. a) describes protein molecule exposed to an X-ray pulse (FWHM of 2 fs) and follows the progress of its disintegration with time. This describes the time period for which the molecule remains intact under specified conditions (5-10 fs) b) Lysozyme exposed to the same number of photons as a, but here the FWHM of the pulse was 10fs and c) depicts the behavior of lysozyme when exposed to X-ray pulse with FWHM of 50 fs.

For all conditions, the sum of X-ray intensity was fixed at $3x10^{12}$ photons (12 keV) per 100 nm diameter spot (i.e. $3.8x10^{6}$ photons per A^2).

Thus, according to the principle described, extremely short X-ray pulse durations can allow the diffraction to out-run the radiation damage. The photons in the bright X-ray pulse subsequently destroy the molecule but scattering information has already been obtained before the molecule is destroyed.

1.4.3. Advent and principle of X-ray Free Electron Lasers

The 'diffract before destroy' principle is based on extremely short (5 - 10 fs) X-ray pulses with extremely high photon flux. As fore-mentioned in Section 1.3.3, third generation synchrotrons are able to provide bright and microfocused beams, but the brilliance (~$10^{18\text{-}22}$ brilliance units) is not high enough to study nanocrystals or single particles. Also, there was a need for 'short pulses' of X-rays that could potentially outrun radiation damage and hence fourth generation X-ray sources were conceptualized.

X-ray free electron lasers (XFELs) can generate hard X-rays that are several orders of magnitude brighter than third generation synchrotrons (up to10^{32} brilliance units). The first hard X-rays with 50 fs pulse duration were reported to be generated at Linac Coherent Light Source (LCLS) in 2009. Since then, 3 more XFELs of with varying beam parameters have been developed all over the world with 4 (LCLS, SACLA, PAL-XFEL and EuXFEL) being currently available to users.

XFELs are starkly different from synchrotrons because they are linear accelerator-based sources. Electrons ejected from the source are accelerated and are forced on a wiggling path over a mile through an array of alternating periodic dipoles (undulators) (depicted in Figure 1.10). The movement leads the electrons to emit X-rays and the interaction with these X-rays leads to bunching of the electrons. Electrons that are in phase with the electromagnetic wave are accelerated at the same pace, while adding energy to the lagging electrons to bring them in phase. This manifests as electron 'bunching' where tuned electrons travel at the same phase and emit extremely coherent radiation with respect to each other, adding to the amplified flux. The resultant photons produce a strong electromagnetic field that influences electron bunches that are downstream from it to be better defined, and hence this principle of pulse generation is called Self-Amplified Spontaneous Emission (SASE). Due to the iterative coupling between the two fields, there

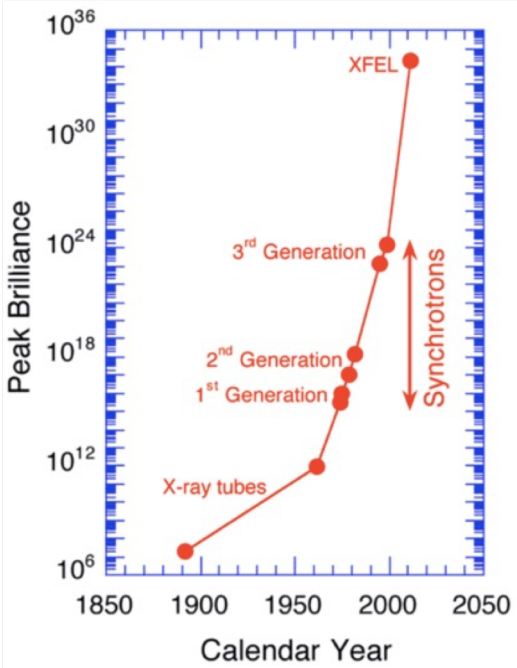

Figure 1.9: **Increased brightness of X-ray sources.**

Over the years, the need for higher flux has driven the x-ray sources to be brighter and several upgrades of synchrotron sources have led to both increase in photon flux and beam coherence. The SASE principle yields extremely short and yet intense pulses leading to amplified peak brilliance for XFELs when compared to traditional synchrotrons. Image from www.psi.ch

is a non-linear increase in emission and this allows for emittance of extremely bright, ultra-short duration of X-ray pulses.

For utilizing the characteristics of an XFEL beam, several complimentary methods have been developed. Firstly, crystallization methods for growing homogenous nano / microcrystals using batch method or free-interface diffusion (Kupitz et al., 2014) have been established. For protein crystals that are very stable and that readily form large crystals, methods are generated for obtaining smaller crystals by "crushing" large crystals by systematic homogenization using a Hampton seed-bead (Cat # HR2-320) or glass beads (Kupitz et al., 2017). Another area of method development was creating strategies for delivering sample to the X-ray interaction region. Crystals cannot withstand more than one XFEL pulse, so in order to match the high repetition rate, rapid regeneration of crystals was necessary. This influenced the naming of the technique as 'serial femtosecond crystallography' (SFX) as microcrystals serially interact with a fs X-ray laser pulse. For samples that have mother liquors compatible with hydraulic pump-based systems, gas dynamic virtual nozzle (GDVN) (DePonte et al., 2008) has proven to be very effective. Using this method microcrystals in random orientation can be injected through a fine glass capillaries and the resulting 'jet' of microcrystals is focused using an inert gas and this permits stable data collection with minimum beam jitter and background scattering.

While being the working horse for sample delivery, they run with high flow rates of 10 - 20 ul / min and were therefore difficult to use for samples, where only a small amount of microcrystals was available. More recently , a viscous sample injector has been developed, which reduces the flow rate to 1 – 200 nl / min (Weierstall et al., 2014) and using this injector, methods have been developed to deliver crystals in viscous media. They can either be grown in the viscous media (favorable for crystals that grow in lipidic cubic phases) or crystals can be embedded into viscous media after crystallization has already

be performed. The viscous media that have shown promising results include lipid-cubic-phase (LCP) (Fromme et al., 2015), agarose (Conrad et al., 2015), oil-free hyaluronic acid (Sugahara et al., 2016) or high molecular weight poly-ethylene glycol (Martin-Garcia et al., 2017), These experiments were performed at XFEL and have recently also been used for serial crystallography data collection at synchrotron sources. Fixed target approaches (Fuller et al., 2017; Roedig et al., 2015) also reduce sample consumption and have been proven immensely successful.

In addition, progress in detector technology, data reduction and data analysis (Hart, Barty et.al. 2012, White et.al. 2012,) have paved the way for application of the technique in various fields. Here, one major biological application of XFELs i.e. studying the dynamics of proteins using time-resolved fs crystallography will be discussed.

1.4.4. Time-resolved experiments to study protein dynamics

The combination of high photon flux and extremely short pulses of XFELs and related technological advances have enabled visualization of symmetric single particles, scattering envelopes of molecules in solution, crystals grown in-vivo, damage sensitive metalloproteins etc. Difficult to crystallize integral membrane proteins (e.g. GPCRs) that form only microcrystals in LCP have also been studied extensively using fs XFEL pulses (Caffrey et al., 2014; Liu et al., 2013). A striking contribution made by serial femtosecond nano-crystallography is in the study of structural dynamics of macromolecules.

Protein function is deeply associated with its structural dynamics. Static position of atoms in a macromolecule contribute to our global understanding of its shape but in order to study the mechanism of a multi-step reaction, changes in the protein conformation at different time-points need to be visualized. Hence, 'time-resolved'

crystallography involves obtaining snapshots of the protein in action and then putting them together to form 'molecular movies'.

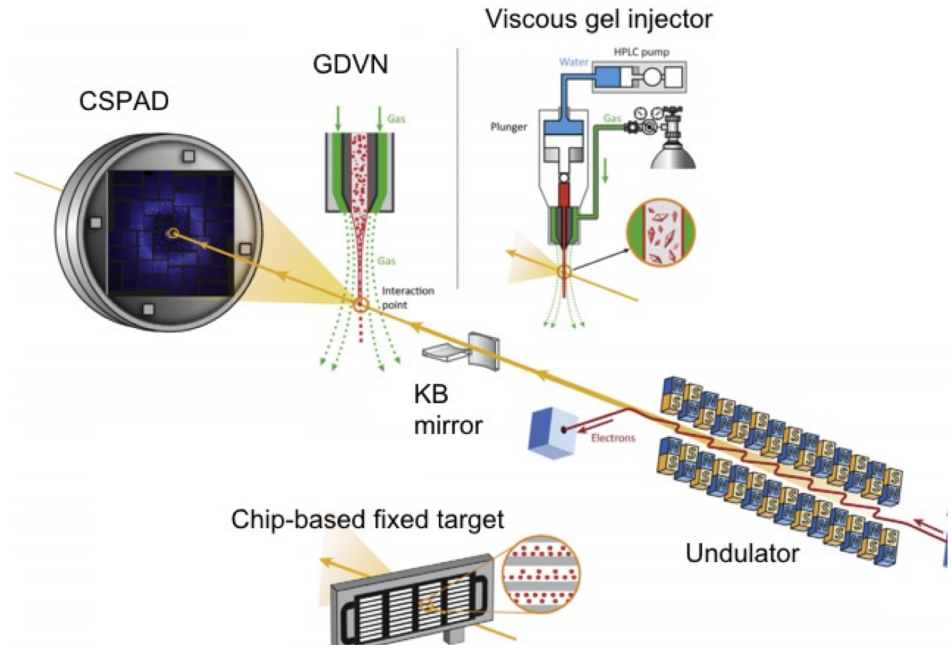

Figure 1.10: **Strategy for using XFELs for serial femtosecond crystallography.**

Undulators induce SASE that generates bright X-ray pulses. These are focused using KB-mirrors into the interaction region with sample that maybe delivered using Gas Dynamic Virtual Nozzle (GDVN), Viscous gel injector or fixed target approaches. Diffraction patterns generated are collected by CSPAD pixel array detector. Image edited from Johansson et.al., 2017.

The principle of time-resolved crystallography is based on initiating a reaction in all molecules in the crystal and imaging the conformational changes at specified time-points along the course of the reaction. Depending on the nature of the study, the reaction initiation can done by using light (pump-probe), by mixing with small molecules (substrate, inhibitors , ligands) or physical factors (temperature, pH etc.).

First time resolved crystallography experiments were done at synchrotrons, where large crystals and a polychromatic 'pink' beam was used for Laue diffraction. Since, the

Bragg condition is dependent on the wavelength, a solution for constructive interference at a given angle and at a fixed wavelength can be represented as a sphere in the reciprocal lattice called Ewald sphere. In a Laue experiment, the X-ray beam has a broad bandwidth of 1 – 5 %. The Ewald sphere has different radii based on the energy of the incident beam and thereby multiple planes in a crystal meet the Bragg condition at once. Thereby a large part of the reciprocal space can be probed . However the reflections become very closely spaced and the patterns are difficult to index.

The range of wavelength in the case of a pink beam, helps in collecting complete reflections covering a large continuous range of the Ewald sphere. Also, the complete spectrum has significantly more photon flux, leading to improved scattering caused by different energies. As a large part of the Ewald sphere is covered in one shot, fewer diffraction patterns are needed for a complete data set in comparison to monochromatic data collection. However, large crystals that are not very prone to X-ray damage are necessary.

Unfortunately, using the traditional approach for obtaining X-ray pulses, the shortest time duration that can explored using shutter systems is about 100 picoseconds. This excludes key biological processes because light absorption, bond breakage, and isomerizations of molecules occur over a few fs. Radiation damage caused by the broad spectrum is also significantly larger and the lack of cryo-preservation (in order to study reaction dynamics) leads to damage both in the molecules and the crystal lattice. Non light driven systems are even more difficult to study as the rate of diffusion of chemical agents across the crystal generates heterogeneous states in different molecules in the crystal and this could take several seconds. Assuming that does not affect crystal diffraction, the electron density maps generated by such crystals will be inconclusive because it would represent different conformations and the resultant structure would have inaccuracies.

Additionally, since one diffraction pattern is not sufficient for generating enough Bragg reflections for solving a structure and collecting a dataset involves initiating the reaction more than once. This restricts the application of this method for studying irreversible reactions (Moffat, n.d.).

As described earlier, SFX utilizes a new crystal for each shot, potentially outrunning radiation damage. The extremely short X-ray pulses generated by an XFEL permit trapping short-lived reaction intermediates (Pande et al., 2016) and the high beam-brilliance permits analysis of weakly scattering microcrystals, that can be uniformly excited leading to homogenous progression of the state of all molecules in the crystal. The strategy for TR-SFX at XFELs is discussed further in Chapter 2 and 3 using PSII as an example.

XFELs permit specialized experiments that need ultrashort pulses or for studying damage-free structures of proteins or single particles. With rapid advances being made in synchrotrons and other complimentary techniques like cryo-electron microscopy and micro electron diffraction, many avenues are now available for studying the structures of macromolecules, but SFX at XFELs is considered to be the primary method for time resolved studies of biomolecules. Also, more XFELs have been made available for the researchers over the last year and this has permitted support for a growing user-base.

1.5 Cryogenic Electron Microscopy

Crystallization of macromolecules and more importantly producing well-diffracting, large crystals can require significant cost in protein production and effort in crystallization spanning decades of time (Ng et al., 2003). SFX overcomes disadvantages with respect to radiation damage inherent in standard methods of X-ray diffraction (Chapman et al., 2011; Schlichting, 2015), but producing large amounts of homogenous

microcrystals needs a lot of sample, skill and precision. Also, restraining protein molecules in a crystalline state may select for a single molecular conformational state or might induce structural artifacts that do not reflect the physiological state, especially for the surface residues and points of crystal contacts (Singh et al., 2018).

With recent advances, Cryogenic Electron Microscopy (Cryo-EM) has emerged as a powerful tool for structural biologists. In 2015, a buzz was created in the scientific community when Nature Methods recognized Cryo-EM as 'the Method of the Year'. Subsequently, the technique was greatly acknowledged when Dubochet, Frank, and Henderson were awarded the 'Nobel prize in Chemistry' in 2017 for conceptualizing, pioneering, and making the technique applicable for biological samples (CALLAWAY, 2017).

The key advantage that distinguishes Cryo-EM is the ability to study macromolecules in a frozen hydrated state (discussed further in Section 5.3). Moreover, for Single Particle Imaging (SPI) methods there is no need for crystals, large production of protein or large national facilities for data collection which make the technique more universally accessible and versatile to study a larger realm of macromolecules. For other techniques such as Cryogenic Electron Tomography (CryoET) (Lučić et al., 2005), which has the potential to image frozen hydrated cells to organoids at molecular resolutions, the ability to address truly native assembly states in a physiologically relevant context is now possible. Microcrystalline electron diffraction (MicroED) is also available and proven electron diffraction of micron to nanometer sized crystals can achieve medium to high resolution structures of even large protein complexes (Rodriguez et al., 2017).

The recent technological advances (described in section 1.5.2.), especially the introduction of direct electron detectors which allow to correct for electron damage by fast frame rates, which allows for extrapolation to the structure of the molecule before it was

damaged by the electron beam brought fast advances in the Cryo-EM field. Before these advances it was believed that high resolution structures determined by by SPI and Cryo-EM in general would be limited to highly ordered icosahedral complexes in the megadalton size range like viruses. In 2014, Lu and co-workers were able to solve a 4.5 A structure of a 170 kDa asymmetrical membrane protein (γ-secretase) involved in Alzheimer's disease (Lu et al., 2014). Shortly thereafter, a 2.2 A structure of β-galactosidase bound to its inhibitor was solved (Bartesaghi et.al., 2015), proving the potential for solving high resolution structures using Cryo-EM.

Cryo-EM has been established for biomolecules after systematically overcoming challenges with respect to lack of contrast, establishing cryo-conditions that minimize sample disruption , instrumentation, image correction and processing. The major breakthrough was propelled by the development of the CMOS-APS direct electron detector

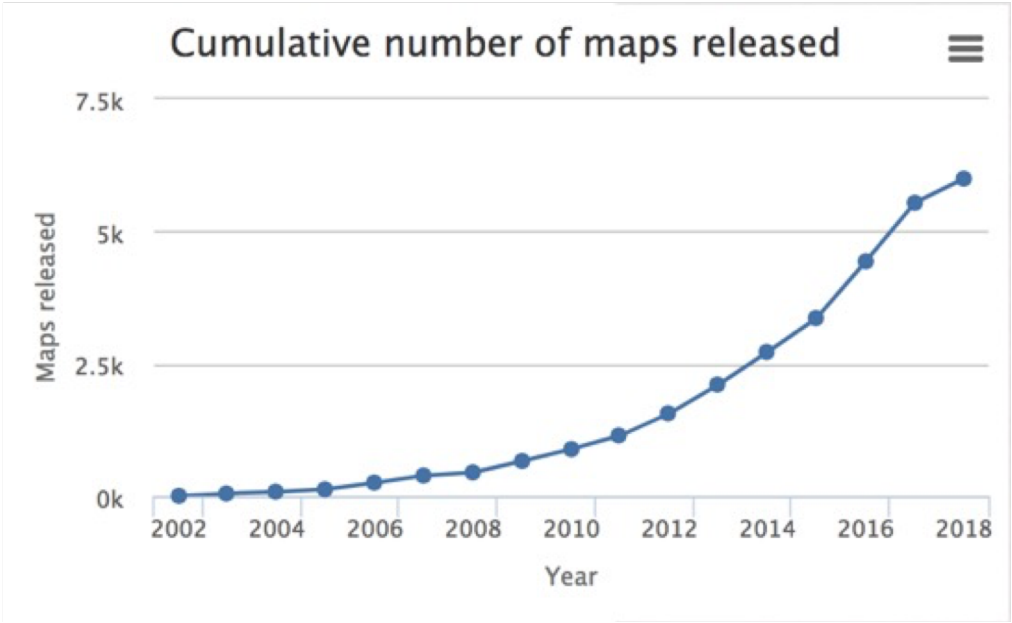

Figure 1.11: **Sum of all density maps released in EMDB for biomolecules.**
Statistics were retrieved on 08 April 2018. A total of 5998 maps have been reported with 456 maps being solved in 2018. This steep slope indicates the increase in popularity of Cryo-EM among structural biologists.

and the ability to overcome the resolution loss created by beam induced motion and ionization that occurs during imaging of frozen hydrated material as well as the poor signal to noise ratio (SNR) in low dose images of weak phase objects.

According to the Electron Microscopy Data Bank (EMDB), there is a steep slope of upwards trend in structures of biological macromolecules being solved using Electron Microscopy as depicted in Figure 1.11. The following sections briefly summarize the principals involved in cryo-EM and describe aspects that have contributed to the success of this new and burgeoning technique.

1.5.1. Transmission Electron Microscopy

The first electron microscope was invented by Ernst Ruska and Max Knoll in 1931 at the Berlin Technische Hochschule with the first commercial instruments being available in 1939. These instruments only achieved 10 nm resolutions due to the primitive electromagnetic lenses, however the wavelength of an electron beam (controlled by the acceleration voltage), is 3.70 pm at 100 KeV and 1.96 pm at 300 keV. This is much smaller than that of visible light photons (250 nm to 800 nm) or even x-rays (0.01 nm to 10 nm) and thereby has the potential to permit visualization of sub-Angstrom features in modern Aberration Corrected EMs (ACEMs). These modern aberration corrected EMs allow visualization of the arrangement of atoms, electronic bonds and band gaps in hard material, but traditionally, had limited resolution in soft matter such as biological macromolecules because of the large ionizing strength of the high voltage beams, that lead to massive damage of the sample. Further challenges are the weak phasing power provided by the low atomic number atoms in biological macromolecules, and the need for imaging in a high vacuum environment that is incompatible with hydrated samples.

Initially, to overcome these limitations, biologist dehydrated their samples, embedding them in plastic resins for thin sectioning and induced contrast with heavy metal atom stains specific for biological functional groups such as phosphates and amines. These steps limited the resolution and native state of the macromolecules in cells and tissues. The development of cryogenic TEM first allowed the introduction of hydrated samples into the high vacuum environment of the electron microscope, while also reducing the effects of the ionizing electron beam on soft materials and the molecular artefacts induced by dehydration and heavy atom staining. This vitrification (Adrian and Dubochet et.al., 1984), thus overcame significant limitations in imaging of soft matter by electron sources.

Electron microscopes utilize high voltage potentials to accelerate electrons from a point source filament called an electron gun. Unlike x-rays, electrons are readily focused due to their inherent negative charge using a series of electromagnetic lenses. Electron beams require 10^{-9} Torr vacuum to maintain coherence but otherwise an EM shows similarities to an optical light microscope with condenser and objective lenses.

There are multiple interactions that can occur at the level of the specimen but these can most simply be understood as either elastic scattering or inelastic scattering. In elastic scattering, the energy of the electrons is not altered by the scattering event and these electrons are used for imaging. Inelastically scattered electrons interact with the specimen and can induce a number of spectroscopically relevant events that are useful in determining elemental composition and arrangement, but generate noise in images and contribute to chromatic aberration (Buban et al., 2010) (David Williams and Barry Carter, “Transmission Electron Microscopy: A textbook for material sciences”).

Image formation, simply put, arises from elastically scattered electrons selected by an aperture, focused by the objective lens generating an amplitude contrast and further passed through projector lens for magnification before being recorded.

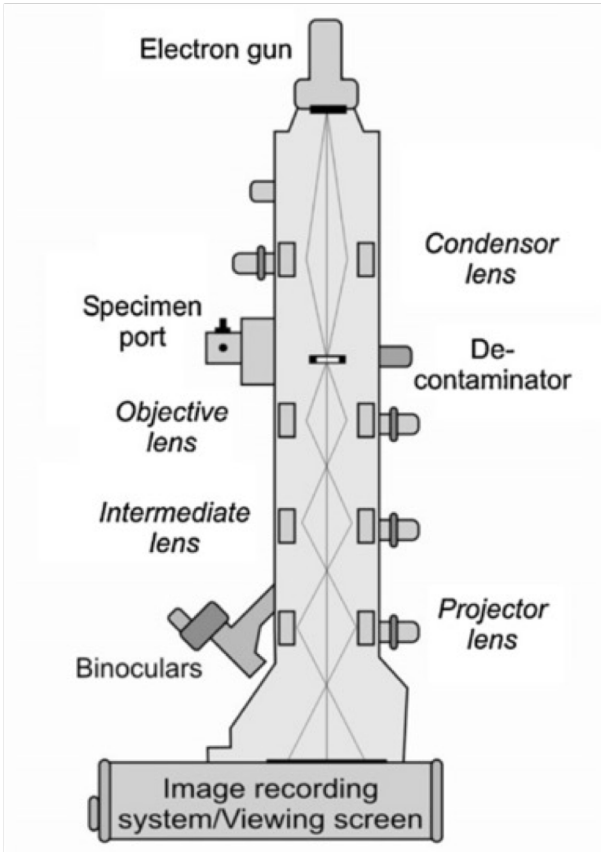

Figure 1.12: **General schematic of a TEM.** Seen in the image is the path of the electrons in a Transmission Electron Microscope and various components used to focus the electron beam. Image from Kuntsche et.al., 2011.

1.5.2. Resolution revolution

Several factors limit the resolution of structures generated by EM, but the most prevalent reasons are not related to the optics of the modern electron microscopes in use today which can achieve point resolutions of 1.9 A readily in TEMs and 0.8 A in ACEMs. The key factors that limit biological macromolecular resolution are sample drift and bean

induced motions as well as damage of the sample generated by its interaction with the electron beam, which blur images. Further factors are sample heterogeneity or conformation flexibility which limit the ability to correctly sort the particles into subclasses which is needed to allow for averaging of molecules. The electron beam is much more damaging than X-rays as interaction of electrons with matter is 1000 times stronger that interaction with X-rays. The electron induced damage thereby very fast destroys the molecules. Collaborative efforts in various fields have contributed towards achieving near-atomic resolution and this 'resolution revolution' can be attributed to the following key factors.

1.5.3. Progress in instrumentation

In modern electron microscopes, the electron source is a highly coherent Field Emission Gun (FEG). Electrons are emitted when a strong positive field (> 10^6 V/m) is created by the anode placed near the sharp field emission tip, made of tungsten (W) (Galvin, 1997). FEGs work better than former thermionic sources because they produce colder point electron sources in the filament, with lower thermal energy spread i.e. more spatial and temporal coherence. The electron beams thus generated are further focused by spherical lenses. Improved focusing lenses with lower spherical and chromatic aberrations, also contribute towards improvement in the coherence of the beam. Furthermore, using advanced energy filters, in-elastically scattered waves can be filtered out in the column, leading to increased SNR (Orlova and Saibil, 2011).

Optimization in sample preparation techniques by employing various strategies for vitrification (discussed further in section 5.3) have greatly contributed to preserving the sample during freezing by avoidance of ice-formation. Plunge freezing (Dobro et al., 2010) can be performed by using several automated freezing robots by Leica, FEI or Gatan. These

offer various features that may be suitable for specific samples and the superior quality of the vitreous “glass-like” ice is highly reproducible for numerous grids (Thompson et.al., 2016). Efficiency of data collection for Cryo-EM was enhanced by automation using software packages like UCSFImage (Li et al., 2015), Leginon (Suloway et al., 2005) and SerialEM (Mastronarde, 2005).

In order to harness the complete potential of Cryo-EM, higher SNRs are desirable and the increased efficiency of detectors has played a significant role here. Previously used scintillator based charged coupled devices predicted the location of transmitted electrons with low detective quantum efficiency (Wu et al., 2016). The new generation of Direct-electron Detection Devices (DDD) use complimentary metal-oxide semiconductor (CMOS) cameras that have a faster read-out that permit collection of dose-fractionated image stacks (Grigorieff, 2013). Using these stacks, correction of stage or beam-induced motion can be performed, thus, extracting the high resolution features of the images collected (Campbell et al., 2012). DDDs and data collection as stacks also present a strategy to exclude high-frequency noise produced by radiation damage in later frames (Li et al., 2013) thereby enabling high resolution structure determination approaching a resolution close to 2 A.

1.5.4. Improvements in image processing

Since the images obtained by Cryo-EM are 2D projections of a 3D structures, interpreting such superimposed structures can be difficult (Egelman, 2016). A breakthrough that permitted error-minimized 3D classification was the development of statistical algorithms based on maximum-likelihood procedures (Sigworth, 2016). At low SNRs, this method is less susceptible to initial model bias and over-refinement. Subsequently, several alternatives of this approach have been developed and currently,

regularized likelihood approaches in the RELION software package (Scheres, 2012) have proven to be powerful for both 3D classification and high-resolution reconstruction, leading to their immense popularity.

Beam-induced motions in sample (discussed further in Section 5.5.2) have been monitored by using the movie mode of the DDDs (Campbell et al., 2012). These motions are caused by both expansion of the carbon film and radical generation in the sample. Correction of these motions lead to improvement in SNR for individual particle images and leads to overall improvement in resolution by 'unbluring' the images (Bai et al., 2015). Finally, improvements in computer hardware have allowed for larger reconstructions to be computed by 64-bit memory addressing and faster CPUs.

Collectively, improvements associated with Cryo-EM have contributed towards understanding of biological systems, without the need for crystallization, making it increasingly popular with structural biologists. All techniques in structural biology discussed here, have specific advantages compared to each other and when used complimentarily, are advancing our ability to study complex systems and attain accurate knowledge that is relevant to the scientific community.

1.6 Objectives of this thesis

A greater understanding of the structural details of proteins involved in photosynthesis would contribute in mechanistic details of both excitation energy and electron transfer. Using TR-SFX, nanocrystals can be illuminated "on the fly" and resultant changes in protein conformation can be captured by interaction of the crystals with the XFEL beam, potentially without radiation damage. This presents an opportunity to evaluate changes in the oxygen-evolving cluster of PSII, unlocking the secrets of

effectively trapping solar energy in Photosynthesis which might be applied in the future for artificial systems.

The structure of PSI from the thermophilic cyanobacterium TS elongatus has been solved to 2.5 A (Jordan et al., 2001) by X-ray crystallography. But long range disorder indicated by high mosaicity has prevented improvement in the structure for more than a decade. The goal of this part of my thesis was to develop innovative methods for growing well-ordered large crystals to improve the resolution of the Photosystem I structure. This would contribute in our understanding of interactions between chlorophylls with other cofactors and our understanding how PSI achieves a quantum efficiency of close to 99.99 % for the excitation energy transfer. Also, PSI can exist in the membrane of cyanobacteria as monomers, trimers and tetramers in different organisms and their inter-monomer interactions are not completely understood. A higher resolution structure would help in understanding the advantages provided to the organism because of oligomerization of PSI.

Another objective that is explored in this thesis is using PSI as a model protein for Cryo-EM. Comparing structures generated by complimentary techniques would help validate the structure of PSI, eventually enabling the structural elucidation of difficult to crystallize large complexes involved in photosynthesis.

References

Bai, X., McMullan, G., Scheres, S.H.., 2015. How cryo-EM is revolutionizing structural biology. Trends in Biochemical Sciences 40, 49–57. https://doi.org/10.1016/j.tibs.2014.10.005

Bragg, W.L., 1913. The Structure of Some Crystals as Indicated by Their Diffraction of X-rays. Proceedings of the Royal Society A: Mathematical, Physical and Engineering Sciences 89, 248–277. https://doi.org/10.1098/rspa.1913.0083

Buban, J.P., Ramasse, Q., Gipson, B., Browning, N.D., Stahlberg, H., 2010. High-resolution low-dose scanning transmission electron microscopy. Journal of Electron Microscopy 59, 103–112. https://doi.org/10.1093/jmicro/dfp052

Caffrey, M., Li, D., Howe, N., Shah, S.T.A., 2014. “Hit and run” serial femtosecond crystallography of a membrane kinase in the lipid cubic phase. Philosophical Transactions of the Royal Society B: Biological Sciences 369, 20130621–20130621. https://doi.org/10.1098/rstb.2013.0621

CALLAWAY, E., n.d. Molecular-imaging pioneers scoop Nobel 1.

Campbell, M.G., Cheng, A., Brilot, A.F., Moeller, A., Lyumkis, D., Veesler, D., Pan, J., Harrison, S.C., Potter, C.S., Carragher, B., Grigorieff, N., 2012. Movies of Ice-Embedded Particles Enhance Resolution in Electron Cryo-Microscopy. Structure 20, 1823–1828. https://doi.org/10.1016/j.str.2012.08.026

Chapman, H.N., Fromme, P., Barty, A., White, T.A., Kirian, R.A., Aquila, A., Hunter, M.S., Schulz, J., DePonte, D.P., Weierstall, U., Doak, R.B., Maia, F.R.N.C., Martin, A.V., Schlichting, I., Lomb, L., Coppola, N., Shoeman, R.L., Epp, S.W., Hartmann, R., Rolles, D., Rudenko, A., Foucar, L., Kimmel, N., Weidenspointner, G., Holl, P., Liang, M., Barthelmess, M., Caleman, C., Boutet, S., Bogan, M.J., Krzywinski, J., Bostedt, C., Bajt, S., Gumprecht, L., Rudek, B., Erk, B., Schmidt, C., Hömke, A., Reich, C., Pietschner, D., Strüder, L., Hauser, G., Gorke, H., Ullrich, J., Herrmann, S., Schaller, G., Schopper, F., Soltau, H., Kühnel, K.-U., Messerschmidt, M., Bozek, J.D., Hau-Riege, S.P., Frank, M., Hampton, C.Y., Sierra, R.G., Starodub, D., Williams, G.J., Hajdu, J., Timneanu, N., Seibert, M.M., Andreasson, J., Rocker, A., Jönsson, O., Svenda, M., Stern, S., Nass, K., Andritschke, R., Schröter, C.-D., Krasniqi, F., Bott, M., Schmidt, K.E., Wang, X., Grotjohann, I., Holton, J.M., Barends, T.R.M., Neutze, R., Marchesini, S., Fromme, R., Schorb, S., Rupp, D., Adolph, M., Gorkhover, T., Andersson, I., Hirsemann, H., Potdevin, G., Graafsma, H., Nilsson, B., Spence, J.C.H., 2011. Femtosecond X-ray protein nanocrystallography. Nature 470, 73–77. https://doi.org/10.1038/nature09750

Conrad, C.E., Basu, S., James, D., Wang, D., Schaffer, A., Roy-Chowdhury, S., Zatsepin, N.A., Aquila, A., Coe, J., Gati, C., Hunter, M.S., Koglin, J.E., Kupitz, C., Nelson, G., Subramanian, G., White, T.A., Zhao, Y., Zook, J., Boutet, S., Cherezov, V., Spence, J.C.H., Fromme, R., Weierstall, U., Fromme, P., 2015. A novel inert crystal delivery medium for serial femtosecond crystallography. IUCrJ 2, 421–430. https://doi.org/10.1107/S2052252515009811

DePonte, D.P., Weierstall, U., Schmidt, K., Warner, J., Starodub, D., Spence, J.C.H., Doak, R.B., 2008. Gas dynamic virtual nozzle for generation of microscopic droplet streams. Journal of Physics D: Applied Physics 41, 195505. https://doi.org/10.1088/0022-3727/41/19/195505

Dobro, M.J., Melanson, L.A., Jensen, G.J., McDowall, A.W., 2010. Plunge Freezing for Electron Cryomicroscopy, in: Methods in Enzymology. Elsevier, pp. 63–82. https://doi.org/10.1016/S0076-6879(10)81003-1

Egelman, E.H., 2016. The Current Revolution in Cryo-EM. Biophysical Journal 110, 1008–1012. https://doi.org/10.1016/j.bpj.2016.02.001

Eng, P.J., Newville, M., Rivers, M.L., Sutton, S.R., 1998. Dynamically figured Kirkpatrick Baez x-ray microfocusing optics, in: McNulty, I. (Ed.), . pp. 145–156. https://doi.org/10.1117/12.330342

Fromme, R., Ishchenko, A., Metz, M., Chowdhury, S.R., Basu, S., Boutet, S., Fromme, P., White, T.A., Barty, A., Spence, J.C.H., Weierstall, U., Liu, W., Cherezov, V., 2015. Serial femtosecond crystallography of soluble proteins in lipidic cubic phase. IUCrJ 2, 545–551. https://doi.org/10.1107/S2052252515013160

Fuller, F.D., Gul, S., Chatterjee, R., Burgie, E.S., Young, I.D., Lebrette, H., Srinivas, V., Brewster, A.S., Michels-Clark, T., Clinger, J.A., Andi, B., Ibrahim, M., Pastor, E., de Lichtenberg, C., Hussein, R., Pollock, C.J., Zhang, M., Stan, C.A., Kroll, T., Fransson, T., Weninger, C., Kubin, M., Aller, P., Lassalle, L., Bräuer, P., Miller, M.D., Amin, M., Koroidov, S., Roessler, C.G., Allaire, M., Sierra, R.G., Docker, P.T., Glownia, J.M., Nelson, S., Koglin, J.E., Zhu, D., Chollet, M., Song, S., Lemke, H., Liang, M., Sokaras, D., Alonso-Mori, R., Zouni, A., Messinger, J., Bergmann, U., Boal, A.K., Bollinger, J.M., Krebs, C., Högbom, M., Phillips, G.N., Vierstra, R.D., Sauter, N.K., Orville, A.M., Kern, J., Yachandra, V.K., Yano, J., 2017. Drop-on-demand sample delivery for studying biocatalysts in action at X-ray free-electron lasers. Nature Methods 14, 443–449. https://doi.org/10.1038/nmeth.4195

Garman, E.F., 2010. Radiation damage in macromolecular crystallography: what is it and why should we care? Acta Crystallographica Section D Biological Crystallography 66, 339–351. https://doi.org/10.1107/S0907444910008656

Grigorieff, N., 2013. Direct detection pays off for electron cryo-microscopy. eLife 2. https://doi.org/10.7554/eLife.00573

Henderson, R., 1995. The potential and limitations of neutrons, electrons and X-rays for atomic resolution microscopy of unstained biological molecules. Quarterly Reviews of Biophysics 28, 171. https://doi.org/10.1017/S003358350000305X

Hirata, K., Shinzawa-Itoh, K., Yano, N., Takemura, S., Kato, K., Hatanaka, M., Muramoto, K., Kawahara, T., Tsukihara, T., Yamashita, E., Tono, K., Ueno, G., Hikima, T., Murakami, H., Inubushi, Y., Yabashi, M., Ishikawa, T., Yamamoto, M., Ogura, T., Sugimoto, H., Shen, J.-R., Yoshikawa, S., Ago, H., 2014. Determination of damage-free crystal structure of an X-ray–sensitive protein using an XFEL. Nature Methods 11, 734–736. https://doi.org/10.1038/nmeth.2962

Holton, J.M., 2009. A beginner's guide to radiation damage. Journal of Synchrotron Radiation 16, 133–142. https://doi.org/10.1107/S0909049509004361

Holton, J.M., Frankel, K.A., 2010. The minimum crystal size needed for a complete diffraction data set. Acta Crystallographica Section D Biological Crystallography 66, 393–408. https://doi.org/10.1107/S0907444910007262

Jordan, P., Fromme, P., Witt, H.T., Klukas, O., Saenger, W., Krauû, N., 2001. Three-dimensional structure of cyanobacterial photosystem I at 2.5 AÊ resolution 411, 9.

Kupitz, C., Grotjohann, I., Conrad, C.E., Roy-Chowdhury, S., Fromme, R., Fromme, P., 2014. Microcrystallization techniques for serial femtosecond crystallography using photosystem II from Thermosynechococcus elongatus as a model system. Philosophical Transactions of the Royal Society B: Biological Sciences 369, 20130316–20130316. https://doi.org/10.1098/rstb.2013.0316

Kupitz, C., Olmos, J.L., Holl, M., Tremblay, L., Pande, K., Pandey, S., Oberthür, D., Hunter, M., Liang, M., Aquila, A., Tenboer, J., Calvey, G., Katz, A., Chen, Y., Wiedorn, M.O., Knoska, J., Meents, A., Majriani, V., Norwood, T., Poudyal, I., Grant, T., Miller, M.D., Xu, W., Tolstikova, A., Morgan, A., Metz, M., Martin-Garcia, J.M., Zook, J.D., Roy-Chowdhury, S., Coe, J., Nagaratnam, N., Meza, D., Fromme, R., Basu, S., Frank, M., White, T., Barty, A., Bajt, S., Yefanov, O., Chapman, H.N., Zatsepin, N., Nelson, G., Weierstall, U., Spence, J., Schwander, P., Pollack, L., Fromme, P., Ourmazd, A., Phillips, G.N., Schmidt, M., 2017. Structural enzymology using X-ray free electron lasers. Structural Dynamics 4, 044003. https://doi.org/10.1063/1.4972069

Li, X., Mooney, P., Zheng, S., Booth, C.R., Braunfeld, M.B., Gubbens, S., Agard, D.A., Cheng, Y., 2013. Electron counting and beam-induced motion correction enable near-atomic-resolution single-particle cryo-EM. Nature Methods 10, 584–590. https://doi.org/10.1038/nmeth.2472

Li, X., Zheng, S., Agard, D.A., Cheng, Y., 2015. Asynchronous data acquisition and on-the-fly analysis of dose fractionated cryoEM images by UCSFImage. Journal of Structural Biology 192, 174–178. https://doi.org/10.1016/j.jsb.2015.09.003

Liu, W., Wacker, D., Gati, C., Han, G.W., James, D., Wang, D., Nelson, G., Weierstall, U., Katritch, V., Barty, A., Zatsepin, N.A., Li, D., Messerschmidt, M., Boutet, S., Williams, G.J., Koglin, J.E., Seibert, M.M., Wang, C., Shah, S.T.A., Basu, S., Fromme, R., Kupitz, C., Rendek, K.N., Grotjohann, I., Fromme, P., Kirian, R.A., Beyerlein, K.R., White, T.A., Chapman, H.N., Caffrey, M., Spence, J.C.H., Stevens, R.C., Cherezov, V., 2013. Serial Femtosecond Crystallography of G Protein-Coupled Receptors. Science 342, 1521–1524. https://doi.org/10.1126/science.1244142

Loll, B., Kern, J., Saenger, W., Zouni, A., Biesiadka, J., 2005. Towards complete cofactor arrangement in the 3.0 Å resolution structure of photosystem II. Nature 438, 1040–1044. https://doi.org/10.1038/nature04224

Lu, P., Bai, X., Ma, D., Xie, T., Yan, C., Sun, L., Yang, G., Zhao, Y., Zhou, R., Scheres, S.H.W., Shi, Y., 2014. Three-dimensional structure of human γ-secretase. Nature 512, 166–170. https://doi.org/10.1038/nature13567

Lučić, V., Förster, F., Baumeister, W., 2005. STRUCTURAL STUDIES BY ELECTRON TOMOGRAPHY: From Cells to Molecules. Annual Review of Biochemistry 74, 833–865. https://doi.org/10.1146/annurev.biochem.73.011303.074112

Martin-Garcia, J.M., Conrad, C.E., Nelson, G., Stander, N., Zatsepin, N.A., Zook, J., Zhu, L., Geiger, J., Chun, E., Kissick, D., Hilgart, M.C., Ogata, C., Ishchenko, A., Nagaratnam, N., Roy-Chowdhury, S., Coe, J., Subramanian, G., Schaffer, A., James, D., Ketwala, G., Venugopalan, N., Xu, S., Corcoran, S., Ferguson, D., Weierstall, U., Spence, J.C.H., Cherezov, V., Fromme, P., Fischetti, R.F., Liu, W., 2017. Serial millisecond crystallography of membrane and soluble protein microcrystals using synchrotron radiation. IUCrJ 4, 439–454. https://doi.org/10.1107/S205225251700570X

Mastronarde, D.N., 2005. Automated electron microscope tomography using robust prediction of specimen movements. Journal of Structural Biology 152, 36–51. https://doi.org/10.1016/j.jsb.2005.07.007

Meents, A., Gutmann, S., Wagner, A., Schulze-Briese, C., 2010. Origin and temperature dependence of radiation damage in biological samples at cryogenic temperatures. Proceedings of the National Academy of Sciences 107, 1094–1099. https://doi.org/10.1073/pnas.0905481107

Moffat, K., n.d. Time-Resolved Crystallography 9.

Mueller, C., Marx, A., Epp, S.W., Zhong, Y., Kuo, A., Balo, A.R., Soman, J., Schotte, F., Lemke, H.T., Owen, R.L., Pai, E.F., Pearson, A.R., Olson, J.S., Anfinrud, P.A., Ernst, O.P., Dwayne Miller, R.J., 2015. Fixed target matrix for femtosecond time-resolved and in situ serial micro-crystallography. Structural Dynamics 2, 054302. https://doi.org/10.1063/1.4928706

Nave, C., 1998. A Description of Imperfections in Protein Crystals. Acta Crystallographica Section D Biological Crystallography 54, 848–853. https://doi.org/10.1107/S0907444998001875

Neutze, R., Hajdu, J., 1997. Femtosecond time resolution in x-ray diffraction experiments. Proceedings of the National Academy of Sciences 94, 5651–5655. https://doi.org/10.1073/pnas.94.11.5651

Neutze, R., Wouts, R., Hajdu, J., 2000. Potential for biomolecular imaging with femtosecond X-ray pulses 406, 6.

Ng, J.D., Gavira, J.A., Garcı´a-Ruı´z, J.M., 2003. Protein crystallization by capillary counterdiffusion for applied crystallographic structure determination. Journal of Structural Biology 142, 218–231. https://doi.org/10.1016/S1047-8477(03)00052-2

Orlova, E.V., Saibil, H.R., 2011. Structural Analysis of Macromolecular Assemblies by Electron Microscopy. Chemical Reviews 111, 7710–7748. https://doi.org/10.1021/cr100353t

Pande, K., Hutchison, C.D.M., Groenhof, G., Aquila, A., Robinson, J.S., Tenboer, J., Basu, S., Boutet, S., DePonte, D.P., Liang, M., White, T.A., Zatsepin, N.A., Yefanov, O., Morozov, D., Oberthuer, D., Gati, C., Subramanian, G., James, D.,

Zhao, Y., Koralek, J., Brayshaw, J., Kupitz, C., Conrad, C., Roy-Chowdhury, S., Coe, J.D., Metz, M., Xavier, P.L., Grant, T.D., Koglin, J.E., Ketawala, G., Fromme, R., rajer, V., Henning, R., Spence, J.C.H., Ourmazd, A., Schwander, P., Weierstall, U., Frank, M., Fromme, P., Barty, A., Chapman, H.N., Moffat, K., van Thor, J.J., Schmidt, M., 2016. Femtosecond structural dynamics drives the trans/cis isomerization in photoactive yellow protein. Science 352, 725–729. https://doi.org/10.1126/science.aad5081

Rodriguez, J.A., Eisenberg, D.S., Gonen, T., 2017. Taking the measure of MicroED. Current Opinion in Structural Biology 46, 79–86. https://doi.org/10.1016/j.sbi.2017.06.004

Roedig, P., Vartiainen, I., Duman, R., Panneerselvam, S., Stübe, N., Lorbeer, O., Warmer, M., Sutton, G., Stuart, D.I., Weckert, E., David, C., Wagner, A., Meents, A., 2015. A micro-patterned silicon chip as sample holder for macromolecular crystallography experiments with minimal background scattering. Scientific Reports 5. https://doi.org/10.1038/srep10451

Scheres, S.H.W., 2012. RELION: Implementation of a Bayesian approach to cryo-EM structure determination. Journal of Structural Biology 180, 519–530. https://doi.org/10.1016/j.jsb.2012.09.006

Schlichting, I., 2015. Serial femtosecond crystallography: the first five years. IUCrJ 2, 246–255. https://doi.org/10.1107/S205225251402702X

Schmidt, M., 2013. Mix and Inject: Reaction Initiation by Diffusion for Time-Resolved Macromolecular Crystallography. Advances in Condensed Matter Physics 2013, 1–10. https://doi.org/10.1155/2013/167276

Schotte, F., Cho, H.S., Kaila, V.R.I., Kamikubo, H., Dashdorj, N., Henry, E.R., Graber, T.J., Henning, R., Wulff, M., Hummer, G., Kataoka, M., Anfinrud, P.A., 2012. Watching a signaling protein function in real time via 100-ps time-resolved Laue crystallography. Proceedings of the National Academy of Sciences 109, 19256–19261. https://doi.org/10.1073/pnas.1210938109

Sigworth, F.J., 2016. Principles of cryo-EM single-particle image processing. Microscopy 65, 57–67. https://doi.org/10.1093/jmicro/dfv370

Singh, D., Berntsen, K., Baakman, C., Vriend, G., Lahiri, T., 2018. A Critical Note on Symmetry Contact Artifacts and the Evaluation of the Quality of Homology Models. Symmetry 10, 25. https://doi.org/10.3390/sym10010025

Sugahara, M., Song, C., Suzuki, M., Masuda, T., Inoue, S., Nakane, T., Yumoto, F., Nango, E., Tanaka, R., Tono, K., Joti, Y., Kameshima, T., Hatsui, T., Yabashi, M., Nureki, O., Numata, K., Iwata, S., 2016. Oil-free hyaluronic acid matrix for serial femtosecond crystallography. Scientific Reports 6. https://doi.org/10.1038/srep24484

Suloway, C., Pulokas, J., Fellmann, D., Cheng, A., Guerra, F., Quispe, J., Stagg, S., Potter, C.S., Carragher, B., 2005. Automated molecular microscopy: The new Leginon

system. Journal of Structural Biology 151, 41–60. https://doi.org/10.1016/j.jsb.2005.03.010

Weierstall, U., James, D., Wang, C., White, T.A., Wang, D., Liu, W., Spence, J.C.H., Bruce Doak, R., Nelson, G., Fromme, P., Fromme, R., Grotjohann, I., Kupitz, C., Zatsepin, N.A., Liu, H., Basu, S., Wacker, D., Won Han, G., Katritch, V., Boutet, S., Messerschmidt, M., Williams, G.J., Koglin, J.E., Marvin Seibert, M., Klinker, M., Gati, C., Shoeman, R.L., Barty, A., Chapman, H.N., Kirian, R.A., Beyerlein, K.R., Stevens, R.C., Li, D., Shah, S.T.A., Howe, N., Caffrey, M., Cherezov, V., 2014. Lipidic cubic phase injector facilitates membrane protein serial femtosecond crystallography. Nature Communications 5. https://doi.org/10.1038/ncomms4309

Wu, S., Armache, J.-P., Cheng, Y., 2016. Single-particle cryo-EM data acquisition by using direct electron detection camera. Microscopy 65, 35–41. https://doi.org/10.1093/jmicro/dfv355

CHAPTER 2

CRYSTALLIZATION OF PHOTOSYSTEM II FOR TIME RESOLVED STRUCTURAL STUDIES USING X-RAY FREE ELECTRON LASER

Jesse Coe, Christopher Kupitz, Shibom Basu, Chelsie E. Conrad, Shatabdi Roy-Chowdhury, Raimund Fromme, Petra Fromme*

Department of Chemistry and Biochemistry, Arizona State University, Tempe, Arizona, USA

This chapter is a published review in Methods in Enzymology (vol 557 in 2015) on PSII and time-resolved studies at XFELs. Described here are details of protein purification, crystallization, characterization, sample delivery, data analysis and data interpretation for a typical TR-SFX experiment. My contribution was in writing the sections describing protein microcrystallization techniques and characterization of microcrystals. I also edited the manuscript and incorporated referee comments before resubmission. Copyright clearance from Elsevier has been procured (Appendix B).

Abstract

Photosystem II (PSII) is a membrane protein supercomplex that executes the initial reaction of photosynthesis in higher plants, algae and cyanobacteria. It captures the light from the sun to catalyze a transmembrane charge separation. In a series of four charge separation events, utilizing the energy from four photons, PSII oxidizes two water molecules to obtain dioxygen, 4 protons and 4 electrons. The light reactions of photosystems I and II (PSI and II) result in the formation of an electrochemical transmembrane proton gradient that is used for the production of ATP. Electrons that are

subsequently transferred from PSI via the soluble protein ferredoxin to ferredoxin-$NADP^+$ reductase that reduces $NADP^+$ to NADPH. The products of photosynthesis and the elemental oxygen evolved sustain all higher life on Earth. All oxygen in the atmosphere is produced by the oxygen evolving complex (OEC) in Photosystem II, a process that changed our planet from an anoxygenic to an oxygenic atmosphere 2.5 billion years ago. In this chapter, we provide recent insight into the mechanisms of this process and methods used in probing this question.

2.1 Introduction

Two and a half billion years ago oxygenic photosynthesis evolved resulting in the drastic oxygenation of Earth's atmosphere which led to an explosion of biodiversity and, eventually, the evolution of higher organisms. Photosystem II (PSII) is crucial to oxygenic photosynthesis. As indicated by the close homology of the OEC across many species, it has only substantially evolved once and the core functions and structure have been maintained through billions of years of evolution. PSII is large membrane protein complex made up of 19 protein subunits and over 50 non-covalent cofactors. During photoactivation, the OEC of this massive complex proceeds through a five state photochemical reaction, the Kok cycle, over the course of which four charge separations occur (Fig 1). One electron and one proton are extracted in each of the charge separation events, leading to two water molecules being deconstructed until the formation of dioxygen each cycle. Photosystem II is able to oxidize water, driven by visible light and catalyzed by earth abundant metals at a low overpotential of +1.1 V (Wydrzynski et.al., 2006). However, with such a high redox potential, it operates at the limit of the stability of biomolecules. The unraveling of the mechanism of water splitting in PSII is one of the major goals in bioenergetics as it would open the door to the development of synthetic

oxygen evolving systems that combine the major catalytic features of PSII with the stability of artificial systems.

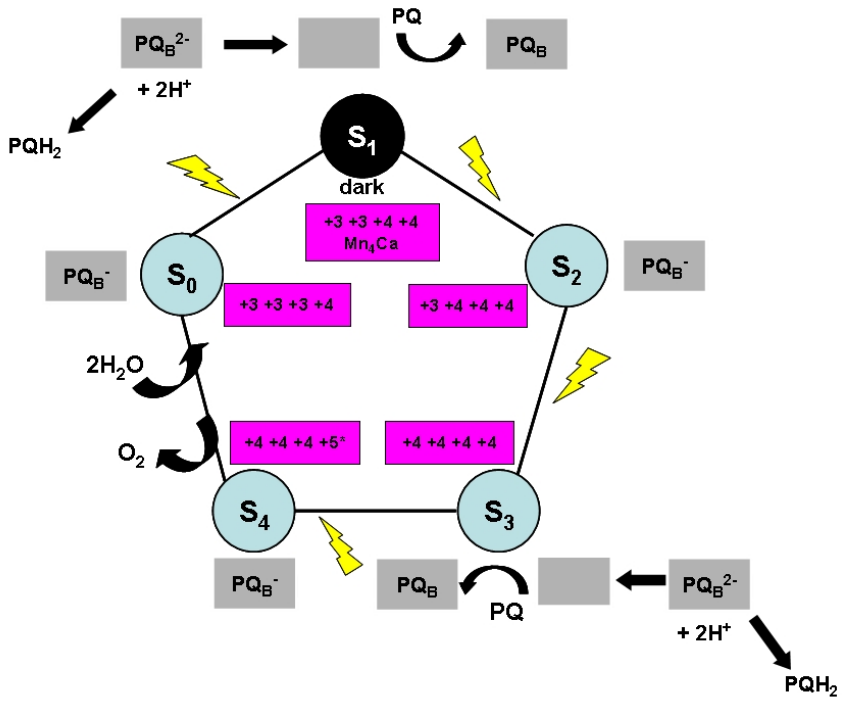

Figure 2.1: **Schematic of the Kok cycle showing photo induced kok cycle progression**

S-state transition from the dark S1 state to the S4 state where oxygen evolution occurs followed by a final photoexcitation returning the PSII to the dark S1 state. PQB is reduced at each excitation, leaving and being replaced by a fresh PQB upon arrival at the S3 and S1 states. Figure originally published in Kupitz and Basu et al., Nature 2014.

The first static structure of PSII was determined to 3.8 Å in 2001 (Zouni). The resolution was increased subsequently (Ferreira et al., 2004; Loll et al., 2005; Umena et al., 2011) and the highest resolution structures are now available at the near atomic resolution of 1.9 Å (Suga et al., 2015; Umena et al., 2011). In order to understand the catalytic mechanism at work, time resolved studies with microsecond time resolution are needed to explore the multiple photoexcited states in the Kok cycle (Renger, 2012).

Traditional macrocrystallography is unable to unravel the structure of the OEC in its different oxidation states due to site specific radiation damage of the OEC by X-ray photoreduction (Yano et al., 2005). X-ray absorption fine structure spectroscopic studies have indicated that the manganese ions in the OEC possess a high propensity to site specific X-ray induced reduction (Allakhverdiev, 2005). A bias may also arise with cryo-cooled crystals as data are collected far removed from biologically relevant temperatures. The recently developed method of serial femtosecond X-ray crystallography (SFX) has been used to investigate the structure of selected photoexcited states of PSII (Kern et al., 2014, 2013; Christopher Kupitz et al., 2014). Very recently, X-ray free electron lasers (XFELs) have also been used to determine the first high resolution undamaged dark structure of Photosystem II based on serial data collection on large cryo-cooled crystals (Suga et al., 2015).

Fundamentally, SFX is based upon using highly coherent, extremely brilliant, femtosecond hard X-ray pulses to collect thousands of X-ray diffraction snapshots on a hydrated stream of small crystals at room temperature (Chapman et al., 2011), enabling diffraction information to be obtained before the ensuing Coulomb explosion destroys the molecules including each measured crystal (Neutze et al., 2000). In this way, radiation damage is "outrun" in the data collection and samples can be probed at more biologically mimetic conditions compared to traditional protein macrocrystallography. Furthermore, by using a fresh crystal to produce each diffraction pattern, time-resolved photoexcitation processes can be probed by coupling an optical pump probe to the sample prior to interaction with the X-ray beam (Aquila et al., 2012; Neutze and Moffat, 2012; Spence et al., 2012). For the first time, irreversible processes are now able to be probed in a time resolved experiment due to the use of discrete crystals for each diffraction pattern. A delay time between the optical pumping and beam interaction as well as the number of times

the sample is flashed with light can be modulated to explore different transitory states. Recent work has advanced the knowledge of the structure and further advancements will ultimately be able to resolve the mechanism of photosynthetic water splitting and oxygen evolution. The method of time-resolved SFX (TR-SFX) has the potential to lead to a "molecular movie" of photosynthetic water splitting in the future. In this book chapter recent advancements of methods developed for TR-SFX of Photosystem II will be summarized and compared.

2.2. Isolation of Photosystem II

All structures solved so far from PSII are based on Photosystem II isolated from the thermophilic cyanobacteria *Thermosynechococcus elongatus* (*T. elongatus*) (Ferreira et al., 2004; Kern et al., 2014, 2013; Kupitz et al., 2014; Loll et al., 2005) and *Thermosynechococcus vulcanus (TS vulcanus)* (Kamiya and Shen, 2003; Suga et al., 2015; Umena et al., 2011). As Photosystem II undergoes the process of photodamage and repair (Aro et al., 1993) the reproducible growth of large qualities of the cyanobacteria is an essential prerequisite of all functional studies. Our group uses a large 122 L photobioreactor that has been developed together with the Pulse Institute, that controls temperature, pH, CO_2 and air flux and measure cell density which can be coupled to the light intensity for growth of *TS elongatus* for reproducible growth of the cells at low light conditions to minimize photodamage. The complete isolation procedure from cell harvest to growth of crystals is performed in one setting within 48 hours under dim green light which involves 3 re-crystallization steps. The methods have recently been published in Kupitz et al., 2014 *Phil. Trans. R. Soc. B.*

2.3. Crystallization for studies with FELs

Due to X-ray damage, macromolecular crystallography requires very large single crystals of PSII on the order of millimeters in size to allow for a shift of the crystals after each image during data collection. However, even with an extremely careful shift strategy such as applied in Umena et al., 2011, photoreduction is difficult to minimize, leading to a photoreduced structure of the OEC.

SFX studies depend on a continuously fresh stream of small crystals to obtain diffraction before destruction. This leads to the need for size homogeneous nano or microcrystals (on the order of 500 nm - 5 μm) created using novel crystallization techniques. New methods have been developed by our team using free interface crystallization to allow for reproducible growth of large quantities of microcrystals of PSII with a very narrow size distribution of centered around 1 um^3 as described in Kupitz et al., 2014, *Phil. Trans. R. Soc. B.* We will discuss the different methods used for the growth of PSII microcrystals below in more detail.

2.3.1. Batch methods and establishing the phase diagram

The batch method describes crystallization through a homogenized solution containing the protein and precipitant. Initial trials to establish knowledge of phase space are easily accessible using this method, owing to the highly controllable and quantifiable solution environment. Seed crystals can be added at different points in phase space and monitored to map out the phase diagram. Seed crystals will dissolve in the non-saturated zone, grow without additional nucleation in the metastable zone and induce nucleation of additional crystals in the nucleation zone. Particularly important is that the amount of induced nucleation scales with distance from the border between the

metastable and nucleation zones, permitting optimization of conditions with respect to yield, crystal size and homogeneity.

2.3.2. Free interface diffusion

Figure 2.1 shows a schematic of the free interface diffusion (FID) method developed for the growth of PSII nanocrystals that have been used for our TR-SFX studies (Kupitz et al., 2014). The method is based on the idea that in order to develop a so called "shower"

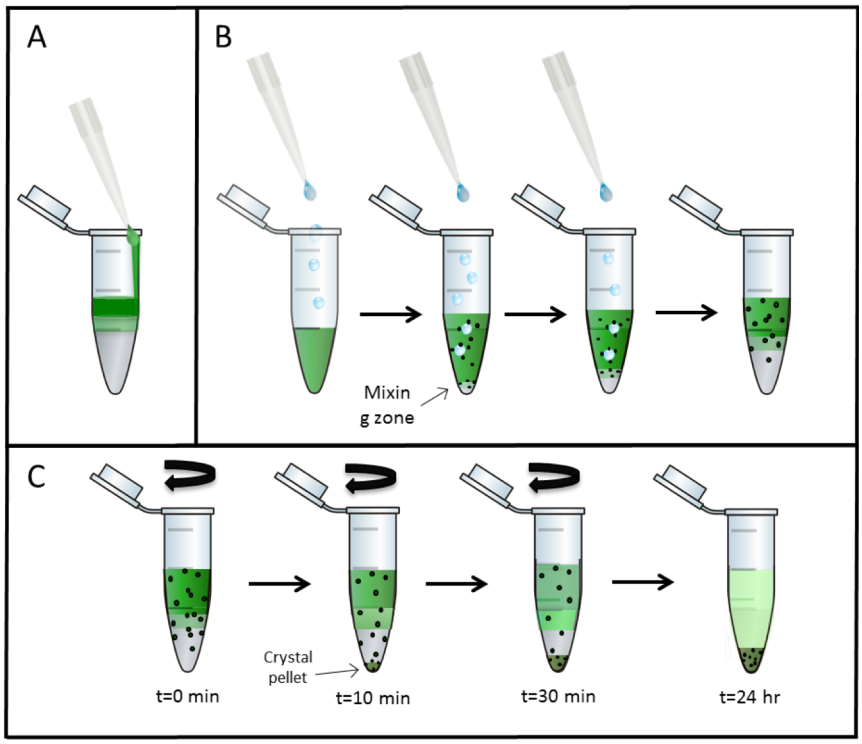

Figure 2.2: **Stepwise procedure depicting FID and FID centrifugation nanocrystallization techniques.**

(a) shows a minimal mixing layering scheme between the protein (green) and the precipitant (white). This results in few small crystals originating at the interface. (b) shows the precipitant being dropped through the protein, creating a slightly larger mixing zone than (a), resulting in a large shower of microcrystals. (c) shows the time progression when the experimental setup depicted in (b) is subjected to centrifugation, expediting the formation of crystals and causing a pellet of size homogeneous crystals to form. *Figure originally published in Kupitz et al., 2014.*

of small crystals, one must rapidly access a point in the nucleation zone of phase space so that a high nucleation rate is achieved. This provides an alternative to vapor diffusion experiments where it is often difficult to control crystal growth at high supersaturation.

The following procedure describes a way to access the phase space. This construction also results in the deposition of crystals into a pellet, which can be easily collected and allows for further quenching and control of crystal density. Free interface diffusion has been used for growth of larger crystals in a traditional setup, where crystallization occurs inside a capillary (Ng et al., 2003) By use of thin capillaries, diffusion is slowed so larger crystals are grown along a concentration gradient (McPHERSON, 1990). In contrast, for growth of nanocrystals rapid nucleation is desired. The precipitant, which has a higher density than the protein solution, is slowly added dropwise to the protein solution (see fig 2.2). The drops of precipitant passing through the protein solution cause the protein to interact with a high concentration of precipitant. This continues as the dense precipitant forms a layer underneath the solubilized protein. The interface between the two solutions allows for rapid nucleation. Once the crystals reach a certain size, they sediment into the precipitant where their growth is quenched. Centrifugation immediately after the formation of the interface not only results in crystals that can be seen within 30 minutes but also results in a more homogenous size distribution of crystals due to a rapid density separation. Thereby, the FID method provides an intrinsic quenching of crystal growth and a uniform size distribution for PSII crystals of 1 μm ± 500 nm (C. Kupitz et al., 2014).

2.3.3 Quenching

Once a yield of crystals has been determined to be at an acceptable size and distribution, it is desirable to quench any further growth prior to diffraction or during sample delivery. While the FID setup has a temporary quenching mechanism, it is not

sustainable due to the slow onset of equilibrium and complete mixing of the layers. It is important to remove the free protein that could lead to growth of existing crystals, further leading to clogging of injectors and a broader size distribution of crystals. Once the crystals form a pellet, the supernatant is removed and replaced by stabilization buffer that contains 1.25 times of all solutes in the crystallizing precipitant solution. This ensures the stabilization of existing crystals, both in the absence of free protein and through the presence of a more thermodynamically unfavorable solute environment, enabling a strong preference for PSII molecules to remain in the solid crystal phase.

2.3.4 Quantification of natural plastoquinone and addition of PQ_{decyl}

In order to investigate conformational changes at both the acceptor and donor site of PSII and to allow multiple laser excitation steps, it is important to verify the quinone content of the PSII in the crystals. PQ_B is a mobile electron carrier and light exposure must therefore be avoided during all preparation steps to ensure high occupancy of the QB bindings site with PQ. We have determined the PQ content of our crystals using high pressure liquid chromatography (HPLC) with a (C-18) column after each PEG 2000 precipitation step. The protein was then subjected to a pigment extraction using acetone according to the previously published protocol (Patzlaff and Barry, 1996). The presumed ratio of chlorophyll *a* to PQ is 76:4 at full quinone occupancy in *T. elongatus*. The area under each peak was integrated to obtain a ratio between chlorophyll *a* and PQ in the extracted sample. From this ratio, a percentage of PQ_B occupancy was calculated from an average value taken from 3 HPLC runs. This resulted in occupancies of 91.8 % before initial crystallization, 88.4 after the first recrystallization, 86.4 after the second recrystallization and 81.1 % after the third recrystallization step.

After two optical events, Q_B becomes doubly reduced to PQ^{2-} and leaves the binding site as PQH_2 and thus needs to be replaced for further oxidation to occur in order to reach the S_4 state. However, PQ is extremely difficult to obtain by synthesis or purification due to poor solubility caused by the long isoprene tail. As a substitute, a derivative of PQ with the same head group but an N-decyl chain instead of the isoprene tail, referred to as PQ_{decyl}, was synthesized. This PQ_{decyl} was added to the crystals so that it could repopulate the binding site after the departure of the native PQH_2. Thus the addition of the PQ_{decyl} allows for the S_4 state to be reached even when the protein is not in its' natural membrane environment.

2.4. Detection and characterization of nano and microcrystals

2.4.1. Optical microscopy

During all crystallization trials, drops taken from an individual experiment can be imaged using optical light microscopy, by which crystals > 1um can be detected. However, one must be cautious drawing conclusions from optical microscopy (OM) alone since the size of the crystals are on or past the edge of what is visible and reliance on OM alone cannot identify nanocrystals < 1 um. One of the most useful methods in OM is the use of polarized light to check for birefringence since protein crystals often possess refractive anisotropy. This can help distinguish between crystalline protein and amorphous precipitate, provided crystals are > 1 um. Another caution should be mentioned that many salts are also birefringent and, since the birefringence signal will scale with the size of the crystal, crystals that are on the order of 1 μm or less will not be recognizable as such by birefringence.

2.4.2. Ultraviolet fluorescence microscopy

The use of ultraviolet fluorescence microscopy (UVM) allows the confirmation of protein in the crystals via tryptophan fluorescence. This is complimentary to OM when trying to determine whether or not a birefringent signal comes from a salt or protein crystal. Diffuse signal can also indicate under-saturated conditions or the presence of free protein amongst crystals. In the general case of non SONICC active protein crystals (see section 2.4.3) that may have low birefringence or have a birefringent salt as a precipitant, discrete spots in a UVM image can provide an alternative indication of crystals.

2.4.3. Second order non-linear imaging of chiral crystals

The second order non-linear imaging of chiral crystals (SONICC) technique is an ideal method for detecting crystals of a chiral molecule with non-centrosymmetric crystals, which is common among protein crystals (Wampler et al., 2008). When a substantially intense electric field is produced by a laser pulse, molecular dipoles are induced. In the case of a chiral crystal, these induced dipoles are anisotropic on their potential energy surface and allow the sampling of nonlinear, even numbered higher order polarizability terms such as the second generation harmonic (frequency doubling) (Haupert and Simpson, 2011). Enhanced signal can be measured at half the wavelength of the incident pulse, indicative of chiral crystals due to constructive interference provided by the ordered lattice. PSII is crystallized in space group of $P2_12_12_1$ which is SONICC active and provides positive confirmation of crystals too small to image optically, distinguishing them from amorphous precipitate or identifying them in a visibly clear drop. Protein crystals as small as 100 nm in size can be detected with SONICC (Wampler et al., 2008). Second harmonic generated signal was measured at 532 nm, indicative of a two photon

process that is only enhanced by the presence of crystals with anisotropic unit cells and is negligible otherwise.

2.4.4. Dynamic light scattering

Dynamic light scattering (DLS) allows the calculation of particle size and size distribution by using a temporal autocorrelation function of the scattered light signal over time in tandem with the Stokes-Einstein equation for particle radius. This comes from the stochastic Brownian motion of particles resulting in a time dependent scattering intensity caused by interference with the surrounding particles. The first order autocorrelation function is $g(q;\tau) = e^{-q^2 D_t \tau}$ as a function of the scattering radius q with delay time τ being parameterized. The diffusion coefficient, D_t, can then be identified and further used to calculate the hydrodynamic radius, r, assuming a sphere with known viscosity, η, at a temperature T. Through computational Fourier decomposition, multiple signals can be identified in the raw data leading to measurement of size dispersion. Thus, once other methods have been employed to confirm the existence of crystals, DLS provides the ability to monitor size and homogeneity at various time intervals during crystallization.

2.5. Time-resolved crystallography of PSII using FELs

The TR-SFX approach using FELs allows for the determination of the structure of undamaged biomolecules at room temperature, as diffraction occurs before destruction takes place (Barty et al., 2012). Furthermore, time resolved studies can be performed where a reaction is initiated by light or rapid mixing, even on irreversible processes due to the serial delivery of the single crystals in a liquid jet where each femtosecond X-ray pulse hits a new crystal.

Time resolved studies in crystallography were pioneered with the Laue method which uses a relatively polychromatic "pink" beam and large crystals to study light induced reversible reactions. Pioneering work has been done with the p21-GTP complex and PYP (Rajagopal et al., 2005; Šrajer et al., 2001). However Laue crystallography cannot be used for the study of the S-state cycle of Photosystem II due to the X-ray induced reduction of the metal cluster of the OEC. Further limitations are the limited light penetration of the large crystals, prohibiting a uniform population of transitory states. SFX overcomes these problems and opens a new window of opportunity for time resolved studies towards molecular movies of biomolecules at work.

2.5.1. Considerations for PSII in TR-SFX

For time resolved studies it is important that a sufficient population of the protein molecules must be in the same state when the crystal is probed by the X-rays in order to elucidate changes in the electron density of conformationally active localities. Thus, for light-induced time resolved experiments, it is imperative that crystals be small enough so that a high majority of the molecules in the crystal are excited by a saturating laser flash. Furthermore, when processing serial data it is important that Bragg diffraction intensities be comparable between. This leads to the need for size homogeneous nano or microcrystals (on the order of 500 nm to 5 μm) to allow maximal uniform excitation from the optical pump laser.

Recently, the dark state of Photosystem II was investigated at the FEL at SACLA by a group led by Jian-Ren Shen (Suga et al., 2015). In this study they collected FEL data on PSII crystals using an alternate fixed target approach whereby they solved the first high resolution undamaged dark structure of Photosystem II based on data collection of very large single crystals at cryogenic temperatures (Suga et al., 2015). The dark structure was

determined at 1.9 Å resolution and showed smaller distances between Mn atoms of the metal cluster of the OEC compared to the first high resolution structure of PSII based on data collection at synchrotrons (Umena et al., 2011). In this incredibly vast experiment, data were collected on 336 individual large crystals of millimeter size with femtosecond X-ray pulses at the FEL in SACLA. To minimize progression of X-ray damage, data were collected under cryogenic conditions with a defocused beam (1 μm). With the FEL's relatively large beam focus, the crystals had to be translated 50 μm between each shot.

While this breakthrough work led to the first undamaged high resolution structure of the dark state of PSII, time resolved studies, however, will be very difficult using this setup as uniform light excitation cannot be achieved with large single crystals. Additionally, data collection at cryogenic temperatures would not allow progression of the S-states beyond the S2 state which is reached after a single laser excitation.

When the PSII is excited, light is captured by a large antenna system and the excitation energy is transferred into the center of the complex, where charge separation takes catalyzed by the primary donor P680. The charge is passed through an electron transfer chain from P680 through chlorophyll *a*, a pheophytin, the plastoquinone PQ_A and finally to the terminal acceptor plastoquinone PQ_B. After two charge separation events, PQ_B is doubly reduced to PQ^{2-}, picks up two protons and leaves the binding site as plastoquinol PQH_2.

Once PQH_2 departs, it is subsequently replaced by another PQ_B from the PQ pool located in the photosynthetic membrane. $P680^+$ is concurrently reduced by extracting one electron at a time from 2 substrate water molecules bound at the OEC via the redox active tyrosine. After 4 electrons have been extracted in subsequent charge separation events, oxygen is evolved. The OEC consists of a cubanoid Mn_4O_5Ca cluster which undergoes four corresponding oxidation events and cycles through the Kok cycle. In the absence of light,

PSII's ground state is S_1 state where one positive charge has already been accumulated in PQ_B. The oxidation states of the four manganese atoms in the OEC is currently under debate but one likely scenario consists of oxidation states of (+3+3+3+4) for the S0 state (+3+3+4+4) for the S_1 ground state, (+3+4+4+4) for S_2, (+4+4+4+4) for S_3, and (+4+4+4+5) for S_4. In order to ensure that the desired excited states (S_2 and S_3) are being reached, it is necessary to verify the enzymatic activity (oxygen evolution) and quinone exchange.

2.5.2. The pump probe experiment

In the time resolved SFX experiments an optical pump laser is used to excite the crystals preceding interaction with the probe XFEL beam. This technique necessitates a laser excitation scheme with the goal to achieve a maximum excited population amongst PSII molecules in the crystals in each pump pulse and allowing for uniform evolution of transition states between each pump. Two different setups have been developed for TR-SFX studies on PSII.

In the experimental scheme described (Kupitz et al., 2014), the crystals are delivered to the FEL beam in a fast running jet (10 m/s) at ambient temperature and hydrated in their mother liquor. The experimental setup is depicted in Figure 2.3. The optical laser pulses were triggered by the linac coherent light source (LCLS), meaning that the time delay between the flashes is known exactly and is independent of the flow rate of the liquid jet. The fast running jet uses high amounts of sample at a flow rate of 10 µL/min. However, it ensures that the sample is fully replenished before the next FEL pulse arrives, eliminating the possibility of upstream excitation or damage. Data are collected simultaneously in pulse by pulse alternating light and dark sets, where the pump lasers are triggered with a frequency of 60 Hz synched to the 120 Hz LCLS FEL pulses. To

reiterate, this manifests as one snapshot being a “dark” snapshot with the next one being “light” snapshot and so on, resulting in 60 dark images and 60 light images collected per second. This ensures that all variables during data collection are identical for the light and dark data sets. Data was also collected without any laser excitation and comparison shows that the data of the purely dark runs and the alternating dark/light runs are identical. The laser excitation scheme is shown in the bottom of Figure 3. Delay times of 210 μs between flashes 1 and 2 and 560 μs between flash 2 and the "probing" with the FEL pulse were used, corresponding to three times the measured time constants of the OEC progression from the S_1 state to the S_2 state and from the S_2 state to the S_3 state (Dekker and Grondelle, n.d.). Data in the literature for the electron transfer between PQ_A and PQ_B greatly vary and are in the range of 200-800us. Future planned studies will extend the time points to up to 2ms.

Ideal time delays between flashes should be in the range between 200 μs and 2 ms to study the conformational changes associated with electron transfer at the acceptor site and oxidation of the Mn_4CaO_x cluster at the donor site. A variation of time delays, including longer time delays up to 2 ms and an improvement in resolution of the structural model are important to the resolution of conformational changes at atomic detail in any future work.

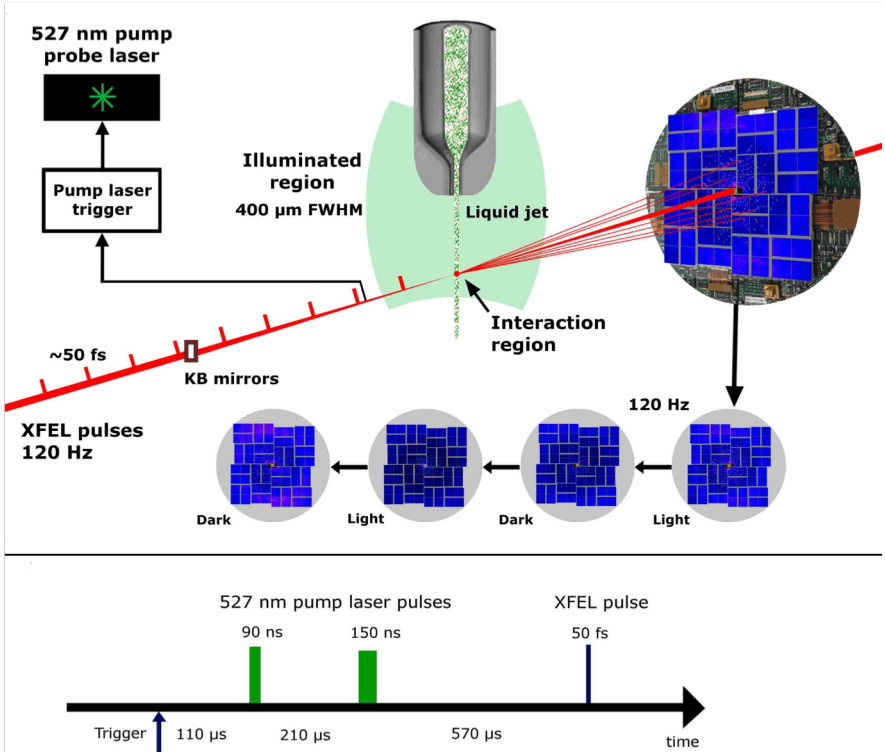

Figure 2.3: **Diagram of the experimental setup for the TR-SFX**

Experiment where the S_1 and S_3 states are probed alternately at 60 Hz each. The optical pump laser scheme is shown at the bottom, indicating delay times of 210 µs between the first and second pump and 570 µs between the second pump and interaction with the FEL beam, allowing population of the S_2 and S_3 states respectively. *Figure originally published in Kupitz et al., Nature 2014.*

An alternative approach used by Kern et al. (Kern et al., 2014, 2013) for TR-SFX studies. In this approach, the crystals are delivered to the FEL beam in a slow running jet where the sample is exposed to light by flowing across multiple windows in the nozzle. In this setup, the time delays between the first sets of laser excitations are dictated by the flow rate of the sample in the nozzle and only the last flash is triggered by the incoming FEL pulse. While this sample delivery method has the advantage of low sample consumption, it is limited in that the time delay for the first set of flashes is determined by the flow rate, which is often not constant and also varies within the nozzle as there is an

order of magnitude difference in the flow rates of the center and sides of the nozzle. This limits the setup to long time delays between the flashes with an average time delay between the first flashes on the order of 500 ms. This number is only a rough estimate as the flow rates have not been directly determined and were instead estimated from volume filled into the reservoirs and the time the sample ran out (Kern et al., 2014). Regardless, these long time delays inhibit realizing the conformational changes at the acceptor site as PQ_A^- is oxidized by side reaction with oxygen in 2-3 ms before arrival of the second electron (de Wijn and van Gorkom, 2001).

In summary, the most commonly successful sample delivery method for TR-SFX to date is the gas dynamic virtual nozzle (GDVN) which uses amplified liquid pressure and gas focusing to deliver the sample (DePonte et al., 2008). It has not only be used for the TR-SFX studies on PSII but also formed the basis for the first TR-SFX study that reached atomic resolution, using the photoactive yellow protein as a model system (Tenboer et al., 2014). Using the lipidic cubic phase (LCP) as a delivery media allows for minimal sample consumption with flow rates on the order of nL/min (Weierstall et al., 2014). This media has also been shown to successfully support membrane protein crystals with data sets solved with less than 0.5 mg (Liu et al., 2013). However, the crystals must be grown in the LCP, necessitating possibly new conditions, and the optical density of the material and slow flow rate is prohibitive towards pump probe studies. Another recent approach to SFX sample delivery is through the use of a nanoflow electrospinning microjet (Sierra et al., 2012). This method conserves sample by use of an applied electrical current to induce an electrospinning jet, as opposed to gas focusing, and the use of a viscous media such as glycerol to control droplet formation which allows a flow rate for PSII crystals around 3 μL/min (Kern et al., 2013). While this balances the need for sample conservation with a jet that is able to be optically pumped, the nature of the jet only allows for delay times on

the order of seconds and concern arises with regards to structural artifacts generated by the applied voltage on the protein. A primary drawback is sample consumption with typical flow rates of 10-15 μL/min but this allows access to the microsecond time range for pump probe experiments and avoids any possible upstream scattering excitation.

2.5.3 Evaluating PSII SFX data

For this work (Kupitz et al., 2014), the program Cheetah (Barty et al., 2014), developed specifically for SFX data, was used for background correction and hit-finding. The patterns were then indexed and merged using the *CrystFEL* software suite (White et al., 2012) and refined with the *Phenix* software suite (Adams et al., 2002). In SFX each diffraction snapshot represents a thin slice through reciprocal space, resulting in each measured reflection representing only a partial measure of scattering factor. Furthermore the intensity between individual X-ray shots varies by more than 200%. In light of this, the determination of accurate structure factors requires a high multiplicity of Bragg intensities with a recommended minimum of 50, a sharp contrast to traditional synchrotron crystallography. A multiplicity of > 600 for the dark data set and > 300 for the double flash data sets (putative S3 state) have been achieved in the Kupitz et al. experiment (2014). Kern et al. (2014) applied a specific program for data evaluation. A key difference between this program and Cheetah is that it uses resolution to select images, leading to low multiplicity of the data in the higher resolution shells. By contrast, the hits are selected in Cheetah according to a threshold of spots at a selected signal to noise ratio.

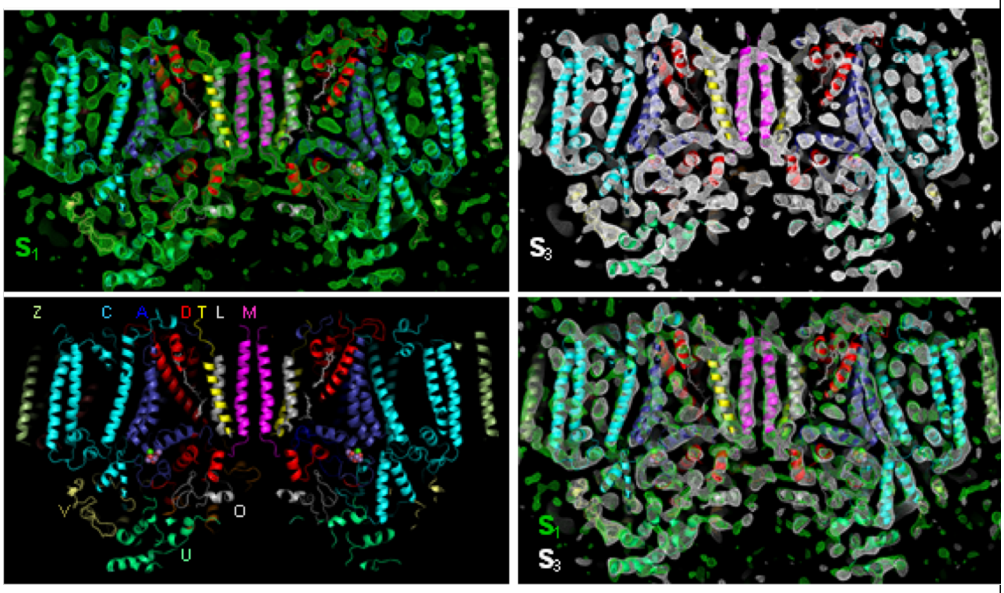

Figure 2.4: **Electron density omit maps at 1.5 σ of the PSII homodimer.**

(a) The dark (S1 ground) state (b) The doubly excited (putative S_3 state) (c) Ribbon and loop model of PSII with labeled subunits (d) Overlay of S_1 and putative S_3 states, revealing conformational changes evolved in progression through the Kok cycle. *Figure originally published in Kupitz et al., Nature 2014.*

2.5.4. Structural changes of PSII in the Kok cycle

In Kupitz et al. the structure of PSII was solved at 5.0 Å and 5.5 Å for dark and double excited data sets respectively. Large changes were detected in the unit cell constants between the dark S_1 state and the double flash putative S_3 state, which are reversed in triple flash experiments.

Despite the large changes of the unit cell constants, the overall dimensions of PSII do not increase as shown in the overlay of the transmembrane helices in Figure 4d. However, larger differences are detected in the acceptor side loop regions and the non-heme iron coordinated thereby (Fig.5). After PQH_2 is formed and leaves the Q_B binding site, an empty binding site ensues which could trigger the changes of the loops structures

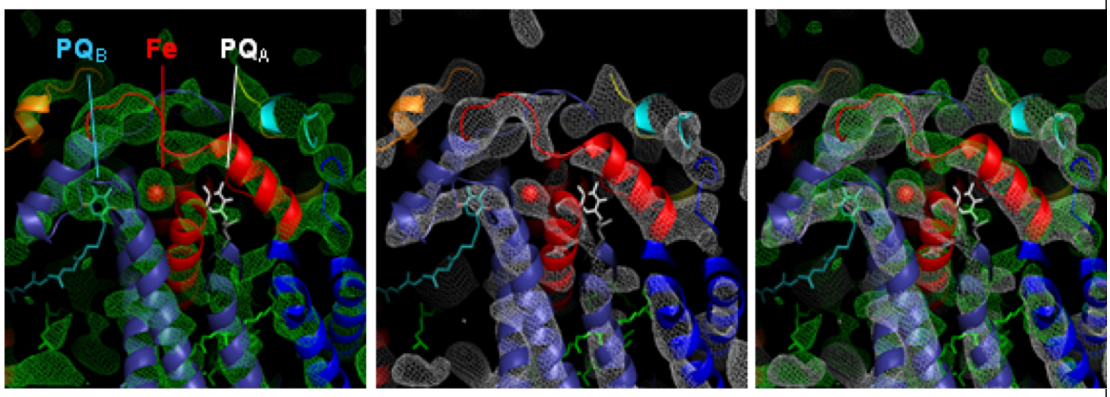

Figure 2.5: **Overlap of omit maps**

Overlay of omit maps for the dark S1 (green) and double flash (putative S3 s (white) state. (A) view of the transmembrane region of Photoystem II along the membrane plane (B) more detailed view of the acceptor site which contains the binding sites for PQA and PQB. Note the non-heme iron (red sphere) and the loop regions exhibiting significant conformational changes between the two states. Figure originally published in Kupitz et al., Nature 2014.

and the expansion of the unit cell constants. The fact that all crystals undergo this change in unit cell constant is an independent indication for the homogenous progression of PSII in our crystals through the Kok cycle. This change is reversible as it is reversed in a 3-flash experiment where PQ_{decyl} is incorporated to allow for the binding site to be filled before the third flash arrives.

In order to detect conformational changes of the OEC and avoid phase bias simulated annealed omit maps were calculated of the OEC and its protein environment (see Fig. 6a,6b). These omit maps tentatively show changes in the OEC and surrounding environment. From the omit map shown in Fig. 6b, an elongation of the Mn_4CaO_x portion of the OEC can be seen in the S_3 state with respect to the S_1 dark state. This may allow for the second substrate water molecule to bind between the 'dangler' Mn4 and the Mn_3CaO_4 cubane-like structure during the S-state transition. This is in agreement with hybrid density functional theoretical modeling (Isobe et al., 2012) which has shown that the substrate water has a probable minimum on its potential energy surface when coordinated

by the Mn4 and modulated by the O5 (Fig. 6c). Furthermore, a decrease in Mn-Ca^{2+} distances seen through extended X-ray absorption fine structure spectroscopy, pointing

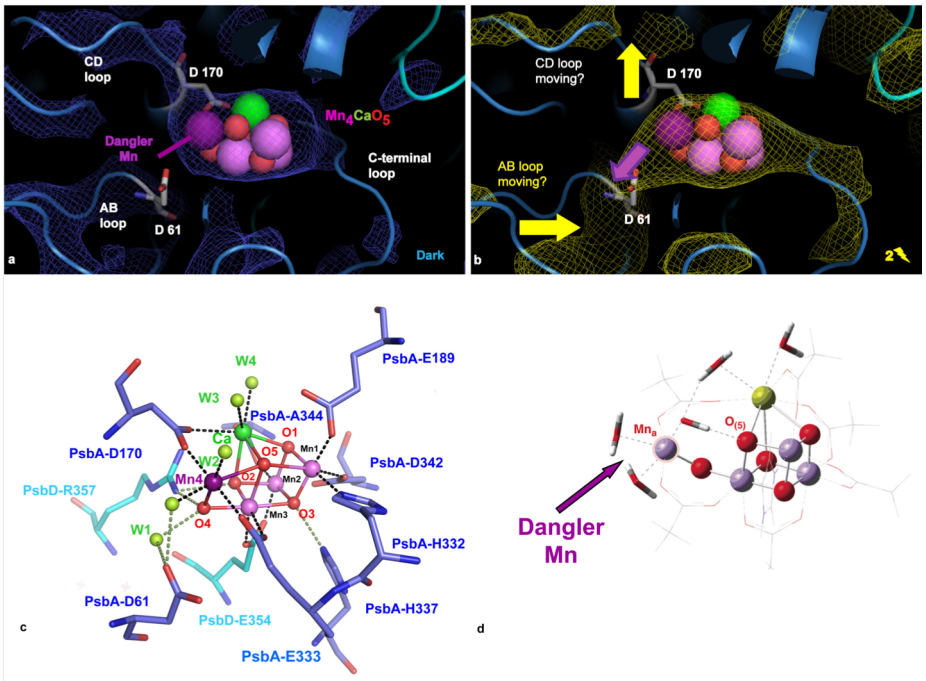

Figure 2.6: **Simulated annealing omit maps of the OEC.**

(a) and (b) exhibit the S1 and S3 states respectively at 1.5σ. In (b), the blue represents the S1 state whereas the yellow represents the S3 state for comparison. (c) shows the crystal structure from the 1.9Å structure of the OEC from Umena et al. (d) shows the proposed S3 state derived from DFT calculations performed in Isobe et al. Figure originally published in Kupitz et al., Nature 2014.

to a change in the character of the Mn4-O5 bond that would occur during elongation.

The observed electron density changes shown in Fig. 6 agree with the recent theoretical studies of Isobe and coworkers (Isobe et al., 2012), who predicted a "breakage" of the dangler Mn from the cubane cluster in the S3 state. In addition to the elongation of the electron density in the direction of the dangler Mn, the overall dimensions of the Mn4CaO5 cluster appears to shrink in the S_3 state, and the distance between the Ca and the 3 Mn in the cluster decreases, as part of the Ca sticks out of the electron density map in the S_3 state. Extended x-ray absorption fine structure (EXAFS) studies on Photosystem

II where the Ca was substituted with Sr showed very similar spectra in S_1 and S_2, indicating that no significant changes occur in the Mn-Mn or Mn-Ca distances in this S_2-state transition, while significant changes in EXAFS spectra were observed in the S_3 state (Pushkar et al., 2008), which included the prediction that the distances between Mn and Ca would shrink in the S_3 state. Experimental findings in Kupitz et al. (2014) support a shrinking of the Mn_4CaO_5 cluster in S_3 which would support the hypothesis of a condensation of the Mn_4CaO_5 cluster in S_3 based on the Jahn-Teller (JT) effect which has also been studied in several model Mn compounds (for more details on studies on Mn model compounds see Yamaguchi et al., 2013 and references therein). Mn-O distances derived from recently published model Mn-O and Mn3Ca-O cubane structures (Kanady et al., 2011; Mukherjee et al., 2012) indicate that Mn-O distances depend on the oxidation states of the Mn-ions. The average Mn (II)-O distance is 2.2 Å, the average Mn (III)-O distance is 2.0 Å and shrinks to 1.8 Å for the Mn (IV)-O distance . Based on X-ray absorption and emission spectroscopy, two models exist for the oxidation states of the Mn_4CaO_5 in S_3, which is either described as Mn (III)(IV)3 or Mn (IV)4 (Dau et al., 2012; Yano and Yachandra, 2007). In the model of S_3 where all Mn ions have reached the Mn (IV) oxidation state, a significant shrinking of the dimension of the cluster is expected due to the JT distortion with the average Mn-O distance being reduced to 1.8 Å (Yamaguchi et al., 2013). The shrinking of the overall dimensions of the metal cluster, which is supported by our maps of the putative S_3 state, appears to be the first experimental indication of the role that the JT distortion plays in the mechanism of water splitting (Kanady et al., 2011).

Changes are also visible in the protein environment of the metal cluster. These are much more difficult to interpret and validate at low resolution than the changes of the metal cluster and have to be confirmed at higher resolution. While the dark state SA omit map (Figs. 4a, 5a) matches the structural model of dark state (Umena et al., 2011), there

are significant changes visible on the SA omit map of the double flash putative S3 state. The SA-omit map of the putative S_3 state is suggestive of conformational changes which may indicate movement of the CD loop (including the ligand D170) away from the cluster. If this could be confirmed at higher resolution, it would indicate that ASP170, which provides ligands to both Ca and the danger Mn in the dark state, may not be a ligand in the higher S-states. The loop between the transmembrane helices A and B (AB loop) may change its confirmation so that it moves closer to the metal cluster. A density feature connects this loop at the position of Asp61 to the dangler Mn of the metal cluster in the putative S_3 state. Mutagenesis studies and recent spectroscopic evidence also support the current interpretation. Mutagenesis experiments have questioned Asp170 as a ligand in the higher S-states, as mutants still show 80% oxygen evolving activity and the FTIR spectra are not significantly altered in mutants of Asp170 (Debus, Strickler, Walker & Hillier, 2005). While Asp61 only serves as a second sphere ligand in the 1.9 Å crystal structure (Umena, Kawakami, Shen & Kamiya, 2011) mutagenesis studies indicated an important role in the water oxidation process as the S_2 to S_3 transition is blocked in Asp61 mutants (Debus, 2014; Dilbeck et al., 2013; Pokhrel and Brudvig, 2014).

At low resolution an interpretation of changes in the protein environment is challenging and the question may arise: how robust are these changes in the SA omit map? Three validation tests have been performed, comprised of the annealing temperature of the SA omit map (Figure 7a), splitting of the data for both the dark and light data sets in half and calculation of the SA omit maps with the split data sets (Figure 7b), and calculation of the SA omit maps for the light and dark states using exactly the same structure factors (Figure 7c). The results in Figure 7 and the comparison with the SA omit map in Figure 6 shows that the changes of the metal cluster and its protein environment between the dark and putative S_3 state are visible in all cases.

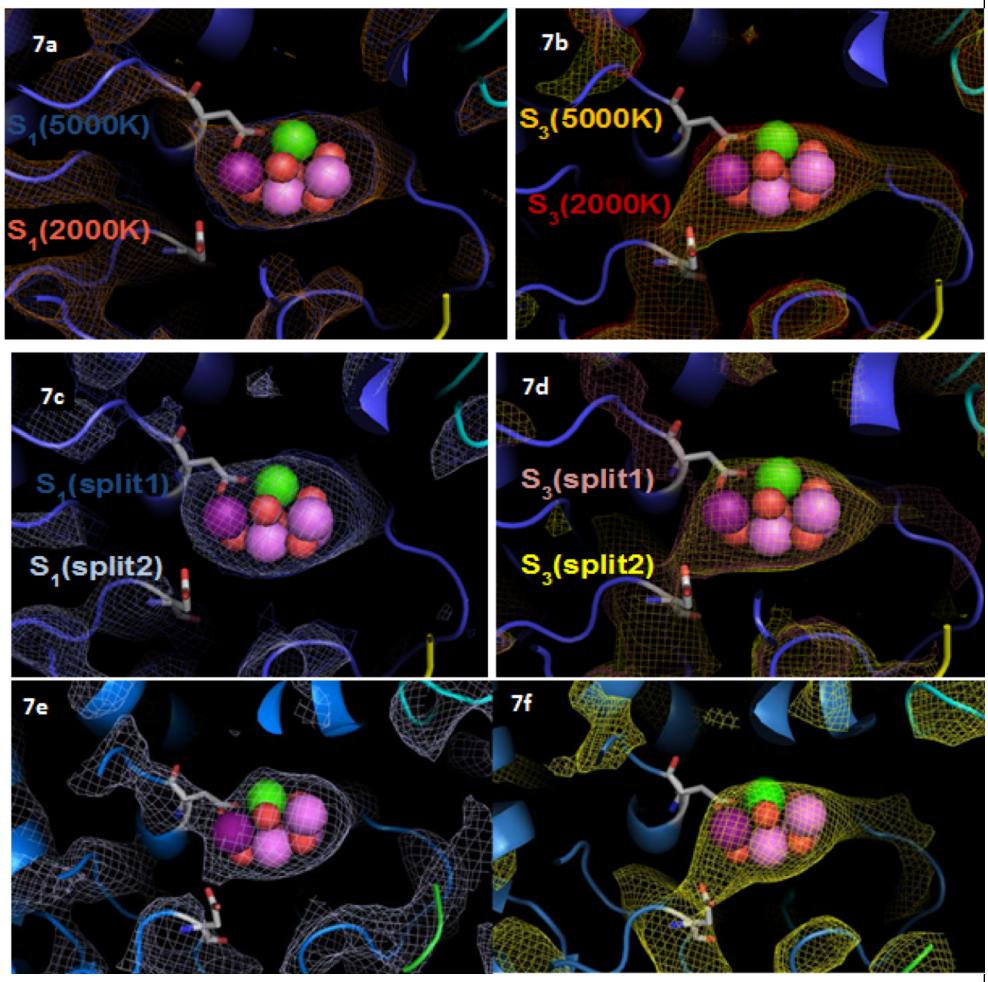

Figure 2.7: **Structure validation by SA omit maps.**

(A and B) Comparison between SA omit-maps of the two halves of the randomly split dark data set (S_1) at the contour level of 1.5 σ (A) and Comparison between SA omit-maps of the two halves of the double-excited data set (S_3) at a contour level of 1.5 σ (B). (C and D) Comparison between two SA omit maps made at two different start temperatures (2000 K and 5000 K) for S_1 state at 1.5 σ level (C) and the comparison between the two SA omit maps made at two different start temperatures (2000 K and 5000 K) for S_3 state at 1.5 σ contour level (D). (E and F) SA-omit maps calculated at 500 K with the same hkl values at 1.5 contour level for the dark data set (E) and the double flash data set (F).

2.6. Summary

The structures of PSII in the S_1 and S_3 states were determined at 5.0 and 5.5 Å respectively by TR-SFX. The experiments required new developments in crystal growth and crystal characterization so that a high density of microcrystals of Photosystem II of very homogenous size could be achieved.. Uniform growth of nano and microcrystals requires knowledge of the phase diagram and analytical techniques such as SONICC and DLS are crucial to detection and characterization. Using the pump-probe TR-SFX setup, radiation free snapshots of the S-state cycle can be recorded at biological temperatures, allowing for deeper understanding of the enzymatic mechanism behind PSII. Future developments may eventually lead to an evolution from snapshots of transitory states to molecular movies, enabling thorough understanding of enzymatic mechanisms such as PSII. Elucidating the mechanism of photosynthetic water oxidation and oxygen evolution is critical to the understanding the underlying photosynthetic mechanism and holds high potential for applications such as renewable energy and membrane protein bioengineering.

Reference:

Adams, P.D., Grosse-Kunstleve, R.W., Hung, L.-W., Ioerger, T.R., McCoy, A.J., Moriarty, N.W., Read, R.J., Sacchettini, J.C., Sauter, N.K., Terwilliger, T.C., 2002. *PHENIX* : building new software for automated crystallographic structure determination. Acta Crystallographica Section D Biological Crystallography 58, 1948–1954. https://doi.org/10.1107/S0907444902016657

Allakhverdiev, S.I., 2005. Systematic Analysis of the Relation of Electron Transport and ATP Synthesis to the Photodamage and Repair of Photosystem II in Synechocystis. PLANT PHYSIOLOGY 137, 263–273. https://doi.org/10.1104/pp.104.054478

Aquila, A., Hunter, M.S., Doak, R.B., Kirian, R.A., Fromme, P., White, T.A., Andreasson, J., Arnlund, D., Bajt, S., Barends, T.R.M., Barthelmess, M., Bogan, M.J., Bostedt, C., Bottin, H., Bozek, J.D., Caleman, C., Coppola, N., Davidsson, J., DePonte, D.P., Elser, V., Epp, S.W., Erk, B., Fleckenstein, H., Foucar, L., Frank, M., Fromme, R., Graafsma, H., Grotjohann, I., Gumprecht, L., Hajdu, J., Hampton,

C.Y., Hartmann, A., Hartmann, R., Hau-Riege, S., Hauser, G., Hirsemann, H., Holl, P., Holton, J.M., Hömke, A., Johansson, L., Kimmel, N., Kassemeyer, S., Krasniqi, F., Kühnel, K.-U., Liang, M., Lomb, L., Malmerberg, E., Marchesini, S., Martin, A.V., Maia, F.R.N.C., Messerschmidt, M., Nass, K., Reich, C., Neutze, R., Rolles, D., Rudek, B., Rudenko, A., Schlichting, I., Schmidt, C., Schmidt, K.E., Schulz, J., Seibert, M.M., Shoeman, R.L., Sierra, R., Soltau, H., Starodub, D., Stellato, F., Stern, S., Strüder, L., Timneanu, N., Ullrich, J., Wang, X., Williams, G.J., Weidenspointner, G., Weierstall, U., Wunderer, C., Barty, A., Spence, J.C.H., Chapman, H.N., 2012. Time-resolved protein nanocrystallography using an X-ray free-electron laser. Optics Express 20, 2706. https://doi.org/10.1364/OE.20.002706

Aro, E.-M., Virgin, I., Andersson, B., 1993. Photoinhibition of Photosystem II. Inactivation, protein damage and turnover. Biochimica et Biophysica Acta (BBA) - Bioenergetics 1143, 113–134. https://doi.org/10.1016/0005-2728(93)90134-2

Barty, A., Caleman, C., Aquila, A., Timneanu, N., Lomb, L., White, T.A., Andreasson, J., Arnlund, D., Bajt, S., Barends, T.R.M., Barthelmess, M., Bogan, M.J., Bostedt, C., Bozek, J.D., Coffee, R., Coppola, N., Davidsson, J., DePonte, D.P., Doak, R.B., Ekeberg, T., Elser, V., Epp, S.W., Erk, B., Fleckenstein, H., Foucar, L., Fromme, P., Graafsma, H., Gumprecht, L., Hajdu, J., Hampton, C.Y., Hartmann, R., Hartmann, A., Hauser, G., Hirsemann, H., Holl, P., Hunter, M.S., Johansson, L., Kassemeyer, S., Kimmel, N., Kirian, R.A., Liang, M., Maia, F.R.N.C., Malmerberg, E., Marchesini, S., Martin, A.V., Nass, K., Neutze, R., Reich, C., Rolles, D., Rudek, B., Rudenko, A., Scott, H., Schlichting, I., Schulz, J., Seibert, M.M., Shoeman, R.L., Sierra, R.G., Soltau, H., Spence, J.C.H., Stellato, F., Stern, S., Strüder, L., Ullrich, J., Wang, X., Weidenspointner, G., Weierstall, U., Wunderer, C.B., Chapman, H.N., 2012. Self-terminating diffraction gates femtosecond X-ray nanocrystallography measurements. Nature Photonics 6, 35–40. https://doi.org/10.1038/nphoton.2011.297

Barty, A., Kirian, R.A., Maia, F.R.N.C., Hantke, M., Yoon, C.H., White, T.A., Chapman, H., 2014. *Cheetah* : software for high-throughput reduction and analysis of serial femtosecond X-ray diffraction data. Journal of Applied Crystallography 47, 1118–1131. https://doi.org/10.1107/S1600576714007626

Chapman, H.N., Fromme, P., Barty, A., White, T.A., Kirian, R.A., Aquila, A., Hunter, M.S., Schulz, J., DePonte, D.P., Weierstall, U., Doak, R.B., Maia, F.R.N.C., Martin, A.V., Schlichting, I., Lomb, L., Coppola, N., Shoeman, R.L., Epp, S.W., Hartmann, R., Rolles, D., Rudenko, A., Foucar, L., Kimmel, N., Weidenspointner, G., Holl, P., Liang, M., Barthelmess, M., Caleman, C., Boutet, S., Bogan, M.J., Krzywinski, J., Bostedt, C., Bajt, S., Gumprecht, L., Rudek, B., Erk, B., Schmidt, C., Hömke, A., Reich, C., Pietschner, D., Strüder, L., Hauser, G., Gorke, H., Ullrich, J., Herrmann, S., Schaller, G., Schopper, F., Soltau, H., Kühnel, K.-U., Messerschmidt, M., Bozek, J.D., Hau-Riege, S.P., Frank, M., Hampton, C.Y., Sierra, R.G., Starodub, D., Williams, G.J., Hajdu, J., Timneanu, N., Seibert, M.M., Andreasson, J., Rocker, A., Jönsson, O., Svenda, M., Stern, S., Nass, K., Andritschke, R., Schröter, C.-D., Krasniqi, F., Bott, M., Schmidt, K.E., Wang, X., Grotjohann, I., Holton, J.M., Barends, T.R.M., Neutze, R., Marchesini, S., Fromme, R., Schorb, S., Rupp, D., Adolph, M., Gorkhover, T., Andersson, I.,

Hirsemann, H., Potdevin, G., Graafsma, H., Nilsson, B., Spence, J.C.H., 2011. Femtosecond X-ray protein nanocrystallography. Nature 470, 73–77. https://doi.org/10.1038/nature09750

Dau, H., Zaharieva, I., Haumann, M., 2012. Recent developments in research on water oxidation by photosystem II. Current Opinion in Chemical Biology 16, 3–10. https://doi.org/10.1016/j.cbpa.2012.02.011

de Wijn, R., van Gorkom, H.J., 2001. Kinetics of Electron Transfer from Q_A to Q_B in Photosystem II †. Biochemistry 40, 11912–11922. https://doi.org/10.1021/bi010852r

Debus, R.J., 2014. Evidence from FTIR Difference Spectroscopy That D1-Asp61 Influences the Water Reactions of the Oxygen-Evolving Mn_4CaO_5 Cluster of Photosystem II. Biochemistry 53, 2941–2955. https://doi.org/10.1021/bi500309f

Dekker, J.P., Grondelle, R.V., n.d. Primary charge separation in Photosystem II 14.

DePonte, D.P., Weierstall, U., Schmidt, K., Warner, J., Starodub, D., Spence, J.C.H., Doak, R.B., 2008. Gas dynamic virtual nozzle for generation of microscopic droplet streams. Journal of Physics D: Applied Physics 41, 195505. https://doi.org/10.1088/0022-3727/41/19/195505

Dilbeck, P.L., Bao, H., Neveu, C.L., Burnap, R.L., 2013. Perturbing the Water Cavity Surrounding the Manganese Cluster by Mutating the Residue D1-Valine 185 Has a Strong Effect on the Water Oxidation Mechanism of Photosystem II. Biochemistry 52, 6824–6833. https://doi.org/10.1021/bi400930g

Ferreira, K.N., Iverson, T.M., Maghlaoui, K., Barber, J., Iwata, S., 2004. Architecture of the Photosynthetic Oxygen-Evolving Center 303, 9.

Haupert, L.M., Simpson, G.J., 2011. Screening of protein crystallization trials by second order nonlinear optical imaging of chiral crystals (SONICC). Methods 55, 379–386. https://doi.org/10.1016/j.ymeth.2011.11.003

Isobe, H., Shoji, M., Yamanaka, S., Umena, Y., Kawakami, K., Kamiya, N., Shen, J.-R., Yamaguchi, K., 2012. Theoretical illumination of water-inserted structures of the CaMn4O5 cluster in the S2 and S3 states of oxygen-evolving complex of photosystem II: full geometry optimizations by B3LYP hybrid density functional. Dalton Transactions 41, 13727. https://doi.org/10.1039/c2dt31420g

Kamiya, N., Shen, J.-R., 2003. Crystal structure of oxygen-evolving photosystem II from Thermosynechococcus vulcanus at 3.7-A resolution. Proceedings of the National Academy of Sciences 100, 98–103. https://doi.org/10.1073/pnas.0135651100

Kanady, J.S., Tsui, E.Y., Day, M.W., Agapie, T., 2011. A Synthetic Model of the Mn3Ca Subsite of the Oxygen-Evolving Complex in Photosystem II. Science 333, 733–736. https://doi.org/10.1126/science.1206036

Kern, J., Alonso-Mori, R., Tran, R., Hattne, J., Gildea, R.J., Echols, N., Glockner, C., Hellmich, J., Laksmono, H., Sierra, R.G., Lassalle-Kaiser, B., Koroidov, S., Lampe, A., Han, G., Gul, S., DiFiore, D., Milathianaki, D., Fry, A.R., Miahnahri, A., Schafer, D.W., Messerschmidt, M., Seibert, M.M., Koglin, J.E., Sokaras, D., Weng, T.-C., Sellberg, J., Latimer, M.J., Grosse-Kunstleve, R.W., Zwart, P.H., White, W.E., Glatzel, P., Adams, P.D., Bogan, M.J., Williams, G.J., Boutet, S., Messinger, J., Zouni, A., Sauter, N.K., Yachandra, V.K., Bergmann, U., Yano, J., 2013. Simultaneous Femtosecond X-ray Spectroscopy and Diffraction of Photosystem II at Room Temperature. Science 340, 491–495. https://doi.org/10.1126/science.1234273

Kern, J., Tran, R., Alonso-Mori, R., Koroidov, S., Echols, N., Hattne, J., Ibrahim, M., Gul, S., Laksmono, H., Sierra, R.G., Gildea, R.J., Han, G., Hellmich, J., Lassalle-Kaiser, B., Chatterjee, R., Brewster, A.S., Stan, C.A., Glöckner, C., Lampe, A., DiFiore, D., Milathianaki, D., Fry, A.R., Seibert, M.M., Koglin, J.E., Gallo, E., Uhlig, J., Sokaras, D., Weng, T.-C., Zwart, P.H., Skinner, D.E., Bogan, M.J., Messerschmidt, M., Glatzel, P., Williams, G.J., Boutet, S., Adams, P.D., Zouni, A., Messinger, J., Sauter, N.K., Bergmann, U., Yano, J., Yachandra, V.K., 2014. Taking snapshots of photosynthetic water oxidation using femtosecond X-ray diffraction and spectroscopy. Nature Communications 5. https://doi.org/10.1038/ncomms5371

Kupitz, Christopher, Basu, S., Grotjohann, I., Fromme, R., Zatsepin, N.A., Rendek, K.N., Hunter, M.S., Shoeman, R.L., White, T.A., Wang, D., James, D., Yang, J.-H., Cobb, D.E., Reeder, B., Sierra, R.G., Liu, H., Barty, A., Aquila, A.L., Deponte, D., Kirian, R.A., Bari, S., Bergkamp, J.J., Beyerlein, K.R., Bogan, M.J., Caleman, C., Chao, T.-C., Conrad, C.E., Davis, K.M., Fleckenstein, H., Galli, L., Hau-Riege, S.P., Kassemeyer, S., Laksmono, H., Liang, M., Lomb, L., Marchesini, S., Martin, A.V., Messerschmidt, M., Milathianaki, D., Nass, K., Ros, A., Roy-Chowdhury, S., Schmidt, K., Seibert, M., Steinbrener, J., Stellato, F., Yan, L., Yoon, C., Moore, T.A., Moore, A.L., Pushkar, Y., Williams, G.J., Boutet, S., Doak, R.B., Weierstall, U., Frank, M., Chapman, H.N., Spence, J.C.H., Fromme, P., 2014. Serial time-resolved crystallography of photosystem II using a femtosecond X-ray laser. Nature 513, 261–265. https://doi.org/10.1038/nature13453

Kupitz, C., Grotjohann, I., Conrad, C.E., Roy-Chowdhury, S., Fromme, R., Fromme, P., 2014. Microcrystallization techniques for serial femtosecond crystallography using photosystem II from Thermosynechococcus elongatus as a model system. Philosophical Transactions of the Royal Society B: Biological Sciences 369, 20130316–20130316. https://doi.org/10.1098/rstb.2013.0316

Loll, B., Kern, J., Saenger, W., Zouni, A., Biesiadka, J., 2005. Towards complete cofactor arrangement in the 3.0 Å resolution structure of photosystem II. Nature 438, 1040–1044. https://doi.org/10.1038/nature04224

McPHERSON, A., 1990. Current approaches to macromolecular crystallization. European Journal of Biochemistry 189, 1–23. https://doi.org/10.1111/j.1432-1033.1990.tb15454.x

Mukherjee, S., Stull, J.A., Yano, J., Stamatatos, T.C., Pringouri, K., Stich, T.A., Abboud, K.A., Britt, R.D., Yachandra, V.K., Christou, G., 2012. Synthetic model of the asymmetric [Mn3CaO4] cubane core of the oxygen-evolving complex of photosystem II. Proceedings of the National Academy of Sciences 109, 2257–2262. https://doi.org/10.1073/pnas.1115290109

Neutze, R., Moffat, K., 2012. Time-resolved structural studies at synchrotrons and X-ray free electron lasers: opportunities and challenges. Current Opinion in Structural Biology 22, 651–659. https://doi.org/10.1016/j.sbi.2012.08.006

Neutze, R., Wouts, R., Hajdu, J., 2000. Potential for biomolecular imaging with femtosecond X-ray pulses 406, 6.

Ng, J.D., Gavira, J.A., Garcı´a-Ruı´z, J.M., 2003. Protein crystallization by capillary counterdiffusion for applied crystallographic structure determination. Journal of Structural Biology 142, 218–231. https://doi.org/10.1016/S1047-8477(03)00052-2

Patzlaff, J.S., Barry, B.A., 1996. Pigment Quantitation and Analysis by HPLC Reverse Phase Chromatography: A Characterization of Antenna Size in Oxygen-Evolving Photosystem II Preparations from Cyanobacteria and Plants †. Biochemistry 35, 7802–7811. https://doi.org/10.1021/bi960056z

Pokhrel, R., Brudvig, G.W., 2014. Oxygen-evolving complex of photosystem II: correlating structure with spectroscopy. Physical Chemistry Chemical Physics 16, 11812. https://doi.org/10.1039/c4cp00493k

Pushkar, Y., Yano, J., Sauer, K., Boussac, A., Yachandra, V.K., 2008. Structural changes in the Mn4Ca cluster and the mechanism of photosynthetic water splitting. Proceedings of the National Academy of Sciences 105, 1879–1884. https://doi.org/10.1073/pnas.0707092105

Rajagopal, S., Anderson, S., Srajer, V., Schmidt, M., Pahl, R., Moffat, K., 2005. A Structural Pathway for Signaling in the E46Q Mutant of Photoactive Yellow Protein. Structure 13, 55–63. https://doi.org/10.1016/j.str.2004.10.016

Renger, G., 2012. Mechanism of light induced water splitting in Photosystem II of oxygen evolving photosynthetic organisms. Biochimica et Biophysica Acta (BBA) - Bioenergetics 1817, 1164–1176. https://doi.org/10.1016/j.bbabio.2012.02.005

Sierra, R.G., Laksmono, H., Kern, J., Tran, R., Hattne, J., Alonso-Mori, R., Lassalle-Kaiser, B., Glöckner, C., Hellmich, J., Schafer, D.W., Echols, N., Gildea, R.J., Grosse-Kunstleve, R.W., Sellberg, J., McQueen, T.A., Fry, A.R., Messerschmidt, M.M., Miahnahri, A., Seibert, M.M., Hampton, C.Y., Starodub, D., Loh, N.D., Sokaras, D., Weng, T.-C., Zwart, P.H., Glatzel, P., Milathianaki, D., White, W.E., Adams, P.D., Williams, G.J., Boutet, S., Zouni, A., Messinger, J., Sauter, N.K., Bergmann, U., Yano, J., Yachandra, V.K., Bogan, M.J., 2012. Nanoflow electrospinning serial femtosecond crystallography. Acta Crystallographica Section D Biological Crystallography 68, 1584–1587. https://doi.org/10.1107/S0907444912038152

Spence, J.C.H., Weierstall, U., Chapman, H.N., 2012. X-ray lasers for structural and dynamic biology. Reports on Progress in Physics 75, 102601. https://doi.org/10.1088/0034-4885/75/10/102601

Šrajer, V., Ren, Z., Teng, T.-Y., Schmidt, M., Ursby, T., Bourgeois, D., Pradervand, C., Schildkamp, W., Wulff, M., Moffat, K., 2001. Protein Conformational Relaxation and Ligand Migration in Myoglobin: A Nanosecond to Millisecond Molecular Movie from Time-Resolved Laue X-ray Diffraction †. Biochemistry 40, 13802–13815. https://doi.org/10.1021/bi010715u

Suga, M., Akita, F., Hirata, K., Ueno, G., Murakami, H., Nakajima, Y., Shimizu, T., Yamashita, K., Yamamoto, M., Ago, H., Shen, J.-R., 2015. Native structure of photosystem II at 1.95 Å resolution viewed by femtosecond X-ray pulses. Nature 517, 99–103. https://doi.org/10.1038/nature13991

Tenboer, J., Basu, S., Zatsepin, N., Pande, K., Milathianaki, D., Frank, M., Hunter, M., Boutet, S., Williams, G.J., Koglin, J.E., Oberthuer, D., Heymann, M., Kupitz, C., Conrad, C., Coe, J., Roy-Chowdhury, S., Weierstall, U., James, D., Wang, D., Grant, T., Barty, A., Yefanov, O., Scales, J., Gati, C., Seuring, C., Srajer, V., Henning, R., Schwander, P., Fromme, R., Ourmazd, A., Moffat, K., Van Thor, J.J., Spence, J.C.H., Fromme, P., Chapman, H.N., Schmidt, M., 2014. Time-resolved serial crystallography captures high-resolution intermediates of photoactive yellow protein. Science 346, 1242–1246. https://doi.org/10.1126/science.1259357

Umena, Y., Kawakami, K., Shen, J.-R., Kamiya, N., 2011. Crystal structure of oxygen-evolving photosystem II at a resolution of 1.9 Å. Nature 473, 55–60. https://doi.org/10.1038/nature09913

Wampler, R.D., Begue, N.J., Simpson, G.J., 2008. Molecular Design Strategies for Optimizing the Nonlinear Optical Properties of Chiral Crystals. Crystal Growth & Design 8, 2589–2594. https://doi.org/10.1021/cg700732n

Weierstall, U., James, D., Wang, C., White, T.A., Wang, D., Liu, W., Spence, J.C.H., Bruce Doak, R., Nelson, G., Fromme, P., Fromme, R., Grotjohann, I., Kupitz, C., Zatsepin, N.A., Liu, H., Basu, S., Wacker, D., Won Han, G., Katritch, V., Boutet, S., Messerschmidt, M., Williams, G.J., Koglin, J.E., Marvin Seibert, M., Klinker, M., Gati, C., Shoeman, R.L., Barty, A., Chapman, H.N., Kirian, R.A., Beyerlein, K.R., Stevens, R.C., Li, D., Shah, S.T.A., Howe, N., Caffrey, M., Cherezov, V., 2014. Lipidic cubic phase injector facilitates membrane protein serial femtosecond crystallography. Nature Communications 5. https://doi.org/10.1038/ncomms4309

White, T.A., Kirian, R.A., Martin, A.V., Aquila, A., Nass, K., Barty, A., Chapman, H.N., 2012. *CrystFEL* : a software suite for snapshot serial crystallography. Journal of Applied Crystallography 45, 335–341. https://doi.org/10.1107/S0021889812002312

Yamaguchi, K., Isobe, H., Yamanaka, S., Saito, T., Kanda, K., Shoji, M., Umena, Y., Kawakami, K., Shen, J.-R., Kamiya, N., Okumura, M., 2013. Full geometry optimizations of the mixed-valence $CaMn_4O_4X(H_2O)_4$ (X=OH or O) cluster in

OEC of PS II: Degree of symmetry breaking of the labile Mn-X-Mn bond revealed by several hybrid DFT calculations. International Journal of Quantum Chemistry 113, 525–541. https://doi.org/10.1002/qua.24117

Yano, J., Kern, J., Irrgang, K.-D., Latimer, M.J., Bergmann, U., Glatzel, P., Pushkar, Y., Biesiadka, J., Loll, B., Sauer, K., Messinger, J., Zouni, A., Yachandra, V.K., 2005. X-ray damage to the Mn4Ca complex in single crystals of photosystem II: A case study for metalloprotein crystallography. Proceedings of the National Academy of Sciences 102, 12047–12052. https://doi.org/10.1073/pnas.0505207102

Yano, J., Yachandra, V.K., 2007. Oxidation state changes of the Mn4Ca cluster in Photosystem II. Photosynthesis Research 92, 289–303. https://doi.org/10.1007/s11120-007-9153-5

CHAPTER 3

RECENT ADVANCES IN TIME-RESOLVED SERIAL FEMTOSECOND CRYSTALLOGRAPHY OF PHOTOSYSTEM II

Chapter 2 discusses the steps involved in purification and crystallization of PSII for performing time-resolved crystallography with microcrystals at XFELs. In order to understand the mechanism of oxidation of water, a time-resolved two-flash study has been described where the structure of PSII was visualized in the dark (S_1) and double-excited (S_3) state. The results described in chapter 2 presented an insight into structural changes associated with the transition of the OEC through the Kok cycle (Figure 2.1), however the details of the S-state transition were restricted due to the lack in high resolution features (resolution cutoff was 5 A for the dark structure and 5.5 A for the S_3 structure) (Kupitz et al., 2014). The primary goal for the subsequent experiments was to improve the diffraction quality of microcrystals for performing three-flash experiments with PSII to potentially trap the transient S_4 state. For this, extensive optimizations have been made in cell culture, protein preparation, crystallization, sample delivery and data analysis and this chapter explores the aspects that have contributed most significantly.

The process of oxidation of water performed by PSII is a multi-step redox reaction that splits water into molecular oxygen (O_2), electrons and protons using light energy. As described in section 1.2, all products of this process are essential for survival of higher life on Earth. Additionally, the scope of understanding the details of charge separation in PSII that drives the water splitting process has great implications for the development of artificial photosynthesis and also may have an impact on improving the efficiency of natural photosynthesis in crops, making this study vital in the field of photosynthesis.

3.1. Culture growth for T. elongatus

Cyanobacterial growth has been studied extensively (Kuan et al., 2015) and based on the organism of interest, optimum conditions have been defined. For thermophilic cyanobacteria, temperature and pH controlled photo-bioreactors are known to work best. Our initial precultures were grown in a simple setup consisting of 10 L Nalgene cell culture bottles (as illustrated in Figure 3.1 B). These were later improvised using 10 L bioreactors (Figure 3.1 A) and large scale growth was performed in Medusa bioreactor (Figure 3.1 C).

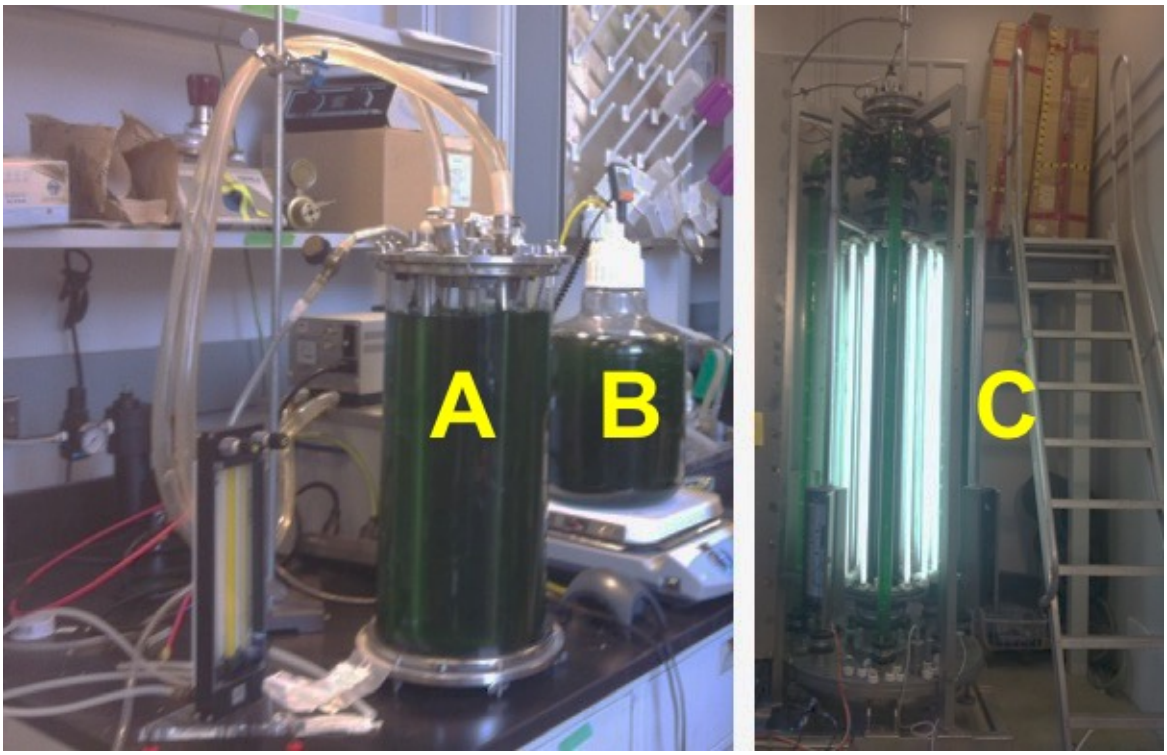

Figure 3.1: **Cell pre-culture and Medusa bioreactor**

A) Pre-culture bioreactor equipped with heated water-bath and flow-meter to adjust the air-low to the growing culture B) Pre-culture Nalgene tanks with stirring heat-plates were connected to an aquarium pump (not seen) for effective air-flow and C) 120 L Medusa photo-bioreactor was used for large-scale culture growth. The bright white fluorescent lights are seen in close proximity to the glass tubes containing cyanobacterial culture. The culture travels from the central column of the bioreactor to the dark tank underneath, then moves to the upper glass chamber through the thinner columns at the periphery. The ladder provided access to top of reactor for introducing media and bioreactor maintenance.

3.1.1. Preparation of inoculum

The Nalgene set-up (Figure 3.1 B) consisted of heated stirring plate and a 10 L bottle that was equipped with a lid for aseptic transfer for introducing a gas-flow/ aeration pipe that was connected to an aquarium pump. The lid also permitted a temperature probe to be introduced in the medium for maintaining optimum temperature conditions for cell growth. The stirring heat plate was kept at 50 C to prevent heat damage to the plastic bottle and the stir plate over time. The culture was between 47 - 50 C. While the Nalgene set-up was easy to build and maintain, to ensure rigorous aeration of the medium, a 10 L bioreactor was assembled (Figure 3.1 A). In this case, the reactor was heated using a water-bath set to 56 C. Air enriched with 2% CO2 from gas-lines was passed through a filter (Speedaire by Grainger, Cat# 4ZL48) before introducing in the bioreactor via a flow-meter. This permitted the use of high pressure regulators that provided much more gas-flow in the form of bubbles than aquarium pumps. The Autoclaved Nalgene bottles or bioreactor were filled with BG-11 medium and warmed up to 56 C. Additional micronutrient solution is also necessary for sustained growth of the cells. The composition and protocol for preparing the medium and micronutrient solution are described in Appendix 1. The solutions were prepared freshly with purified milli-Q water but were not autoclaved before use.

At the start of a culture cycle, about 5 g of frozen pellet of cells (not thawed) was introduced in the warm buffer (56 C) and dark adapted, where the 10 L chambers were covered with foil to prevent any light contamination. This ensured that only the most viable cells survived and ferociously grew to yield superior cells during the subsequent large scale culturing. The culture density was closely monitored by measuring the absorbance of the cell culture at 720 nm. At this wavelength, the photosynthetic apparatus does not absorb significant amount of light and the absorbance values can be attributed to

the scattering of particles i.e. cell density. Once the pre-culture reached O.D. values of 0.15 at 720 nm (takes 5 - 7 days), the protecting foil layer was removed and the culture was permitted to grow in light available in the room.

Hereafter, the culture was monitored every day. Temperature was maintained between 50 - 58 C and pH between 7 - 8. Additionally, the absorbance spectrum of the culture (400 – 800 nm) was also measured. As the culture grew, flood lights were directed to permit the culture to grow with sufficient light at all time. When the culture reached the optimum density of 0.4 O.D. units at 720 nm, it was used to inoculate the 120 L Medusa bioreactor (Figure 3.1 C).

3.1.2. Considerations for 120 L culturing

For large scale culturing, 100 L of medium was warmed to 56 C and 10 L of pre-culture was added to the buffer. Remaining solution (12 L) was compensated using purified water at 56 C. For effective adaptation, the lights on the bioreactor were turned off overnight and the part of the bioreactor exposed to sunlight was covered using metal protective shields, while fluorescent room light was kept on. Next day, a sample of the culture was monitored to check if the cells had started to grow. When the culture regained absorbance of 0.15 O.D. units at 720 nm, lights were turned on and metal shields were removed to promote further cell growth. Figure 3.2 describes a typical trajectory of spectrums for a growth period in Medusa. Gradual increased absorbance throughout the spectrum indicates overall health of the cells and their photosynthetic components.

During the growth period, two factors were closely monitored in the absorbance spectrum. Firstly, the peak seen at 620 - 650 nm corresponded to the light-harvesting phycobillisome antennae proteins. If this was the major peak seen in the spectrum, it indicated towards stress caused by inadequate light exposure to the cells. This may be

because of high cell density or low light intensity. If high absorbance values were observed at 620 – 650 nm at low cell density, incident light intensity was increased to rectify the low light stress. Secondly, the peak at 680 nm was monitored for the peak maxima. This was usually observed to be at 680.5 or 681 nm. If this shifted to values below 680 nm, the batch of cells was not used for isolating PSII and for subsequent rounds of culturing, the light intensity was decreased to prevent any photodamage.

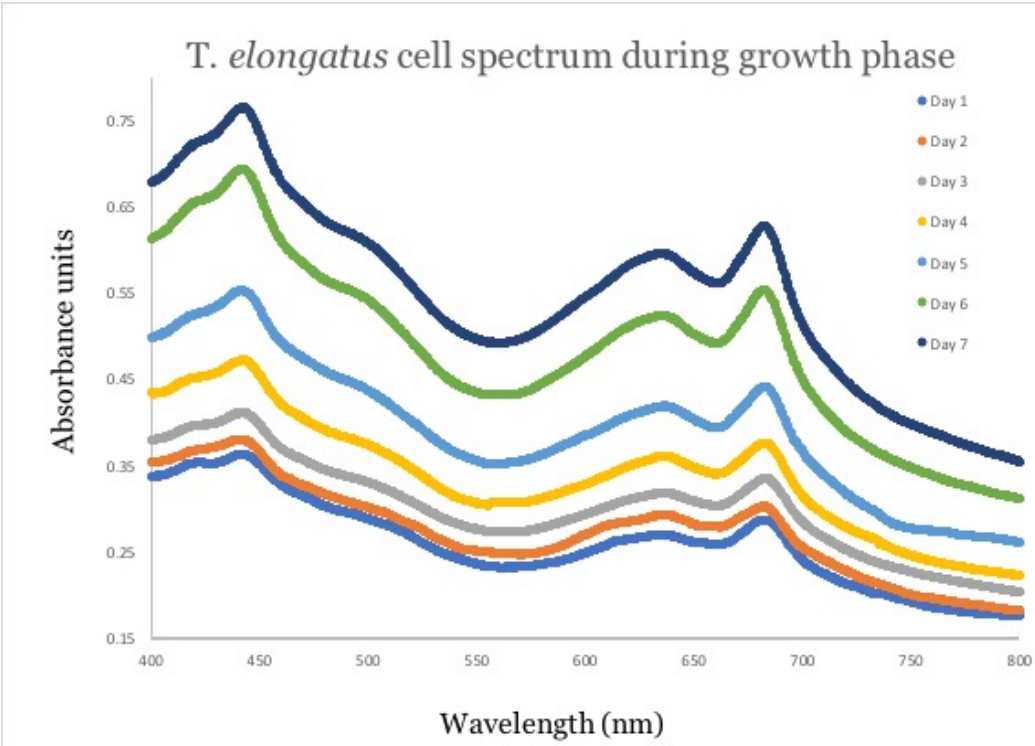

Figure 3.2: **Series of Absorbance spectra for *T. elonagtus* during cell growth**

Spectra obtained everyday were compared to observe trends seen in overall culture. Increased absorbance at 720 nm indicated increased cell density. Both the peaks observed at short wavelength (430-450 nm) and at longer wavelength of 680 nm corresponded to chlorophyll moleules. The peak at 620-650 nm indicated presence of phycobili-proteins. Light intensity was maintained such that the peak at 650 was lower than the peak at 680.

Indeed cells grown at low light have a ratio of PSI to PSII of (about 8:1) so PSI with an absorption max of 681 nm dominates the spectrum. While these cells have more PSI than PSI the PSII is of better quality as it experience less photodamage. At higher light intensity the ratio of PSI to PSII (with an absorption max of 672.5 nm) shifts with PSI trimer being actively degraded, however up to 70% of the PSII is in the process of repair and so the quality of PSII is not suitable for crystallization.

Light conditions were maintained using Medusa's illumination system. At inoculation, the culture was kept at 0 % light intensity (fluorescent bulbs were turned off). Once the culture started to grow, the % illumination was increased to 30 %. Hereafter, every day the intensity was gently increased by 20% per day and by the 5th day after inoculation, the light intensity was maximum i.e. 100 % illumination, (controlled by the

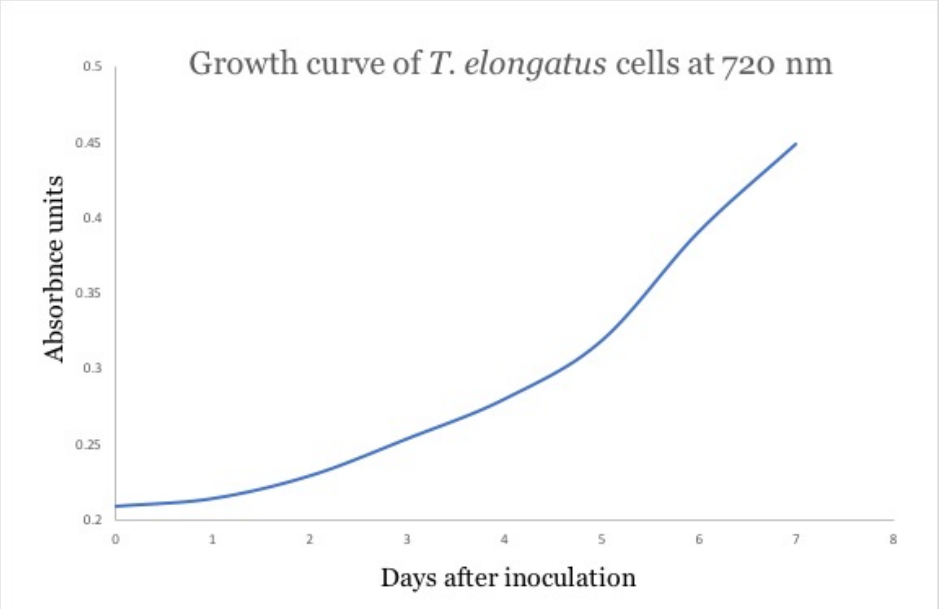

Figure 3.3: **Absorbance at 720 nm monitored after inoculation**

As seen in the curve, Day 7 was the day of harvest and it was soon after it reached the logarithmic phase. Permitting cells to overgrow beyond 0.6 O.D. units in Medusa usually resulted in stress due to inadequate light exposure that was indicated by increase in phycobilins. This also resulted in slower rate of cell division and onset of the stationary phase of a growth curve.

knob on the controller). The air-flow was maintained at 'max' at all time with 'auto' mode and maximum CO_2 concentration permissible. The temperature was maintained at 56 C.

As mentioned above, the absorbance values at 720 - 750 nm were seen due to the scattering of cells. As soon as the culture reached 0.4 (O.D. units) at 720 nm, the culture was harvested to ensure that the it was still in the log phase. As seen in Figure 3.3, gradual increase in absorbance at 720 nm indicated higher cell density i.e. cell growth. When the value crossed 0.4 O.D. units, the culture was considered 'ready' for harvest. The first growth cycle in Medusa lasted between 4 – 7 days. For large scale culturing, in order to maximize the yield, continuous culture was maintained. In this process, 70 L of the culture was harvested and the remaining 50 L of cells were diluted with additional medium for further cell growth for next harvest, which would be in 3 – 5 days.

3.1.3. Cell harvest and storage

70 L of culture from Medusa was collected in a large plastic container for harvest. The first stage of concentration was performed using Cole Parmer's Masterflex Peristaltic Pump tangential flow filter system (Cat# 200-1558). This set-up is a positive displacement pump/filter setup where a constant fraction of solvent is flowing through the tangential filter and can be discarded while the cells are concentrated in each of the flow cycles. The filter was primed using 10 L of purified water to wash away any residue of old cleaning solutions or cells. Cell culture collected from Medusa was then introduced in the filter/pump system via pipes without introducing any air into the system. The pump valve was set midway to ensure that half of the solution was concentrated by flowing above the filter and half was discarded as flow through. The discarded buffer was clear and gradually, the recirculated culture became denser as the total volume decreased such that all culture could be accommodated in the filter unit.

Then, the concentrated cell suspension was collected from the pipe and filter unit. The direction of flow was then reversed and cells were collected in a fresh 5 L plastic beaker by flushing the system with purified water. When the cell suspension was collected, the direction of flow was reversed again to ensure that all cells were obtained. At this stage, the suspension had the volume of about 2 – 2.5 L. These initial steps were carried out fairly quickly to prevent the culture from cooling down to room temperature. The beaker with the collected cell suspension was stored in a bigger container of hot water to keep the cells as warm as possible to keep the cells viable.

The collected cells were spun down at 7000 g at room temperature in 4 - 6 (250 mL) centrifuge bottles. The discarded supernatant was clear indicating that cell were intact during cell harvest. After the first centrifugation round, additional cell suspension was added on top of the initial pellet and centrifugation was continued until all cells were separated from the supernatant. When all the culture was concentrated, the cell pellets could be harvested. The centrifuge bottles were inverted on paper towels to discard any fluid. Runny pellets were not preferred for isolation of PSII since they indicated a mixture of viable and dead cells. Cell pellets were scooped out of the centrifuge bottles in one swift motion using a spatula and collected in a pre-weighed ziplock bag. Up to 2 pellets of 20 – 30 g each were stored (at -80 C) in a bag but the bag was folded to make sure that the pellets don't freeze together during storage. Cryoprotectants were not added to the cells as they can kill the cells and also because they might interfere with the downstream isolation and purification procedures. Date of harvest, absorption maxima around 680 and other culturing details were mentioned on the bag. Typically, for 70 L of culture at absorbance of 0.4 units at 720 nm, 50 – 60 grams of *T. elongatus* cells were harvested and stored at -80C until further use.

The peristaltic pump set-up was thoroughly cleaned to prevent older cells from contaminating future harvests. First another 10 L of purified water was passed through each direction of flow. Next, 10 L of hot water (~ 50 C) was passed in each direction of flow. For intensive cleaning, both ends of the pipes were connected and hot water was circulated throughout the set-up for 10 – 15 minutes. This water was discarded and the set-up was refilled with hot water. This time, the water was passed in the opposite direction of flow for 10 – 15 minutes. This was followed by 10 L of 10 % bleach solution, which was passed through each direction of flow to avoid fungal or bacterial growth. Finally, the set-up was cleaned by flushing 10 L of purified water from each direction of flow and the set-up was stored in purified water to prevent the filter from drying out and compromising subsequent harvests.

3.2. Cell disruption, isolation of thylakoids and detergent screen for establishing conditions for solubilization of PSII

Kupitz et.al (2014) describes the PSII isolation, purification and crystallization in great detail. Briefly, the cells are disrupted by passing them twice through a microfluidizer (Microfluidics Model M-110 L) on ice. Cell debris is removed by centrifugation at 11,000 g for 10 min at 4C, followed by two washing steps with buffer (20 mM MES at pH 6, 10 mM $CaCl_2$, 10 mM $MgCl_2$). For solubilization of PSII, the thylakoids were resuspended in a small volume of 20 – 30 mL buffer (20 mM MES at pH 6, 10 mM $CaCl_2$, 10 mM $MgCl_2$, 200 mM D-mannitol, 20 % glycerol) and the chlorophyll concentration was determined as described in Porra et.al (1989) by extracting 80% acetone with a molar extinction coefficient of 76,780.

In order to optimize the solubilizing conditions, the effective detergent concentration (protein : detergent ratio) was varied. The initial conditions described in

Kupitz et.al. were solubilization at 0.74 mM chlorophyll and 1 % β-DDM, with solubilization for 60 minutes at room temperature. A systematic study was conducted where the concentration of chlorophyll and detergent at solubilization was studied. For the same batch of cells, thylakoid membranes were adjusted to a chlorophyll concentration of 0.74 mM and were divided into four sections. PSII was extracted at different detergent concentrations of 0.5%, 0.6%, 0.7% and the previously established 1% β-DDM and yield, oxygen evolving activity as well as resulting crystal quality was compared. The results are shown in Figure 3.7 and they indicate that higher quality of intact PSII and subsequently crystals of improved order for serial femtosecond crystallography were achieved at a detergent concentration of 0.5 %.

3.2.1. Anion-Exchange chromatography

Strong interactions with ion-exchange medium can cause disassembly of fragile PSII dimers. To avoid this, a weak tentacle anion-exchange resin was used for purification of the detergent solubilized PSII. The material used was Toyopearl DEAE 650-M (Tosch Biosciences LLC, Cat # 07988) beads with long and flexible linkers with diethylaminoethyl exchange groups attached to the charged groups of the protein, allowing a gentle interaction between protein and resin.

The resin was packed in XK 26/70 columns (70 cm length, 26 mm inner diameter) (GE healthcare Cat # 18-1000-71), using 1.5 times (15 mL/min) the flow-rate used for purification based on the recommendation from the manufacture. New resin was washed in purified water to remove any fines and the clean resin was allowed to settle for 30-60 minutes. Excess water was removed from the resin and this concentrated material was poured into clean column housing. A reservoir was connected to the top of the column and the material was compressed using FPLC (AktaPure, GE Healthcare) at 5 ml/min.

Gradually, the flow-rate was increased by 1 ml/min, every 10 minutes. Eventually, at 15 mL/min, the column was permitted to pack for about an hour with purified water. The final pressure with connected lines was desired to be less than 0.4 MPa. Next, the resin was exposed to high salt (buffer B) A_{150} (20 mM MES pH 6.0, 10 mM $CaCl_2$, 10 mM $MgCl_2$, 150 mM $MgSO_4$, 20 % glycerol, 0.02 % β-DDM) for 1 column volume (~ 300 mL) to ensure uniform packing throughout the column. The void volume of a packed column was determined to be ~ 200mL.

Preparation of thylakoid membranes and protein solubilization has been extensively discussed in section 4.3.1. Prior to chromatography, the membrane extract was ultracentrifuged to remove insolubilized debris. During this time, the columns were equilibrated with 10 % buffer B against buffer A (20 mM MES pH 6.0, 10 mM $CaCl_2$, 10 mM $MgCl_2$, 20 % glycerol, 0.02 % β-DDM) for 2 column volumes at a flow rate of 10 ml/min till stable conductivity of ~3.4 mS was achieved. The column was maintained at 4 C using a cooled water jacket connected to a water bath. The top 80 % of the solution obtained after ultracentrifugation in the ultracentrifuge tubes contained PSII and was collected in a graduated cylinder to measure the sample volume. The chlorophyll concentration of the retrieved extract was determined (as described in section 4.3). Membrane extract equivalent to 18 μmoles of chlorophyll was separated in a fresh graduated cylinder and diluted 1:4 using buffer A. This was done to minimize the interaction time of PSII with high detergent concentrations, that could potentially cause further protein degradation. This prepared sample aliquot was manually applied on the column after filtering through 0.22 μ syringe filter.

During anion exchange chromatography, a program with constant flow-rate was run to ensure consistency among all the runs as described in Table 3.1. The column was equilibrated with 10 % buffer B. Figure 3.4 describes that all unbound material was washed

off the column at 10 % buffer B (15 mM $MgSO_4$) using 3 column volumes of buffer. Wavelengths of 280, 672 and 681 nm were monitored to verify that PSI and PSII remained on the column while other components of the extract (like traces of phycobillisomes) were washed off the column before increasing the salt concentration. After the sample was applied on the resin, slowly the salt concentration was increased to wash loosely bound material.

The chromatogram shown in Figure 3.4 shows the absorbance at 280 nm (all protein material) during the run. The wavelength of 672 nm (in purple) corresponds to PSII and 681 nm (red) corresponds to PSI.

% A_{150}	Volume (mL) at flow rate 10 mL/min
10	100
10/13	680
13/28	300
100	300
10	300 or till conductivity returned back to 3.4 mS

Table 3.1: **Scheme for chromatography in purification of PSII dimers**

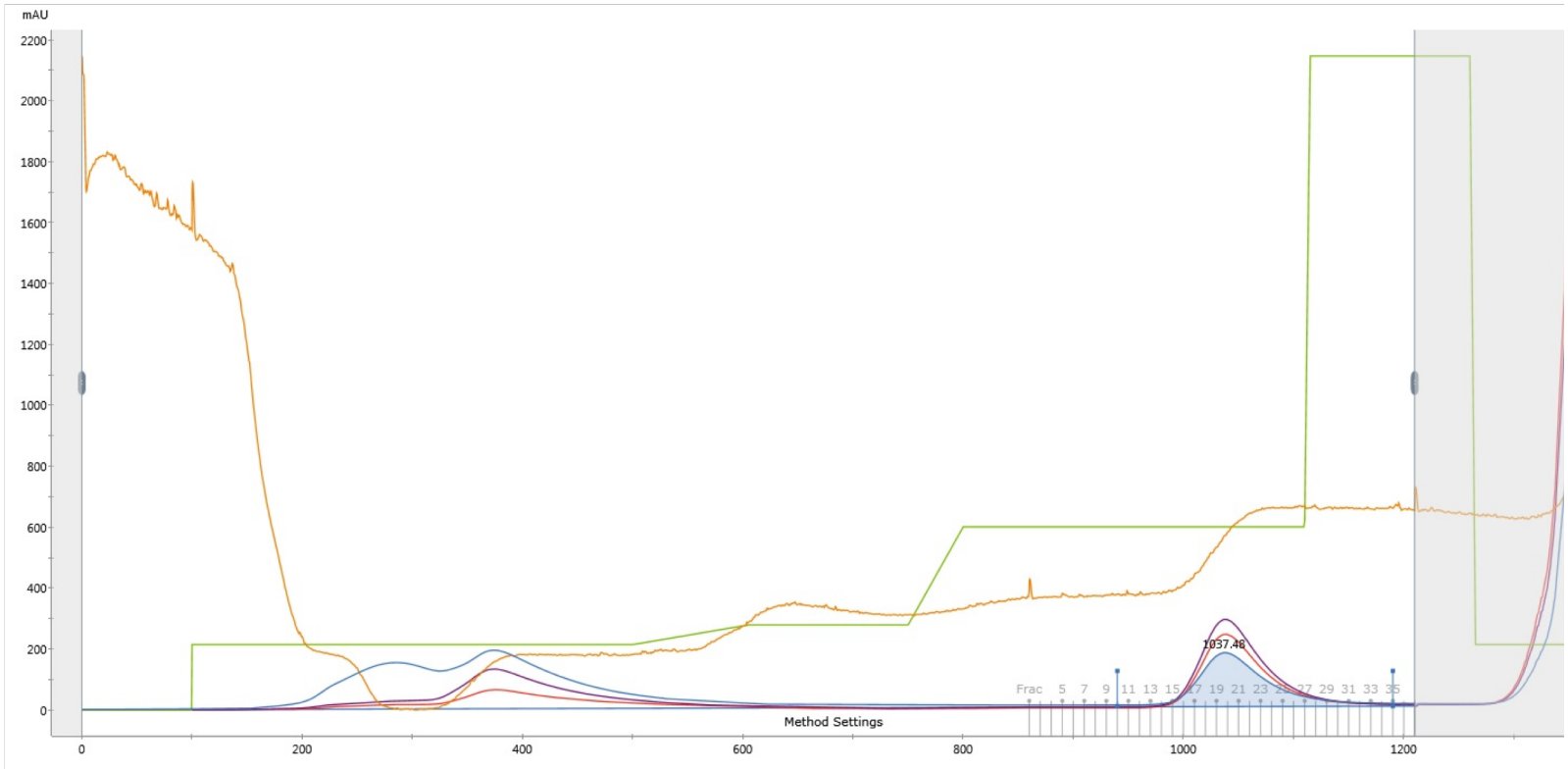

Figure 3.4: **Anion-exchange chromatography of PSII**

The green curve indicates the % B buffer being applied, orange corresponds to the conductivity of the flow-through and blue curve is the absorbance monitored at 280 nm by the in-built UV-spectrophotometer. PSII dimer peak (marked in blue) was eluted at 42 mM $MgSO_4$ and fractions (as indicated in the image) were collected. Later, PSI was washed off the column at high salt concentrations.

After removal of unbound material, weakly bound protein molecules like monomers of PSI and PSII were eluted with 13 % buffer B (19.5 mM $MgSO_4$). When the monitored wavelengths had returned to baseline (indicating removal of the monomeric PSI and II, PSII dimers were eluted at 28 % buffer B (42 mM $MgSO_4$) and the corresponding fractions collected. Strongly bound PSI trimers were washed off at 100 % buffer B and the column was re-equilibrated with 10 % buffer B before loading the next aliquot for purification. FPLC buffers (A & B) contained 20 % glycerol for maintaining the stability of PSII. But glycerol hinders the crystallization of PSI, which is crystallized at low ionic strength. Hence, for most preps, PSI was discarded and not isolated during the PSII preparation. In order to isolate PSI, a procedure was developed recently by Jesse Coe (dissertation, School of Molecular Sciences, ASU 2018) from the last column run of a PSII preparation, which involves intensive buffer exchange to wash off the glycerol on the column before PSI is eluted. The purified fractions of PSII dimers were collected and concentrated using a 100 kDa cutoff centrifugal filter (Millipore Amicon Ultracell 100 kDa) immediately after elusion. These were spun at 4000 RCF at 4 C using a swinging bucket rotor (SLA-3000). Since the capacity of each filter was 15 mL, they needed to be refilled every 10 minutes to accommodate for all available purified PSII to ensure that the filter was not running dry. The centrifugation was permitted to continue till all excess buffer was removed and the protein was concentrated to about 1 mM chlorophyll.

If precipitation was not being performed right away, PSII was concentrated to 6 – 8 mM chlorophyll and frozen using liquid nitrogen. Additional 20% glycerol was added to concentrated PSII solution using positive displacement pipettes. This solution was sucked into plastic capillary (bull-semen tubes) ensuring that an air bubble was left between the filter and PSII solution and also the PSII solution and the end of the capillary. About 350 – 400 μL of solution was introduced per capillary and rapidly frozen in shallow container

of liquid nitrogen. These capillaries were then stored in cryotubes in cryo-canes at liquid nitrogen temperatures.

3.2.2 Further purification and crystallization of PSII

PSII isolated with varying concentrations of detergent during extraction was crystallized in parallel to minimize discrepancies. The chlorophyll concentration of the PSII adjusted to 0.5 mM using buffer C (100 mM PIPES pH 7.0, 5 mM CaCl2, 0.03% β-DDM). Batch precipitation (as described in section 2.3.1) using buffer D_{15} (100 mM PIPES pH 7.0, 5 mM CaCl2, 15 % PEG 2000) was performed in 50 mL falcon tubes, using equal volume of precipitant as the volume of protein solution available. Final protein and precipitant concentration of the solution was 0.25 mM chlorophyll with 7.5 % PEG 2000. The solution was incubated at 4 C for an hour without stirring to allow PSII nano/ microcrystals to form. PSII complexes that are damaged and free chlorophylls remain in the supernatant, leading to purification by crystallization.

A droplet of precipitate/ nanocrystals was used for imaging the material using a light microscope and then the precipitate spun down at 5000 RCF for 10 minutes, This was then gently dissolved in buffer C by pipetting mixing. The solution obtained was checked for absence of lumps and uniform homogenization was ensured. Chlorophyll concentration of the protein solution was determined and adjusted to 0.5 mM, followed by another precipitation using buffer D_{13} and another hour of incubation at 4 C. The final purification step was repeating the steps with D_{11} precipitation with the pellet obtained from the previous step. This yields 10-20 μm sized crystals after 6 - 12 hours of incubation at 4 C in complete darkness (falcon tubes wrapped in Al foil).

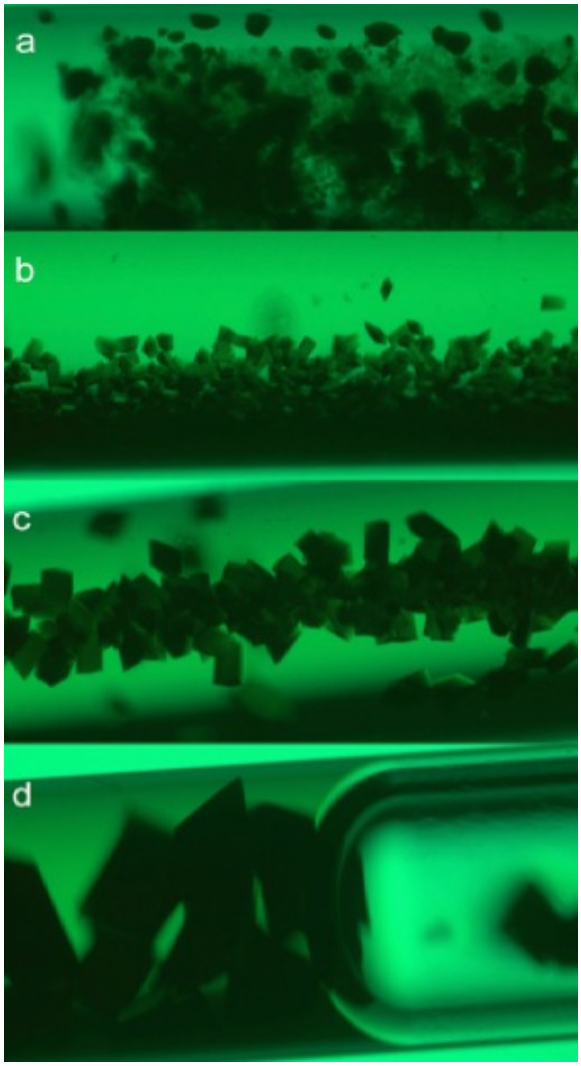

Figure 3.5: **Crystallization results from varying concentration of PEG 2000.**

Panels a-d indicate capillaries at varying PEG concentrations from 5-2 %. As seen in the figure, decreasing concentration of precipitant yields few larger crystals due to lower nucleation that leads to availability of more protein for growth of the existing nuclei resulting in larger crystals. At 5 % PEG (panel a), amorphous precipitate is also seen surrounding the crystals, indicating harsh precipitation leading to loss of protein that could be crystallized.
Image from Ingo Grotjohann.

As explained in section 3.2, a screen of 0.5 - 1 % β-DDM was performed in order to analyze if excess detergent causes harmful structural changes in the protein due to 'over-solubilization'. In order to examine the differences in crystal quality among the protein extracted, batch crystallization was performed using capillaries aimed at growth of large crystals that are suitable for X-ray diffraction at our home X-ray source. PSII precipitant obtained from D_{11} step (5.5 % PEG 2000) was dissolved in minimal volume of buffer C and its concentration was adjusted at 5 mM chlorophyll. 10 μL of prepared protein solution was mixed on a clean parafilm with equal volume of precipitant D_4 to D_{10} (corresponding to 2-5 % final PEG concentration) in 0.25 % increments. The prepared solution was sucked into glass capillaries

(inner diameter = 500 μm) and incubated at 20 C for 3-5 days. The results are summarized in Table 3.2.

3.2.3. Observations and Results

The experiment was set-up in triplicates and the best observed capillary is reported in Table 3.2

%PEG → %β-DDM	2	2.25	2.5	2.75	3	3.25	3.5	3.75	4
0.5 %	clear, no crystals	clear	**150-200 um diamonds**	**250-300 um diamonds**	**large 300-450 um & med 150-200 um diamonds**	**150-400 um sharp diamonds**	Fine particles	Fine particles	Fine particles
0.6 %	no crystals	Clear still growing no crystals	No crystals	**Random shaped 80-150 um ~20 crystals**	**Rectangular / diamond-like 50-100 um crystals**	~50-75 μm diamond shaped	Fine particles stuck to tube	20-50 μm sharp diamonds ~100	Fine particles amorphous precipitate seen
0.7 %	clear, no crystals	clear, no crystals	clear, no crystals	200-300 um diamonds, still growing	**300 um diamonds**	**300-400 um random shaped, some boats**	**Large 250-300 um & medium 100-200 um diamonds**	Fine particles	Fine particles
1 %	**>150 μm**	Fine needles	**large diamonds >100 μm**	**>100μm diamond shaped**	**Large diamonds 250 μm**	**>150 μm sharp diamonds**	Sharp diamond shape 50-100μm	Fine particles	Fine particles

Table 3.2 : **Crystals observed after 3 days**

The table indicates % of β-DDM used for PSII extraction against % PEG used for crystallization. Note that crystallization of all capillaries was performed at 0.015 % β-DDM and only the detergent concentration at membrane solubilization was variable. Conditions marked in bold were harvested and used for diffraction analysis.

Larger crystals were seen at lower PEG concentrations due to limited nucleation (phase diagram described in section 4.4.1). The conditions highlighted in bold in Table 3.1 were harvested in buffer E_8 (100 mM PIPES pH 7.0, 5 mM CaCl2, 8 % PEG 2000, 0.015% β-DDM) by breaking capillaries in a glass well. Crystals were fished using appropriate sized loops and X-ray diffraction was performed at room temperature in dim green light.

Larger crystals were seen at lower PEG concentrations due to limited nucleation (phase diagram described in section 4.4.1). The results indicate that slightly higher PEG

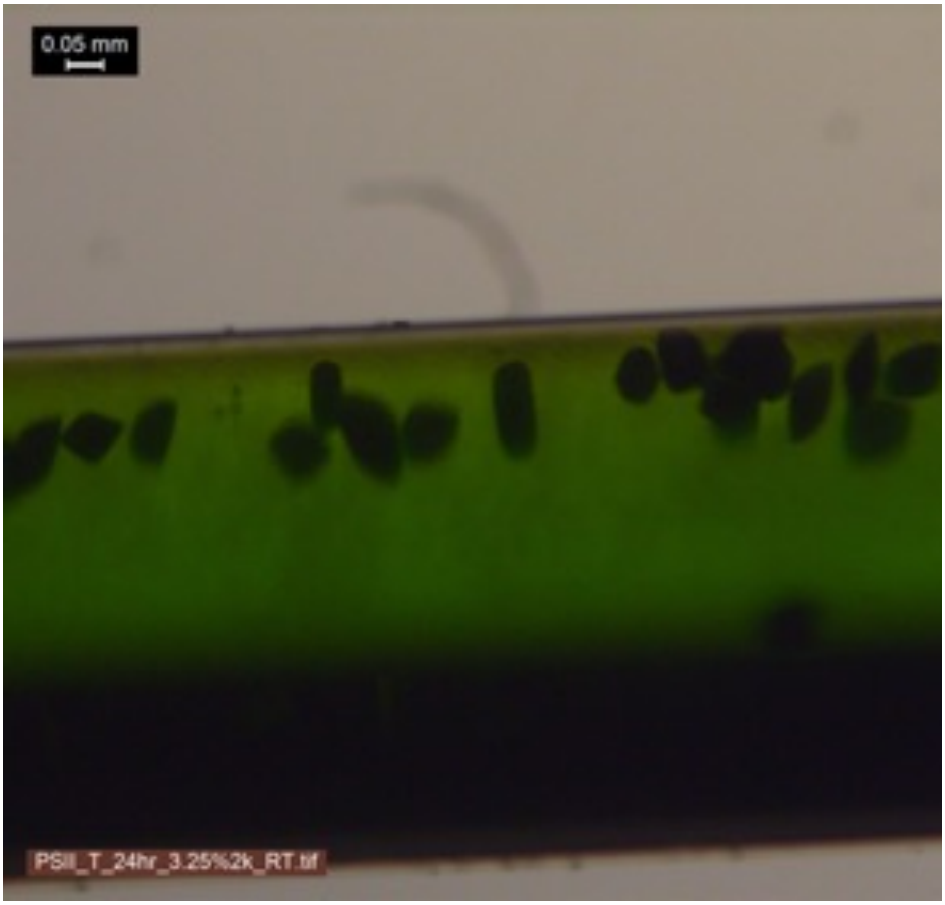

Figure 3.6: **Sample of capillary with grown crystals**

Sharp crystals of PSII were seen in various capillaries described in Table 3.2. This figure depicts crystals grown at 3.25 % PEG 2000 with 0.5 % β-DDM extraction. Crystals seen have sharp edges with the average size of about 100 μm

concentrations are required for crystallization for PSII extracted with increasing detergent concentration. Crystals grown under the conditions highlighted in bold in Table 3.2 were harvested in buffer D_8 (100 mM PIPES pH 7.0, 5 mM CaCl2, 8 % PEG 2000, 0.015% β-DDM) by breaking capillaries in a glass well. Crystals were fished using appropriate sized loops and X-ray diffraction was performed at room temperature in dim green light.

The crystals of protein extracted at 1 % β-DDM were studied against protein extracted at 0.5 % β-DDM. X-ray diffraction data was collected at the home X-ray source (Rigaku microfocus rotating anode X-ray generator Micromax-007HF). Best diffraction obtained at both conditions has been described in Figure 3.7. The 5.53 A shadow in a) is due to scattering of the loop which held the crystal. The absence of that ring from b) merely indicates that the loop was not in the path of X-rays during data collection. The crystals were subjected to 30 seconds of exposure and 5 images were taken from each crystal at -90°, -45°, 0°, 45° and 90° in order to cover 180° across the crystal. Best diffraction obtained from all conditions that were analyzed have been enlisted in Table 3.3. Overall, PSII isolated at 0.5 % β-DDM produced the best diffracting crystals. Diffraction patterns highlighted in grey have been compared in Figure 3.7.

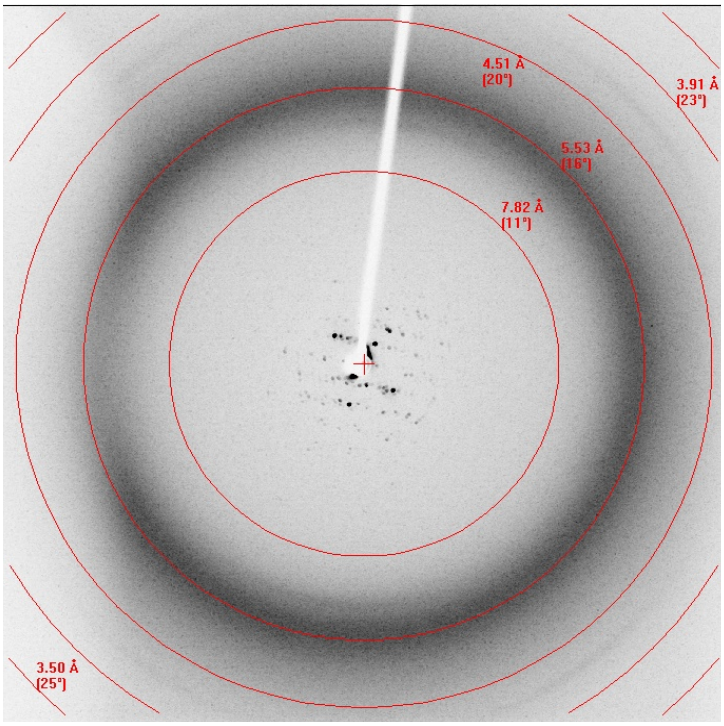

Figure 3.7a: Best diffraction from crystals from PSII isolated at 1 % β-DDM

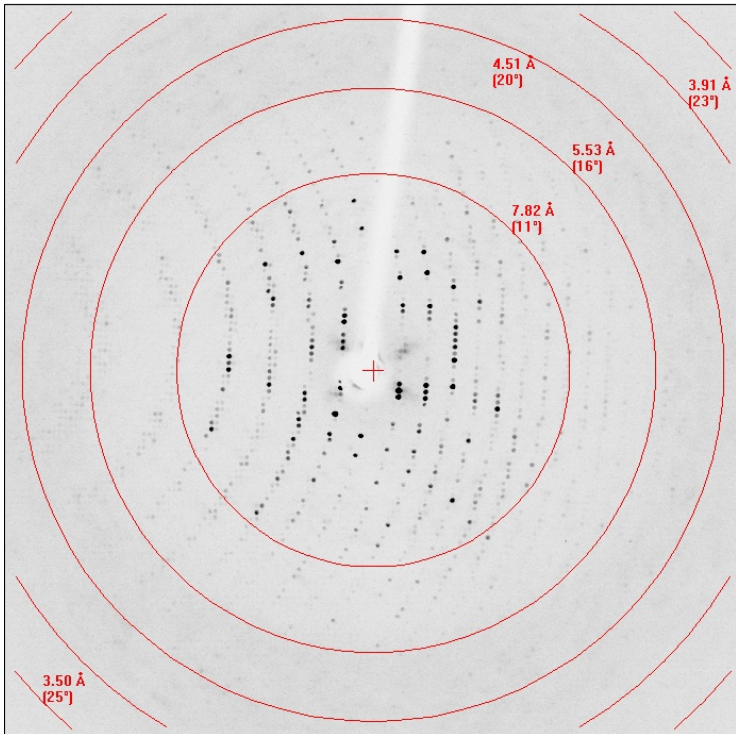

Figure 3.7b: Best diffraction from crystals grown from PSII isolated at 0.5 % β-DDM. Details have been explained in Table 3.3

%PEG→ %β-DDM	2.5%	2.75%	3%	3.25%	3.5%
0.5 %	6.3 A	4.35 A	4.8 A	5.1 A	
0.6%		7.1 A	6.6 A		
0.7%			8.2 A	9.6 A	7.8 A
1%		13.8 A	11.3 A	14.1 A	

Table 3.3: **Best diffraction obtained from PSII crystals**

% β-DDM at protein extraction vs % PEG at crystallization. The two boxes highlighted in grey correspond to the diffraction patterns shown in figure 3.7. In column labeled 3% a clear trend of worsening quality of crystals is seen in direct correlation with % β-DDM used for membrane solubilization with 0.5 % showing best results.

Extracting membrane proteins from their natural bilayer environment often requires an excess of detergent (Seddon et al., 2004). But even mild non-ionic detergents like long chained β-DDM (structure described in figure 4.7) can have detrimental effects on the protein upon prolonged exposure at high concentrations. Over-solubilization may remove smaller outer subunits from the protein complex and that in turn might lead to decreased protein stability, leading to poor quality of X-ray diffraction from resulting crystals. One significant conclusion drawn from this analysis is to reduce the detergent concentration during the extraction process, in order to restrict over-solubilization of membrane proteins and obtain protein at higher stability for crystallization and X-ray structure analysis.

3.3. Microseeding for microcrystallization

Dimers of PSII purified by Anion-Exchange chromatography were further purified by a series of crystallization steps. These steps are described in section 3.2.2. The final

purification step was carried out extremely carefully at final conditions of 0.25 mM chlorophyll concentration crystallized with 5.5 % PEG 2000 by incubation dark at 4 C for 6 – 12 hours after the PEG solution was added.

3.2.1. PSII crystals have different morphologies

PSII is an extremely difficult to crystallize protein and thereby the consistent reproducible growth of large amounts of 10-15 μm sharp crystals has been a challenge. Different batches of protein behave differently under the same conditions. For example, at the final purification step (D_{11} precipitation), using the exact same set-up, with same buffers, after identical incubation conditions, two representative batches of crystals appear drastically different (fig 3.8). This is usually seen in different batches of protein from different batches of cells. This may also be caused due to Ostwald ripening where small rigid units redeposit on each other to create larger particles. Since the solution reaches the supersaturated phase too fast, secondary nucleation occurs at the surface of growing crystals leading to appearance of large crystal-clusters as seen in fig 3.8B. When

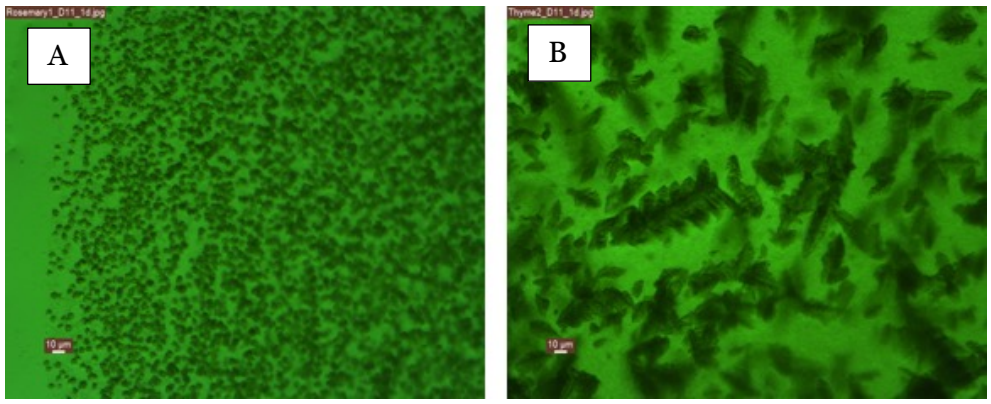

Figure: 3.8: **PSII microcrystals have different morphologies**

PSII preparations named a) Rosemary and b) Thyme were crystallized in parallel using batch method in identical conditions of 5.5 % PEG 2000. Image was captured after 14 hours of incubation at 4 C in the dark.

exposed to X-rays, these exhibit increased mosaicity and diffract poorly. They are particularly unusable for TR-SFX since they cannot be homogenously illuminated and can clog injector based delivery systems.

In order to prepare large amounts of homogenous crystals, various methods were employed. Free interface diffusion and Free interface diffusion centrifugation (Kupitz et al., 2014) have been optimized for 1-5 μm crystals. For larger 15-20 μm crystals, the batch method has yielded better results (both methods have been described in section 2.3). In order to minimize crystals from growing into each other, various protein and precipitant concentrations were explored but that did not result in remarkable progress. Another approach was to terminate crystallization after 2 hours of precipitation by removing the uncrystallized protein and adding excess of precipitant buffer (100 mM Pipes pH 7.0, 5 mM CaCl2, 20 % PEG 2000, 0.015 % β-DDM). The primary challenge with preparing samples suitable for SFX was that every crystal preparation behaved differently and there was an urgent need to have a large number of crystals of similar size, shape and diffraction quality. This challenge was overcome by microseeding procedures.

3.2.2. Preparation of seed stock

Since nucleation needed to be controlled, the supersaturated metastable zone of the phase space was explored. Providing microseeds at this step enhanced total crystal yield and the morphology of resulting crystals were identical to the crystals used for seeding. In other attempts, performing the seeding step twice or 'double seeding' contributed in considerable improvement in diffraction resolution (Dods et al., 2017).

Optimum seed stock was prepared by combining 100 μL crystal pellet obtained from D_{11} with 500 μL of precipitant buffer (100 mM Pipes pH 7, 5 mM CaCl2, 9 % PEG 2000) in a 1.5 mL microcentrifuge tube. 25 mg of 425-600 μM sized glass beads (Sigma

Cat # G9268) were added to the crystal suspension. This tube was vortexed for 5 seconds and placed on ice for 10 seconds. This was done to prevent crystal dissolution by sudden increase in sample temperature. The vortex - ice cycle was performed for 10 cycles and resulting 'seed stock' was faint green in color.

3.2.3. Precipitation at 9 % PEG 2000

The seed stock was diluted 1:100 in cold precipitant solution $D_{7\text{-}10}$ (100 mM Pipes pH 7, 5 mM CaCl2, 7-10 % PEG 2000). The pellet obtained from D_{11} precipitation was gently dissolved in buffer C, chlorophyll concentration was determined and adjusted to 0.5, 0.6 and 0.7 mM. The precipitate solutions + seeds were gently mixed until homogenous and then, added dropwise to stirring PSII solution at 4 C. Once the

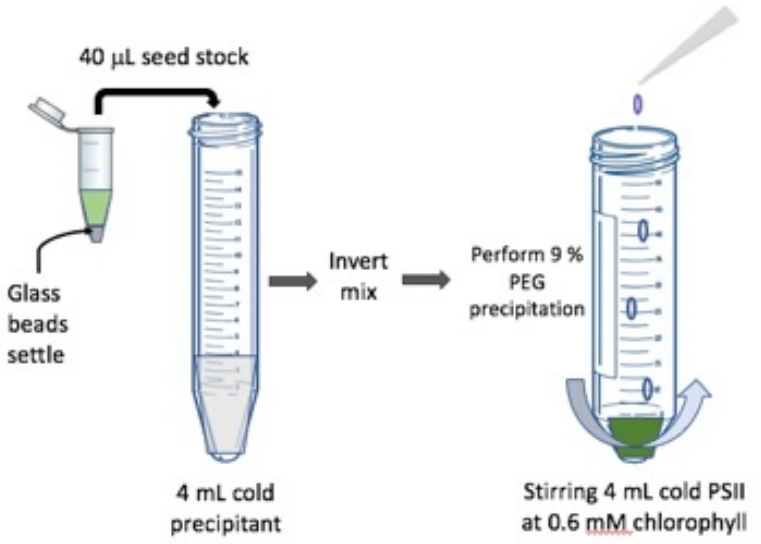

Figure 3.9: **Schematic representation for micro-seeding**

Seeds were introduced in cold precipitant solution (D_7-D_{10}) in 1:100 ratio by volume. Equal amounts of precipitant was added to volume of protein available at 0.5 - 0.7 mM chlorophyll. Most reproducible results with homogenous crystals at 20 µm were observed at final concentrations of 0.3 mM chlorophyll with 4.5 % PEG 2000.

precipitation was complete, the solution was permitted to mix for another 30 seconds, stir-bar was removed and sample was incubated for 30 - 40 hours at 4 C in the dark.

3.2.4. Results

Addition of seeds made from either sharp crystals grown at D_{11} or 1-5 μm crystals grown at D_{13} resulted in dramatic improvements in crystal morphology. If crystallization was performed at 4.5 % PEG 2000 in the absence of seeds, very little protein was crystallized and about 90 % of PSII would remain in solution. Introduction of seeds at 4.5 % PEG 2000 permitted crystal growth at the metastable zone. By separating the steps of nucleation and crystal growth, crystallization conditions could be explored and better diffracting crystals could be grown.

The microseeding procedure could be used successfully to make uniform 15 – 20 μm PSII crystals from ALL preps (shown in Figure 3.10). In the past about half the preps would yield crystalline clusters that were not suitable for TR-SFX since the excitation would not be suitable, they restrict smooth operation of the GDVN systems and can also be poorly diffracting with multiple low resolution patterns. The ability of using all protein for the final experiment was a significant achievement which ensured that all preps yielded good quality crystals that could be utilized for Time-resolved pump-probe experiments, which eventually meant that all protein that was isolated and crystallized was suitable for use i.e. more efficient use for available protein.

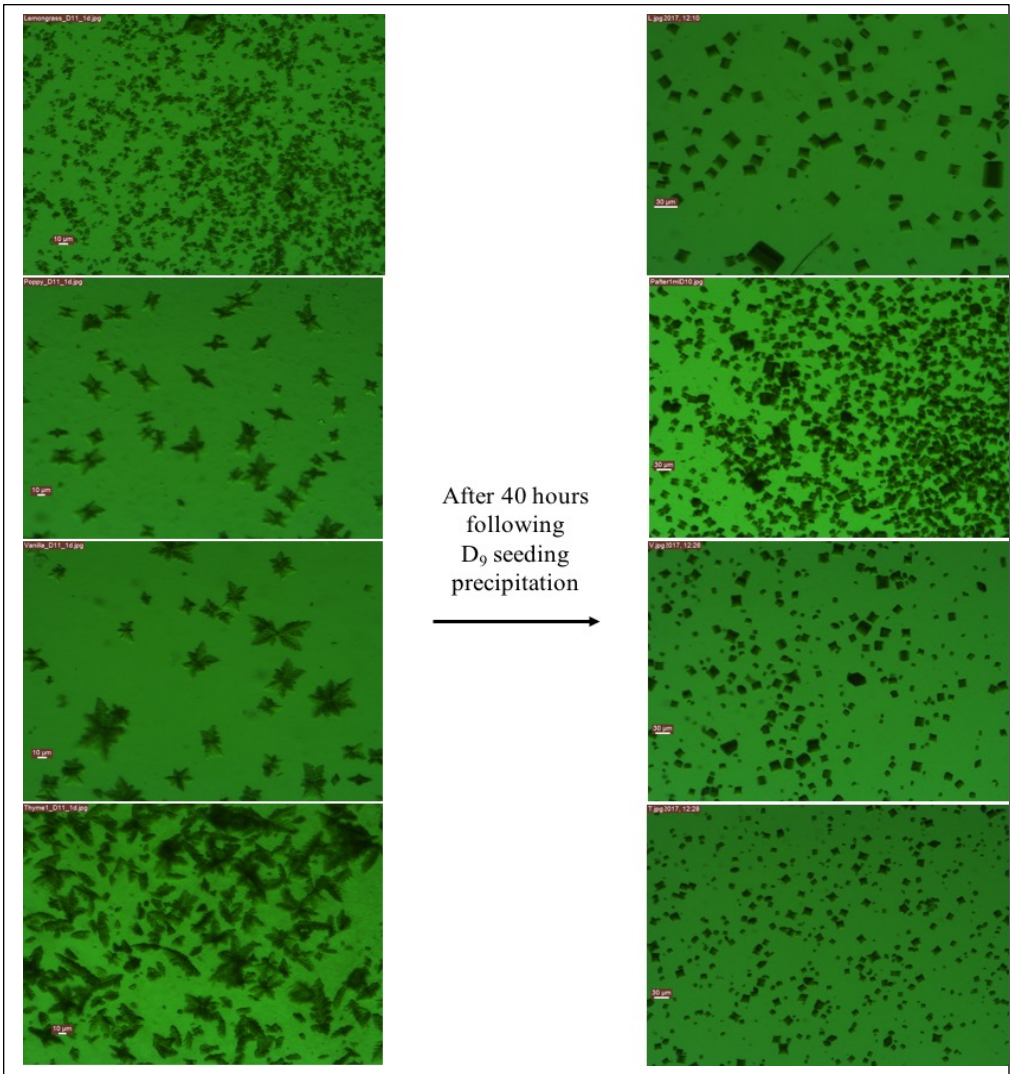

Figure 3.10: **Effect of microseeding**

Panel on the left are images of crystal preparations obtained from D_{11} precipitation. Crystals shown in image 3.8A were crushed and added to lower precipitate D_9 in order to grow bigger crystals. The scale-bar in each image was set to 30 μm and homogenous 15-20 μm PSII crystals were obtained.
It must be noted that image on the left and the right is that of the SAME protein preparation.

3.3. Characterization of PSII activity as microcrystals

As explained in section 2.5.1, PSII molecules transition through 5 oxidation states (S-state transition) in the photo-cycle and each S state has varying life-times upon photo-excitation. Section 2.3.4 introduces that, in presence of light and electron acceptors, active PSII molecules are able to catalyze the transfer of electrons from water to Q_B, generating O_2. As PSII in the dark is predominantly in the S_1 state, under flashing light, majority of the evolved O_2 is expected to be at the 3rd flash, as PSII transitions from S_1 to S_4 and then to the S_0 state.

3.3.1. Experimental set-up of Clark based microcell

Functional characterization of the four-step photocatalytic cycle in PSII crystals is essential for TR-SFX studies. The objective is homogenous transition of all molecules in the crystal through the S states in the Kok cycle using laser flashes. This presents some challenges because X-ray crystallography cannot determine the oxidation states of atoms or distinguish among molecules in different oxidation states. For this purpose, other supplementary techniques like X-ray emission spectroscopy (Yano et al., 2005); (Pushkar et al., 2010), Fourier transform infrared spectroscopy (Kato et al., 2018), EPR spectroscopy (Han et al., 2008), extended X-ray absorption fine structure (EXAFS) (Grundmeier and Dau, 2012) etc. have been employed in the literature. Described here is a method for understanding S-state advances by analysis of flash-induced O_2 yield.

In order to ensure saturation of photochemical steps, it was essential to illuminate all molecules in the crystal uniformly. Hence, a short flash of high light intensity was essential to maintain clean state transitions. For this purpose, a high pressure Xe flash lamp exciting PSII in the or visible spectral region was used with FWHM of 1 μs. The optical energy delivered was optimized based on the yield of O_2 at the third flash.

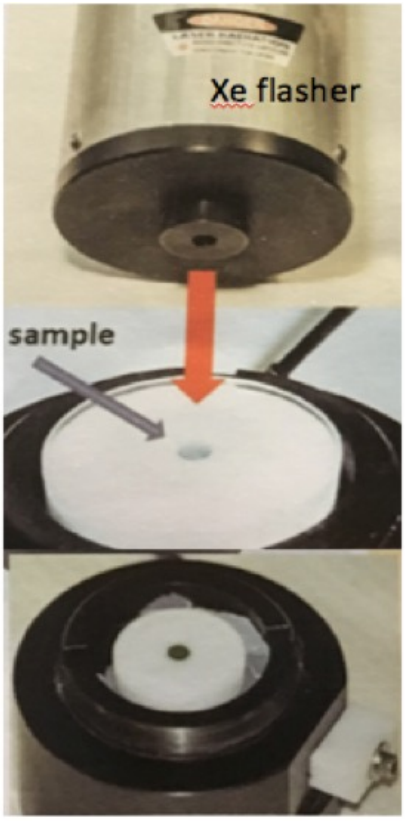

Figure 3.11: **Assembly of electrochemical O_2 microcell**

The sample holder and direction of flashing light have been illustrated with the red arrow. The electrode is placed underneath the sample holder separated by a semi-permeable membrane. So, the order of components bottom to top were: electrode, membrane, sample in sample holder, covered by glass slide, topped with Xe lamp.

The measurements were carried out in the home-built microcell (Ananyev & Dismukes, 1996), using a Pt-Ir electrode covered by a thin membrane. The 75 % Pt + 25 % Ir alloy ensured long term mechanical stability and chemical resistance, i.e. homogenous electrode surface. Placing the membrane between the electrode and the sample prevented diffusion of added electron acceptors (different types of quinones) to the electrode surface. O_2 yield was directly proportional to the current required to reduce O_2.

PSII crystals were diluted to 0.015 mM chlorophyll in buffer D_{11} + 0.02 % β-DDM for maximum sensitivity of the experiment. At higher concentrations, saturations were not observed in the first 4 flashes, because too high crystal density prevented the transmission of saturating light throughout the sample volume. The dilutions were made in crystal stabilization buffer (100 mM Pipes pH 7.0, 5 mM CaCl2, 11 % PEG 2000, 0.015 % β-DDM). Small organic quinones were used as electron acceptors to maximize O_2 yield. These were directly introduced into the sample by pipette mixing. The sample holder was covered by

a glass slide to maintain near-anerobic conditions in the sample. This was done because O_2 from air can accept electrons from the Q_B^{2-} sites and interferes with analysis (Ananyev & Dismukes, 1996).

3.3.2. Effect of electron acceptors on O2 yield of PSII

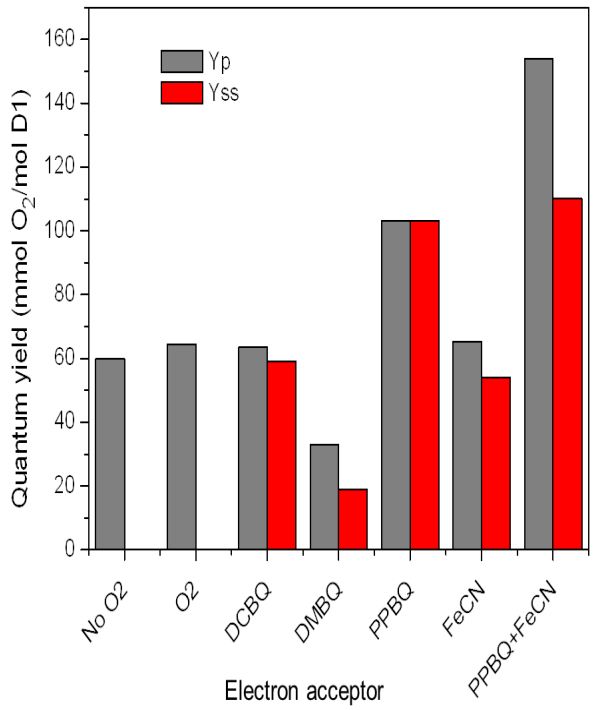

Figure 3.12: **Effect of electron acceptors on yield of flash-induced O_2**

Grey curves indicate average yield from the first 4 flashes (Y_P) in comparison with average yield from steady state (Y_{SS}). The decrease in overall yield can be attributed to the accumulation of quinol form during continued illumination.

Due to the nature of S-state mechanism, 3 sequential flashes would advance the centers from (dark) S_1-> S_2-> S_3-> S_4^* states. Only the PSII molecules progressing to S_3 state can go through the transient S_4 state and spontaneously move to So by O_2 evolution. Hence, in an ideal kok system that is dark adapted, O_2 would be expected to release at flash numbers 3 + 4n (n=0, 1, 2...) (Vinyard et.al, 2013) (depicted in Figure 3.13). This 4-flash based transition through the kok-cycle is visualized as 4-period oscillations in PSII.

The effect of several electron acceptors was analyzed on the O_2 yield. These were 2,6-dichloro-1,4-benzoquinone (DCBQ), 2,6-dimethyl-1,4-benzoquinone (DMBQ), 2-phenyl-1,4-benzoquinone (PPBQ) and ferricyanide (FeCN). The O_2 yield seen for the first 4 flashes (1 cycle) was compared to the yield seen at steady state of PSII molecules in presence of various acceptors. These have been normalized and plotted in Figure 3.12. The synchronization and thereby the oxygen yield decreases with the number of cycles due to misses and double hits. Furthermore the amount of electron acceptor decreases due to the accumulation of the

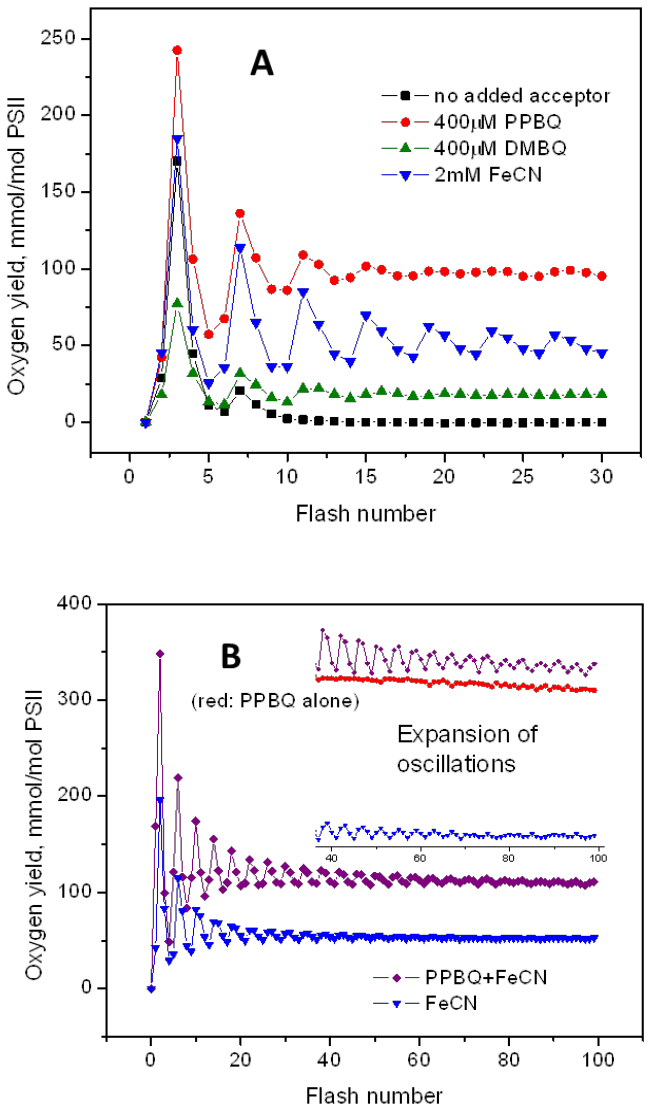

Figure 3.13: **O_2 yield at corresponding light flashes**

A) depicts O_2 yields seen upon exposure of PSII crystals to 30 continuous flashes of light in presence of various electron acceptors. PPBQ shows the highest O_2 yield and FeCN shows highest number of oscillations.
B) compares FeCN as a sole acceptor compared to FeCN in combination with PPBQ. Inset shows expansion of oscillations at higher flash numbers in PPBQ + FeCN compared to PPBQ alone.

reduced quinols during continuous illumination The O_2 oscillation can be prolonged upon replenishing the supernatant with fresh quinones, indicating no damage to PSII molecules in crystals.

As seen in figure 3.12, the combination of PPBQ with FeCN yielded the maximum O_2 evolution, this is expected as FeCN reoxidizes the quionol to quinoneThe concentration of quinones was optimized at 400 μM, whereas that of FeCN was optimized at 2 mM based on O_2 yield titrations. PPBQ is a quinone with very low solubility that was made available to PSII by dissolving it in DMSO. FeCN, on the other hand is a water-soluble oxidant that has the potential to oxidize the quinol form of PPBQ.

PSII microcrystals grown by the method described in section 3.2, efficiently perform water oxidation for 1 cycle even in the absence of external electron acceptor (control, black curve in fig 3.13A) and this confirms the presence of intrinsic quinones at both the Q_A and Q_B plastoquinone binding sites. Addition of PPBQ, as an artificial quinone electron accpetor enhances the O_2 evolution and permits PSII to oscillate through several cycles of the kok-cycle. For TR-SFX experiments, PPBQ was added to dark-adapted PSII microcrystals to ensure highest activity of crystals when excited with 1-3 pump laser pulses for capturing intermediates of the S-cycle.

3.4. Sample delivery using Fixed-target Roadrunner 2

Advances in X-ray sources and increased popularity of Serial Crystallography have increased the demand on improved faster frame-rate detectors and novel sample delivery techniques, both at synchrotrons and XFELs. Due to the high brilliance of XFEL pulses, the crystals in its path are damaged by a single X-ray pulse. Along with the repetition rate of 120 Hz, there is an absolute need for fast sample exchange between shots.

Sample delivery for SFX has been established using liquid jets generated by use of a Gas Dynamic Virtual Nozzle (DePonte et al., 2008) (Set-up explained in figures 1.13 and 2.3). This method has been adapted for several experiments and can be manipulated to yield jets focused down to a few micrometers. But still only about 1 in 10,000 crystals interacts with X-ray pulses. Also, due to the construction of the capillary, larger better diffracting crystals (more than 20 μm) have to be filtered out before sample delivery to avoid clogging events. Liquid jets present another disadvantage of background scattering. This is particularly adverse for small weakly diffracting crystals whose diffraction signal might be buried in the background. Finally, the sample for liquid injection is stored in a reservoir and during the course of the experiment, the crystals can settle, leading to inhomogeneity in delivery, clogs or back pressure. A few anti-settling devices (Lomb et al., 2012) have been explored for this purpose, but during data collection, eventually, crystals continue to settle. With Roadrunner2, (Roedig et al., 2017) fixed target systems are currently able to utilize all pulses of the XFEL (LCLS) and overcome shortcomings of the injector based approach.

3.4.1. Experimental set-up for Roadrunner2

The Roadrunner setup consists of high-precision x and y precision motor driven scanning stages mounted on a horizontal translation stage and a vertical rotation axis (orientation depicted in figure 3.15). A high-magnification inline microscope was used to visualize samples and their support structure. In order to minimize the background scattering signal, single-crystalline silicon wavers were used as the substrate material for the micro-patterned chips (Roedig et al., 2015) which contain holes or wells in which the crystals reside. The X-ray beam is focused to the central hole in each well, thereby

minimizing the background signal. The experiments are performed in a closed humidified Helium filled chamber which decreases the number of photons scattered by air.

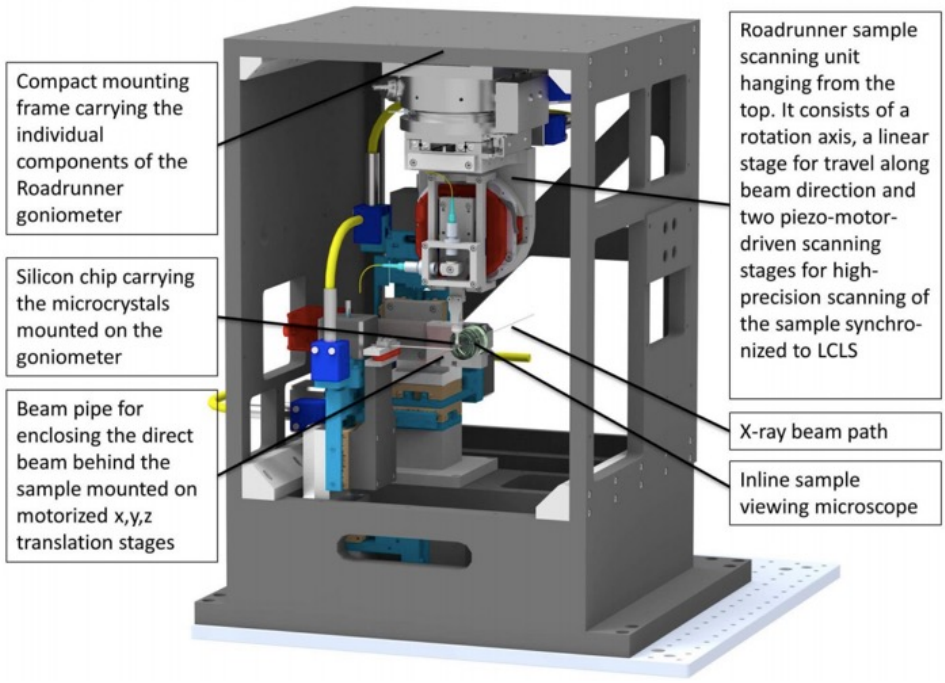

Figure 3.14: **Technical overview of Roadrunner goniometer**

The goniometer consists of three main components: an inline sample-viewing microscope, a high-precision scanning unit for fast scanning, and a motorized beam pipe unit. All components are mounted on a common support frame to achieve high mechanical stability. The minimum possible distance between sample and detector surface is 50 mm and this allows for the collection of high-resolution diffraction data. Image from Roedig et.al., 2017

The chips are aligned in the path of the XFEL and scanned such that each pulse encounters a new pore. The windows of the silicon chips used for fixed-target experiments can manufactured according to the size of the crystals under study, thereby permitting SFX of larger microcrystals (15-50 μm) that diffract more strongly to be investigated by SFX.

3.4.2. Considerations for conducting time-resolved experiments using fixed-target approaches

For TR-SFX with Roadrunner2, special adjustments needed to be made. In order to prevent light exposure of neighboring crystals, pores on the chip were enclosed in compartments that were more like funnels. Both the pump laser pulses and the XFEL pulses were introduced to the chip compartment via an inline microscope as shown in figure 3.15.A

A dichroic aperture was placed very close to the surface of the chip (3mm) which guarantee a illumination spot of 100x 25um, which prevented illumination of neighboring

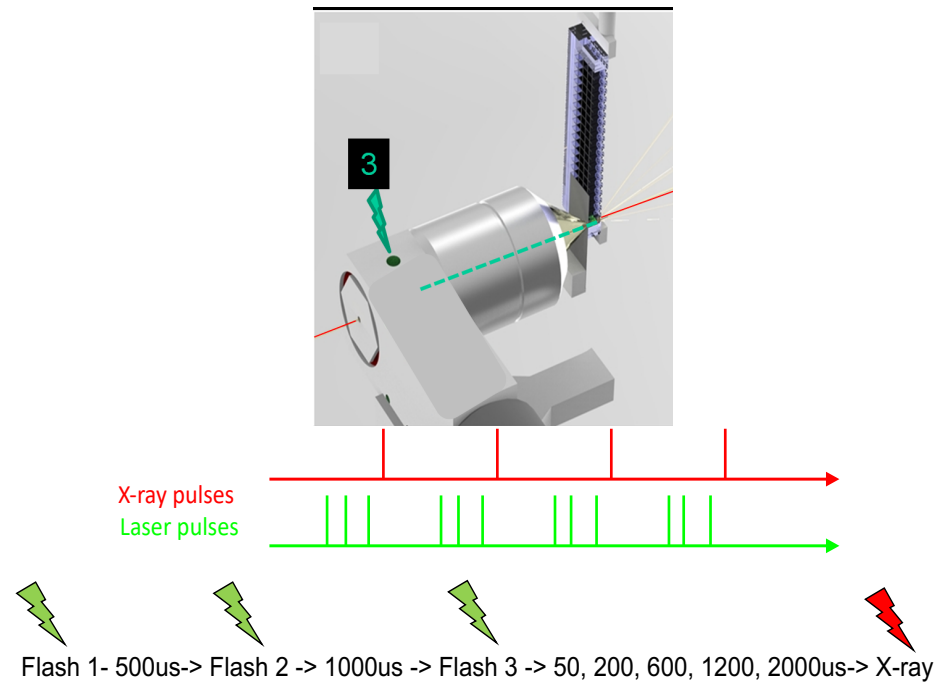

Figure 3.15: **Simplified representation of TR-SFX using Roadrunner2**

Top image shows the strategy for laser excitation for TR-SFX of PSII where pump and probe pulses were introduced through the in-line microscope and the bottom scheme indicates the laser excitation scheme for three-flash excitation of PSII crystals. The focal size of pump laser and chip raster scanning speed was adjusted to ensure that the same compartment received 3 laser flashed before x-ray pulse.

wells. An additional infra-red LED was installed in the He chamber to visualize the chip for initial alignment.

200 μL of crystal suspension was applied gently at the center of the silicon chip. Without disturbing the chip, the droplet was spread uniformly over the windows under the humidified stream of air, which prevented immediate crystal dehydration. The mother liquor rapidly filled the micro-chambers and formed a meniscus. Excess solvent was removed by bringing a wedge of Whatman No.1 filter paper in close contact with the bottom side of the chip. This blotting process needs to be done carefully, because the chips are fragile and some mother liquor needs to be retained on the chips to conserve hydrated crystals. Crystals that are larger than the pore-size were retained on the chip.

Figure 3.16: **Assembled chip before and after sample loading**

Panel A) depicts a silicon chip mounted on a holder with a magnetic base that connects to the Roadrunner goniometer head. Also seen is a sleeve (containing cotton pad soaked with buffer) used to cover the loaded chip to prevent crystal dehydration. B) is an image of a chip loaded with ~ 50 % coverage of pores. This was further optimized for maximum coverage without microcrystal overlap to prevent multi-crystal hits because of over-crowding of crystals.

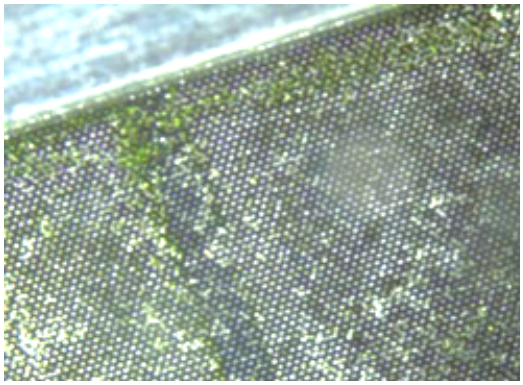

Figure 3.17**: Loaded chip are susceptible to dehydration**

After crystals are deposited on the chip surface, excess mother liquor is blotted from the other side of the chip. As seen in the figure, soon after the blotting event, if the chip is left exposed to air, the crystals at the edges begin to dry out. In order to collect data without crystal dehydration, excessive humidification of the He chamber (> 99% humidity) was essential.

Following the blotting event, a sleeve (depicted in figure 3.17) that contained a cotton pad soaked with buffer (100 mM Pipes pH 7.0, 5 mM CaCl2, 11 % PEG 2000) was gently slid on top of the chip to maintain the moisture in the crystal surrounding. This sleeve was ultimately covered in foil and black cloth to keep the crystals well-hydrated and dark-adapted.

3.4.3. Humidity control is necessary to prevent crystal dehydration

Initial experiments of SFX with PSII microcrystals without photoexcitation were performed in the MFX (Macromolecular femtosecond crystallography) hutch at LCLS. Over the course of four 12-hour shifts, data on 15-20 μm PSII crystals was collected on 33 chips resulting in 744,404 hits. Most hits obtained were valid and the final indexing rate was 83 % leading to 621,303 indexed diffraction patterns. But, upon initial analysis, the unit cell dimension ranges were much broader (+/- 5 A in one dimension) compared to

sample delivery in a jet and showed an oscillation pattern that was co-related to the pattern of the raster scan. The maximal resolution of diffraction obtained also showed similar oscillation, indicating the crystal shrinkage and/or swelling was affecting the quality of the crystals. This was largely attributed to the uneven distribution of humidity in the He chamber. This led to the crystals along the edges of the chip to dry out faster, while crystals close to the inlet of humidified He seemed to swell showing larger unit cell constants than what has been observed in the liquid jet and this led to the oscillations based on the pattern of the scan.

Figure 3.18: **Humidity set-up to maintain crystal hydration.**

Image depicts a series of bottles of water in a water bath set to 50 C. Gas is bubbled through these bottles and the resultant 'wet' He is introduced in the chamber with the goniometer head.

For recent experiments, to ensure uniform hydration across the silicon surface, the humidification chamber was re-built to allow for uniform humidification and 4 humidity sensors were installed (one at each corner of the chamber) which were closely monitored and their values recorded during data collection of each chip. In the first experiment, the incoming helium gas was bubbled through a network of bottles containing bubbling warm (50 C) water to ensure that the gas was as 'wet' as possible, which led to the "over-humidification" and crystal swelling in the first experiments. In the optimized new setup used for the time-resolved experiments the water temperature was set to 25C. Humidity sensors were installed at 4 check-points in the chamber (flow-chart depicted in figure 3.20), to ensure constant humidity at 98-99%. Any changes in these conditions would lead the crystals to dry out, shrink or swell and thereby and lose or decrease their diffractive capacity. The status of the humidity and gas flow in the hutch was monitored using a control panel (as seen in figure 3.20). This indicated if loose connections caused a disconnect in the path of the He gas through the network of bottles, temperature at every component of the humidity pathway and % humidity at the 4 humidity sensors that were installed in the He chamber was recorded.. If humidity detected by any of the sensors in the chamber was below 98 %, the controller would alert the user twith a "humidity is low alarm" so we could double check the components involved in the system.

Better regulation of humidity certainly minimized the variations in unit-cell parameters that were previously seen, but slight fluctuations are still present. Further analysis of the miore than 250 000 patterns obtained from the time resolved fixed-target experiments would reveal how much of the data is suitable for data analysis and structure determination. By resolving these challenges in future investigations, fixed target approaches can become mainstream for sample delivery at XFELs.

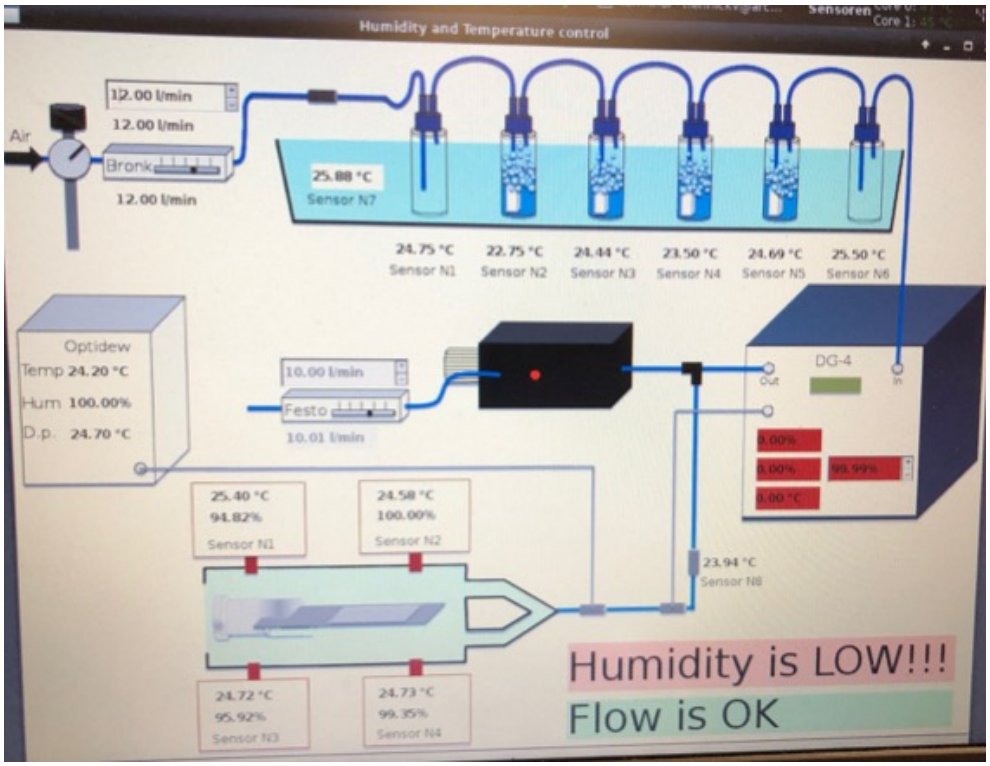

Figure 3.19: **Humidity and Temperature controller**

The figure depicts a cartoon of all components involved in the humidity control. This was constantly monitored for optimal humidity when a chip loaded with PSII crystals was mounted in the chamber. Bottom left indicates the 4 sensors installed in the corners of the He chamber and if any of these detected less than 98 % humidity, an alert was highlighted (as seen bottom right).

3.4.4. Efficiency of fixed-target vs injection systems

Depending on the hole size and distance between the holes, one chip may provide between 40 000 and 100,000 pores. Because of high loading density of crystals that can be achieved and the very precise and synchronized movement of the stage with respect to X-ray pulses, hit-rates (fraction of X-ray pulses interacting with crystal) with Roadrunner2 can approach 80 %, resulting in very efficient use of microcrystals. Thus, one successful chip can potentially yield enough patterns to solve the structure of the molecule under study. In comparison, liquid jets yield average hit-rates of 10 - 30 % which can go down to

0.1-5 % for crystals larger than 10 μm. Also, in order to maintain the stability of the jet, sample needs to be flown at a constant speed of approx.. 10 m/second and most of the crystalline sample ends up being wasted.

The amount of sample consumed by fixed target chips was an order of magnitude lower than injection systems because of the size of crystals and chip-holes were optimized, most crystals could be brought to interact with XFEL pulses. Setting up Roadrunner system and aligning the chip is complex and time consuming, but the rewards of the time invested both in sample preparation and data collection were reaped.

3.5. Updates from data analysis

As stated in chapter 2, SFX data are evaluated using special software packages (*Cheetah* and *CrystFEL*). The updated version of *Cheetah* efficiently performs hit-finding, frame sorting, identifies & integrates Bragg spots and prepares all selected frames for subsequent analysis (Barty et al., 2014). The improvements in the software packages has not only enhanced the percentage of patterns indexed, but has also impacted overall quality of data. Since each crystal diffraction pattern is a still image and thereby all reflections are "partials" and there is shot-to-shot variation in crystal size, crystal orientation as well as X-ray energy and intensity between pulses in SFX, ten-thousands of diffraction patterns are required for one time point in a TR-SFX experiment. One key features of the Cheetah software is that, on each detector pixel (Hart 2012) in each image, background subtraction was performed prior to accurate Bragg peak characterization (Barty et al., 2014). As described in section 2.5.3, CrysttFEL was used for merging and scaling the data (White et.al., 2012).

3.5.1 Summary of data collected using injection vs fixed target approaches

Month /	Hits	Indexed	Excitation Strategy
08 / 2008	--	--	1 Flash, Laser not recorded
01 / 2012	169,626	58,962 (34.7%)	Dark, 1 Flash and 2 Flash
06 / 2012	53,614	19,681 (36.7%)	Dark, 3 Flash alternate (210,
11 / 2014	59,798	22,812 (38.1%)	1 Flash alternate
10 / 2015	94,958	35,257 (37.1%)	Dark, 2 Flash and 3 Flash
08 / 2016	76,565	59,700 (77.9%)	Dark, 3 Flash alternate
11 / 2016	744,404	621,303	Dark
09 / 2017	863,112	485,875	Dark, 3 Flash

Table 3.4: **The table enumerates data collected at PSII beam-times at LCLS.**
The final two rows highlighted in grey are experiments performed by fixed target delivery system. All previous experiments used GDVN injection systems.

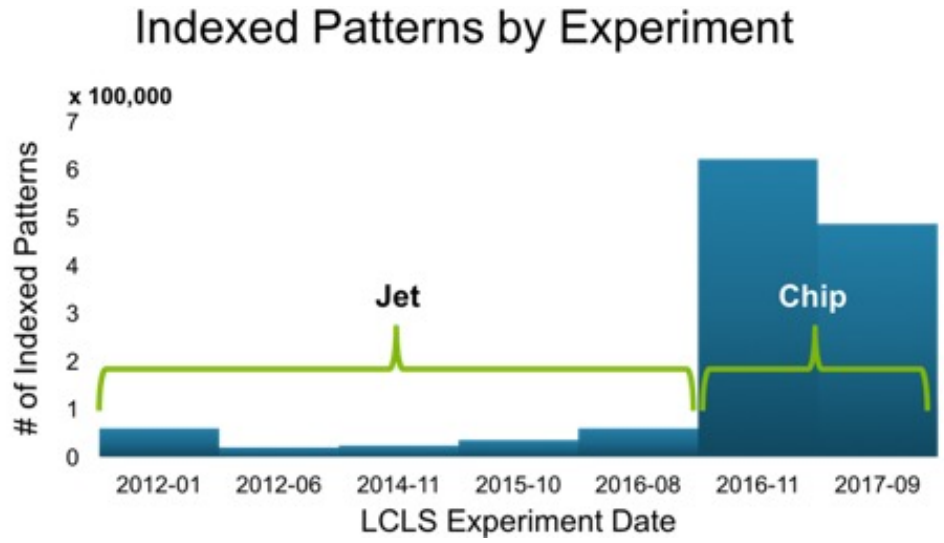

Figure 3.20: **Schematic representation of patterns collected by SFX of PSII**
Plotted are indexed diffraction patterns obtained by injection and fixed target systems

Liquid injection systems were perfectly suited for LCLS's high repetition rate of 120 Hz. With Roadrunner2, the ability to utilize all pulses of the XFEL was extended to fixed-target systems (Roedig et al., 2015). Table 3.3 and fig 3.21 summarize results of SFX performed with PSII. But the dramatic increase in number of indexed patterns had so far limited benefits since the unit cell dimensions were not constant. This was seen with samples of various protein crystals and it is a severe current limitation of the fixed target sample delivery technique. Attempts to interpret the collected data are underway, which include subdividing the data sets based on the unit cell dimensions as a basis for evaluation of the time-resolved experiments but the groundwork for all components involved in the experiment has been laid.

3.5.2. Improved resolution

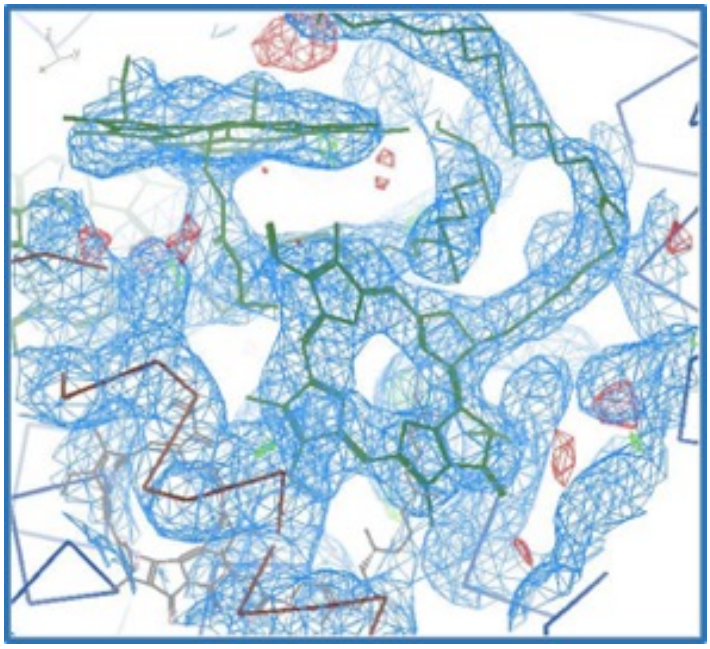

Figure 3.21: **Electron density of pheophytin of PSII to 3.3 A**

Improved resolution in diffraction contributes to better definition in electron density that can be seen at the tail and as the lack of density at the center of pheophytin.

As discussed in section 3.2, microseeding was attempted for growing homogenous 15-20 μm crystals. The enhanced size of the micro-crystals, greatly improved the quality of data reported in Chapter 2. Currently, the electron density from contributing Bragg reflections extends up to 3.3 A (fig 3.22).

3.5.3. Extending resolution beyond Bragg limit

Kupitz and Basu et.al. (2014) presents notable progress in understanding the mechanism of S-state transition, where the dark state structure of PSII was solved to 5 A and two-flash S3 state was solved at 5.5 A. In order to improve upon the results, near-

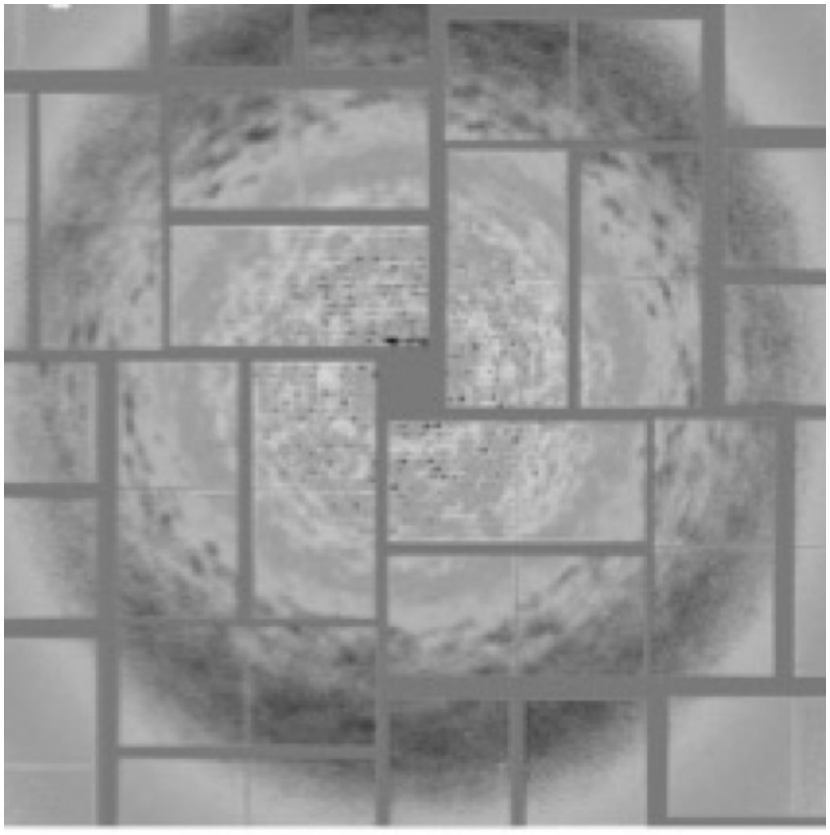

Figure 3.22: **Diffraction pattern of PSII microcrystals shows strong diffused scattering.**
SFX of 15-20 μm PSII crystals shows Bragg peaks restricted well within the water ring, but diffused scattering is seen at higher resolution.

atomic resolution structures of (1.5 -2 A) of intermediate states are necessary to visualize O=O bond formation and changes in the OEC. But for large membrane protein complexes like PSII, it is extremely challenging to grow well-diffracting crystals.

Upon close observation of the data collected on 15-20 μm crystals, it was discovered that while the Bragg diffraction was cutoff in the medium resolution range of 4-5 A, the patterns contained coherent diffused scattering streaks that extended well beyond the Bragg peaks, as seen in figure 3.23. These continuously modulated diffraction intensities can be utilized to improve the structure solved by simply considering the Bragg reflections.

The defining aspect of a crystal is translational symmetry, i.e. regularity over a long range of order which results in the constructive interference of the waves diffracted from each molecule into narrow Bragg peaks. If one of the molecules that makes up the structural units of a crystal is slightly displaced from the ideal lattice by an amount s, the phase of the diffracted wave from this unit is changed by $2\pi s/d$ at the scattering angle of 2θ, where d is the resolution (Ayyer et.al., 2016). For random displacement σ of all molecules along a given co-ordinate, and if q indicated $1/d$, Bragg intensities would diminish according to the Debye-Waller factor i.e. $\exp(-4\pi^2 q^2 \sigma^2)$ (Borie 1965). In such a condition, while the Bragg peaks are lost, an incoherent sum of the molecular Fraunhofer diffraction of individual molecules arises to compensate for the energy of Bragg peaks as shown in figure 3.24.

The observation of this phenomenon has implications as it gives access to the single molecule diffraction pattern modulated by the space group packing of the molecules in the unit cell. This continuous diffraction allows high sampling of reciprocal space, avoiding the phase problem experienced in Bragg diffraction. By using iterative phasing algorithms (Miao et.al., 1999) (Chapman et al., 2006) of coherent diffractive imaging and

aligned molecule diffraction, continuous diffused scattering (created by translational displacement of molecules) can be used to obtain a real-space image of the molecule beyond the Bragg limit (Ayyer et al., 2016).

The details steps for utilizing diffused scattering to improve the resolution of the resultant structure of PSII are discussed in Ayyer et.al., 2016. Essentially, the Bragg and continuous diffraction were treated as two distinct sources of data for the same structure. Starting with a known model of PSII, electron density was generated map was generated by molecular replacement to 4.5 A by using the Bragg peaks. This map was then used to

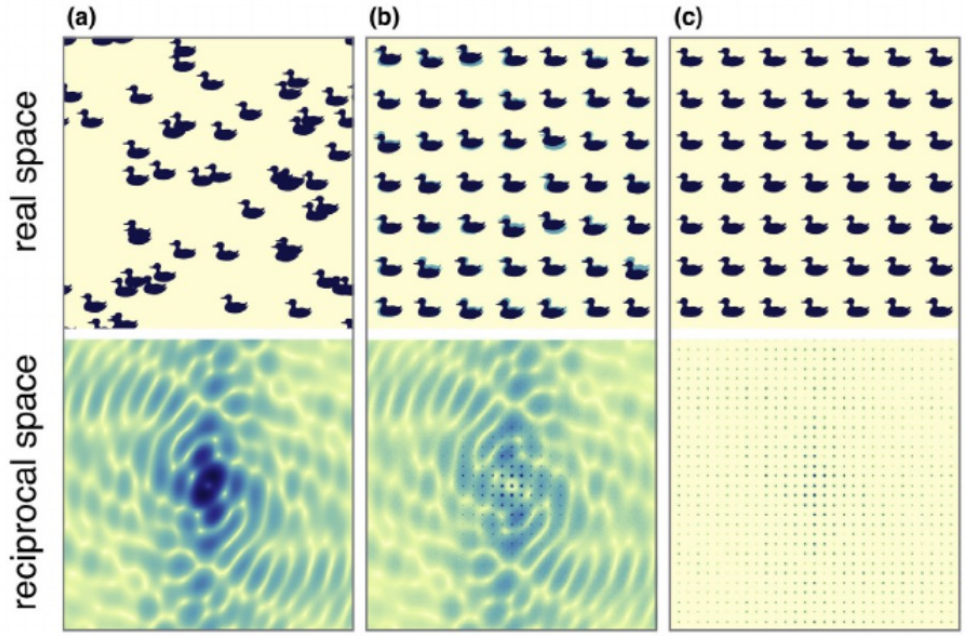

Figure 3.23: **Diffraction depends on translational correlation between individual units**

Image from Chapman and Fromme (2017) describes how the lattice order can contribute to continuous diffraction. The requirement is that the ensemble needs to be of identical objects that are in the same orientation. a) a gas of aligned objects gives rise to the incoherent sum of their molecular transforms, b) a crystal with slight translational disorder consists of both the Bragg peaks to a lower resolution and single molecule diffraction to higher resolutions, c) Periodic array of scattering molecules in perfect crystals produces coherent spots.

generate a low-resolution binary mask of the smoothed molecular envelop of single PSII dimer, which can generate a 3D image of electron density by iterative phasing of the continuous diffraction. Iterative phasing of the continuous diffraction data from 4.5–3.3 A was then performed on the collected continuous diffraction data using the difference-map algorithm (Elser, 2003) and constrained by the 4.5 A support.

After the phasing converged, the phases and amplitudes from the combined diffraction sphere were Fourier transformed to produce a 3.3 Å structure. Through averaging of multiple random starts, a self-consistent electron density to 3.5 Å was achieved and validated by Fourier shell correlation and the phase retrieval transfer function (Shapiro et al., 2005). Further refinement of this structure was performed using a pseudo-crystallographic method (Fischer et al., 2015). Resultant significant improvement in resolution following the incorporation of continuous data can be seen in figure 3.25. Helices show a much better definition of side-chains and the co-factors are also visualized to a greater extent with better fit between the electron density and the structural model generated.

Data collected at XFEL generated by ultrashort coherent pulses do not contain dynamic disorder among the molecules and hence, only the static disorder (that contributes to continuous diffraction) is captured. The restricted Bragg resolution in the PSII microcrystals is caused by intrinsic disorder that maybe caused by weak crystal contacts or thermal motions within the crystals, leading to translational disorder of the position of PSII molecules in the crystals. While the translational disorder is an intrinsic feature of the PSII crystals , which is independent from the size of the crystals, small crystals have lower growth based disorder like mosaicity and this permits the diffused scattering to be evaluated much more precise than when data are collected from larger crystals at Synchrotron sources where high mosaicity leads to a broadening of the diffuse

scattering. Thereby SFX at XFELs is ideally suited to take benefit of the random small translational displacement that can be evaluated by the technique described above **(Chapman and Fromme, 2017)**.

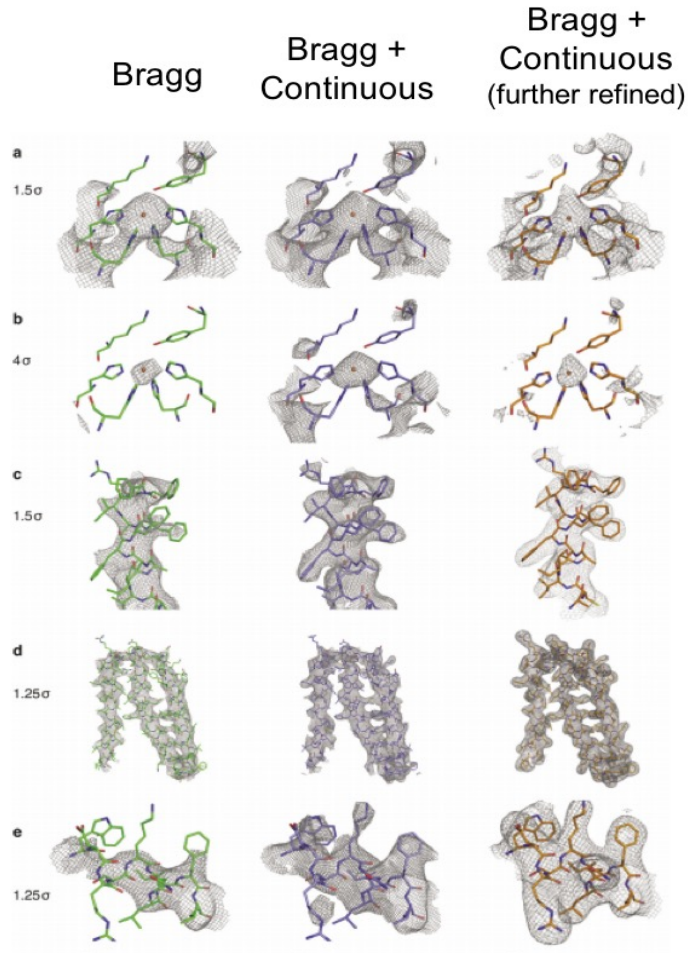

Figure 3.24: **Electron density maps of regions of PSII**

Described here are selections showing improvement between structures from Bragg data only (green, left), from the diffraction sphere including continuous diffraction and Bragg derived scaffolding (blue, center) and post pseudo-crystallographic refinement (orange, right). σ indicates the contour value of the electron density map. a) and b) show the Non-heme iron coordinated by 2 His residues from D1 (chain A) and 2 from D2 (chain D) contoured at 1.5 and 4 σ; c) Part of an α-helix (chain T) shows better fit of the side chains in the density; d) Helices of chains Y and Z show more details and better agreement to the model at increased resolution when continuous diffraction is considered; e) Detailed view of a section of chain Z depicts that using only the Bragg diffraction, no electron density is visible around the side chains of Trp, Lys and Arg, but the model fits better into the map when using the continuous diffraction. Image from Ayyer et.al., 2016.

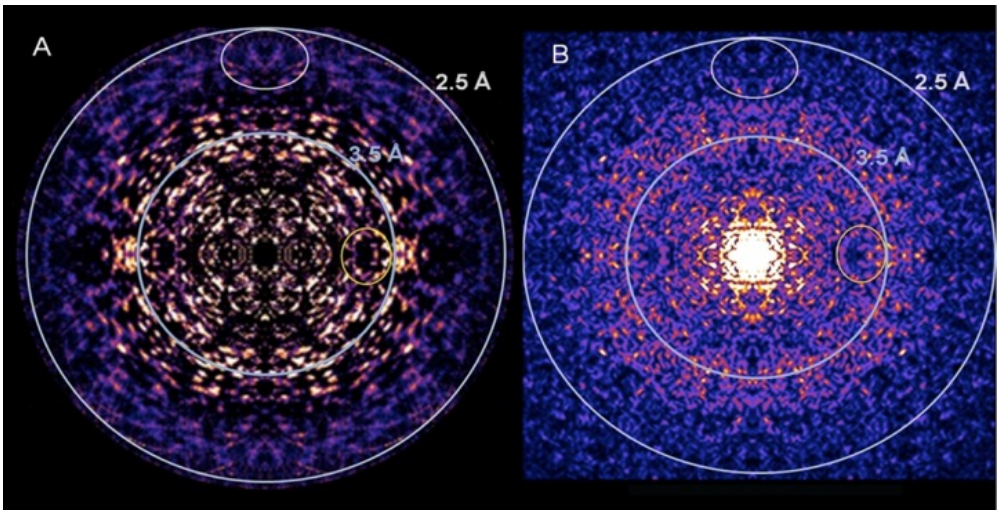

Figure 3.25: **Continuous diffraction data collected in PSII microcrystals.**

Shows an YZ slice through 3D merge of experimental continuous diffraction data-set and b) is the simulation of the diffraction pattern obtained from a single PSII molecule. Highlighted are the similarities seen in the features of both images. Resolution rings correspond to 3.5 and 2.5 A, indicating that in a) when diffused scattering data is incorporated along with Bragg reflections, resolution can be greatly improved to 2.5 A.

Using micro-seeds for growing 15-20 μm crystals contributed to significant improvement in diffraction quality of crystals as explained in section 3.5.2. In addition, strong continuous diffused scattering is seen beyond the Bragg peaks and this can be utilized to further improve the structure. Using micro-seeds for growing 15-20 μm crystals contributed to significant improvement in diffraction quality of crystals as explained in section 3.5.2. In addition, strong continuous diffused scattering is seen beyond the Bragg peaks and this can be utilized to further improve the structure.

Optimization of conditions in all aspects of the experiment have greatly contributed in overall improvement of data quality. PSI flat-panel bioreactors are built for uniform exposure to the growing cell culture. The resulting culture is robust and provides

consistent protein preparations. Decreasing the concentration of detergent for membrane extraction was a remarkable change. Over-solubilization by prolonged exposure to high concentration of detergent can damage exposed sub-units of the protein. Since these are not involved in the crystal contacts, precipitation and crystallization can continue, but the quality of crystals is inferior as shown by diffraction data in Table 3.2.

Free-interface diffusion was optimized for growing 1-5 μm sized crystals. But growing larger 15-20 μm crystals needed controlled environments. Since a large amount of sample is required for SFX, batch method was extensively perfected using 50 mL falcon tubes. Technique of microseeding was established using crushed PSII crystals to grow sharp crystals for all PSII preparations. The activity of these crystals was texted using a clark-based microcell. Maximum O_2 evolution was seen in the presence of PPBQ and FeCN and the crystals continue to oscillate through the S-cycle for more than a 100 light pulses, confirming the PSII activity at room temperature for SFX studies.

TR-SFX was performed on PSII at the MFX hutch of LCLS using Roadrunner goniometer system. Although the fixed target approach needs $1/10^{th}$ of the fraction of the sample needed and provides more diffraction patterns, oscillations in the unit cell dimensions are seen. This challenge needs to be resolved but for now, Roadrunner system is promising for samples with limited amount of crystals that are not compatible with viscous medium. Bragg peaks of the data collected resulted in a dark structure of PSII solved to 3.3 A. But continuous diffraction extends to the edge of the detector and when combined with the Bragg data can result in improvement of the structure up to 2 A.

Photosystem II continues to fascinate researchers and the mechanism of oxidation of water is highly sought after using many techniques. By using TR-SFX, structural details upon light excitation are being explored and a high resolution structure of active PSII can resolve the conflicting theories proposed by enthusiasts of photosynthesis.

References:

Ananyev, G.M., Dismukes, G.C., 1996a. Assembly of the Tetra-Mn Site of Photosynthetic Water Oxidation by Photoactivation: Mn Stoichiometry and Detection of a New Intermediate †. Biochemistry (Mosc.) 35, 4102–4109. https://doi.org/10.1021/bi952667h

Ananyev, G.M., Dismukes, G.C., 1996b. High-Resolution Kinetic Studies of the Reassembly of the Tetra-Manganese Cluster of Photosynthetic Water Oxidation: Proton Equilibrium, Cations, and Electrostatics †. Biochemistry (Mosc.) 35, 14608–14617. https://doi.org/10.1021/bi960894t

Ayyer, K., Yefanov, O.M., Oberthür, D., Roy-Chowdhury, S., Galli, L., Mariani, V., Basu, S., Coe, J., Conrad, C.E., Fromme, R., Schaffer, A., Dörner, K., James, D., Kupitz, C., Metz, M., Nelson, G., Xavier, P.L., Beyerlein, K.R., Schmidt, M., Sarrou, I., Spence, J.C.H., Weierstall, U., White, T.A., Yang, J.-H., Zhao, Y., Liang, M., Aquila, A., Hunter, M.S., Robinson, J.S., Koglin, J.E., Boutet, S., Fromme, P., Barty, A., Chapman, H.N., 2016. Macromolecular diffractive imaging using imperfect crystals. Nature 530, 202–206. https://doi.org/10.1038/nature16949

Barty, A., Kirian, R.A., Maia, F.R.N.C., Hantke, M., Yoon, C.H., White, T.A., Chapman, H., 2014. *Cheetah* : software for high-throughput reduction and analysis of serial femtosecond X-ray diffraction data. J. Appl. Crystallogr. 47, 1118–1131. https://doi.org/10.1107/S1600576714007626

Borie, B., n.d. X-Ray Diffraction in Crystals, Imperfect Crystals, and Amorphous Bodies. 2.

Chapman, H.N., Barty, A., Marchesini, S., Noy, A., Hau-Riege, S.P., Cui, C., Howells, M.R., Rosen, R., He, H., Spence, J.C.H., Weierstall, U., Beetz, T., Jacobsen, C., Shapiro, D., 2006. High-resolution ab initio three-dimensional x-ray diffraction microscopy. J. Opt. Soc. Am. A 23, 1179. https://doi.org/10.1364/JOSAA.23.001179

Chapman, H.N., Fromme, P., 2017. Structure determination based on continuous diffraction from macromolecular crystals. Curr. Opin. Struct. Biol. 45, 170–177. https://doi.org/10.1016/j.sbi.2017.07.008

DePonte, D.P., Weierstall, U., Schmidt, K., Warner, J., Starodub, D., Spence, J.C.H., Doak, R.B., 2008. Gas dynamic virtual nozzle for generation of microscopic droplet streams. J. Phys. Appl. Phys. 41, 195505. https://doi.org/10.1088/0022-3727/41/19/195505

Dods, R., Båth, P., Arnlund, D., Beyerlein, K.R., Nelson, G., Liang, M., Harimoorthy, R., Berntsen, P., Malmerberg, E., Johansson, L., Andersson, R., Bosman, R., Carbajo, S., Claesson, E., Conrad, C.E., Dahl, P., Hammarin, G., Hunter, M.S., Li, C., Lisova, S., Milathianaki, D., Robinson, J., Safari, C., Sharma, A., Williams, G., Wickstrand, C., Yefanov, O., Davidsson, J., DePonte, D.P., Barty, A., Brändén, G., Neutze, R., 2017. From Macrocrystals to Microcrystals: A Strategy for Membrane Protein Serial Crystallography. Structure 25, 1461-1468.e2. https://doi.org/10.1016/j.str.2017.07.002

Elser, V., 2003. Random projections and the optimization of an algorithm for phase retrieval. J. Phys. Math. Gen. 36, 2995–3007. https://doi.org/10.1088/0305-4470/36/12/309

Fischer, N., Neumann, P., Konevega, A.L., Bock, L.V., Ficner, R., Rodnina, M.V., Stark, H., 2015. Structure of the E. coli ribosome–EF-Tu complex at <3 Å resolution by Cs-corrected cryo-EM. Nature 520, 567–570. https://doi.org/10.1038/nature14275

Grundmeier, A., Dau, H., 2012. Structural models of the manganese complex of photosystem II and mechanistic implications. Biochim. Biophys. Acta BBA - Bioenerg. 1817, 88–105. https://doi.org/10.1016/j.bbabio.2011.07.004

Han, G., Ho, F.M., Havelius, K.G.V., Morvaridi, S.F., Mamedov, F., Styring, S., 2008. Direct quantification of the four individual S states in Photosystem II using EPR spectroscopy. Biochim. Biophys. Acta BBA - Bioenerg. 1777, 496–503. https://doi.org/10.1016/j.bbabio.2008.03.007

Hart, P., 2012 The Comell-SLAC Pixel Array Detector at LCLS 4.

Kato, Y., Akita, F., Nakajima, Y., Suga, M., Umena, Y., Shen, J.-R., Noguchi, T., 2018. Fourier Transform Infrared Analysis of the S-State Cycle of Water Oxidation in the Microcrystals of Photosystem II. J. Phys. Chem. Lett. 9, 2121–2126. https://doi.org/10.1021/acs.jpclett.8b00638

Kuan, D., Duff, S., Posarac, D., Bi, X., 2015. Growth optimization of *Synechococcus elongatus* PCC7942 in lab flasks and a 2-D photobioreactor. Can. J. Chem. Eng. 93, 640–647. https://doi.org/10.1002/cjce.22154

Kupitz, Christopher, Basu, S., Grotjohann, I., Fromme, R., Zatsepin, N.A., Rendek, K.N., Hunter, M.S., Shoeman, R.L., White, T.A., Wang, D., James, D., Yang, J.-H., Cobb, D.E., Reeder, B., Sierra, R.G., Liu, H., Barty, A., Aquila, A.L., Deponte, D., Kirian, R.A., Bari, S., Bergkamp, J.J., Beyerlein, K.R., Bogan, M.J., Caleman, C., Chao, T.-C., Conrad, C.E., Davis, K.M., Fleckenstein, H., Galli, L., Hau-Riege, S.P., Kassemeyer, S., Laksmono, H., Liang, M., Lomb, L., Marchesini, S., Martin,

A.V., Messerschmidt, M., Milathianaki, D., Nass, K., Ros, A., Roy-Chowdhury, S., Schmidt, K., Seibert, M., Steinbrener, J., Stellato, F., Yan, L., Yoon, C., Moore, T.A., Moore, A.L., Pushkar, Y., Williams, G.J., Boutet, S., Doak, R.B., Weierstall, U., Frank, M., Chapman, H.N., Spence, J.C.H., Fromme, P., 2014. Serial time-resolved crystallography of photosystem II using a femtosecond X-ray laser. Nature 513, 261–265. https://doi.org/10.1038/nature13453

Kupitz, C., Grotjohann, I., Conrad, C.E., Roy-Chowdhury, S., Fromme, R., Fromme, P., 2014. Microcrystallization techniques for serial femtosecond crystallography using photosystem II from Thermosynechococcus elongatus as a model system. Philos. Trans. R. Soc. B Biol. Sci. 369, 20130316–20130316. https://doi.org/10.1098/rstb.2013.0316

Lomb, L., Steinbrener, J., Bari, S., Beisel, D., Berndt, D., Kieser, C., Lukat, M., Neef, N., Shoeman, R.L., 2012. An anti-settling sample delivery instrument for serial femtosecond crystallography. J. Appl. Crystallogr. 45, 674–678. https://doi.org/10.1107/S0021889812024557

Miao, J., Charalambous, P., Kirz, J., Sayre, D., 1999. Extending the methodology of X-ray crystallography to allow imaging of micrometre-sized non-crystalline specimens. Nature 400, 342–344. https://doi.org/10.1038/22498

Murata, N., Takahashi, S., Nishiyama, Y., Allakhverdiev, S.I., 2007. Photoinhibition of photosystem II under environmental stress. Biochim. Biophys. Acta BBA - Bioenerg. 1767, 414–421. https://doi.org/10.1016/j.bbabio.2006.11.019

Pushkar, Y., Long, X., Glatzel, P., Brudvig, G.W., Dismukes, G.C., Collins, T.J., Yachandra, V.K., Yano, J., Bergmann, U., 2010. Direct Detection of Oxygen Ligation to the Mn4Ca Cluster of Photosystem II by X-ray Emission Spectroscopy. Angew. Chem. Int. Ed. 49, 800–803. https://doi.org/10.1002/anie.200905366

Roedig, P., Ginn, H.M., Pakendorf, T., Sutton, G., Harlos, K., Walter, T.S., Meyer, J., Fischer, P., Duman, R., Vartiainen, I., Reime, B., Warmer, M., Brewster, A.S., Young, I.D., Michels-Clark, T., Sauter, N.K., Kotecha, A., Kelly, J., Rowlands, D.J., Sikorsky, M., Nelson, S., Damiani, D.S., Alonso-Mori, R., Ren, J., Fry, E.E., David, C., Stuart, D.I., Wagner, A., Meents, A., 2017. High-speed fixed-target serial virus crystallography. Nat. Methods 14, 805–810. https://doi.org/10.1038/nmeth.4335

Roedig, P., Vartiainen, I., Duman, R., Panneerselvam, S., Stübe, N., Lorbeer, O., Warmer, M., Sutton, G., Stuart, D.I., Weckert, E., David, C., Wagner, A., Meents, A., 2015. A micro-patterned silicon chip as sample holder for macromolecular

crystallography experiments with minimal background scattering. Sci. Rep. 5. https://doi.org/10.1038/srep10451

Seddon, A.M., Curnow, P., Booth, P.J., 2004. Membrane proteins, lipids and detergents: not just a soap opera. Biochim. Biophys. Acta BBA - Biomembr. 1666, 105–117. https://doi.org/10.1016/j.bbamem.2004.04.011

Shapiro, D., Thibault, P., Beetz, T., Elser, V., Howells, M., Jacobsen, C., Kirz, J., Lima, E., Miao, H., Neiman, A.M., Sayre, D., 2005. Biological imaging by soft x-ray diffraction microscopy. Proc. Natl. Acad. Sci. 102, 15343–15346. https://doi.org/10.1073/pnas.0503305102

Vinyard, D.J., Zachary, C.E., Ananyev, G., Dismukes, G.C., 2013. Thermodynamically accurate modeling of the catalytic cycle of photosynthetic oxygen evolution: A mathematical solution to asymmetric Markov chains. Biochim. Biophys. Acta BBA - Bioenerg. 1827, 861–868. https://doi.org/10.1016/j.bbabio.2013.04.008

Yano, J., Kern, J., Irrgang, K.-D., Latimer, M.J., Bergmann, U., Glatzel, P., Pushkar, Y., Biesiadka, J., Loll, B., Sauer, K., Messinger, J., Zouni, A., Yachandra, V.K., 2005. X-ray damage to the Mn4Ca complex in single crystals of photosystem II: A case study for metalloprotein crystallography. Proc. Natl. Acad. Sci. 102, 12047–12052. https://doi.org/10.1073/pnas.0505207102

CHAPTER 4

HIGH RESOLUTION STRUCTURE OF PHOTOSYSTEM I TO 2 A

Photosystem I (PSI) is a large membrane protein ligand complex which is central for oxygenic photosynthesis. PSI primarily functions as a Type I Reaction Center (RC) to convert light energy into chemical energy. As described in Chapter 1., PSI is responsible for the light-induced charge-separation that transfers an electron from the luminal side (from plastocyanin) to the stromal side (to ferredoxin i.e. Fd) of the thylakoid membrane. This electron-transfer catalyzed by PSI provides the very negative redox potential for the

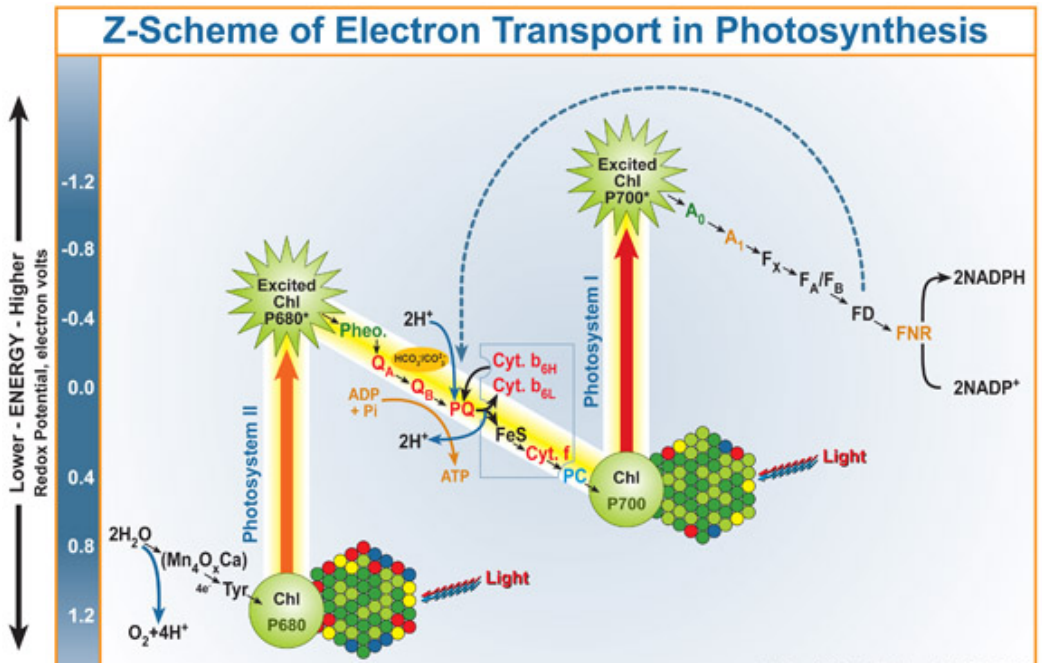

Figure 4.1: **Z-scheme of Photosynthesis**

Energetic representation of photo-initiated energy transfer through the thylakoid membrane in oxygenic photosynthesis. From oxidation of water at PSII to reduction of $NADP^+$, the electron travels an energetically downhill pathway through a series of proteins and cofactors. This is powered by the photon absorption events at the reaction centers PSII (P680) and PSI (P700). Image from Govindjee and Wilbert Veit (2010)

reduction of $NADP^+$ and H^+ to NADPH, that further contributes the reduced hydrogen for the photosynthetic dark reactions.

Upstream from PSI, Photosystem II (PSII) can utilize light up to λ=680 nm for charge separation and for electron transfer reactions in PSI, this limit is at λ=700 nm. These different limits of providing efficient energy for charge separation were crucial for the discovery of two distinct photosystems and are described as Emerson enhancement. The organization and orientation of photosynthetic protein complexes in the thylakoid membrane has been depicted in Figure 1.2. Upon photo-excitation, the linear electron transport of oxygenic photosynthesis progresses by the electron transfer from PSII via cytochrome b6/f complex to PSI and this is represented by the so called Z-scheme (Figure 4.1) of oxygenic photosynthesis.

4.1. Structure of Photosystem I

4.1.1. Components of PSI

Cyanobacterial PSI is a trimer of heterodimers (1056 kDa) (Figure 4.2) where, each monomer is made of 12 protein subunits and 127 non-covalently bound cofactors. The composition of these cofactors per monomer is described as 96 chlorophyll molecules, 22 carotenoid molecules, 3 4Fe-4S clusters (F_X, F_A, F_B), 4 lipid molecules, 2 phylloquinone molecules and 1 Ca^{2+} ion (Jordan et al., 2001). The diameter is approximately 200 Å with a stromal hump that extends out of the thylakoid membrane by 40 Å.

The large heterodimer at the center of the PSI molecule is formed by protein subunits PsaA and PsaB, which act as a joint RC and core antenna complex. Both subunits have 11 transmembrane helices and together they co-ordinate 79 of the 96 antenna chlorophylls. Most of the carotenoids also show hydrophobic interaction with PsaA or

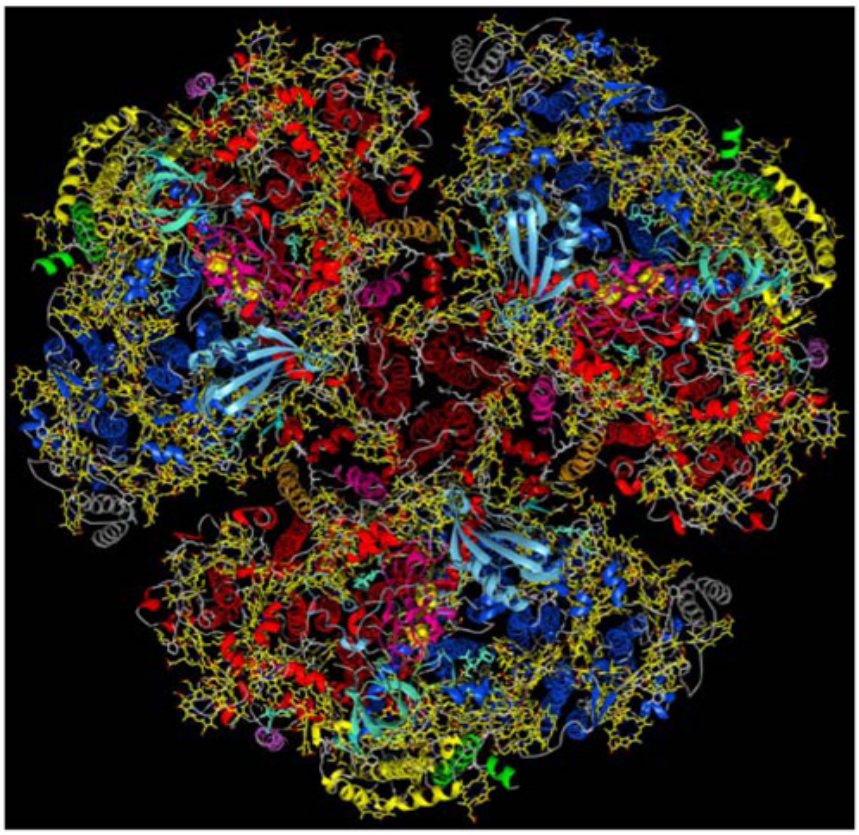

Figure 4.2: **Structural overview of PSI**

Cyanobacterial trimer of PSI as viewed normal to the thylakoid membrane from the stromal side. The structure was solved to 2.5 A resolution (PDB: 1JB0) (Jordan et.al., 2001).

PsaB (Jordan et al., 2001). With respect to the electron transport chain, PsaA and PsaB also co-ordinate majority of the co-factors, containing P_{700}, the electron acceptors A, A_0, A_1, and the first 4Fe-4S cluster F_x as depicted in Figure 4.3.

The core subunits of PsaA and PsaB are surrounded by 7 smaller protein subunits in the membrane: PsaF, PsaI, PsaJ, PsaK, PsaL, PsaM and PsaX. Of these, PsaI, PsaL and PsaM are involved in the trimerization, whereas PsaF, PsaJ, PsaK and PsaX interact with the membrane and are located towards the periphery of the monomer. The stromal hump of PSI comprises of PsaC, PsaD and PsaE subunits. While PsaC contains the 4Fe-4S clusters F_A and F_B, PsaD has been shown to be necessary for the stable assembly of PsaC

and PsaE for docking Fd molecules (Kubota-Kawai et al., 2018) and PsaD along with PsaA has been reported to interact with phycobilisomes for excitation energy transfer.

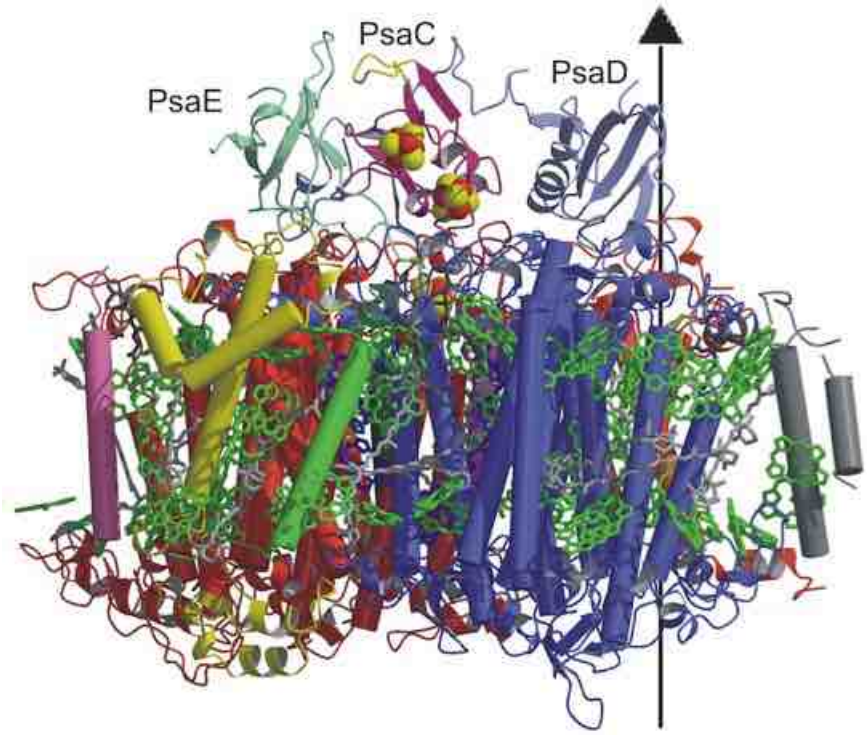

Figure 4.3: **Proteins and cofactors in PSI**

View of PSI parallel to the membrane plane. Depicted in the image antennae chlorophyll molecules (green) among the transmembrane helices, subunits in the stromal hump (PsaE, PsaC and PsaD) and 4Fe-4S clusters associated with the hum (red and yellow). Image from Fromme 2008.

4.1.2. The electron transfer chain of PSI

The electron transfer chain of PSI (described in Figure 4.4) consists of 6 chlorophyll molecules, 2 phylloquinones and 3 4Fe-4S clusters. The chlorophylls associated with PsaA and PsaB loosely follow the pseudo-C_2 symmetry exhibited by the

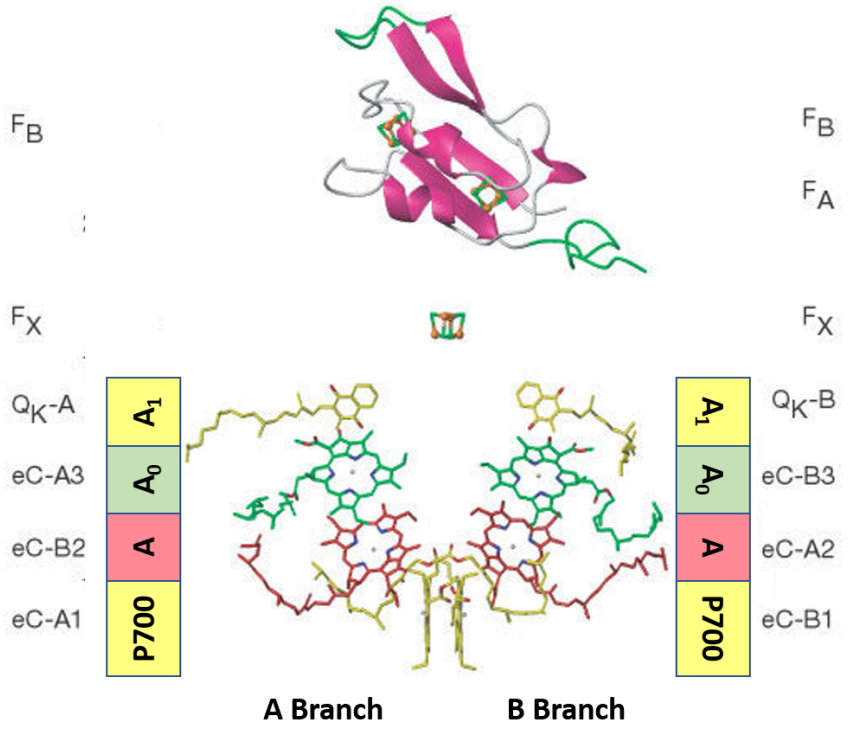

Figure 4.4: **Apparatus for electron transport in PSI**

Schematic representation showing the general positions and cofactors involved in the electron transport chain of PSI (Jordan et.al., 2001). P_{700} is a heterodimer of one chlorophyll a molecule and another chlorophyll a' molecule. A and A_0 are chlorophyll a molecules, A_1 are phylloquinone molecules and F_x, F_A, F_B are 4Fe-4S clusters. Image has been edited from Photosynthetic protein complexes: A structural approach by Krauβ

protein subunits and have an average center to center distance of 9.9 Å within this network (Jordan et al., 2001). This allows for strong excitonic coupling and efficient Förster energy transfer and helps explain the extremely high quantum efficiency for the excitation energy transfer and trapping (99%) found in PSI. Upon absorption of light, the energy is funneled from this antenna system to the primary donor in PSI, P_{700}.

In 1JB0, P_{700} was identified to be a heterodimer of chlorophyll *a* and chlorophyll *a'* (Jordan et al., 2001), the so-called 'special pair', arranged perpendicular to each other with a resulting π-stacked coupling. Once the light energy reaches it, a strongly reducing excited state (P_{700}^*) is formed which initiates charge separation to become P_{700}^+. Illustrated in

Figure 4.4, the electron transfer pathway within PSI can proceed along two different paths, the so-called A- and B- branches corresponding to cofactors mainly bound by PsaA and PsaB respectively. On both sides, these branches consist of two chlorophyll *a* molecules followed by a phylloquinone at which point the paths merge at F_x. F_x is the first of the three iron-sulfur clusters in PSI and it lies along the membrane-normal pseudo-C_2 axis between PsaA and PsaB. It is the only membrane intrinsic 4Fe-4S cluster as the two downstream clusters, F_A and F_B, both reside in the stromal hump, coordinated by PsaC.

The chlorophylls most proximal to P_{700}, termed A, partner with P_{700} to form the charge separated state P_{700+}/A_-. There is even evidence to support the charge separation initiating at A (Muller et al., 2010). Consecutive reduction then proceeds to A_0, another chlorophyll, followed by A_1, a phylloquinone. Though both A- and B-branches are active, they have very different rates in electron transfer with the A-branch showing a much slower (~200 ns) electron transfer from A_1 to F_x than in the B-branch (~10 ns) (Guergova-Kuras et al., 2001). F_x is coordinated by four cysteine residues (very common in natural iron-sulfur clusters) in PsaB that are strictly conserved.

4.1.3. PSI and Ferredoxin

Ultimately, Fd is the terminal acceptor for PSI, unless for Fe-deplete conditions, flavidoxin is known to replace Fd. Based on the charge-density map studies of PSI, the binding pocket proposed was close to the terminal 4Fe-4S cluster, F_B. Based on further analysis by mutagenesis, all subunits of the stromal hump PsaC, PsaD and PsaE were hypothesized to be involved with Fd docking (Fischer, 1998).

Interestingly, in spinach, the redox potentials from F_A and F_B were reported as -540 mV and -590 mV respectively. This suggests that the transfer from F_A to F_B is energetically uphill and that is a disparity with all previous steps in the transport chain

(Brettel, 1997). This suggests that, in the absence of an acceptor, the electron would favor localization at F_A. Upon Fd binding, the changes in the chemical environment favor the electron transport. This mechanism would avoid creation of reactive superoxide, since F_B is closer to the exposed surface when compared to F_A that is buried deeper towards the membrane (Grotjohann and Fromme, 2005).

4.1.4. Co-factors of PSI

As described in Section 4.1.2., the electron transfer takes place at the RC at the center of the protein complex. The role of antenna chlorophylls is to capture light and transfer the excitation energy to the P700 reaction center where charge separation takes place. The arrangement of antenna chlorophylls (shown in green in Figure 4.5) in PSI is such that each chlorophyll has several neighbors and the center-to-center radius is less than 15 A, so energy can be efficiently transferred to the center of the complex via multiple pathways.

PSI also has chlorophyll molecules that absorb at $\lambda > 700$ nm, called 'red' or 'long-wavelength' chlorophylls. The reasons for red shift of the chlorophyll's absorption maybe: strong excitonic coupling with neighboring chlorophylls, interaction with protein residues leading to the variation in the fifth ligand of the Mg^{2+} or the influence of the protein's electrostatic field. These pigments contribute by increasing the spectral width of the light absorbed by PSI or by funneling the excitation energy to the center of the complex. The location and function of these specialized chlorophylls is under investigation but their knowledge would explain the mechanisms involved in evolution or adaptation of cyanobacteria for trapping solar energy.

Carotenoids absorb energy in a spectral region complementary to that of chlorophylls, and thus, act like accessory pigments. Also, they are necessary for structural

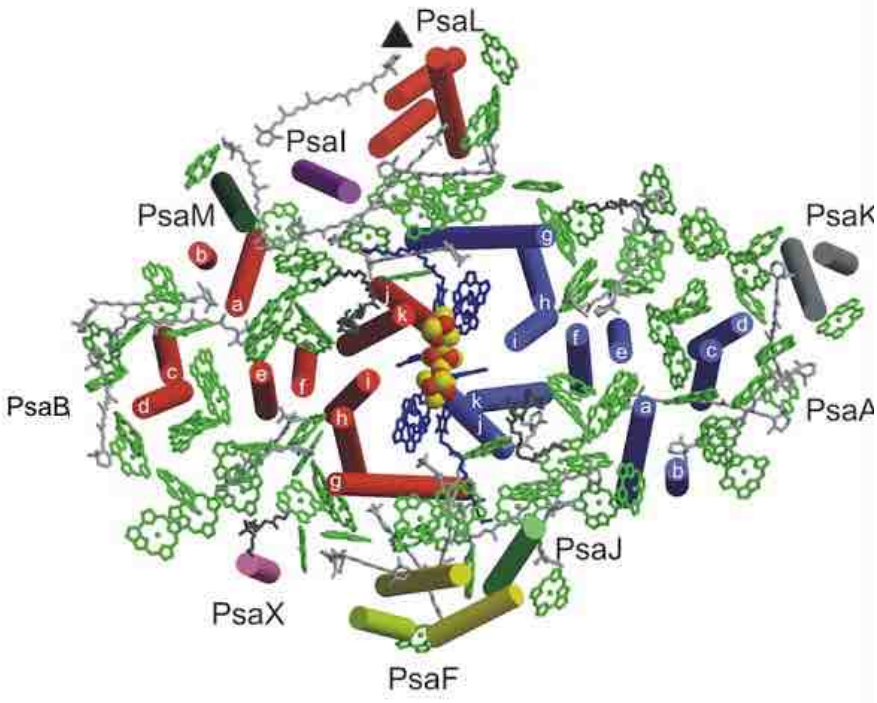

Figure: 4.5: **Co-factors in the PSI monomer, as viewed from the stromal side.**

Transmembrane helices are depicted as cylinders and all loops have been omitted. The 6 chlorophylls and 2 phylloquinones of the electron transport chain are centrally localted and labeled in blue, 90 chlorophylls of the core antenna are green, 22 caroteinoids are light grey and 4 lipid molecules are colored dark grey.

assembly and stabilization of the entire pigment-protein complex (Wang et al., n.d.)(2004). Most importantly, the 22 carotenoids in PSI fulfill a specific function of photo-protection, where they quench the excited triplet state of chlorophyll, preventing singlet oxygen generation and eventually, photo-oxidative damage. The carotenoid triplet state generated during the quenching process is lower in energy and hence, does not contribute in radical generation. They simply return to their ground state by dissipating the excess energy as heat.

In the co-factor assembly of PSI (Figure 4.5), 4 lipid molecules have been assigned. 3 of these are molecules of phosphatidyl-glycerol (PG) and 1 is mono-galactosyl-diacyl-

glycerol (MDGD). 2 of these lipid molecules (seen in Figure 4.5 near helices K and J of subunit PsaA and PsaB), are closely associated with the electron transport chain and are hypothesized to stabilize the structure. In *Synechocystis sp*. mutants, it was proven that PG is essential for photoautotrophic growth (Domonkos, 2004). Also, the reason for the difference in rates of electron transfer between the two branches is not understood and the lipids may play a role in that. 2 other PG molecules are localized at the periphery of the molecule, one at the membrane exposed surface (associated with PsaX) and might be stabilizing this subunit; The other PG molecule is seen at the monomer-monomer interface, associated with the chlorophyll PL1. In this case, PG is proposed to assist with excitation energy transfer or with oligomerization.

4.2. Motivation

The structure of PSI provided the basis for structure based understanding of excitation migration in light harvesting system of the core antenna of PSI (Şener et al., 2004). The first determination of position and orientation of the chlorophylls in the network of chlorophyll antenna molecules in PSI enabled calculations of potential connectivity and rates of excitation transfer between individual chlorophyll molecules (details discussed in Section 4.6.2.). Yet, the precise dynamics of excitation transfer in PSI are not fully understood and this is an active field of study (Konrad et al., 2014).

The questions: why PSI in cyanobacteria is a trimer and what is the advantage for oligomerization of monomers, have been of interest to the scientific community. In the first high resolution structure of PSI (Jordan et al., 2001) a trimeric form has been described (Fromme et al., 2001) and the trimeric form of PSI has also been studied in most classes of cyanobacteria. But over the last few years, two other prominent oligomerization

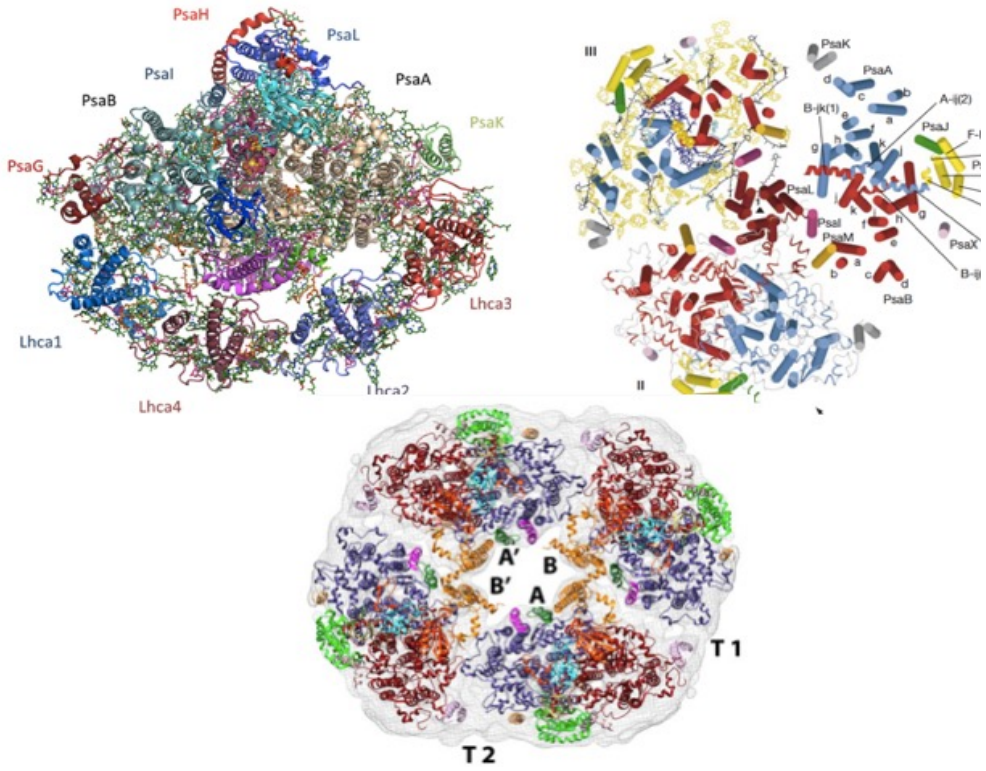

Figure 4.6: **Representative forms of PSI in nature**

Structures of a) monomeric PSI-LHCI supercomplex from P*isum sativum* from Mazor et.al., 2015; b) PSI trimer from *T. elongatus* from Jordan et.al. 2001 and c) The dimer of dimers i.e. tetrameric PSI isolated from cyanobacterial *Chroococcidiopsis sp*. from Semchonok & Li et.al 2016. The subunits of all three complexes are highlighted in different colors. The T1 and T2 in c) indicate the two kinds of interfaces between the dimers.

states have emerged. PSI in pea plants is a monomeric PSI-LHCI supercomplex that consist of 12 core subunits and 4 light-harvesting proteins in the LHCI antenna complex, 156 chlorophylls, 32 carotenes and 14 lipids have been found to be associated with this monomeric structure (Mazor et al., 2015). PSI in dimeric and tetrameric forms had been reported in cyanobacteria *Anabena* (Watanabe et al., 2011), and a medium resolution structure of tetramer from another cyanobacteria *Chroococcidiopsis sp* was solved using cryo-electron microscopy to 6.1 A (Li et al., 2014). The explanations for these

oligomerization states and their evolutionary implications remain unclear. Representative structures of all three forms of PSI have been described in Figure 4.6.

On the same lines, the subtle differences and interconnectivity between individual monomers in PSI is also matter of much interest. Asymmetric unit of a crystallographic space group is a smallest possible closed part of space, that can be repeated to fill the entire lattice using symmetry operations of the specific space group. For 1JB0, the crystallographic space group was assigned as $P6_3$. This hexagonal order indicates higher order of symmetry and the 3 fold trimeric axis was one of the crystallographic axes. According to Matthews coefficient (Matthews 1968; Rupp 2003), only the PSI monomer was seen in the asymmetric unit and eventually the structure solved was that of a single monomer. Since PSI is known to be a trimer, all structural details of the monomer were simply triplicated for all intents and purposes. This may have simplified data processing, but differences among the monomers cannot be visualized in such a dataset. Collecting more data at various orientations and solving the structure with lower symmetry operations, would enable the entire trimer to be in the asymmetric unit and thereby, differences among the monomers can be visualized.

At higher resolution, the interconnecting subunits would also be better defined to understand monomer-to-monomer interaction. Additionally, the number and network of carotenes largely varies among the known structures. Further exploration is needed to understand if this plays a role in efficiency for photo-protection during light stress or transmission of harvested light. Finally, even with several structural models of PSI, a few aspects of the light harvesting and charge separation function remain unclear i.e. what is the role of the red antenna chlorophylls and why it varies between species, whether charge separation is unidirectional or bidirectional, how activity of one monomer affects the other, changes in protein-complex and its environment based on light changes etc. An

updated, higher resolution model of PSI would aid towards understanding these key evolutionary and functional aspects.

4.3. Isolation and purification of PSI

PSI was purified as previously described (Fromme and Witt, 1998) with modifications. *T. elongatus* cell growth has been discussed in Section 3.1.1. During their log phase at a cell density of 0.6 O.D. at 750 nm, the cells were were spun down for 10 min at 7000 g and stored frozen in the form of 20 – 30 gram pellets at – 80 C without any cryo protecting agents as cells do not survive incubation with cryo-protectants.

4.3.1. Preparation of thylakoid membranes

For isolating the membranes, *T. elongatus* cells (20 – 30 g) were resuspended by vigorous shaking in warm cell suspension buffer (20 mM MES at pH 6.4, 10 mM $CaCl_2$, 10 mM $MgCl_2$). The cell suspension was then centrifuged at 7,400 g for 10 min using a fixed angle rotor (SLA-1500, Beckman Coulter), with a Sorvall RC-3C Plus centrifuge (Beckman Coulter) at 24 C. The cell pellet obtained was gently resuspended in lysis buffer (20 mM MES pH 6.4, 10 mM $CaCl_2$, 10 mM $MgCl_2$, 500 mM D-mannitol) to obtain a dense homogenous suspension. Protease inhibition upon cell lysis was prevented by adding PMSF (phenylmethylsulfonyl fluoride) dissolved in Dimethyl Sulfoxide at the desired final concentration of 0.5 mM.

The dense cell suspension was passed through a 16-32 mesh wire sieve to separate non-homogenized pellet chunks and gently poured into the glass reservoir of the microfluidizer (Microfluidics Model M-110 L) for cell breakage. The principle for lysis using a fluidizer is forcing the suspension through a narrow channel, under tremendous

pressure which would induce a large shearing force that would effectively break the cell wall and cell membrane without the need for pre-incubation of the cells with lysozyme, which had previously been used to break down the cell walls of the *T. elongatus* cells before lysis. The standing pressure for such lysis was optimized to be 12 kpsi for breaking on *T. elongatus* cells.

Three wash steps were performed to eliminate membrane associated and cytoplasmic proteins. The recovered thylakoid membrane pellet was kept chilled during the wash steps which were cycles of centrifuging the membrane suspension at 18,270 g for 10 min at 4 C, isolating the pellet, homogenously resuspending in wash buffer followed by another centrifugation step. The first supernatant was frozen at -80C, which could be used for isolation of the phycobillisomes as described in Fromme et.al., IUCrJ, 2015.

4.3.2. Membrane solubilization

The washed thylakoid pellet was resuspended in minimum volume of wash buffer and the chlorophyll concentration was very accurately determined. For this, 3 μL sample was added to 1 mL 80 % acetone solution. Upon contact with acetone, the proteins are denatured by vigorously mixing it using a vortex and pigment molecules were extracted. The 400 – 800 nm absorbance spectrum of the pigment extract is recorded using a UV-VIS spectrophotometer (DU 800 Beckman Coulter) and the absorbance at 664 nm and 710 nm were utilized for calculating the concentration of chlorophyll using Beer – Lambert's law with a molar extinction coefficient of Chl a in acetone of 76780 (Porra et al., 1989).

The Chl concentration of thylakoid suspension obtained was adjusted to 1.5 mM chlorophyll using wash buffer. For membrane protein solubilization, detergent solution was added to isolated membranes at concentrations much higher than the detergent's

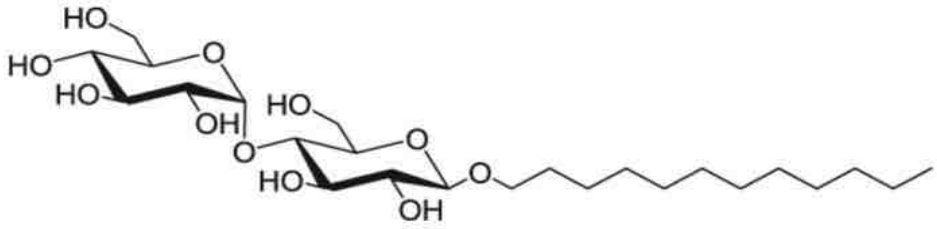

Figure 4.7: **Structure of β-dodecyl maltoside**

For a membrane protein molecule isolated in a detergent micelle, the transmembrane helices are stabilized by the detergent tail. As a result, the hydrophilic head group orients itself towards the solvent, thus 'solubilizing' the membrane protein.

critical micellar concentration (CMC). These excess detergent molecules would act by displacing constituents of the lipid bilayer, thereby extracting the intact protein complexes into solution enclosed by a detergent micelle. The detergent of choice was β-dodecyl maltoside (DDM) for its long chained tail (12 carbon) and gentle nonionic maltose head group (as depicted in Figure 4.7). The CMC for β-DDM is at 0.01 %, but for the purpose of protein solubilization, 1% stock solution was gently added to the prepared membranes while the solution was stirring. The final optimized conditions for this step were membranes at 0.75 mM chlorophyll concentration with 0.5 % β-DDM.

The suspension was permitted to incubate for an hour at room temperature while keeping it light tight. The recovered suspension was centrifuged at 50,000 rpm (184,000 g) using a Ti 70 rotor under vacuum at 4 C using an Optima – 100K centrifuge (Beckman Coulter catalogue # 393253) for 90 min. This permitted the cell debris and unsolubilized membranes to form a pellet and extracted protein-detergent micelles were recovered in the supernatant.

4.3.3. Anion exchange chromatography

The PSI trimers were concentrated in the lowest 30% of the supernatant on top of the pellet that was obtained from the ultracentrifugation step. For further purification, 2/3rd of the supernatant was discarded since it contained PSI monomers and PSII molecules and the remaining solution was gently poured into a graduated cylinder to measure volume of the sample. This recovered membrane extract was filtered using a 0.2 μm syringe filter and its chlorophyll concentration was measured as described in section 4.2.2.

Anion-exchange chromatography was performed for purification of PSI trimers using an empty column (XK 50/60, GR Healthcare, Cat # 28-9889) (inner tube length 60 cm, diameter 5 cm). The column was packed with TOYOPEARL DEAE-650M (Tosoh Bioscience, Cat # 07974) that is a weak anion exchanger. The effective volume contained in the resin slurry (void volume) was ~1100 mL. As preparation for purification, columns were packed using high salt buffer (20 mM MES pH 6.4, 150 mM $MgSO_4$, 0.02% β-DDM) at twice the flow-rate used for purification (i.e. packing flow-rate was 50 mL/min, running flow-rate was 25 mL/min). This was based on resin manufactures instruction to ensure homogenous packing and uniform conditions of pressure and flow throughout the column during purification.

Prior to chromatography, the columns were chilled to 4 C using a cooler connected to the column jacket. The packed resin was first washed with 100 % high salt buffer B (20 mM MES pH 6.4, 150 mM $MgSO_4$, 0.02% β-DDM) to remove any bound molecules. Following the wash step, the column was equilibrated with 30 % buffer B (20 mM MES pH 6.4, 45 mM $MgSO_4$, 0.02% β-DDM), for 2 column volumes (~2250 mL) till conductivity of the flow-through was stabilized. The centrifuged extract was portioned out such that only 50 μmoles of chlorophyll was being applied to each column run for good

separation of all components. Since PSI trimers bind very strongly to the resin, all other proteins were washed at 20 mM MES pH 6.4, 100 mM $MgSO_4$, 0.02% β-DDM, at constant flow rate of 25 mL/min. A band of bound PSI was obtained before eluting the protein using 100 % buffer B (20 mM MES pH 6.4, 150 mM $MgSO_4$, 0.02% β-DDM).

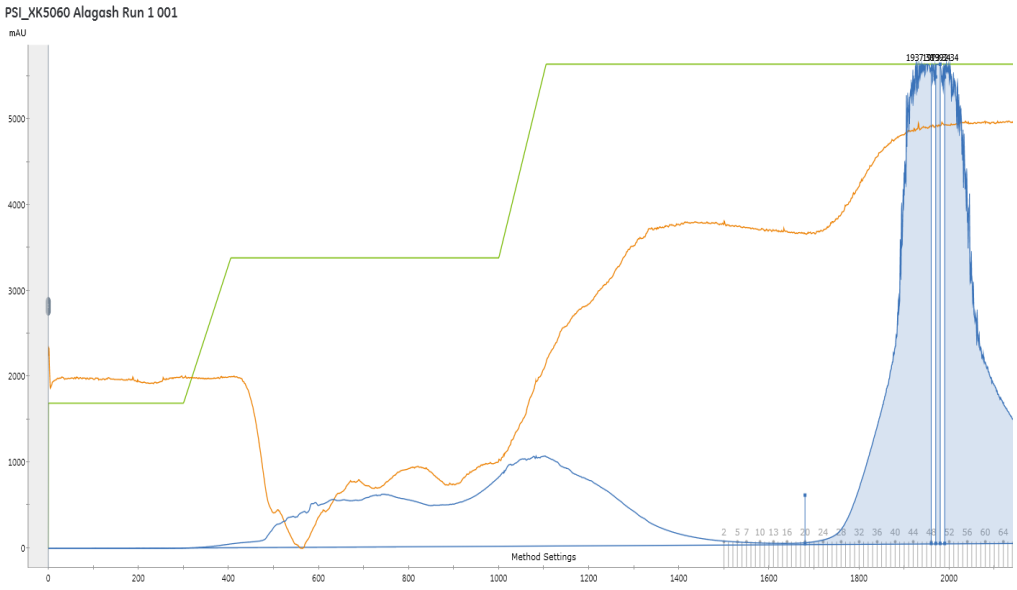

Figure 4.8: **Chromatogram for PSI purification.**

Green line indicates % Buffer B, orange is for conductivity of the flow-through and blue is the read-out of the in-built spectrometer at 280 nm. Loosely bound PSII dimers and PSI monomers are separated during the wash step and the right major peak is the eluted PSI trimers at 150 mM $MgSO_4$

4.3.4. Crystallization by ultrafiltration as the final purification step

The fractions of PSI trimer peak were pooled and concentrated using a 400 mL Millipore stirred cell concentrator (EMD Millipore Catalogue # 5122). The ultrafiltration membrane used was of 100 kDa cutoff (Pall Life Sciences, Part # OM100076) and was pre-soaked in water at 4 C. The assembled ultrafiltration unit with purified PSI was placed on a stirring plate at 4 C in dim green light and permitted to concentrate at less than 10 psi

applied to the set-up using compressed Argon. This gentle pressure would ensure that the eluting high salt buffer is filtered through the membrane. The set-up was monitored to ensure that the membrane is not permitted to run dry, making the protein forming of aggregates.

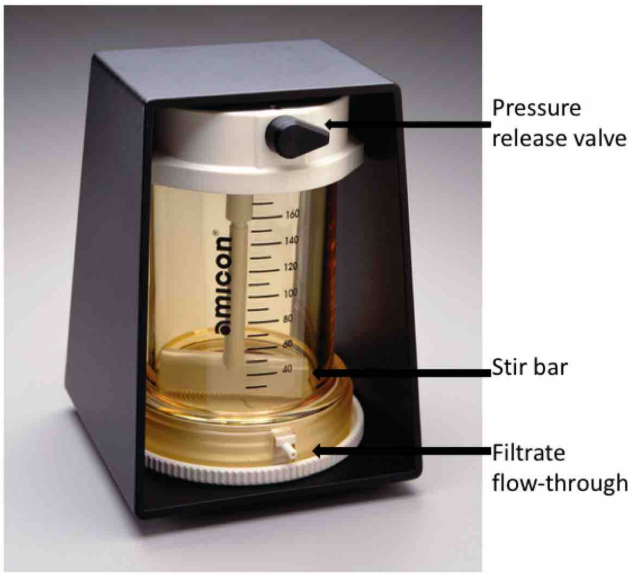

Figure 4.9: **Parts of a Millipore ultrafiltration stirring cell.**

This set-up is used for concentrating purified PSI and for desalting because of its gentle concentrating feature that can be easily adjusted by decreasing the gas-pressure applied or stirring speed of the magnetic stir-bar.

Once the sample volume is concentrated to about 10 mL, the volume of the sample is measured using a pipette and chlorophyll concentration is determined . In the case of PSI, crystallization is carried out by lowering the ionic strength which reduced the protein solubility. As salt concentration is decreased, the surface of the protein is depleted of counter ions, which allows direct crystal contacts to be formed between positively charged groups of molecule A with negative groups of molecule B. Crystallization at low ionic strength is thereby mediated by increase of IONIC interaction, in contrast to

crystallization at high ionic strength where hydrophobic interactions are increased. For the final purification step, the concentrated protein was desalted using crystallization buffer (5 mM MES pH 6.4, 0.02% β-DDM) to dilute the concentrated solution to the desired salt concentration. Since the starting solution had 150 mM $MgSO_4$ and final desired salt concentration is 6 mM $MgSO_4$, by using the relationship between molarity and concentration and estimated initial volume of protein sample, the required amount of crystallization buffer required to be added was calculated. The dilution has to be done dropwise to hinder formation of amorphous precipitate.

The diluted solution was permitted to gently concentrate again using the Millipore stirring cell at 4 C. Crystallites formed and grew in the solution and eventually settled as a mat on the filtration membrane, obstructing the buffer to freely pass through and the rate of filtration slowed down. When the volume reached about 10 mL, stirring was stopped, pressure was released and crystallites were permitted to further grow for 12 hours.

4.3.5. Sedimentation to segregate crystallites

At this stage, the purified PSI sample is a mixture of crystals ranging from 1 - 250 microns in size. The bigger crystals are usually microcrystals grown into each other and need controlled recrystallization. On the other hand, the micron sized small crystals are perfect for experiments at an XFEL. So, the crystals were separated by sedimentation.

Using a small amount of crystallization buffer, all the crystallites are harvested from the ultrafiltration membrane into a 15 mL falcon tube. If crystals were stuck to the stirring set-up, they were gently washed off using a 1 mL micro-pipette. The harvested crystals were portioned out in 500 μL aliquots in 1.5 mL reaction tubes and allowed to settle for 10 minutes.

After the incubation, the dark supernatant was separated into fresh reaction tubes and permitted to settle, this time for 20 minutes. The pellet obtained from the first settling step was combined and additional crystallization buffer was added to ensure the crystals are well hydrated.

After the second sedimentation step, the supernatant started losing its blackish-green color, since the bigger crystals had settled into the pellet. The supernatant thus obtained was separated into fresh reaction tubes again and pellets were combined with extra crystallization buffer. An image of crystallites separated in the second sedimentation step of 20 minutes is included as Figure 4.4. Crystals seen were up to 20 μm in size.

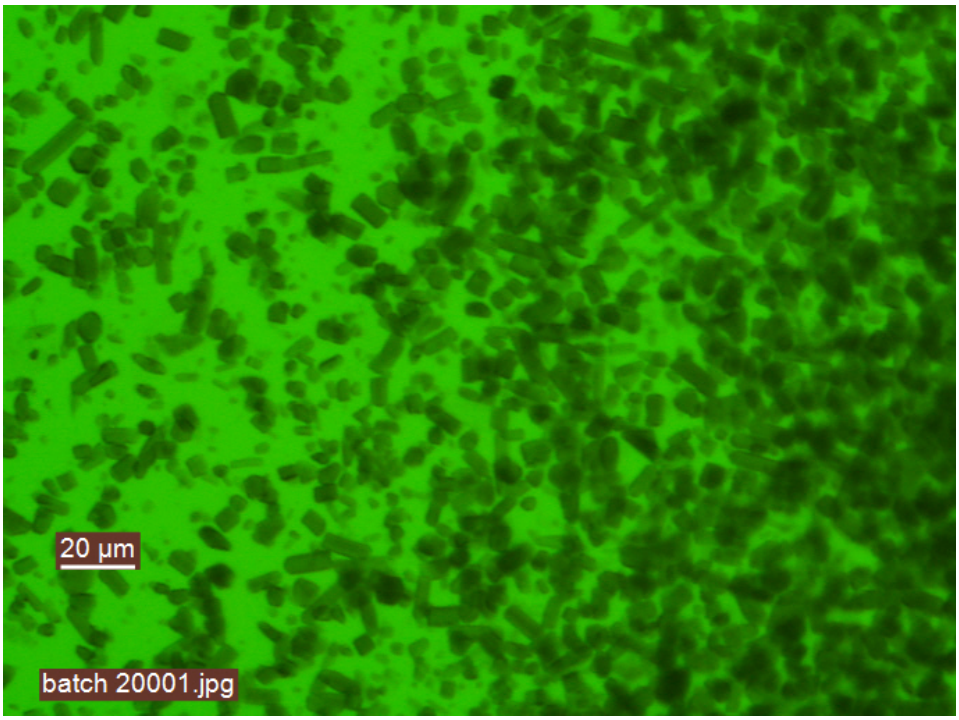

Figure 4.10: **Optical microscopic image of PSI micro-crystals.**

During sedimentation, crystals are segregated by size. This image is a representation of crystallites that sediment in 20 minutes by gravity at 4C. The green background of the image is due to the presence of a green screen and not free PSI protein.

The following third and fourth sedimentation steps were performed for 30 and 40 minutes respectively and the final supernatant obtained was devoid of any color i.e. free PSI protein or crystals. The crystal pellets obtained from the third and fourth sedimentation steps were ranging from 1 – 5 μm in size for the 30 min settling step and sub micrometer for the 40 min settling step and were found to be directly suitable for nano-crystallography (Chapman et al., 2011).

4.4. Crystallization of PSI

For decades, X-Ray crystallography has been employed to understand the large membrane protein complexes involved in photosynthesis. Specifically for PSI from *T. elongatus*, the 2.5 A structure of monomeric PSI was solved first at 6 A in 1993 (Krauss, 1993) then resolution was improved to 4 A (Klukas et al., 1999) until the first high resolution structure was solved in 2001 (Fromme et al., 2001; Jordan et al., 2001). But further improvements in the structure were hindered because large PSI crystals display intrinsic long range disorder. This mosaicity i.e. misalignment of crystalline mosaic blocks during crystal genesis leads to restriction in diffractive properties of the crystal.

Various approaches were tried for making better ordered crystals by further optimization of the original crystallization protocol that lasted 4 - 6 days but, while diffraction spots were visible beyond 2.5 A the data could not be evaluated to higher resolution due to the high mosaicity caused by long range disorder in the crystal. The

method as described in Section 4.3.2., shortens the incubation time of various steps, thereby restricting mosaicity and improving diffractive ability of crystals.

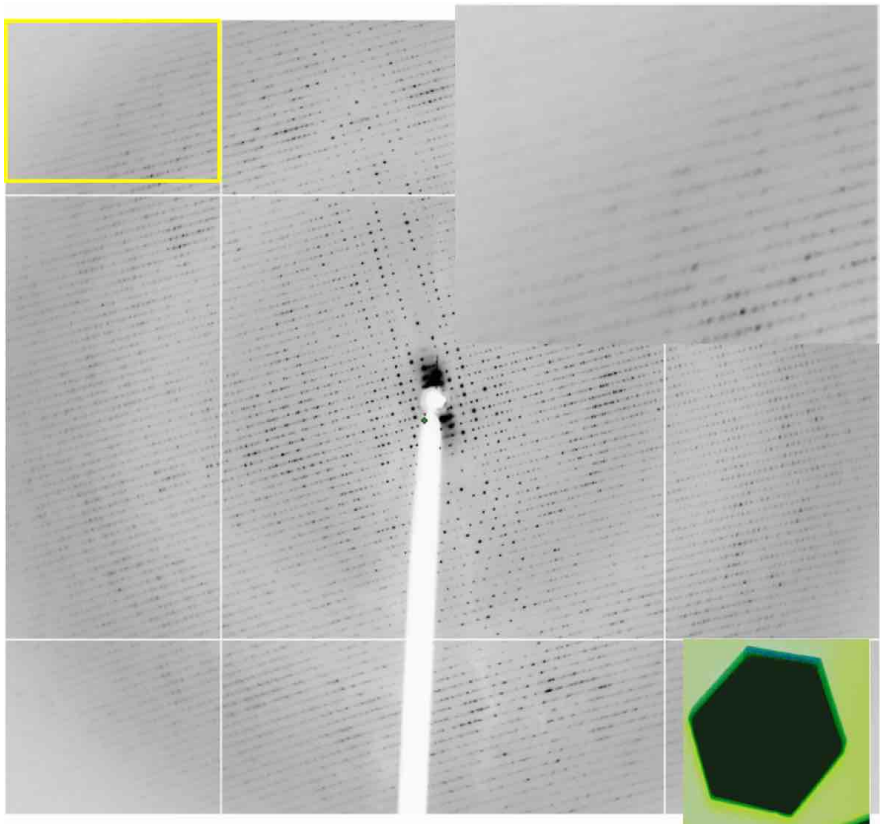

Figure 4.11: **Diffraction Pattern collected at Advances Photon Source in 2011**.

Crystal diffracts well, but analysis is restricted to medium resolution because of spot merging, caused by inherent long range disorder in crystals. This leads to ambiguous indexing and incorrect structure factors.

4.4.1. Exploring the phase diagram for crystallization of proteins

The alternate approach for crystallization of proteins utilizes the concept that is 'reverse of salting in' i.e. reducing the solubility of the protein by reducing the ionic strength of the solution and by inducing electrostatic interactions at high protein concentration (Fromme et.al. 1998).

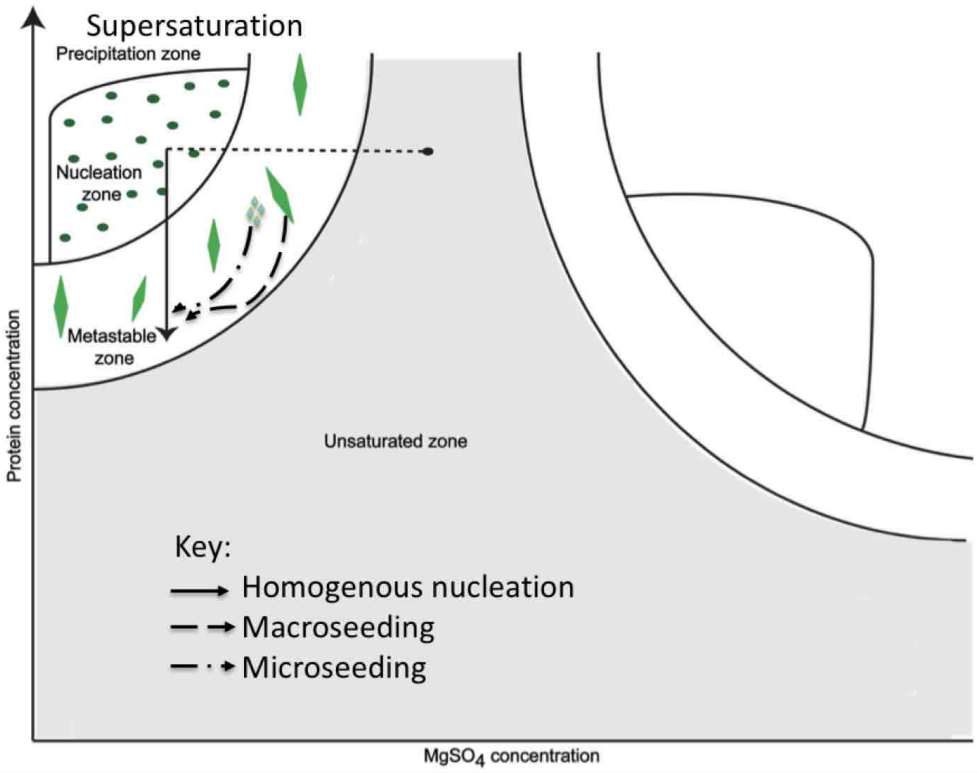

Figure 4.12: **PSI was crystallized under lower ionic strength**.

Various strategies i.e. homogenous nucleation, macroseeding or microseeding can be employed to explore the metastable zone of the phase diagram. Microseeding with a slightly larger gradient of salt concentration yielded PSI crystals with great diffraction quality and low mosaicity as described in section 4.3.2.

At lower levels of supersaturation, in the metastable zone, introduction of previously grown crystals provides a path for the seeds to further add more protein molecules on their periphery and grow into larger crystals (Bergfors, 2003). By performing seeding as a separate step, the optimal conditions (protein and precipitate concentration) for nucleation and specific conditions for crystal growth can be performed under optimal conditions (reaching the nucleation zone can be achieved either fast by rapid dilution, slower by dialysis against low ionic strength buffer or can be reached by concentrating the protein at low ionic strength). Depending on the ionic strength and the protein

concentration as well as the speed of crystallization, crystals ranging from 100nm to 10um can be grown and used for microseeding. If well-ordered 10 – 100 μm sized crystals are available, macroseeding can be utilized.

4.4.2. Macro-crystallization of PSI using dialysis

For the purpose of gentle exchange of precipitant during the time course of a crystallization experiment, either the technique of vapor diffusion or dialysis can be utilized. The principle of dialysis is using a semi-permeable membrane that separates the protein from the precipitant and by gradually changing the precipitant concentration, supersaturation is achieved and the system eventually reaches the metastable zone in the solubility curve. The biggest advantage of using dialysis is, the technique permits gentle manipulation of crystallization conditions without compromising on the required high protein concentration. Additionally, the reaction chamber can be transferred to another vessel and gradual change in precipitant concentration can continue without loss of protein sample.

Having mentioned that, the probable reason why dialysis is less popular than vapor diffusion for protein crystallization is the lack of pre-assembled reactors. The dialysis cells are quartz tubes that can break or rupture the semi-permeable membrane leading to the loss of sample. But with careful handling, dialysis can yield great results. This is especially true for samples like PSI that crystallize under low ionic strength.

As explained in section 4.2.4., ultrafiltration of purified PSI is the final step for protein purification because this step yields crystallites of PSI. Previously, both micro and macro seeding procedures were employed for growing large PSII crystals (Fromme et.al.

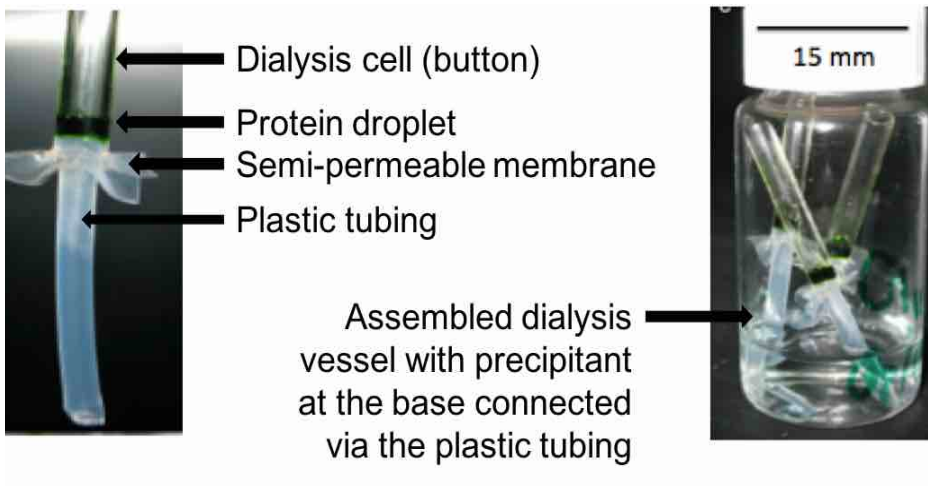

Figure 4.13: **Dialysis for PSI macro-crystallization**.

Vessel containing the protein and precipitate solutions separated by a semi-permeable membrane (cut off 100 KDa). The precipitant solution rises in the plastic tubing by capillary action and interacts with the protein solution across the membrane. To change the crystallization condition, the assembled reaction chamber can be removed and introduced to a fresh vessel with a different precipitate concentration.

1998). But the resulting crystals have been mosaic and diffracted to limited resolution. To improve this process, the macroseeding step using medium sized (~ 100 μm) crystals was identified as the place for optimization.

As crystals mature and the free available protein in their vicinity depletes, their growth halts. Their surface is very smooth, the outermost layer of the crystals being complete and thereby has no steps that allow the next layer to grow easily. But, reusing these matured crystals as seeds might present certain challenges. The completed edges of a mature crystal are thermodynamically less favorable for formation of a new layer (fewer new crystals contacts than in case of a surface with steps) and thereby instead of crystal growth, secondary nucleation is a very common event, where small crystals grow from the surface of the seed crystal in all directions (porcupine crystals). If seeding conditions are perfectly optimized, the seed crystal would dissolve in the beginning, but once supersaturation is achieved, (as dialysis progresses reaching the supersaturated zone at

high protein concentration and very low salt concentration), the seed crystal starts to grow into one large crystal. The problem with this approach is finding and reproducing the perfectly optimized condition.

As opposed to that, the use of microcrystals that are still growing presents fewer experimental challenges and if the seed is introduced in the metastable zone, new layers of protein molecules can be added to the growing crystal without the requirement of partially dissolving the seed crystals. This method of microseeding can yield fewer, larger, better ordered crystals.

In order to test if microcrystal seeds work better, a fresh dialysis experiment was set-up. PSI at 20 mM chlorophyll concentration (80 mg/ml) was dialyzed against 5 mM MES pH 6.4, 0.02% β-DDM, 30 mM $MgSO_4$ for only 3 hours instead of 24 hours. A few freshly growing microcrystals (~ 10 μM) were introduced in the dialysis set-up using the seeding loop and permitted to equilibrate against buffers with lower salt concentrations i.e. 5 mM MES pH 6.4, 0.02% β-DDM, 6 - 10 mM $MgSO_4$ for 18 hours. As explained in section 4.2.4., at 6 mM $MgSO_4$ and at these protein concentrations, spontaneous

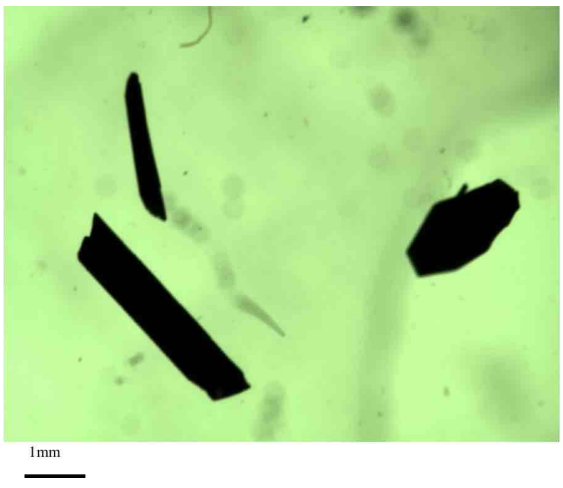

Figure 4.14: **Harvested PSI crystals.**
Crystals grown at 9 mM $MgSO_4$ yielded best results. Crystals harvested were needle like and 2–2.5 mm in the longest dimension.

nucleation can occur, so very small crystals were obtained at this condition. Overall, all gradient conditions yielded in successful crystallization and largest crystals were obtained at 9 mM $MgSO_4$.

4.4.3. Crystal freezing and data collection

The dialysis set-up is extremely efficient and yields good quality crystals. But careful crystal handling for data collection is essential for utilizing their complete potential. Since PSI crystals completely dissolve or are destroyed in the presence of PEG or glycerol solutions (which are often used for other proteins as cryo-protectants), sucrose had been identified as an appropriate cryo-protectant. The concentration of the anti-freeze agent has to be high enough to prevent cubic ice formation in crystals during the flash freezing process. Here, high viscosity of concentrated sucrose solution poses several challenges for crystal freezing.

PSI crystals are harvested in glass wells after disassembly of the dialysis cell. This had to be done with a steady hand and gentle care to not squish the large crystal in the process. The crystal was then fished out using an appropriately sized cryo loop and introduced to sequentially higher sucrose concentrations, which were prepared in buffer (5 mM MES pH 6.4, 0.02% β-DDM) without salt. At sucrose concentration of 1.4 M, the crystals achieved the neutral buoyancy with respect to the freezing solution. As a final freezing step, crystals were introduced to a 1.5 mL reaction tube containing ~ 1 mL of 5 mM MES pH 6.4, 0.02% β-DDM, 10 mM $MgSO_4$, 2 M Sucrose. The tube was turned upside down because the crystals float on top of the dense 2M sucrose solution and turning the tube upside down prevented any possible crystal dehydration. This setup was permitted to incubate at room temperature for 1 hour.

Finally, the prepared crystal was gently removed and flash frozen using liquid nitrogen in cryo loops for data collection to synchrotron sources. The frozen crystals were mounted on the goniometer head at the Advanced Light Source, beamline 501. The data set was collected using an ADSC 315 CCD detector at the wavelength of 0.97 A. The oscillation / frame was 0.33°, 360 frames were collected, corresponding to 120° total .

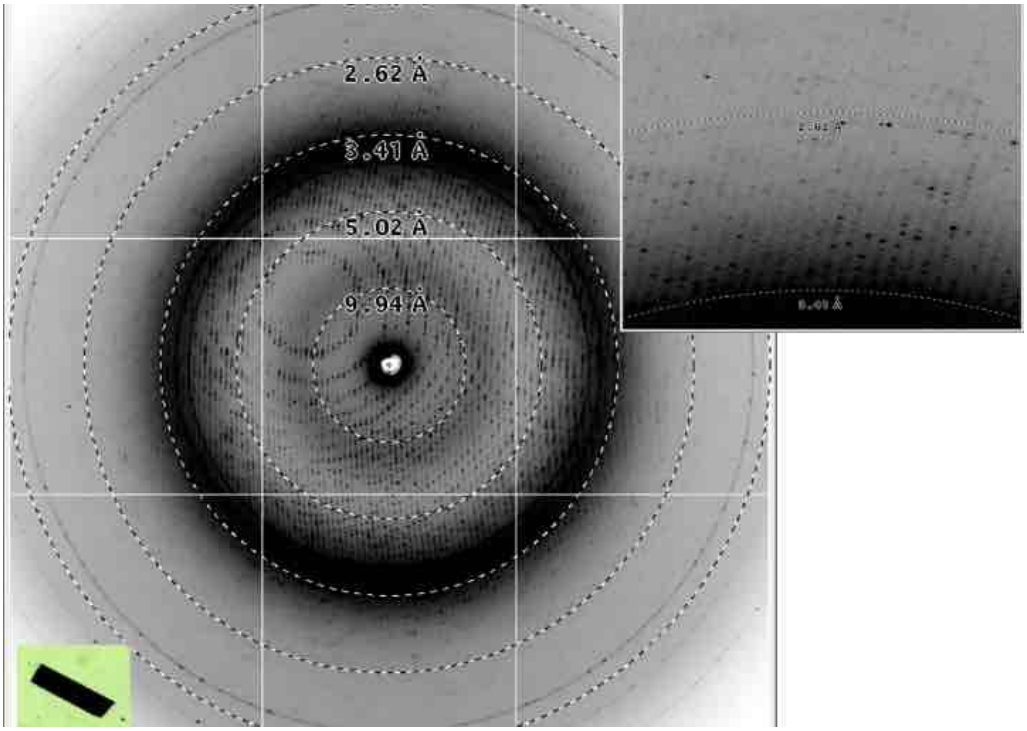

Figure 4.15: **Diffraction pattern of PSI crystals**.

Data collected at Advanced Light Source in 2013. As highlighted in the zoomed in image fraction, diffraction was better than 2.5 A and data was finally analyzed to 2.3 A. The new crystallization strategy resulted in better diffracting crystals with significantly lower inherent disorder i.e. mosaicity.

4.5. Analyzing the collected data

Processing diffraction data is mathematically complex but with the help of several software packages and program suites, well established algorithms can be utilized for

analysis. One such example is the Collaborative Computational Project, Number 4 (CCP4) suite (Winn et al., 2011) which presents an exhaustive and effective pathway for data processing.

The previously solved structure of PSI (PDB ID: 1JB0) was in the hexagonal space group of $P6_3$ with unit cell dimensions of a = 281.00 Å, b = 281.00 Å, c = 165.20 Å, $\alpha = \beta = 90°$ and $\gamma = 120°$ (Jordan et.al. 2001). But the new data set did not comply with the original space group parameters. The new structure could only be solved by application of the monoclinic space group of $P2_1$ which indicates a difference in arrangement of protein molecules with respect to crystal packing. Updated unit cell parameters are a = 277.67 Å, b = 164.93 Å, c = 283.05 Å, $\alpha = 90° \beta = 120°$ and $\gamma = 90°$. In space group $P2_1$, the entire PSI trimer is represented in the asymmetric unit. This permits visualization of inter-monomer differences and details of inter-monomer connectivity.

Indexing and spot-finding was performed using XDS software package (Kabsch, 2010). After assignment of the diffraction spot parameters, diffracted intensities were integrated. An important parameter of data quality is completeness, i.e. coverage of all theoretically possible unique reflections within the measured data-set (Arkhipova et al., 2017). Data collected for the new PSI crystals covered 120° orientation in the crystal. For the lower symmetry space group of $P2_1$, this yielded a completeness of 80 %. To increase the completeness of the data-set, additional diffraction data was collected which contributed towards completing the measured intensities. Since two crystals were involved, additional scaling and merging procedures were necessary. The program *BLEND* from the CCP4 suite prove suitable for this (Foadi et al., 2013). The result of rigorous scaling and merging by *BLEND* was an .mtz file with optimal merged data statistics for further processing.

For further steps, the approach of Molecular Replacement (MR) was used where, the phase component of the structure factors of the known model (1JB0) were utilized to calculate the new structure factors. The quality of the electron density map was finally improved during refinement. This is done by maximizing the agreement between the diffraction data and the model generated by MR. The strategies employed provide flexibility based on the experiment, data quality, resolution range and corresponding restraining parameters (Adams et al., 2002). The software package of PHENIX (Python-based Hierarchical ENvironment for Integrated Xtallography) was used for MR and several rounds of refinement for generating the best data statistics.

Eventually, one of the output files generated was the final model in .pdb format that can be viewed and adjusted by hand for finer structural details. COOT (Crystallographic Object-Oriented Toolkit) (Emsley et.al. 2004) was used for structure visualization and final model building & verification. The data statistics are described in Extended Data Table 4.1.

Table 4.1: **Data table of PSI**

Wavelength	1.0 and 0.977 A
Resolution range	48.78 (2.3)
Space group	P 1 21 1
Unit cell dimensions	a = 277.67 Å, b = 164.93 Å, c = 283.05 Å, $\alpha = 90°$ $\beta = 120°$ and $\gamma = 90°$
Multiplicity	3.0 (2.2)
Completeness (%)	92.14 (75.70)
Mean I/sigma (I)	4.5 (1.3)
Wilson B-factor	34.51
R-merge	0.152 (0.592)
R-meas	0.192 (0.862)
CC1/2	0.969 (0.418)
Reflections used in refinement	905,239 (78,099)
Average mosaicity	0.24
Reflections used for R-free	18,378(1,663)
R-work	0.216(0.308)
R-free	0.246(0.318)
Number of non-hydrogen atoms	75347
macromolecules	52608
ligands	20811

solvents	1928
Protein residues	7131
RMS (bonds)	0.015
RMS (angles)	1.99
Ramachandran favored (%)	93.18
Ramachandran allowed (%)	5.56
Ramachandran outliers (%)	1.26
Rotamer outliers (%)	2.20
Average B-factor	35.53
macromolecules	34.29
ligands	38.55
solvent	36.84

4.6. Improvements in the PSI structure

Since the structure of PSI was already solved (PDB: 1JB0), the overall goal was to improve upon the structure and validate it. With improvements in data processing software and better data quality, the electron density maps generated during refinement

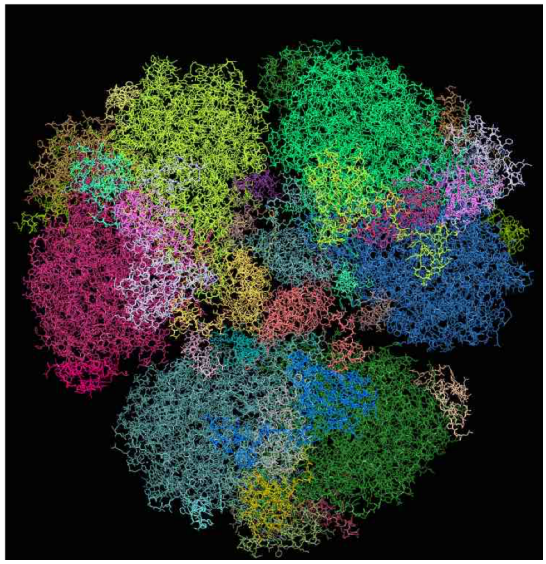

Figure 4.16: **Structure of PSI trimer** Here different subunits are indicated with a different color. Overall structure of PSI is very similar to 1JB0, but here the entire trimer could be evaluated as one particle.

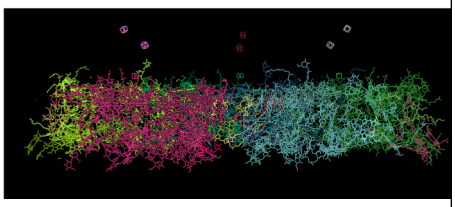

Figure 4.17: **Sideview of all cofactors in PSI trimer** All cofactors of PSI are concentrated in the transmembrane region of the complex, with the exception of 4Fe4S clusters that are associated with PsaC in the stromal hump as seen in top of each monomer in the image.

were superior for the new data set. This led to a few structural revelations which are enlisted here.

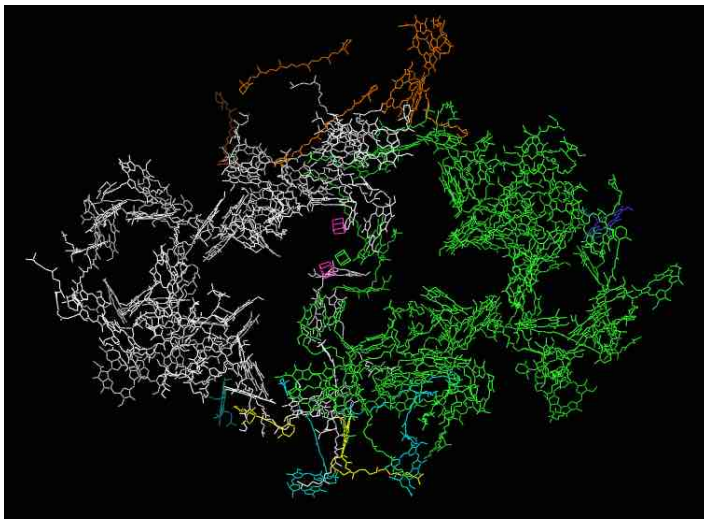

Figure 4.18a: **All cofactors in PSI monomer by subunit**

Cofactors are segregated based on the subunit they are associated with. A is depicted in green, B in white, C in pink, D in yellow, I in light blue, J in cyan, K in dark blue, L in orange and M in brown.

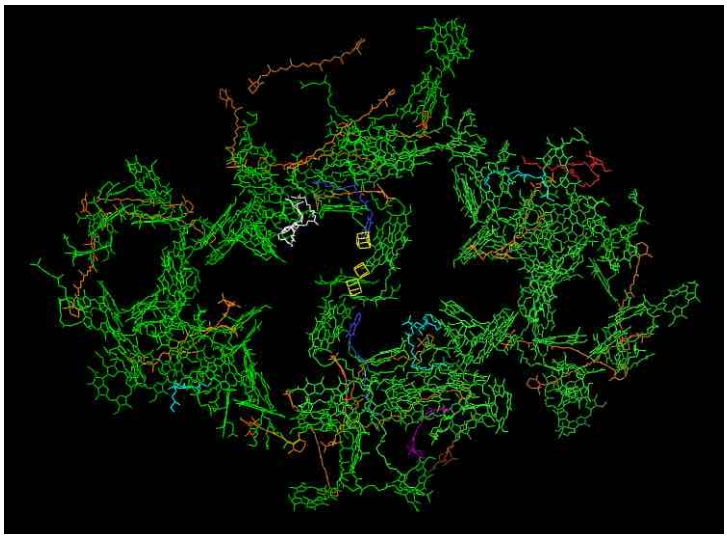

Figure 4.18b: **All cofactors in PSI monomer by molecule**

Cofactors assigned in PSI have been sorted based on the molecule. Green is for chlorophyll, Phylloquinone is illustrated in blue, 4Fe4S clusters in yellow, β-carotene in orange, and 5 types of lipids (shown in brown, cyan, red, white and purple) assigned are described in further detail in section 4.6.3

4.6.1. Chlorophyll tails were completed

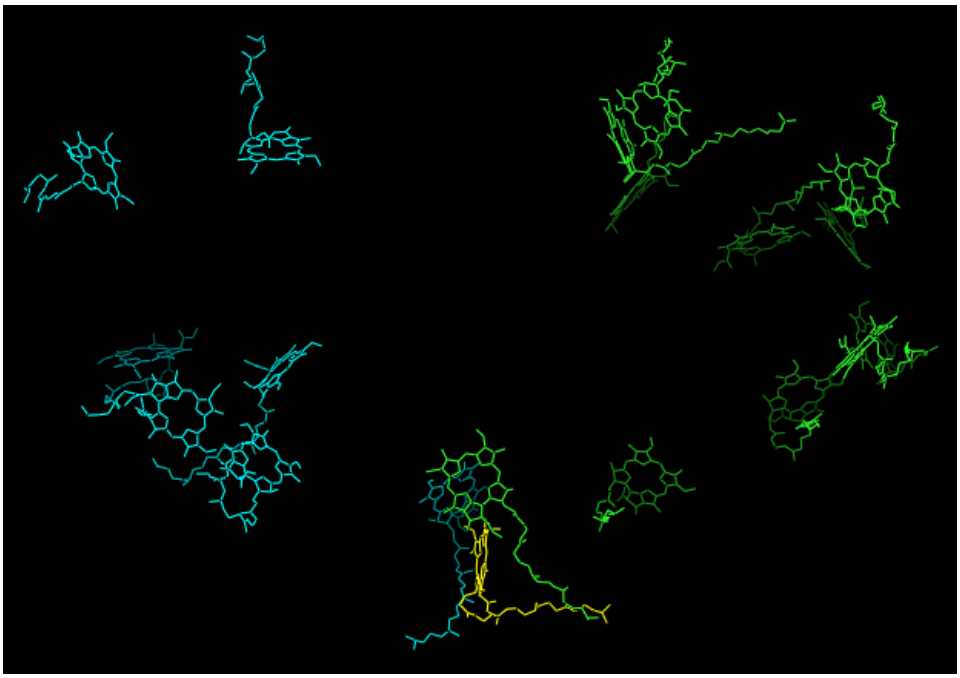

Figure 4.19: **Location of chlorophyll molecules completed in PSI monomer**

Chlorophylls associated with subunit A has been shown in green, B in cyan and F in yellow.

In the original structure of PSI solved in 2001 (Jordan et.al. 2001) due to the lack of electron density, phytol tails of several chlorophyll molecules could not be assigned in the structure and were therefore not modelled in. This was especially seen for peripheral chlorophylls which interact with or are partially embedded into the detergent micelle and thereby may have more degrees of freedom leading to them being less ordered in the crystal lattice and hence, they do not feature well defined electron densities. For 19 chlorophyll molecules per monomer (out of 95) (shown in fig 4.19) (enlisted in Table 4.2), the electron density of the phytol tails was improved and re-assignment was

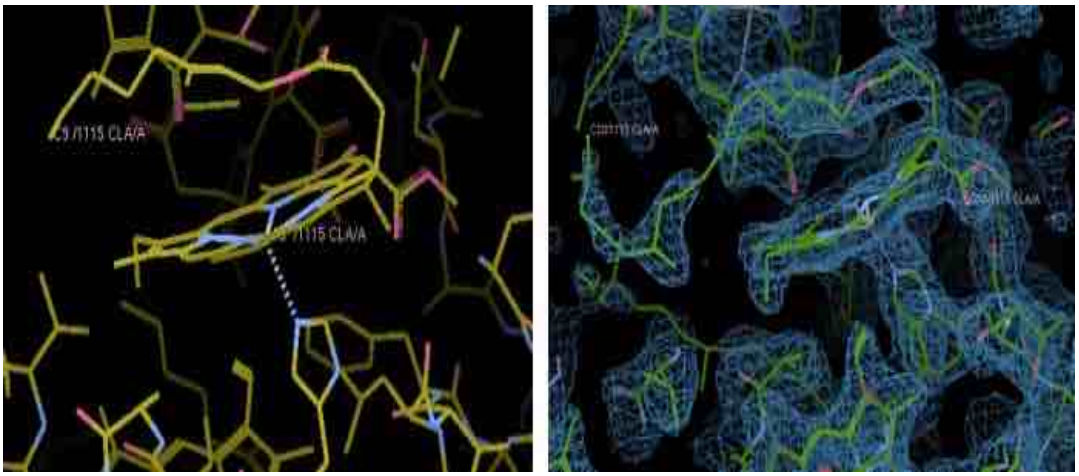

Figure 4.20: **CLA 1115 in 1JBO vs new structure**

Availability of sharper electron density permitted the completion of phytol tails. 19 such chlorophylls were completed but all of them are accessory chlorophylls.

performed based on the electron density for the complete chlorophyll molecules. The previously incomplete chlorophyll-models were replaced by chlorophylls with the full phytol tail and the carbons in the tails were oriented by either another post-refinement step or by aligning the carbon atoms by hand.

It must be noted that all re-assigned chlorophylls are antenna molecules and do not affect the assignment of chlorophylls that are components of electron transfer. The network of antenna chlorophylls contributes in shedding light into potential pathways of excitation energy transfer to the primary electron donor P_{700}.

Subunit of PSI associated with chlorophyll	Residue no.
PsaA	1105, 1110, 1112, 1113, 1115, 1116, 1120, 1129, 1135, 1137, 1139
PsaB	1201, 1208, 1214, 1220, 1222, 1227, 1230
PsaF	1301

Table 4.2: Residue details of chlorophyll molecules re-assigned

4.6.2. Other co-factors have been identified

In addition to chlorophyll molecules, other lipid molecules were also re-assigned based on the shapes of the electron density (listed in Table 4.3) (illustrated in figure 4.20). These include a β-DDM molecule and LMG associated with subunit A and a Digalactosyl-diacyl-glycerol (DGD) molecule associated with subunit B. DGD is an abundant thylakoid lipid in the chloroplast that has been hypothesized to be associated with either biogenenesis or stability of PSI in *Arabidopsis thaliana* (Holzl et.al., 2009)

Additionally, a lutein molecule ((3R,3'R,6S)-4,5-Didehydro-5,6-dihydro-β,β-carotene-3-3'-diol) was assigned in place of a β-carotene in subunit J. Luteins are abundant xanthophylls in higher plants (*Pisum sativum*) and were found in PDB: 4Y28 and reported in Mazor et.al., eLife, 2015. These co-factors are known to bridge the surrounding chlorophylls and also provide photo-protection by chlorophyll triplet quenching (Dall'Osto et al., 2006)

The functional implications of this updated co-factor system needs to be explored further but as of now, it is difficult to conclude if the new cofactors change our knowledge of excitonic coupling in PSI. Especially, the presence of lutein indicates potential pathways of non-photochemical quenching that might be present in cyanobacterial that are comparable to plants.

Table 4.3: **Differences in co-factors between old and new PSI structures**

Subunit of PSI associated with co-factor	1JB0	New structure
PsaA	45 chlorophylls	45 chlorophylls (CLA)
	6 β-carotenes	6 β-carotenes (BCR)
	1 4Fe-4S cluster	1 4Fe-4S cluster (SF4)
	1 phylloquinone	1 phylloquinone (PQN)
	2 1,2-Dipalmitoyl-phosphatidyl-glycerole	2 1,2-Dipalmitoyl-phosphatidyl-glycerole (LHG)
		1 Dodecyl-β-D-maltoside (LMT)
		1 1,2-Distearoyl-monogalactosyl-diglyceride (LMG)
PsaB	42 chlorophylls	42 chlorophylls (CLA)
	7 β-carotenes	7 β-carotenes (BCR)
	1 phylloquinone	1 phylloquinone (PQN)
	1 1,2-Dipalmitoyl-phosphatidyl-glycerole	1 1,2-Dipalmitoyl-phosphatidyl-glycerole (LHG)
	1 1,2-Distearoyl-monogalactosyl-diglyceride	1 Digalactosyl-diacyl-glycerol (DGD)
PsaC	2 4Fe-4S clusters	2 4Fe-4S clusters (SF4)
PsaF	1 chlorophyll	1 chlorophyll (CLA)
	1 β-carotene	1 β-carotene (BCR)
PsaI	2 β-carotenes	2 β-carotenes (BCR)
PsaJ	2 chlorophylls	2 chlorophylls (CLA)
	3 β-carotenes	2 β-carotenes (BCR)
		1 (3R,3'R,6S)-4,5-Didehydro-5,6-dihydro-β,β-carotene-3-3'-diol (LUT)
PsaK	1 chlorophyll	1 chlorophyll (CLA)
PsaL	1 Calcium ion	1 Calcium ion (CA)
	3 chlorophylls	3 chlorophylls (CLA)
	2 β-carotenes	2 β-carotenes (BCR)
PsaM	1 chlorophyll	missing
	1 β-carotene	1 β-carotene (BCR)
PsaX	1 chlorophyll	1 chlorophyll (CLA)

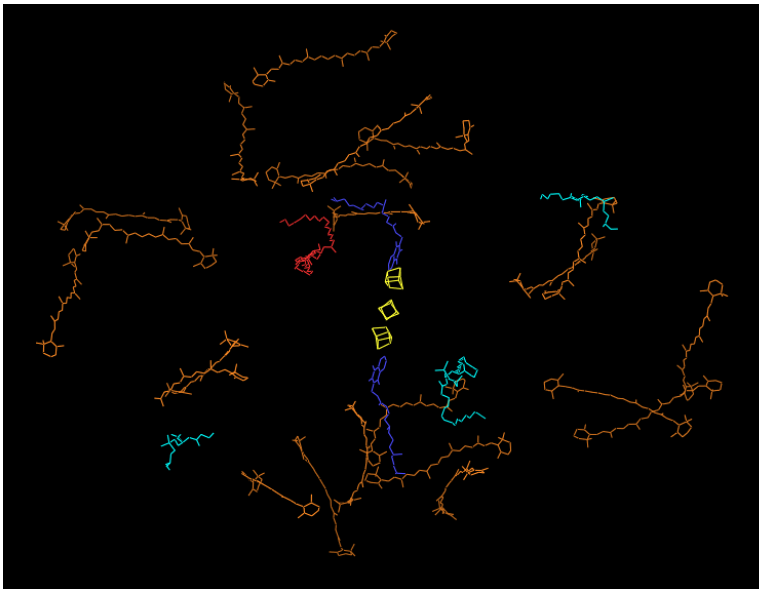

All non-chlorophyll ligands in 1JBO. β-carotenes are marked in orange, cyan is used for LHG, 4Fe-4S cluster is shown in yellow, phylloquinone in blue and LMG in red

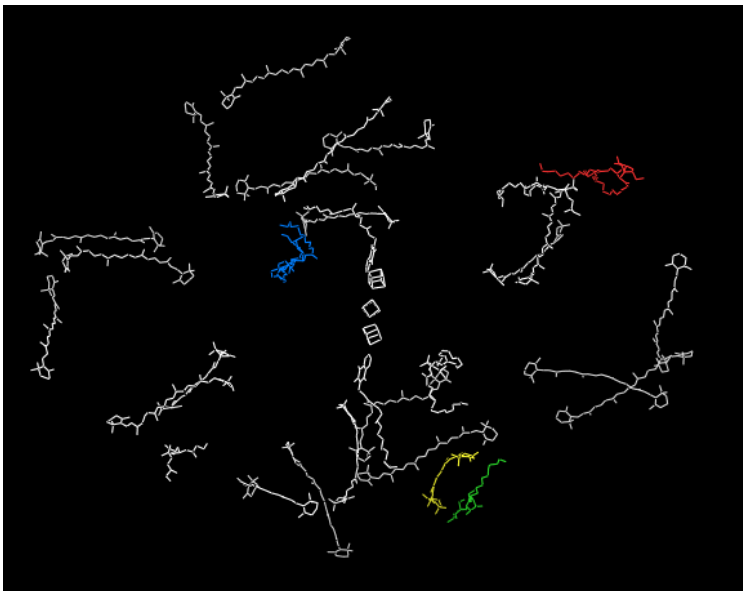

New cofactors assigned in PSI structure are marked in color. β-DDM molecule is marked in green, DGD is marked in blue, LUT molecule is indicated in yellow and LMG is marked in red.

Figure 4.21: **Details of non-chlorophyll ligands in 1JB0 in comparison with the new PSI structure**

4.6.3. Mystery of the missing chlorophyll

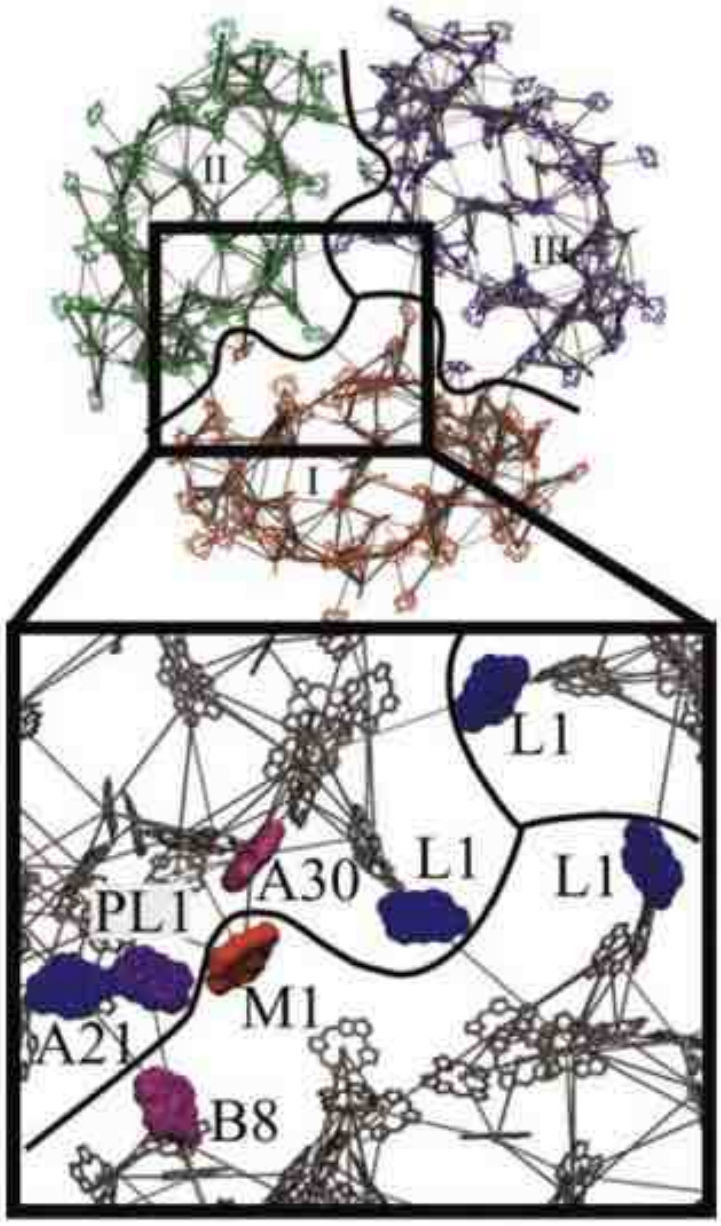

Figure 4:22: **Connection between neighboring monomers in PSI.**

The largest excitation transfer rates are indicated and chlorophyll assigned as M1 was identified to be functioning as a part of the next monomer since it is strongly connected to the neighboring monomeric chlorophylls. In absence of this key molecule, an excitation was suggested to be trapped in the monomer, where it had started. Image from Sener et.al., Journal of Chemical Physics, 2004.

Based on the chlorophylls assigned in 1JB0, several calculations were made to study excitation migration in the PSI trimer (Şener et al., 2004). These suggested a clustered network of strongest excitonic couplings of chlorophyll molecules which formed the basis for the calculation of their energy transfer rates.

Only the chlorophylls close to the monomer monomer boundary were proposed to contribute to the inter-monomer excitation transfer. The chlorophyll M1 (residue 1601) was determined to be key in inter-monomer excitation interactions. In an attempt to understand how excitation transfer would occur in monomeric PSI, the boundary chlorophylls were negated from the estimations. This led to the cross-monomer trapping probability to drop from 39.7 % to 29.7 % (Şener et al., 2005).

Unfortunately, after careful deliberation and several rounds of refinement, the chlorophyll in subunit M could not be assigned in the electron density map and is there not anymore present in the new structure. Deleting the chlorophyll molecule yields better data quality statistics. In the refined structure only 95 chlorophylls were included (without M1). The lack of chlorophyll M1 was also seen in recently published structure from mesophilic *Synechocystis sp*. PDB 5OY0 (Malavath et al., 2018).

Implications of this missing key chlorophyll are worth exploring further. A question that arises from these deductions are: Was the chlorophyll lost during purification and crystallization? But since this is independently proven by the updated structure and the one published by Malavath & Nelson et.al., it seems highly unlikely. The purification and crystallization protocols employed by both groups is vastly different and that simply adds to the deduction of a missing chlorophyll M1.

Second follow-up question would be: what does this mean for inter-monomer excitation cross-over? This remains yet to be determined. Since chlorophylls from monomeric PSI in plants associate with antenna molecules from LHCI, perhaps the newly

assigned co-factors hold an explanation for alternate routes of excitation transfer. Also, since the chlorophyll molecules are more complete and more their position and orientation could be more accurately , determined, the excitation energy pathways in the PSI trimer need to be recalculated and pathways need to be reassigned.

4.6.4. More details seen in K-subunit

The density for the peripheral subunit K for 1JB0 was not well defined and therefore this was the only subunit that was solely modelled as a C-alpha backbone trace as side chains could not be assigned. With improved data quality and better defined electron density maps, the amino acid side chain became visible and could be built into the electron density map. Following several rounds of refinement, the two transmembrane helices fit into the corresponding electron density and the connecting loop could be identified.

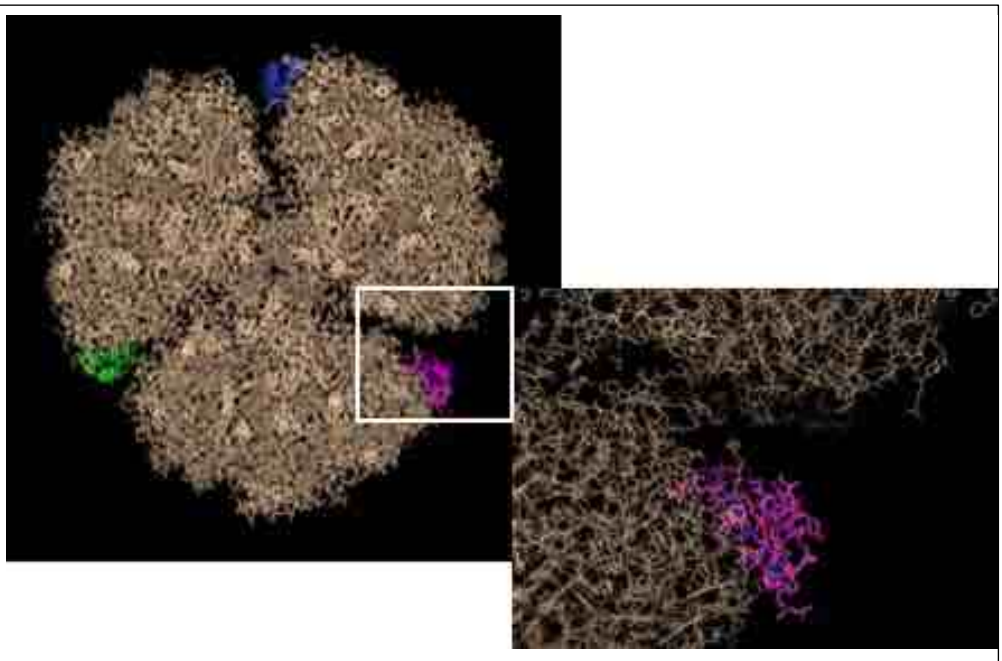

Figure 4.23: **Location of K sub-unit**

Subunit K from monomer I, g from subunit II and T from subunit III are highlighted un magenta, blue and green respectively.

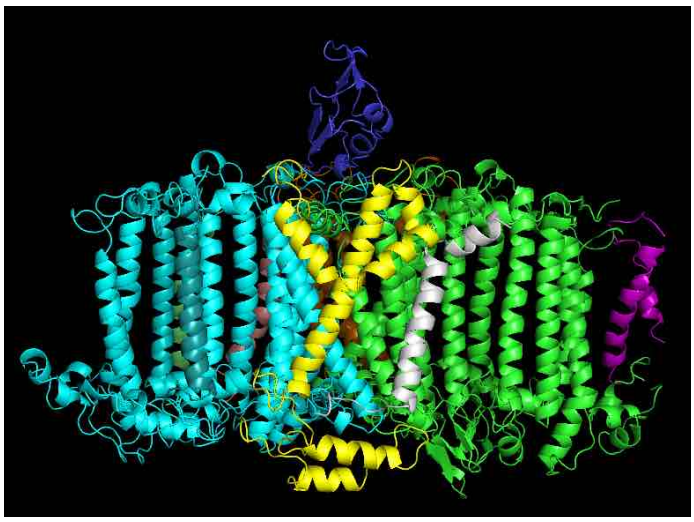

Figure 4.24a: **Transmembrane helices in PSI monomer (Side view)**

Shown in the image are all helices that could be identified by their available densities. Subunit A is shown in green, B in cyan, C in dark blue, D in white, J in yellow and constructed helices on K subunit are in magenta.

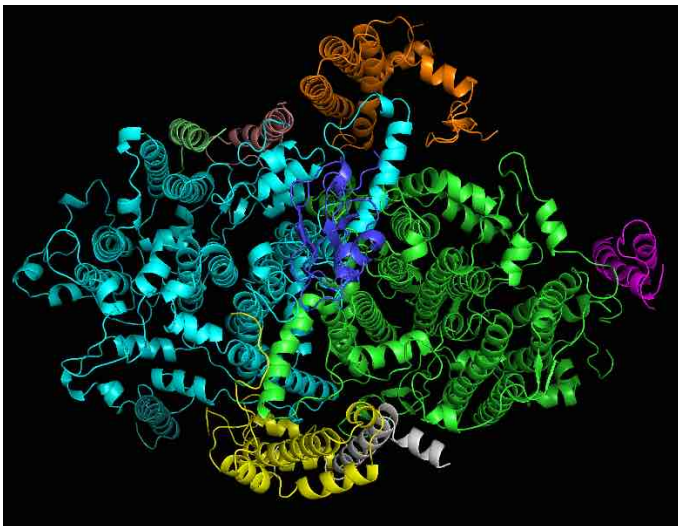

Figure 4.24b: **Transmembrane helices in PSI monomer (Top view)**

Shown in the image are all helices that could be identified by their available densities. Subunit A is shown in green, B in cyan, C in dark blue, D in white, J in yellow, L in brown, M in lime green and the 2 constructed helices on K subunit are in magenta.

4.7. Conclusions and Future work

We are still in the process of refinement and interpretation of the new improved Photosystem I trimer structure. As of now, the current model is 2.3 A structure of trimeric PSI the following cofactors were assigned.

Updated approaches in crystallization of PSI yielded better diffracting, better ordered crystals that diffracted to 2.3 A and showed a strongly decreased average mosaicity (0.24°). The new software *BLEND* in the CCP4 suite, enabled rigorous merging and scaling of data collected from two different crystals to increase the completeness of the dataset. Also, the significant advances in refinement strategies of PHENIX, helped in producing an electron density map with a better defined electron density map and eventually, a superior model.

Various chlorophyll molecules showed better defined electron density in the improved map, which allowed for the assignment of their complete phylol tails. Hence, the updated structure is now more complete and chlorophylls are better assigned . The incomplete K subunit was rebuilt by hand and refined for an assignment of most amino acids. Finally, due to a key missing chlorophyll, the existing understanding of excitation energy transfer among PSI monomers is challenged and needs to be explored further.

The structure shows very good data statistics and that indicates accuracy in structure factors. Additionally, the advantages of oligomerization in cyanobacteria remain unclear. Since higher plants contain a monomeric super-complex of PSI with 4 LHCI proteins, the study of the differences between the excitation transfer in different organisms is very interesting. The new 2.3 A structure could be used as a basis for improved excitation migration calculations in cyanobacterial PSI and this would help understand the reasons for high efficiency of excitation energy transfer in PSI.

As explained in Chapter 3, with the advent of XFELs and improvement of fixed target approaches, there is a possibility of further improving the resolution of the PSI structure. Using thousands of single snapshot SFX diffraction patterns of well-ordered PSI micro crystals, the structure may be further pushed to near-atomic resolution.

Reference:

Adams, P.D., Grosse-Kunstleve, R.W., Hung, L.-W., Ioerger, T.R., McCoy, A.J., Moriarty, N.W., Read, R.J., Sacchettini, J.C., Sauter, N.K., Terwilliger, T.C., 2002. *PHENIX* : building new software for automated crystallographic structure determination. Acta Crystallographica Section D Biological Crystallography 58, 1948–1954. https://doi.org/10.1107/S0907444902016657

Arkhipova, V., Guskov, A., Slotboom, D.-J., 2017. Analysis of the quality of crystallographic data and the limitations of structural models. The Journal of General Physiology 149, 1091–1103. https://doi.org/10.1085/jgp.201711852

Bergfors, T., 2003. Seeds to crystals. Journal of Structural Biology 142, 66–76. https://doi.org/10.1016/S1047-8477(03)00039-X

Brettel, K., 1997. Electron transfer and arrangement of the redox cofactors in photosystem I. Biochimica et Biophysica Acta (BBA) - Bioenergetics 1318, 322–373. https://doi.org/10.1016/S0005-2728(96)00112-0

Chapman, H.N., Fromme, P., Barty, A., White, T.A., Kirian, R.A., Aquila, A., Hunter, M.S., Schulz, J., DePonte, D.P., Weierstall, U., Doak, R.B., Maia, F.R.N.C., Martin, A.V., Schlichting, I., Lomb, L., Coppola, N., Shoeman, R.L., Epp, S.W., Hartmann, R., Rolles, D., Rudenko, A., Foucar, L., Kimmel, N., Weidenspointner, G., Holl, P., Liang, M., Barthelmess, M., Caleman, C., Boutet, S., Bogan, M.J., Krzywinski, J., Bostedt, C., Bajt, S., Gumprecht, L., Rudek, B., Erk, B., Schmidt, C., Hömke, A., Reich, C., Pietschner, D., Strüder, L., Hauser, G., Gorke, H., Ullrich, J., Herrmann, S., Schaller, G., Schopper, F., Soltau, H., Kühnel, K.-U., Messerschmidt, M., Bozek, J.D., Hau-Riege, S.P., Frank, M., Hampton, C.Y., Sierra, R.G., Starodub, D., Williams, G.J., Hajdu, J., Timneanu, N., Seibert, M.M., Andreasson, J., Rocker, A., Jönsson, O., Svenda, M., Stern, S., Nass, K., Andritschke, R., Schröter, C.-D., Krasniqi, F., Bott, M., Schmidt, K.E., Wang, X., Grotjohann, I., Holton, J.M., Barends, T.R.M., Neutze, R., Marchesini, S., Fromme, R., Schorb, S., Rupp, D., Adolph, M., Gorkhover, T., Andersson, I., Hirsemann, H., Potdevin, G., Graafsma, H., Nilsson, B., Spence, J.C.H., 2011. Femtosecond X-ray protein nanocrystallography. Nature 470, 73–77. https://doi.org/10.1038/nature09750

Dall'Osto, L., Lico, C., Alric, J., Giuliano, G., Havaux, M., Bassi, R., 2006. Lutein is needed for efficient chlorophyll triplet quenching in the major LHCII antenna

complex of higher plants and effective photoprotection in vivo under strong light. BMC Plant Biology 20.

Domonkos, I., 2004. Phosphatidylglycerol Is Essential for Oligomerization of Photosystem I Reaction Center. PLANT PHYSIOLOGY 134, 1471–1478. https://doi.org/10.1104/pp.103.037754

Fischer, N., 1998. The PsaC subunit of photosystem I provides an essential lysine residue for fast electron transfer to ferredoxin. The EMBO Journal 17, 849–858. https://doi.org/10.1093/emboj/17.4.849

Foadi, J., Aller, P., Alguel, Y., Cameron, A., Axford, D., Owen, R.L., Armour, W., Waterman, D.G., Iwata, S., Evans, G., 2013. Clustering procedures for the optimal selection of data sets from multiple crystals in macromolecular crystallography. Acta Crystallographica Section D Biological Crystallography 69, 1617–1632. https://doi.org/10.1107/S0907444913012274

Fromme, P., Jordan, P., Krauß, N., 2001. Structure of photosystem I. Biochimica et Biophysica Acta (BBA) - Bioenergetics 1507, 5–31. https://doi.org/10.1016/S0005-2728(01)00195-5

Fromme, P., Witt, H.T., 1998. Improved isolation and crystallization of photosystem I for structural analysis. Biochimica et Biophysica Acta (BBA) - Bioenergetics 1365, 175–184. https://doi.org/10.1016/S0005-2728(98)00059-0

Grotjohann, I., Fromme, P., 2005. Structure of cyanobacterial Photosystem I. Photosynthesis Research 85, 51–72. https://doi.org/10.1007/s11120-005-1440-4

Guergova-Kuras, M., Boudreaux, B., Joliot, A., Joliot, P., Redding, K., 2001. Evidence for two active branches for electron transfer in photosystem I. Proceedings of the National Academy of Sciences 98, 4437–4442. https://doi.org/10.1073/pnas.081078898

Jordan, P., Fromme, P., Witt, H.T., Klukas, O., Saenger, W., Krauû, N., 2001. Three-dimensional structure of cyanobacterial photosystem I at 2.5 AÊ resolution 411, 9.

Kabsch, W., 2010. *XDS*. Acta Crystallographica Section D Biological Crystallography 66, 125–132. https://doi.org/10.1107/S0907444909047337

Klukas, O., Schubert, W.-D., Jordan, P., Krauß, N., Fromme, P., Witt, H.T., Saenger, W., 1999. Photosystem I, an Improved Model of the Stromal Subunits PsaC, PsaD, and PsaE. Journal of Biological Chemistry 274, 7351–7360. https://doi.org/10.1074/jbc.274.11.7351

Kubota-Kawai, H., Mutoh, R., Shinmura, K., Sétif, P., Nowaczyk, M.M., Rögner, M., Ikegami, T., Tanaka, H., Kurisu, G., 2018. X-ray structure of an asymmetrical trimeric ferredoxin–photosystem I complex. Nature Plants 4, 218–224. https://doi.org/10.1038/s41477-018-0130-0

Li, M., Semchonok, D.A., Boekema, E.J., Bruce, B.D., 2014. Characterization and Evolution of Tetrameric Photosystem I from the Thermophilic Cyanobacterium *Chroococcidiopsis* sp TS-821. The Plant Cell 26, 1230–1245. https://doi.org/10.1105/tpc.113.120782

Malavath, T., Caspy, I., Netzer-El, S.Y., Klaiman, D., Nelson, N., 2018. Structure and function of wild-type and subunit-depleted photosystem I in Synechocystis. Biochimica et Biophysica Acta (BBA) - Bioenergetics. https://doi.org/10.1016/j.bbabio.2018.02.002

Mazor, Y., Borovikova, A., Nelson, N., 2015. The structure of plant photosystem I super-complex at 2.8 Å resolution. eLife 4. https://doi.org/10.7554/eLife.07433

Muller, M.G., Slavov, C., Luthra, R., Redding, K.E., Holzwarth, A.R., 2010. Independent initiation of primary electron transfer in the two branches of the photosystem I reaction center. Proceedings of the National Academy of Sciences 107, 4123–4128. https://doi.org/10.1073/pnas.0905407107

Porra, R.J., Thompson, W.A., Kriedemann, P.E., 1989. Determination of accurate extinction coefficients and simultaneous equations for assaying chlorophylls a and b extracted with four different solvents: verification of the concentration of chlorophyll standards by atomic absorption spectroscopy. Biochimica et Biophysica Acta (BBA) - Bioenergetics 975, 384–394. https://doi.org/10.1016/S0005-2728(89)80347-0

Şener, M.K., Jolley, C., Ben-Shem, A., Fromme, P., Nelson, N., Croce, R., Schulten, K., 2005. Comparison of the Light-Harvesting Networks of Plant and Cyanobacterial Photosystem I. Biophysical Journal 89, 1630–1642. https://doi.org/10.1529/biophysj.105.066464

Şener, M.K., Park, S., Lu, D., Damjanović, A., Ritz, T., Fromme, P., Schulten, K., 2004. Excitation migration in trimeric cyanobacterial photosystem I. The Journal of Chemical Physics 120, 11183–11195. https://doi.org/10.1063/1.1739400

Wang, Y., Mao, L., Hu, X., n.d. Insight into the Structural Role of Carotenoids in the Photosystem I: A Quantum Chemical Analysis. Biophysical Journal 15.

Watanabe, M., Kubota, H., Wada, H., Narikawa, R., Ikeuchi, M., 2011. Novel Supercomplex Organization of Photosystem I in Anabaena and Cyanophora paradoxa. Plant and Cell Physiology 52, 162–168. https://doi.org/10.1093/pcp/pcq183

Winn, M.D., Ballard, C.C., Cowtan, K.D., Dodson, E.J., Emsley, P., Evans, P.R., Keegan, R.M., Krissinel, E.B., Leslie, A.G.W., McCoy, A., McNicholas, S.J., Murshudov, G.N., Pannu, N.S., Potterton, E.A., Powell, H.R., Read, R.J., Vagin, A., Wilson, K.S., 2011. Overview of the *CCP* 4 suite and current developments. Acta Crystallographica Section D Biological Crystallography 67, 235–242. https://doi.org/10.1107/S0907444910045749

CHAPTER 5

EXPLORING CRYOGENIC ELECTRON MICROSCOPY FOR STUDYING MEMBRANE PROTEINS AS PHOTOSYSTEM I

5.1. Motivation for Cryo-EM

As discussed in Chapter 4, PSI forms monomeric, trimeric and tetrameric assemblies in different organisms, but the functional differences afforded by oligomerization state are not fully understood. Moreover, the inter-monomer interactions with respect to excitation energy migration of PSI is a critical scientific question where accurate structural assignment of cofactors would play a key role in assigning the probable pathways. Another topic of great interest also mentioned in Chapter 4 is whether there were differences among the monomers of the PSI trimer with respect to their structure and if there is a preference for a specific monomer to undergo charge separation and how this would affect the activity of other monomers in the trimer.

The 2.3 A structure described earlier, shows good data statistics and density for both proteins and cofactors. The newly assigned K sub-unit greatly contributes in our understanding of how the monomers come together for oligomerization. But during post-refinement, the three monomers were treated like triplicates for the efficient use of computational resources and time. This overlap of monomers unfortunately prohibits visualization of differences (if any) among the monomers.

Electron Microscopy (EM) has proven to be a versatile tool to study the structure of macromolecular complexes and the distinct advantages of using Cryo-EM for structural elucidation have been discussed in Section 1.5. Using the Single Particle Imaging (SPI)

mode of Cryo-EM, the entire PSI trimer could be treated as one asymmetric particle and inter-monomeric differences could be identified. Moreover, if crystallization of the protein was inducing structural artifacts leading to inaccuracies, they can be recognized by SPI because rapid vitrification permits the protein to be in a more native physiological state. Also, PSI purified by techniques explained in Section 4.2 is of superior quality, produces well diffracting crystals and has been extensively used as a model protein for nano-crystallography (Chapman et al., 2011; Hunter and Fromme, 2011). Exploring differences in density maps generated by complimentary techniques like Cryo-EM would be greatly insightful for structural biologists studying membrane proteins.

5.2. Sample optimization for Cryo-EM

5.2.1. Negative staining

As explained in Section 1.5, Dubotchet et.al. revolutionarized single particle EM by introducing the concept of specimen vitrification, but lack of heavy scattering atoms results in low contrast in EM images. Prior to investing efforts for sample preparation with Cryo-EM, in order to confirm the suitability of a purified specimen for SPI, a few aspects need to be considered. Primarily, sample homogeneity and stability with respect to composition and conformation needs to be tested. Another important feature is sample dispersion in thin vicinal volumes at the concentrations that are suitable for cryogenic plunge freezing. Thus, initial screening of different batches of sample by negative screening is a fairly quick method for obtaining preliminary understanding if PS1 would withstand thin vicinal films, adopt a preferred orientation, or disperse into single quaternary molecular species.

Negative staining embeds biological material in a layer of heavy atom stain for improved electron contrast. This method of staining easily permits visualization of

biological assemblies such as virus and fibers as unstained areas amid a black background. This quickly allows assessment of homogeneity, oligomeric state, particle dispersion etc. that helps in optimizing conditions prior to performing Cryo-EM (Ohi et.al., 2004). In this technique, the sample deposited on the EM grid is surrounded by heavy atoms that acts as a mordent to support the biological assembly as it is dehydrated. The electron diffraction in negative stained images is solely due to the heavy atoms because they have a much high electron potential due to their high atomic number, which limits the achievable resolution to 25-15 Angstroms or the atomic diameter of the heavy metal salt. Although images obtained by negative stain will never be appropriate for high resolution imaging, the short time to obtain well resolved images of biological assemblies in stain make it a good test for assembly state and biochemical readiness of preparations prior to cryogenic imaging.

In preparation for negative staining, PSI crystallites obtained as described in section 4.2.5 were gently dissolved in a small volume of 5 mM MES pH 6.4, 0.02% β-DDM, 100 mM $MgSO_4$ buffer. The protein obtained was extremely concentrated (~ 100 mM chlorophyll) and was consequently diluted to the final optimized conditions for negative staining i.e. 1 mM chlorophyll using the buffer containing 5 mM MES pH 6.4, 0.02% β-DDM, 30 mM $MgSO_4$.

Uranyl acetate was chosen as the staining solution due to its high contrast and stability. The resolution that could be achieved with this stain was about 2 nm, which would easily resolve the assembly state of the PS1 monomers and the dispersion of the sample. The working solution of 2% was prepared by dissolving 0.2 g of uranyl acetate to 10 mL of boiling deionized water. This solution was then syringe filtered through 0.22 μm filter and wrapped with Al foil for longer term storage of the light sensitive salt.

For negative staining, a carbon coated EM grid was placed on a glass slide and glow discharged using a splutter coater / glow-discharge system for 2 minutes with gentle plasma (Aebi and Pollard, 1987). The carbon layer could be hydrophobic and the process of glow-discharging deposits ions on the grid surface to make them negatively charged i.e. hydrophilic for easy aqueous sample application. A clean piece of parafilm was set-up to as a work clean surface and scored to prevent contamination between droplets. The freshly prepared grid was placed on a 5 μL droplet of diluted sample with the carbon side of the TEM grid facing the drop. Following 2 minute incubation, excess solution was blotted from the carbon surface by touching it to a piece of Whatman no.1. The grid was then successively placed on 2, 15 μL, 2% UA staining solutions on the parafilm and incubated 10-15 seconds with excess staining solution blotted using the filter between each drop. The

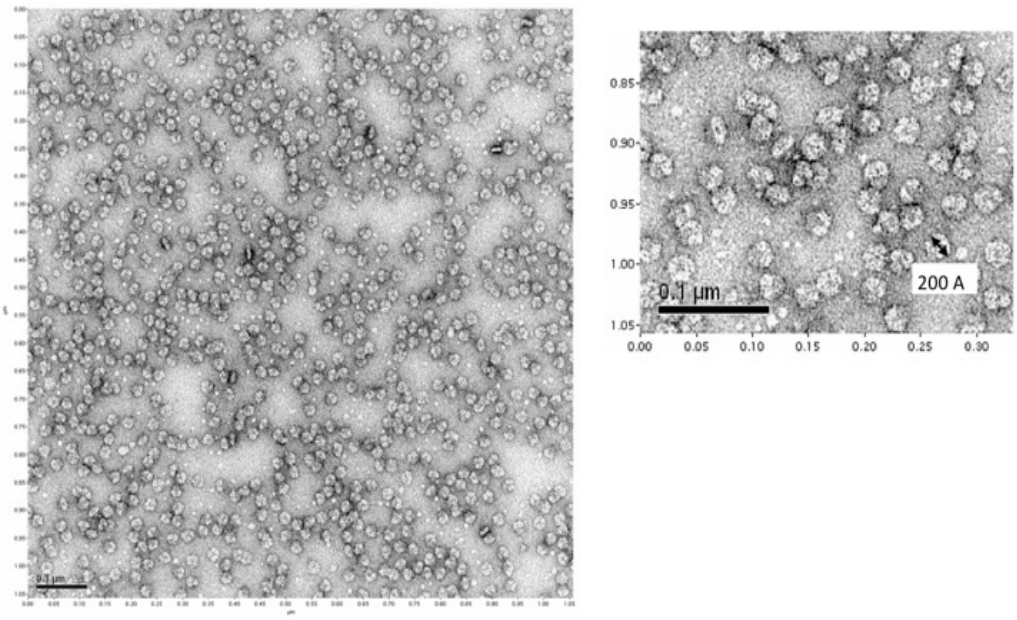

Figure: 5.1: **Negative Staining of PSI trimers.**

The PSI trimers are homogenously dispersed on the grid in a mono-layer. The image obtained displays particles of similar size indicating stability of the trimer in these buffer conditions.

stained grid was dried completely prior to imaging on the Philips CM-12 TEM. PS1 trimers were observed at 40,000X nominal magnification.

Negative staining presents numerous advantages for molecular examination such as high contrast, and speed of procedure, as well as requiring less complex instrumentation and skill. Disadvantages of this technique derive from the drying of sample on the grid during the staining process, because this rids the hydration shell of the protein, causing distortions in its conformation. Moreover, variations in stain thickness can lead to regions of molecule being unrepresented as it is not surrounded by the heavy atom salts (Hoenger et.al., 1996). Despite this shortcomings, the ability to quickly assess a complex in high contrast conditions, albeit at limited resolution with acceptable artefacts, makes it a good place to start ones single molecule examination.

5.2.2. Plunge freezing for Cryo EM

Cryogenic specimen preparation allows for the preservation of biological molecules in amorphous water where projection images contain the diffracted electrons primarily from the biological molecules (Ohi et al., 2004). To obtain vitrification of water, the specimen is applied to a 200-400 mesh copper grid covered with a holey carbon film, blotted, and then rapidly flash-frozen to prevent the water from forming ice crystals. Water has one of the highest heat capacities of most liquids and drawing the heat from the liquid fast enough to avoid water molecule reorganization and expansion to form either cubic of hexagonal ice requires the use of a special cryogen, ethane or propane (cooling rate ~ 10^5 K /sec). The heat capacity of the cryogen at liquid nitrogen temperature is such that unlike nitrogen, it does not phase transition to a gas upon heat absorption from the grid. The thickness of the sample being vitrified is limited in plunge freezing to 5 microns,

which far exceed the thickness through which electrons can pass at 300 KeV acceleration, which is about 1 micron.

PSI protein concentration optimized for negative staining was 1 mM chlorophyll. The recommended concentration for plunge freezing is about an order of magnitude more concentrated with respect to negative staining. Protein concentration for vitrification was optimized to be 10 mM chlorophyll and the specimen volume was adjusted using buffer: 5 mM MES pH 6.4, 0.02% β-DDM, 30 mM $MgSO_4$ buffer.

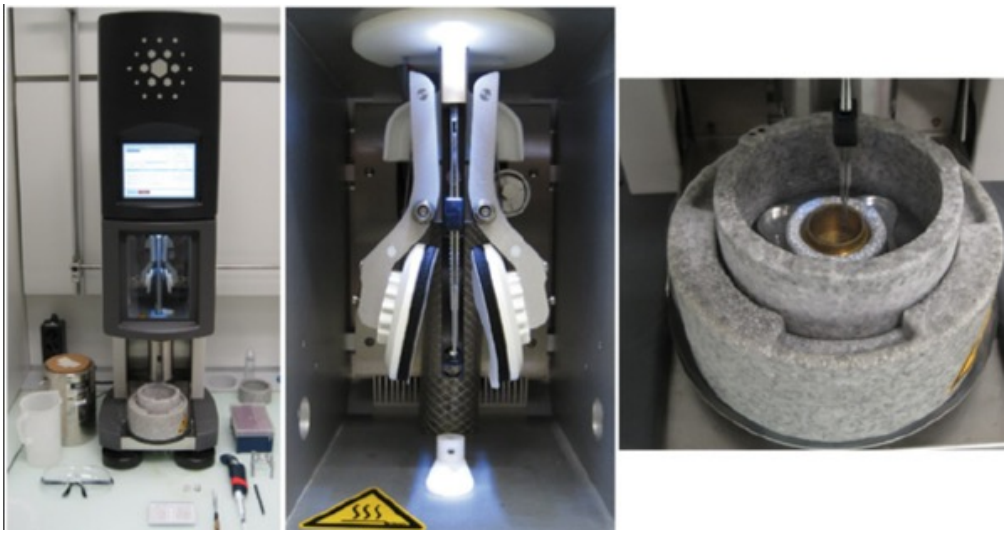

Figure 5.2: **The plunge freezing device.**

FEI Vitrobot fitted with a humidity and temperature controlled chamber. The grid is held by tweezers in the center of the device (left). Sample can be added through an opening aperture on either side of the sample chamber (middle). After a predetermined incubation time, blotting is carried out automatically by filter paper blotting pads mounted on pivoting levers at each side of the sample. After a set blotting time (blotting pressure is also adjustable) the sample held by forceps is rapidly plunged into LN2-cooled ethane liquid or slush. The liquid ethane/nitrogen container is mounted directly below the specimen chamber during plunging and moves down for transfer of the grid to a suitable grid box (right). The sample must be kept in cold nitrogen, below the de-vitrification temperature ≈ -150°C, throughout the process and during transfer to a grid storage box. The frozen sample can then be stored under LN2 until ready for viewing in the TEM. Image and caption from Goldie et.al., 2014.

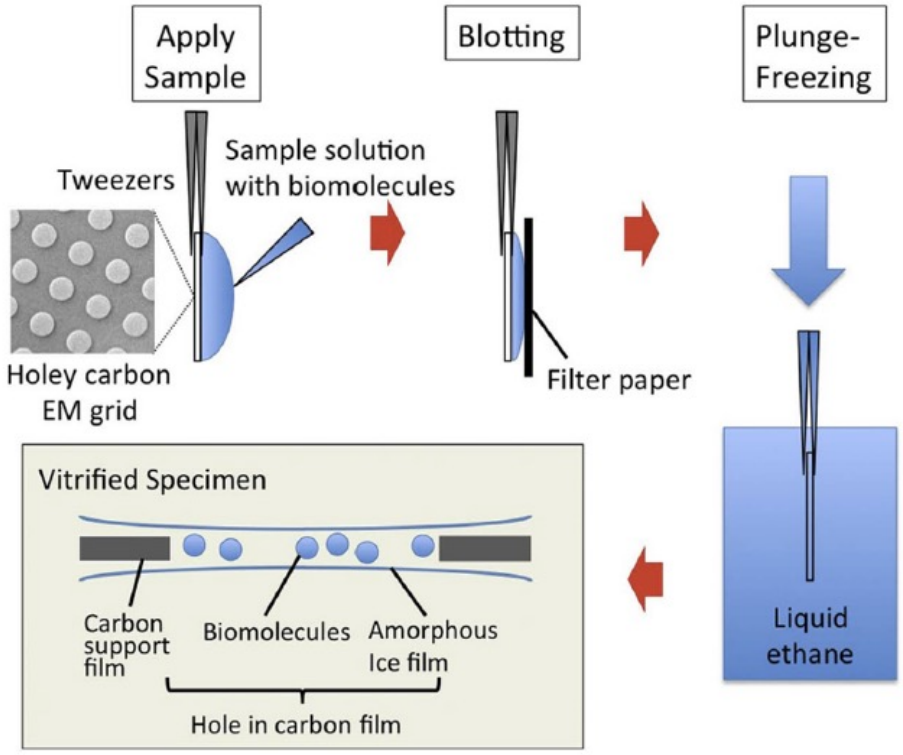

Figure: 5.3: **Steps for plunge-freezing**

Molecules of interest are preserved in a thin layer of amorphous ice embedded in the holes in the carbon film on the grid. Image from Murata et.al., 2017.

A foam reservoir was filled with liquid nitrogen to cool the small copper vessel that hold the liquid ethane. Ethane was condensed in the vial at 3 PSI until it filled the cup. The blotting during the plunge freezing process takes place in a temperature and humidity, controlled chamber, which was regulated at 16˚C and near 100 % relative humidity. Two robotic arms hold Schleicher-Schull 595 blotting paper and remove the excess liquid from the grid surface leaving only a vicinal film in the carbon holes, blot times varied from 3-6 seconds before emersion into the liquified ethane as is depicted in Figure 5.2.b.

5.2.3. Sample optimization

The grids used for electron microscopy are coated with amorphous carbon which act like a substrate for vitrification. But at higher magnification, this carbon appears grainy and can obstruct the signal from the particles by increasing the background noise. The solution to this problem was to make perforations in the carbon layer and vitrification takes place in these 'holey' carbon grids.

Membrane proteins with detergents in their buffer have different surface properties when compared to other macromolecular specimens. PSI molecules showed a high tendency to adsorb strongly to the surrounding carbon, thereby leading to the depletion of particles in ice. Several strategies were utilized for overcoming this hurdle for effective sample preparation.

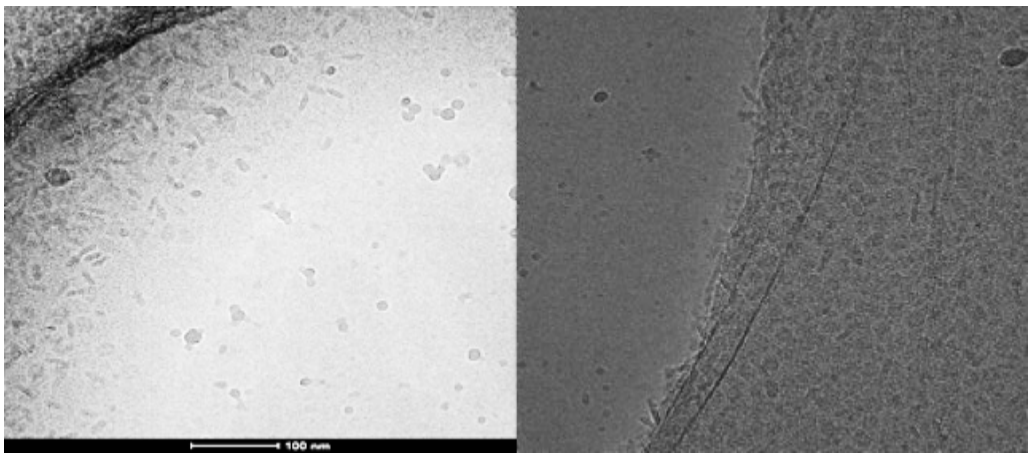

Figure 5.4: **PSI molecules had higher affinity for the amorphous in holey grids.**

As observed in the images, the holes where the particles can be imaged for single particle imaging are empty and all particles are accumulated on the carbon surface.

Strategies employed for improving sample distribution on grid:

As explained in section 5.2, glow discharging makes the grid surface hydrophilic. Varying times of discharge from 5 seconds to 5 minutes were tried to experiment with the surface charges. Also, the sample concentration, salt concentration and blotting times were also manipulated. Additionally, graphene oxide was also deposited on commercially available grids according to successful studies by Pantelic (Pantelic et al., 2010). But, the hydrophobic affinity between the detergent micelle around PSI and amorphous carbon was extremely strong and it makes the protein molecules adhere to the carbon and lie on their transmembrane side as seen in Figure 5.4 (b).

In order to overcome this issue, the grids were pre-primed with buffer containing all salts and detergent (5 mM MES pH 6.4, 0.02% β-DDM, 30 mM $MgSO_4$) prior to sample application. This additional step would ensure that both the holes and the carbon have comparable hydrophilicity for sample application. The parafilm work station was set-up to avoid dust contamination. A 5μL droplet of buffer was placed on the surface and the carbon side of the grid and was permitted to interact with it for 2-3 minutes. This 'wet' grid was mounted on the tweezers for plunge freezing. This time, a factor of dilution was expected due to presence of buffer on the grid and hence, 5x the anticipated concentration of sample i.e. 5 μL of PSI at 0.5 mM chlorophyll was applied to the grids. Blotting was optimized for 2 blotting events of 3 seconds each and sample was frozen as explained in section 5.3.

The detergent buffer priming step had significant effects on the sample preparation. PSI trimers in ice do show some preferential alignment because the transmembrane helices show affinity for the hydrophobic air-water interface, but many trimer molecules were seen distributed on the carbon surface in random orientations (as seen in Figure 5.5) and this permitted for SPI.

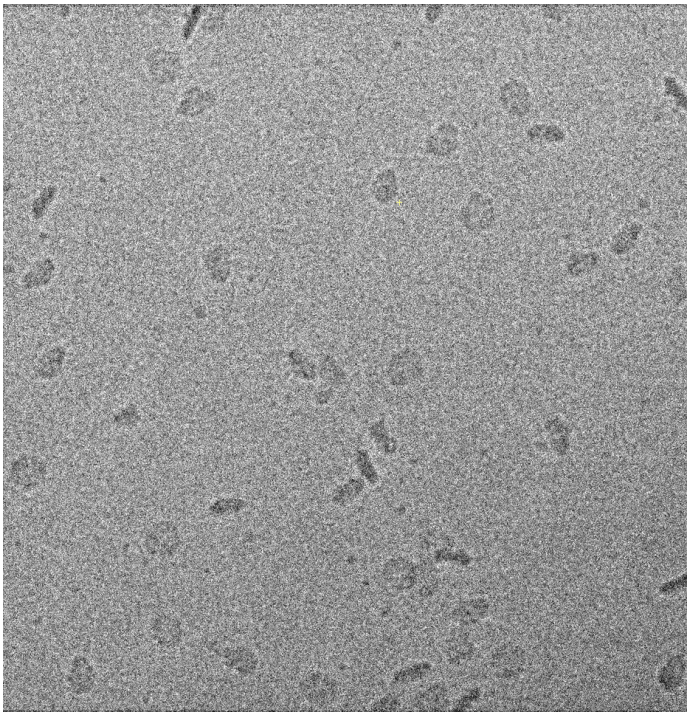

Figure 5.5: **Micrograph of PSI trimers.**

After successful detergent priming, the PSI molecules showed no preferred affinity for the carbon surface and can be located in vitreous ice in random orientations.

5.3. Data collection

Grids were screened for intact regions of well-formed vitreous ice and automated data collection was performed using SerialEM (Mastronarde, 2005) on Titan Krios microscope operated at the voltage of 300 kV equipped with K2 Summit direct electron detector (Gatan ™). A total of 2,100 micrographs were collected at the magnification of 22,500x and the exposure time was limited to 6 seconds to minimize radiation damage making effective dose of 2 electrons / A^2 / frame. Each micrograph stack contained 30 frames with data being collected at 0.2 frames / second.

5.4. Image processing

Since the interaction between the specimen and electron is inelastic, phase contrast needs to be increased by introducing a slight defocus of 1-5 microns for visualizing the particles. Additionally, the lens systems have inherent spherical aberration (C_s) and both these factors affect the acquired images. Before the data can be processed, the images need to be corrected appropriately to ensure accurate and optimal results.

5.4.1. Correction of Contrast Transfer Function

The images collected by EM at focus does not generate much contrast and imperfect imaging conditions (defocusing to generate contrast) lead to loss of information due to phase and amplitude modulation (Frank, 2009). This systematic alteration, Contrast Transfer Function (CTF) is a quasi-periodic sine function in reciprocal space. CTF models the parameters of the actual object, thus permitting estimation of the distortions present in the recorded image (Jeong et.al, 2013). The periodicity of CTF depends on a number of aspects associated with the instrument as described by the CTF formula.

$$\text{Phase CTF} = -2 \sin [\pi(\Delta z \lambda q^2 - C_s \lambda^3 q^4/2)]$$

Here, C_s is the spatial aberration coefficient of the lens system,
z is the extend of defocus during data collection,
q is spatial frequency and
λ indicates the wavelength of the incident electron beam.

For a perfect image, the transfer function would be +1 throughout. But for images collected, the CTF suppresses the spatial information and wherever the function goes to negative, CTF inverts the contrast in images (phase flip by 180°). Since defocus (z) is the

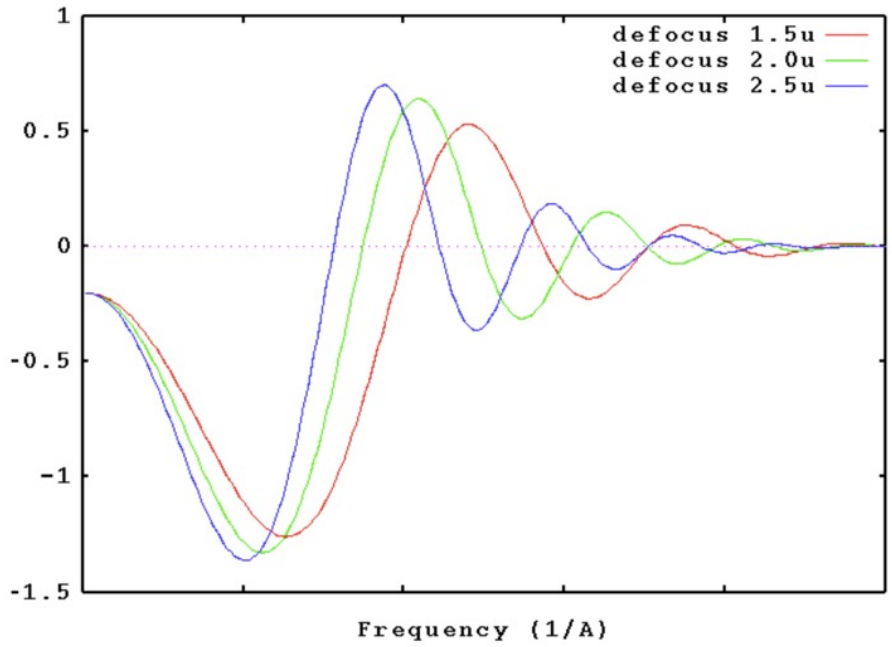

Figure: 5.6: **The effect of envelop functions and defocus on CTF**

The Y axis indicates the value of CTF and the X axis is the spatial frequency. As seen in the figure, the value and location where the value of CTF is zero is dependent on the defocus. Loss of CTF at higher spatial frequency i.e. CTF decay is caused by imperfect imaging conditions. Image from spider.wadsworth.org

only parameter being manipulated during the experiment, it determines the exact locations of zero crossing (where no contrast is transferred and information is lost).

The high-resolution details of an image are dampened by an envelope function of CTF. This 'CTF decay' (as seen in Figure 5.6) maybe caused by a number of factors including loss of spatial coherence at the source, image drift, thickness of vitreous ice, variations in voltage (chromatic aberrations), variation in lens current etc. The frequency of decay is also directly proportional to the image defocus, thus images collected at a large defocus might boost the contrast for low resolution features, but consequently weaken high resolution signal, restricting useful information (Cheng et al., 2015).

For correcting the CTF, several images at different defocus settings are utilized such that the resulting combined values for CTF, cover the entire Fourier space with no gaps. The program CTFFIND4 was employed to calculate and correct for defocus and astigmatism for the data collected. Exact values for defocus parameters were calculated by fitting a model of the microscope's CTF to an image's amplitude spectrum (Rohou and Grigorieff, 2015). The calculated CTF pattern are fit to the semi-circular oscillations in intensity that are induced by the CTF (Thon rings) that can be seen in the power spectrum of the image. For restoring the amplitudes, the FT of each image is multiplied by the CTF. Then, all equivalent views are combined and divided by the square of sum of all CTFs. Additionally, the Wiener filter constant is also considered in CTF correction, represents the SNR in the data, which varies for each sample.

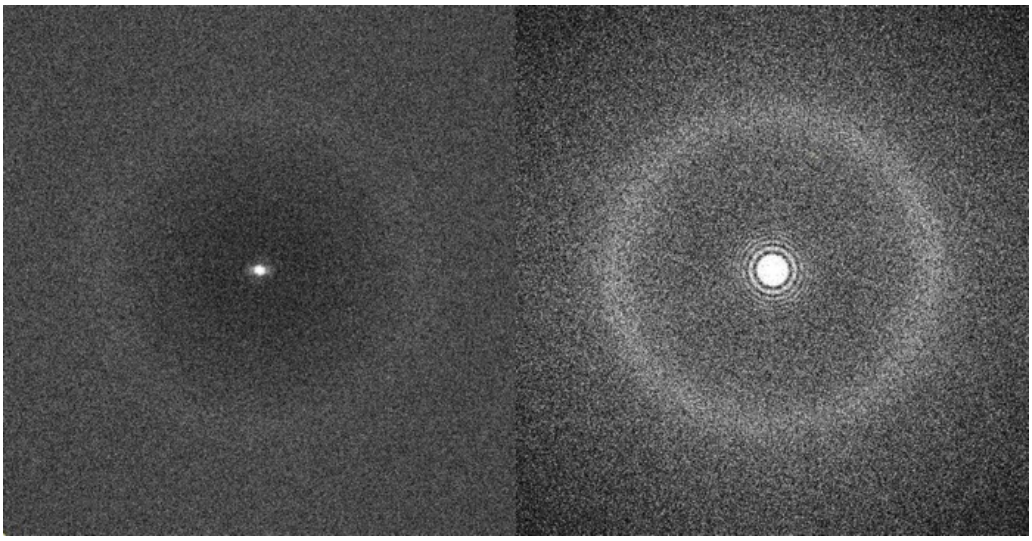

Figure 5.7: **Effect of correction of Fast Fourier Transform on the sum of all collected images.**

The CTF ripples are superimposed on a background of incoherent scattering. Upon background fitting, the corrected FFT shows a more accurate view of the CTF ripples. This is an essential step for accurate estimation of defocus for CTF correction. Image of collected PSI data.

In addition to correcting the amplitude, CTF is also corrected for phase. Wherever the value of contrast is found to be negative, CTF correction results in 'phase flipping' which essentially means a flip in image contrast. This results in white particles to appear 'darker' in corrected micrographs.

5.4.2. Motion Correction

In addition to instrumentation based corrections, the motion induced in the specimen as it is exposed to the electron beam causes significant blurring and eventually leads to loss in contrast in the collected images. This beam induced motion in specimen is believed to be caused by two major factors: build-up of a positive charge on the specimen

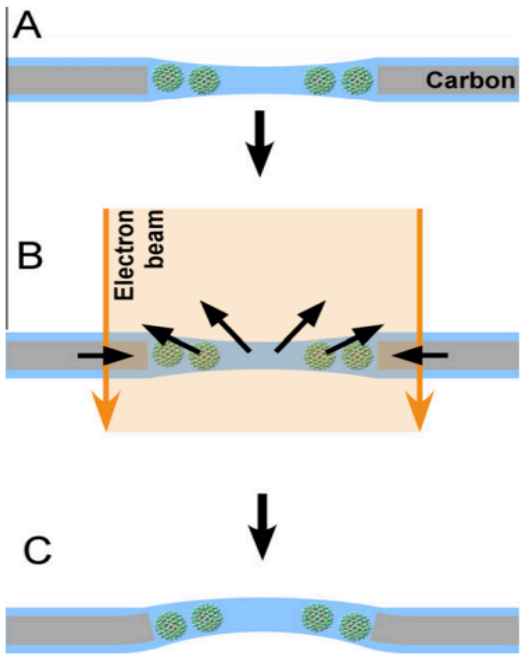

Figure 5.8: **Schematic beam induced motion seen in both ice layer and carbon film.**

As the particles suspended in ice are illuminated, the carbon support film expands slightly and this causes the hole to shrink. At the same time, radiolysis of solvent and macromolecules produces radicals in the ice layer. Both of these effects produce random motion in the particles. Image from Brilot et.al, Journal of Structural Biology (2012).

due to the reaction of the specimen with the high energy electron beam (Brinka et.al, 1998) and also, because of radiolysis of both the sample and the vitrified medium (Glaeser, 2008). Changes have been reported in both the carbon and the ice layer and this leads to both rotational and translational motion in the particles.

It has been experimentally proven that this motion is worst at the beginning of the exposure. To negate the particle rotation and translation upon exposure to the electron beam, movies are recorded at the rate of up to 40 frames / second. Frame alignment and averaging techniques are used to reduce the blurring of the images caused due to the beam induced motion. Accumulation of 5-10 electrons / A^2 dose on the sample before opening the camera shutter is known to boost the high-resolution signal (Brilot et.al., 2012). This is captured by the low-noise image recording by direct electron detectors (Milazzo et al., 2011), since the electron dose can be fractionated over a series of frames.

MotionCorr2 is universally accepted program for correcting beam induced sample motion corrected on movie stacks. It corrects for both global and non-uniform local

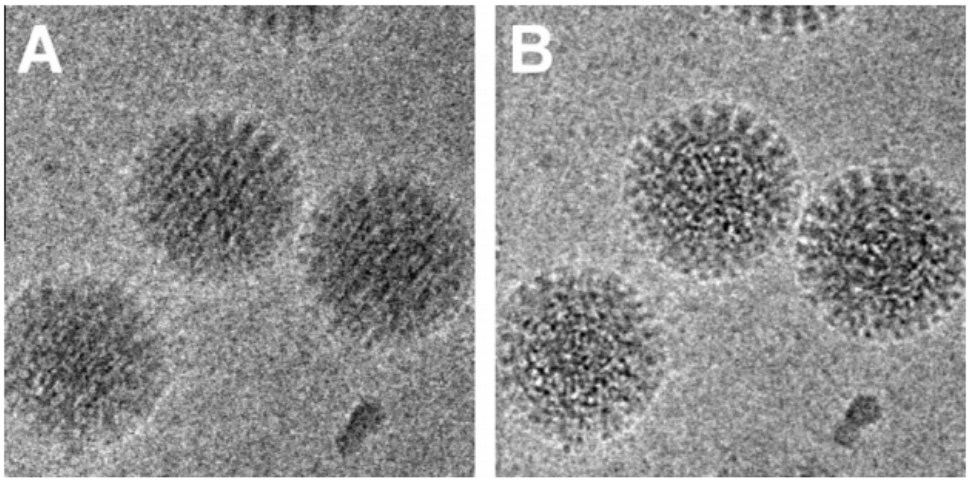

Figure: 5.9: **The effect of movie frame alignment and averaging on beam induced motion.**

The loss of high resolution features and contrast can be reversed by averaging several frames after translationally aligning them with respect to each other. Image from Brilot et.al, Journal of Structural Biology (2012).

motions at every single pixel across the whole frame. Additionally, it also performs gain correction, removes clusters of bad pixels and eventually leads to significant improvement in SNR and resolution upon 3D reconstruction.

5.4.3. Particle selection

After correcting all micrographs in the data set, good micrographs need to be selected based on particle distribution. Then, the labor intensive process of picking the particles from selected micrographs may begin. The particles need to be centered perfectly and all orientations need to be represented while picking the particles. Thus, user bias against less frequently occurring orientations that may have lower contrast must be avoided, since they are necessary for successful structure determination. Since the data was collected at extremely low dose, the contrast for most orientations was poor and in order to maximize the number of particles, picking was performed manually using the graphical user interface of RELION 2.0.

The box size was adjusted to fit the particles (300 A). Once the co-ordinates were identified, the particles were assembled into a stack for further clustering based on their orientations. Using the RELION 2.0 package, 2D classification was performed where the particles were aligned and grouped into homogenous datasets. This is done to eliminate invalid particles / empty boxes and generate high-quality class averages that would significantly improve the SNR for 3D structure determination (Cheng et al., 2015). The 2D clustering is done by K-means algorithm which is a multi-reference alignment where each particle is compared to several seed templates and are assigned to the one they most resemble. This is done iteratively where based on the initial grouping, a new set of templates is generated and all particles are re-assigned (Frank, 2009) (Frank 2006). Using this 'maximum likelihood approach' initial ambiguous assignments are not carried

forward for processing. This increases SNR with each iteration of alignment and clustering leading to several class averages (of differing orientations that are well represented).

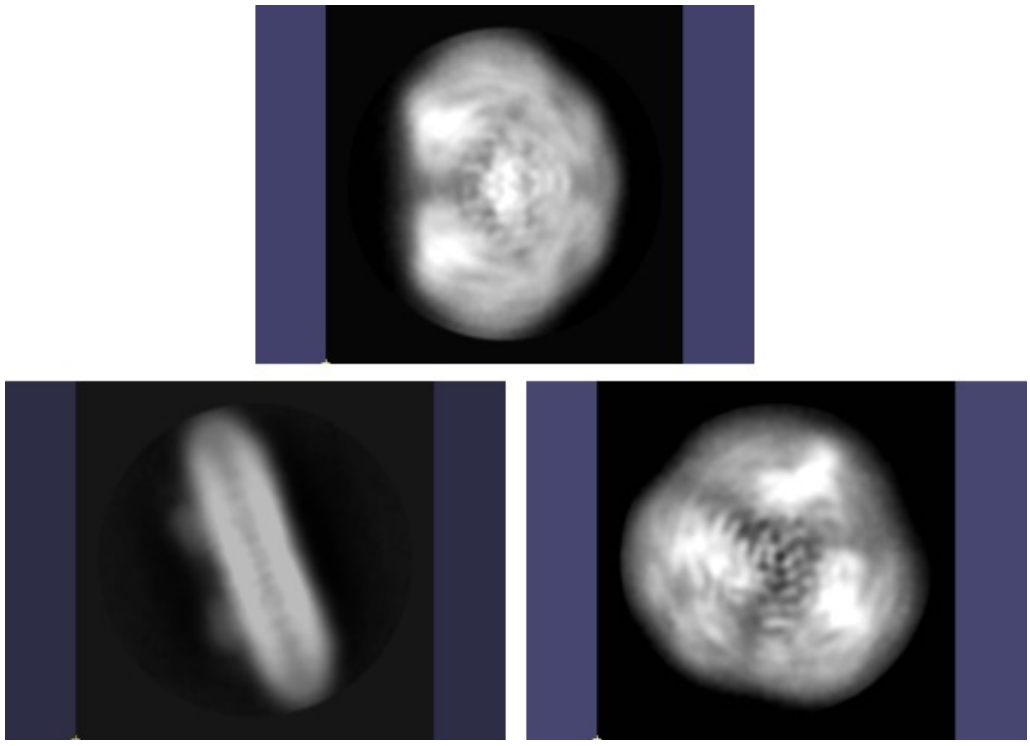

Figure 5.10: **Representative 2D classes.**

After 25 iterations of alignment and clustering, a class of particles is generated that represents particles in the same orientation. Seen in the classes above are a) a transmembrane side-view of PSI, b) particles at an inclined angle and c) top view of the intact PSI trimer.

All picked particles were clustered into 12 classes upon 2D classification. Upon examination, 4 of these classes were composed of bad particles or empty fields and were ignored for calculation of initial structures.

The template of PSI structure solved by X-ray crystallography was not used as a template for initial model building and 3D structure was determined *Ab initio* using computational methods. In the case of RELION 2.0, this is described in a Bayesian likelihood framework, where optimization is performed by iteratively altering the

variables of a function till the most suitable 'best' values are identified (Punjani et al., 2017). Additional information about the data is provided to define a unique structural solution i.e. 'regularization'. The signal and the noise components of the data are described using Gaussian distributions and for reconstruction, these prior parameters are estimated by the data in every iteration as a function of spatial frequency. This generates the least noisy reconstruction because RELION considers the data while calculating the best possible filter, without user intervention (Scheres, 2012).

5.4.4. Ab initio structure determination and refinement

De novo structure determination and 3D classification was performed using Stochastic gradient descent (SGD) optimization scheme that works by quickly by selecting a random subset of images and computes a sum for several hundreds of such subsets. This way, SGD is insensitive to local optima in the data set and the solutions found are more effective than other methods. With 37,000 particles, SGD optimization resulted in a low resolution 3D map from random initialization (Punjani et.al., 2016). Further refinement leads to visualization of higher resolution features for the final map. Here, the orientation parameters of images (projections) are modified to better achieve a match with the reprojections computed by the initial structure. The progress of this is monitored by a particular indicator i.e. Fourier Shell Correlation (FSC) curve that indicates the value for SNR as a function of spatial frequency (Penczek 2010) that is an indicator of the resolution of the map. In order to obtain a FSC curve according to the gold-standard criterion (Henderson, 2013), the data is split into two random subsets and correlation coefficients (for resolution shells extracted from Fourier transforms) are calculated for both volumes independently. This is known to prevent over-fitting (noise accumulation over several iterations) and solutions obtained are reliable (Scheres, 2012). The resolution is cut-off at

the FSC threshold value of 0.143 that was selected based on relating results of EM and X-ray crystallography (Rosenthal and Henderson, 2003). This co-related to a resolution of 4.8 A for the final map.

5.5. Preliminary data

Figure 5.11 – 5.14 show various representations of the structure of PSI particle solved by Cryo EM at the resolution of 4.8 A. Stromal and luminal views are seen. The images are generated using UCSF chimera viewer (Pettersen 2004). Isosurface is the 3D representation of a volume which is determined by the permissible noise in the background. At low isosurface, values (0.002) more noise is permitted to be visualized and that depicts the immediate environment of the particle. Figure 5.13 illustrate low isosurface views of membrane top i.e. stromal and side view of PSI. Both these images clearly show the association of detergent molecules with the transmembrane region of PSI that gives a disc-like appearance to the structure.

At high isosurface values of ~ 0.005, the sharp features of the PSI structure can be seen. These clearly depict the shape, orientation and comparative size of components. Unfortunately, the lack of high resolution details prevent from seeing kinks in helices to confirm amino acid residues, but as seen in Figure 5.14, the helices line up with the available density with high correlation confirming the validity of the structure.

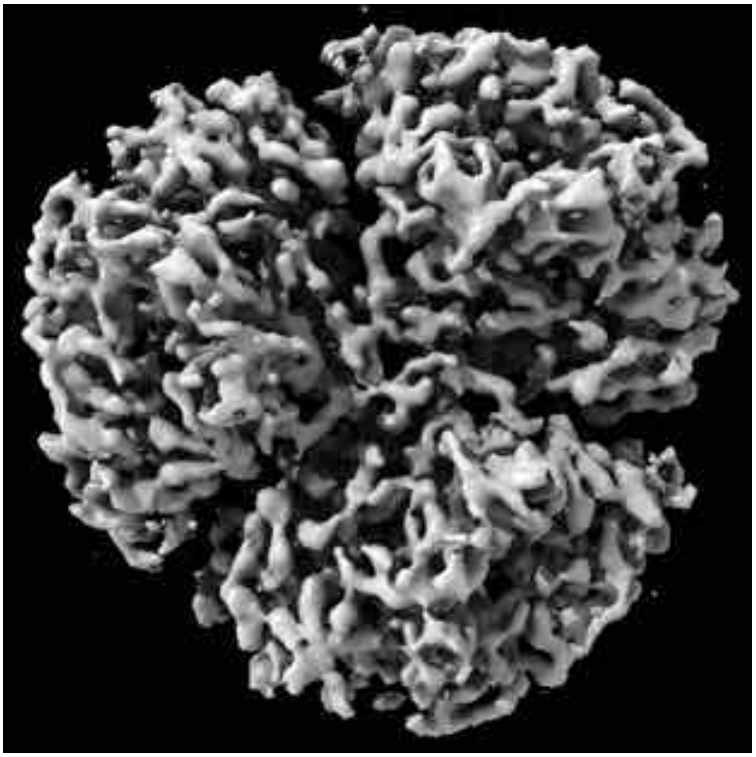

Figure 5.11a: **Stromal view of PSI structure.** The humps comprised of subunits Psa C, Psa D and Psa E are seen on each monomer.

Figure 5.11b: **The luminal view of PSI** looks very distinct from stromal view.

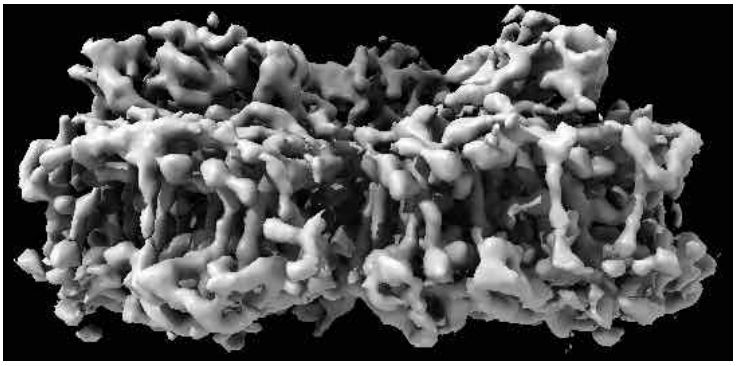

Figure 5.12: **Transmembrane view of PSI**
The stromal hump extending beyond the transmembrane helices can be clearly seen in the side-view of PSI.

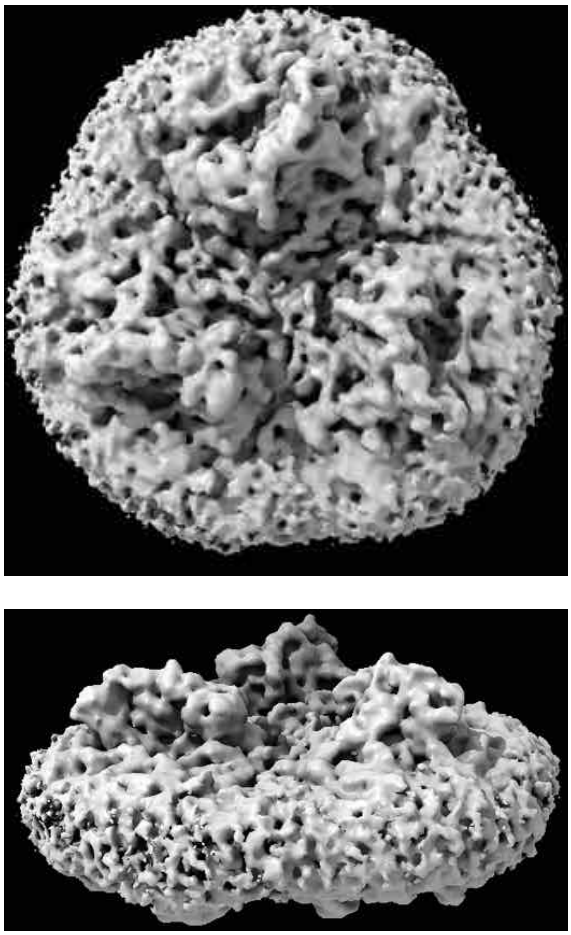

Figure 5.13: **Low iso-surface view of PSI structure (stromal and side views)**
Decreasing the isosurface limit permits noise and reveals disc-like shape of the averaged PSI particle and the lipid-DDM environment

The electron density of the map generated by Cryo-EM correlated perfectly with the sequence of PSI. As seen in Figure 5.14, the zoomed of transmembrane helices of central sub-unit A match very well with of the density of the map.

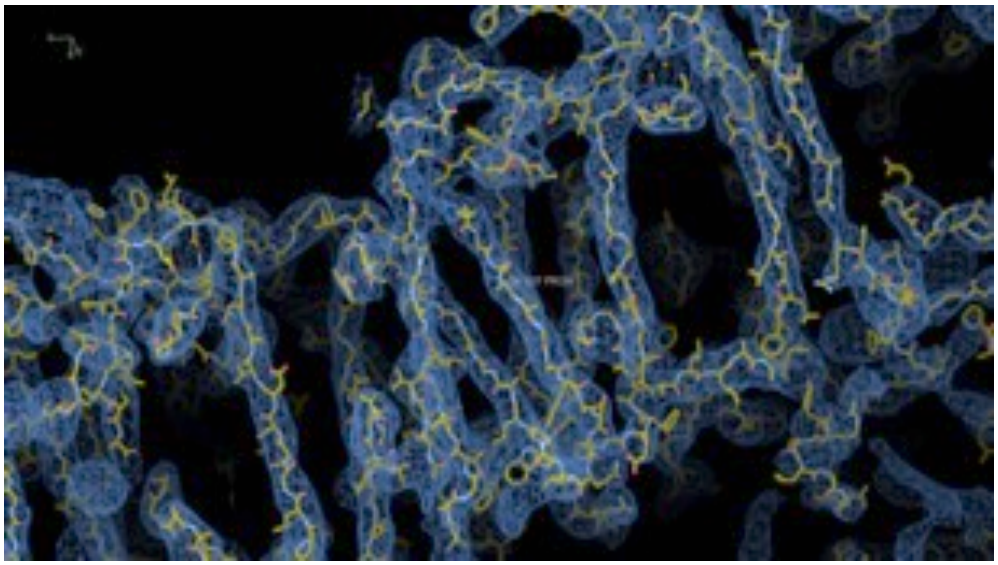

Figure 5.14: **Helices of PSI.**

Zoom-in of the core transmembrane helices of PSI shows great co-relation of the sequence with the available EM density.

Although the map needs further refinement and validation in the form of FSC maps and refinement parameters, the results obtained from preliminary analysis appear to be acceptable. Further processing would improve the structure factors by re-evaluating all model parameters. The structure quality also needs to be quantified to compare the current model with the crystallographic structure solved to 2.3 A. For improving the overall resolution of the structure, more data needs to be collected with better particle distribution in all orientations and probable differences in 3D conformations of PSI need to be explored. Improved number of particles would yield better SNR which would translate to visualization of high resolution features.

5.6. Conclusion and Future prospect

The structure of PSI isolated from *T. elongatus* was solved using Cryo-EM to 4.8 A using aberration corrected state-of-the-art Titan Krios microscope. The purified particles were vitrified using FEI vitrobot on holey carbon grids. These frozen grids were loaded on the microscope and data collection was automated using SerialEM. The micrographs were corrected for distortions created by CTF and beam-induced motion. Sequentially, particles were picked manually using RELION 2.0 software package and the picked particles were used for 2D clustering and generating class averages based on orientation. These were further classified and re-aligned for maximizing SNR and an initial model was generated. This was further perfected by refinement and the resolution was cut-off at 4.8 A according to the FSC gold-standard.

Initial analysis depicts minor differences between the monomers identified by Cryo-EM. But the structure needs further refinement and validation before any interpretations can be made. Unfortunately, because of the lack of high resolution features in the structure all co-factors cannot be precisely assigned and their orientation cannot be visualized. But the success in retrieving phases and building an *ab initio* model from minimal known parameters is promising.

An overlay of the PSI monomers would highlight any possible differences between them and that may indicate if any monomer has a higher tendency for excitation energy transfer. Additionally an overall overlay of Crystallographic and Electron microscopic maps would help in understanding the differences induced in large membrane complexes by complimentary techniques.

Finally, a combination of using the crystallographic data along with EM phases would yield an interesting map. Currently the phases in the structure described in Chapter 4 are derived by MR of the structure solved in 2001 (PDB ID: 1JB0). Whether the use of

phases generated by using a complimentary technique affects the cofactor assignment would be an extremely informative analysis.

Reference:

Aebi, U., Pollard, T.D., 1987. A glow discharge unit to render electron microscope grids and other surfaces hydrophilic. Journal of Electron Microscopy Technique 7, 29–33. https://doi.org/10.1002/jemt.1060070104

Chapman, H.N., Fromme, P., Barty, A., White, T.A., Kirian, R.A., Aquila, A., Hunter, M.S., Schulz, J., DePonte, D.P., Weierstall, U., Doak, R.B., Maia, F.R.N.C., Martin, A.V., Schlichting, I., Lomb, L., Coppola, N., Shoeman, R.L., Epp, S.W., Hartmann, R., Rolles, D., Rudenko, A., Foucar, L., Kimmel, N., Weidenspointner, G., Holl, P., Liang, M., Barthelmess, M., Caleman, C., Boutet, S., Bogan, M.J., Krzywinski, J., Bostedt, C., Bajt, S., Gumprecht, L., Rudek, B., Erk, B., Schmidt, C., Hömke, A., Reich, C., Pietschner, D., Strüder, L., Hauser, G., Gorke, H., Ullrich, J., Herrmann, S., Schaller, G., Schopper, F., Soltau, H., Kühnel, K.-U., Messerschmidt, M., Bozek, J.D., Hau-Riege, S.P., Frank, M., Hampton, C.Y., Sierra, R.G., Starodub, D., Williams, G.J., Hajdu, J., Timneanu, N., Seibert, M.M., Andreasson, J., Rocker, A., Jönsson, O., Svenda, M., Stern, S., Nass, K., Andritschke, R., Schröter, C.-D., Krasniqi, F., Bott, M., Schmidt, K.E., Wang, X., Grotjohann, I., Holton, J.M., Barends, T.R.M., Neutze, R., Marchesini, S., Fromme, R., Schorb, S., Rupp, D., Adolph, M., Gorkhover, T., Andersson, I., Hirsemann, H., Potdevin, G., Graafsma, H., Nilsson, B., Spence, J.C.H., 2011. Femtosecond X-ray protein nanocrystallography. Nature 470, 73–77. https://doi.org/10.1038/nature09750

Cheng, Y., Grigorieff, N., Penczek, P.A., Walz, T., 2015. A Primer to Single-Particle Cryo-Electron Microscopy. Cell 161, 438–449. https://doi.org/10.1016/j.cell.2015.03.050

Frank, J., 2009. Single-particle reconstruction of biological macromolecules in electron microscopy – 30 years. Quarterly Reviews of Biophysics 42, 139. https://doi.org/10.1017/S0033583509990059

Glaeser, R.M., 2008. Retrospective: Radiation damage and its associated "Information Limitations." Journal of Structural Biology 163, 271–276. https://doi.org/10.1016/j.jsb.2008.06.001

Henderson, R., 2013. Avoiding the pitfalls of single particle cryo-electron microscopy: Einstein from noise. Proceedings of the National Academy of Sciences 110, 18037–18041. https://doi.org/10.1073/pnas.1314449110

Hunter, M.S., Fromme, P., 2011. Toward structure determination using membrane–protein nanocrystals and microcrystals. Methods 55, 387–404. https://doi.org/10.1016/j.ymeth.2011.12.006

Li, X., Zheng, S., Agard, D.A., Cheng, Y., 2015. Asynchronous data acquisition and on-the-fly analysis of dose fractionated cryoEM images by UCSFImage. Journal of Structural Biology 192, 174–178. https://doi.org/10.1016/j.jsb.2015.09.003

Mastronarde, D.N., 2005. Automated electron microscope tomography using robust prediction of specimen movements. Journal of Structural Biology 152, 36–51. https://doi.org/10.1016/j.jsb.2005.07.007

Milazzo, A.-C., Cheng, A., Moeller, A., Lyumkis, D., Jacovetty, E., Polukas, J., Ellisman, M.H., Xuong, N.-H., Carragher, B., Potter, C.S., 2011. Initial evaluation of a direct detection device detector for single particle cryo-electron microscopy. Journal of Structural Biology 176, 404–408. https://doi.org/10.1016/j.jsb.2011.09.002

Ohi, M., Li, Y., Cheng, Y., Walz, T., 2004. Negative staining and image classification — powerful tools in modern electron microscopy. Biological Procedures Online 6, 23–34. https://doi.org/10.1251/bpo70

Pantelic, R.S., Meyer, J.C., Kaiser, U., Baumeister, W., Plitzko, J.M., 2010. Graphene oxide: A substrate for optimizing preparations of frozen-hydrated samples. Journal of Structural Biology 170, 152–156. https://doi.org/10.1016/j.jsb.2009.12.020

Punjani, A., Rubinstein, J.L., Fleet, D.J., Brubaker, M.A., 2017. cryoSPARC: algorithms for rapid unsupervised cryo-EM structure determination. Nature Methods 14, 290–296. https://doi.org/10.1038/nmeth.4169

Rohou, A., Grigorieff, N., 2015. CTFFIND4: Fast and accurate defocus estimation from electron micrographs. Journal of Structural Biology 192, 216–221. https://doi.org/10.1016/j.jsb.2015.08.008

Scheres, S.H.W., 2012. RELION: Implementation of a Bayesian approach to cryo-EM structure determination. Journal of Structural Biology 180, 519–530. https://doi.org/10.1016/j.jsb.2012.09.006

CHAPTER 6

SUMMARY OF OTHER PUBLICATIONS

This chapter covers the various projects associated with my work that resulted in peer-reviewed journal articles. They are categorized by the area of application to highlight the scope of research. Every publication has an abstract followed by a brief description of the work and my contribution to it.

6.1. Method development at X-ray sources

6.1.1. Serial millisecond crystallography (Martin-Garcia et al., 2017)

(IUCrJ 4.4 (2017): 439-454)

Jose M. Martin-Garcia, Chelsie E. Conrad, Garrett Nelson, Natasha Stander, Nadia A. Zatsepin, James Zook, Lan Zhu, James Geiger, Eugene Chun, David Kissick, Mark C. Hilgart, Craig Ogata, Andrii Ishchenko, Nirupa Nagaratnam, **Shatabdi Roy-Chowdhury**, Jesse Coe, Ganesh Subramanian, Alexander Schaffer, Daniel James, Gihan Ketwala, Nagarajan Venugopalan, Shenglan Xu, Stephen Corcoran, Dale Ferguson, Uwe Weierstall, John C. H. Spence, Vadim Cherezov, Petra Fromme, Robert F. Fischetti and Wei Liu.

Abstract: Crystal structure determination of biological macromolecules using the novel technique of serial femtosecond crystallography (SFX) is being severely limited by the scarcity of X-ray free electron laser (XFEL) sources. However, recent and future upgrades render synchrotron radiation sources at micro-focused beamlines suitable for room temperature serial crystallography data collection as well. Due to the longer exposure times needed at synchrotrons, serial data collection is termed serial millisecond crystallography (SMX). As a result, the number of SMX experiments is rapidly growing, with a dozen experiments reported so far. Here, we present the first high-viscosity injector-based SMX experiments carried out at a U.S. synchrotron source, the Advanced Photon Source (APS). Micro-crystals (5-20 μm) of a wide variety of proteins including lysozyme, thaumatin, phycocyanin, the human A2A adenosine receptor (A2AAR), the soluble fragment of the membrane lipoprotein Flpp3, 3-deoxy-D-manno-2-octulosunate-8-phosphate synthase (KDO8PS), and proteinase K were screened. Crystals suspended in lipidic cubic phase (LCP) or a high molecular weight poly (ethylene oxide) (PEO) (MW=8,000,000) were delivered to the beam using a high viscosity injector. In-house data reduction (hit-finding) software developed at APS as well as SFX data-reduction and analysis software suites, Cheetah and CrystFEL, enabled efficient on-site SMX data monitoring, reduction and processing. The best diffracting crystals were from A2AAR, phycocyanin, Flpp3, KDO8PS, proteinase K, thaumatin and lysozyme, with hit rates of 3.0 %, 5.0 %, 11.6 %, 1.5 %, 4.2 %, 6.0 % and 34.2 %, respectively. Complete data sets of A2AAR, phycocyanin, Flpp3, proteinase K, and lysozyme were collected and their structures were determined at 3.2 Å, 3.1 Å, 3.0 Å, 2.65 Å, and 2.05 Å resolution,

respectively. Our data demonstrate the feasibility of serial millisecond crystallography from 5–20 m crystals using a high viscosity injector at APS. The resolution of the crystal structures obtained in this study was dictated by the current flux density and crystal size, but upcoming developments in beamline optics and the planned APS-U upgrade will increase intensity by two orders of magnitude. These developments will enable structure determination from smaller and/or weakly diffracting micro-crystals.

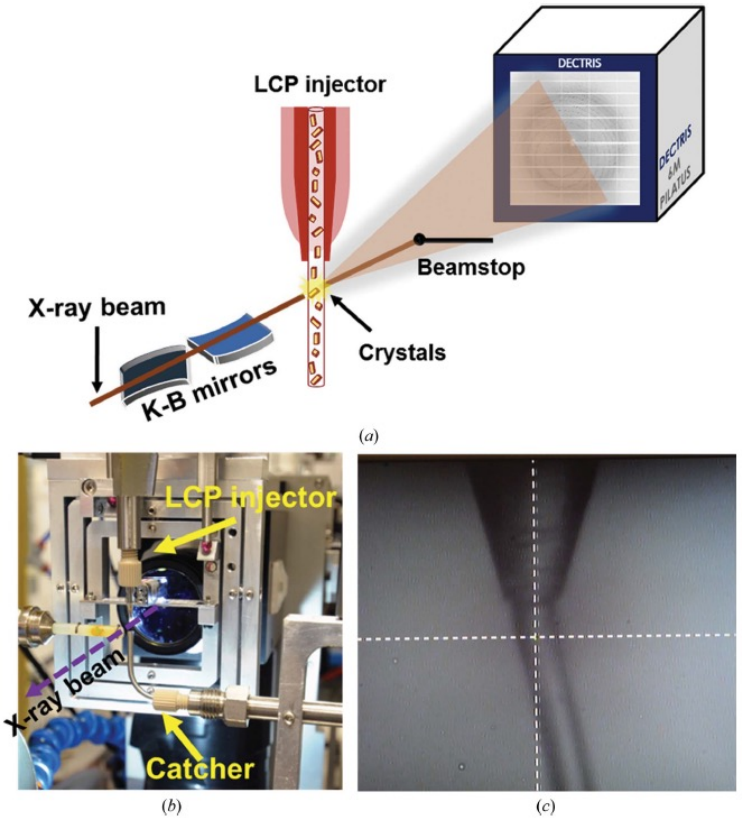

Figure 6.1: **Experimental setup at the GM/CA 23-ID-D beamline.**

Schematic diagram of the setup. (b) LCP injector (Weierstall et al., 2014) mounted on translation stages (not shown). The catcher is also shown. (c) View of the LCP stream extruding out of a 50 mm glass capillary nozzle. The intersection point of the two white dashed lines indicates the position of the X-ray beam.

Nanocrystals and serial crystallography has distinct advantages associated with them and this paper exhibits a proof of principle of performing serial experiments at synchrotrons. Viscous gel injector was used at Advance Photon Source (APS) with lipidic cubic phase (LCP) and 6 % high molecular weight to capture diffraction patterns with millisecond exposures

with microfocus X-rays. Structures of several soluble protein samples and an integral membrane protein ($A_{2A}AR$) were solved better than 3 A resolution.

My contribution to this publication was isolation, purification and crystallization of phycocyanin (PC). In addition, I also contributed in data collection at the synchrotron, along with sample injection and maintaining an extensive log for data analysis.

6.1.2. Femtosecond X-ray diffraction from an aerosolized beam of protein nanocrystals (Awel et al., 2018)

(J. Appl. Cryst. (2018). 51, 133–139)

Salah Awel, Richard A. Kirian, Max O. Wiedorn, Kenneth R. Beyerlein, Nils Roth, Daniel A. Horke, Dominik Oberthu¨r, Juraj Knoska, Valerio Mariani, Andrew Morgan, Luigi Adriano, Alexandra Tolstikova, P. Lourdu Xavier, Oleksandr Yefanov, Andrew Aquila, Anton Barty, **Shatabdi Roy-Chowdhury**, Mark S. Hunter, Daniel James, Joseph S. Robinson, Uwe Weierstall, Andrei V. Rode, Sasˇa Bajt, Jochen Ku¨pper and Henry N. Chapman

Abstract: High-resolution Bragg diffraction from aerosolized single granulovirus nanocrystals using an X-ray free-electron laser is demonstrated. The outer dimensions of the in-vacuum aerosol injector components are identical to conventional liquid-microjet nozzles used in serial diffraction experiments, which allows the injector to be utilized with standard mountings. As compared with liquid-jet injection, the X-ray scattering background is reduced by several orders of magnitude by the use of helium carrier gas rather than liquid. Such reduction is required for diffraction measurements of small macromolecular nanocrystals and single particles. High particle speeds are achieved, making the approach suitable for use at upcoming high-repetition-rate facilities.

Convergent nozzle aerosol injector (CNAI) uses He gas for focusing and generates a jet that produces extremely low background scattering in the diffraction patterns. This is significant for weakly diffracting sensitive crystal samples and continuous diffraction based experiments. Diffraction of granulovirus (GV) was obtained till the edge of the detector (~ 1.9 A).

My contribution for this experiment was optimizing GV crystalline samples in water based medium for reducing pressure required for injection and ease of aerosol generation.

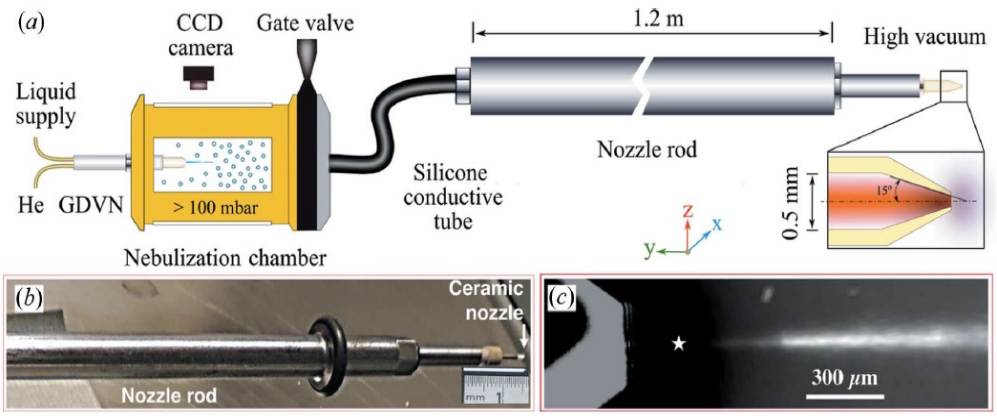

Figure 6.2: **CNAI assembly and its operation during the CXI experiment.**

(a) Sketch of the basic aerosol generation and transportation setup. (b) The aerosol nozzle mounted on the nozzle rod. (c) Time integrated image of a laser-illuminated stream of GV particles exiting the CNAI, recorded using the inline microscope at the CXI instrument. This image was formed by averaging over 3.7 min, with a running median background subtracted from each frame. The CNAI tip is seen in the left portion of the image, and the approximate X-ray focal point is indicated by the star.

6.1.3. Macromolecular diffractive imaging using imperfect crystals (Ayyer et al., 2016)

(Nature 530 (7589), 202-206, 2016)

Kartik Ayyer, Oleksandr M. Yefanov, Dominik Oberthür, **Shatabdi Roy-Chowdhury**, Lorenzo Galli, Valerio Mariani, Shibom Basu, Jesse Coe, Chelsie E. Conrad, Raimund Fromme, Alexander Schaffer, Katerina Dörner, Daniel James, Christopher Kupitz, Markus Metz, Garrett Nelson, Paulraj Lourdu Xavier, Kenneth R. Beyerlein, Marius Schmidt, Iosifina Sarrou, John C. H. Spence, Uwe Weierstall, Thomas A. White, Jay-How Yang, Yun Zhao, Mengning Liang, Andrew Aquila, Mark S. Hunter, Joseph S. Robinson, Jason E. Koglin, Sébastien Boutet, Petra Fromme, Anton Barty & Henry N. Chapman

Abstract: The three-dimensional structures of macromolecules and their complexes are mainly elucidated by X-ray protein crystallography. A major limitation of this method is access to high-quality crystals, which is necessary to ensure X-ray diffraction extends to sufficiently large scattering angles and hence yields information of sufficiently high resolution with which to solve the crystal structure. The observation that crystals with reduced unit-cell volumes and tighter macromolecular packing often produce higher-resolution Bragg peaks suggests that crystallographic resolution for some macromolecules may be limited not by their heterogeneity, but by a deviation of strict positional ordering of the crystalline lattice. Such displacements of molecules from the ideal lattice give rise to a continuous diffraction pattern that is equal to the incoherent sum of diffraction from rigid individual molecular complexes aligned along several discrete crystallographic orientations and that, consequently, contains more information than Bragg peaks alone. Although such continuous diffraction patterns have long been observed—and are of interest as a source of information about the dynamics of proteins4—they have not been used for structure determination. Here we show for crystals of the integral membrane protein complex photosystem II that lattice disorder increases the information content and the resolution of the diffraction pattern well beyond the 4.5-ångström limit of measurable Bragg peaks, which allows us to phase the pattern directly. Using the molecular envelope conventionally determined at 4.5 ångströms as a constraint, we obtain a static image of the photosystem II dimer at a resolution of 3.5 ångströms. This result shows that continuous diffraction can be used to overcome what have long been supposed to be the resolution limits of macromolecular crystallography, using a method that exploits commonly encountered imperfect crystals and enables modelfree phasing.

Continuous diffraction is seen as diffused streaks beyond the Bragg limit. This remarkable paper uses PSII as a model system to prove that the diffused diffraction obtained from microcrystals can be used to improve the resolution of structures solved by using Bragg peaks alone. This paper has been discussed greatly in chapter 3.

I took a lead role in sample preparation for this experiment by optimizing protein purification and crystallization. Since sample had to be handled in dark, I also performed sample loading and perfected conditions for highest hit-rate for maximum data collection.

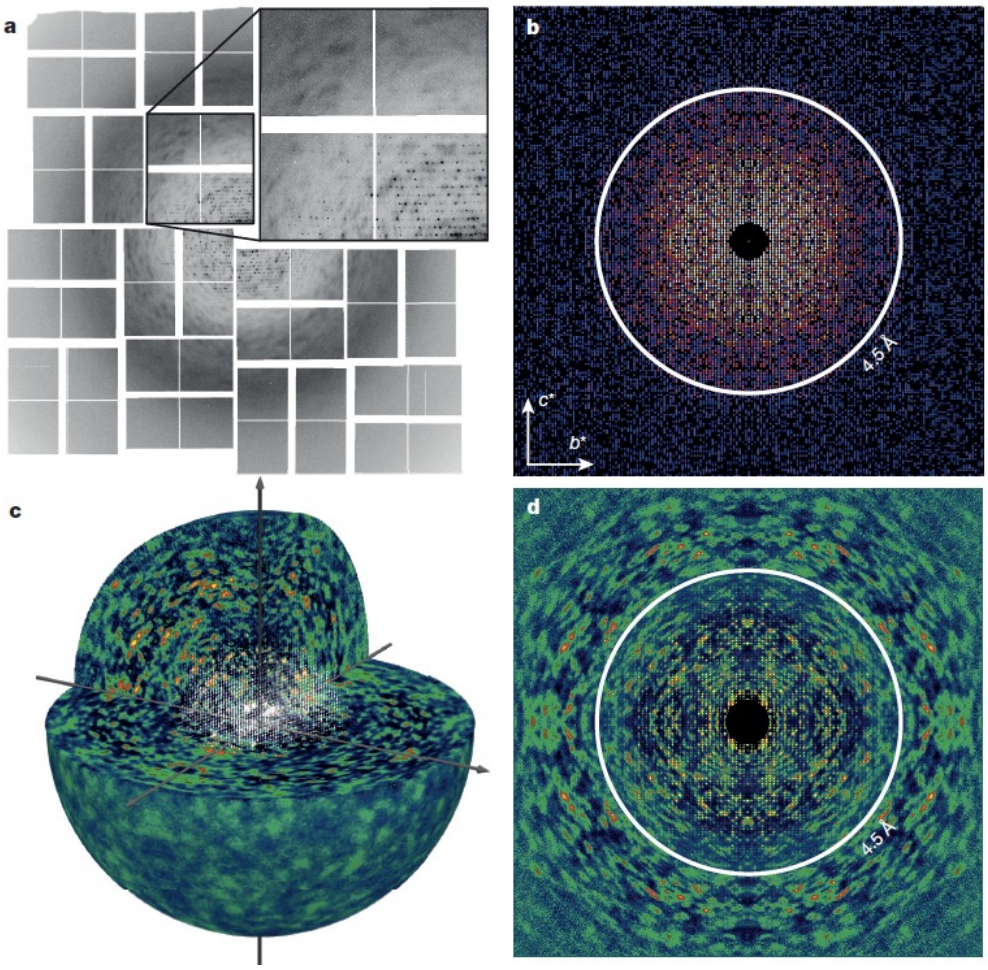

Figure 6.3: **Molecular coherent diffraction.**

a, An XFEL snapshot 'still' diffraction pattern of a PSII microcrystal shows a weak speckle structure beyond the extent of Bragg peaks, which is enhanced in this figure by limiting the displayed pixel values. b, Structure factors obtained from Bragg-peak counts from 25,585 still patterns, displayed as a precession-style pattern of the [001] zone axis. c, A rendering of the entire 3D diffraction volume assembled from the 2,848 strongest patterns. d, A central section of the diffraction volume in c normal to the [100] axis. Speckles are clearly observed beyond the 4.5-Å extent of Bragg diffraction (indicated by the white circles in b and d) to the edge of the detector.

6.1.4. Microfluidic sorting of protein nanocrystals by size for X-ray free-electron laser diffraction (Abdallah et al., 2015b)

(Struct. Dyn. 2, 041719 (2015))

Bahige G. Abdallah, Nadia A. Zatsepin, **Shatabdi Roy-Chowdhury**, Jesse Coe, Chelsie E. Conrad, Katerina D€corner, Raymond G. Sierra, Hilary P. Stevenson, Fernanda Camacho-Alanis, Thomas D. Grant, Garrett Nelson, Daniel James, Guillermo Calero, Rebekka M. Wachter, John C. H. Spence, Uwe Weierstall, Petra Fromme, and Alexandra Ros

Abstract: The advent and application of the X-ray free-electron laser (XFEL) has uncovered the structures of proteins that could not previously be solved using traditional crystallography. While this new technology is powerful, optimization of the process is still needed to improve data quality and analysis efficiency. One area is sample heterogeneity, where variations in crystal size (among other factors) lead to the requirement of large data sets (and thus 10–100 mg of protein) for determining accurate structure factors. To decrease sample dispersity, we developed a high-throughput microfluidic sorter operating on the principle of dielectrophoresis, whereby polydisperse particles can be transported into various fluid streams for size fractionation. Using this microsorter, we isolated several milliliters of photosystem I nanocrystal fractions ranging from 200 to 600 nm in size as characterized by dynamic light scattering, nanoparticle tracking, and electron microscopy. Sorted nanocrystals were delivered in a liquid jet via the gas dynamic virtual nozzle into the path of the XFEL at the Linac Coherent Light Source. We obtained diffraction to 4A° resolution, indicating that the small crystals were not damaged by the sorting process. We also observed the shape transforms of photosystem I nanocrystals, demonstrating that our device can optimize data collection for the shape transform-based phasing method. Using simulations, we show that narrow crystal size distributions can significantly improve merged data quality in serial crystallography. From this proof-of-concept work, we expect that the automated size-sorting of protein crystals will become an important step for sample production by reducing the amount of protein needed for a high quality final structure and the development of novel phasing methods that exploit inter-Bragg reflection intensities or use variations in beam intensity for radiation damage-induced phasing. This method will also permit an analysis of the dependence of crystal quality on crystal size.

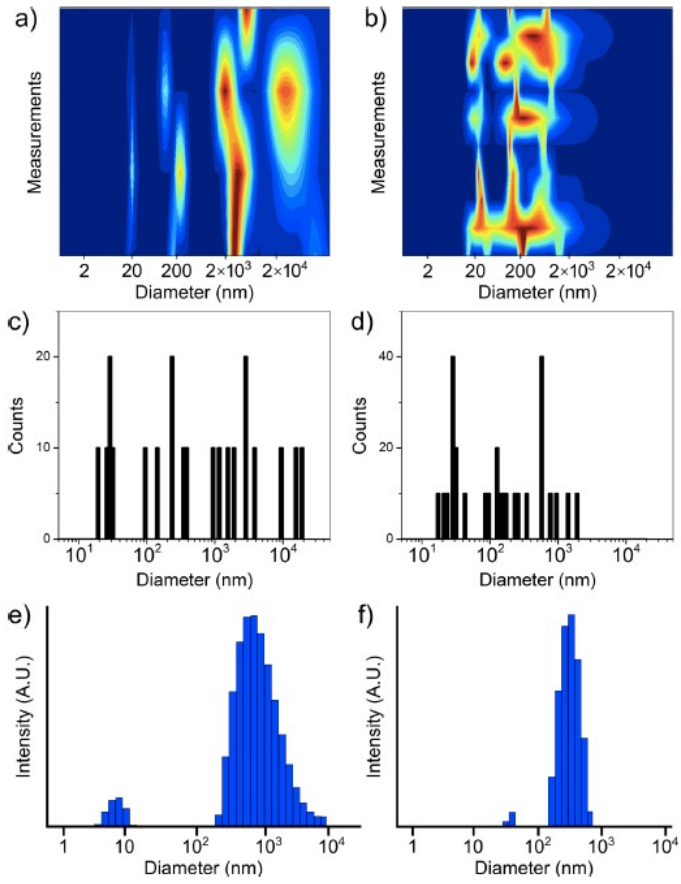

Figure 6.4: **DLS heat map of sorted vs unsorted crystals**

(a) the PSI crystal suspension prior to fractionation, indicating a wide size distribution (200nm to 20 mm), and (b) a PSI crystal fraction collected from the [S] channels indicating a narrowed submicron size distribution (200 nm to 600 nm). Signal increases from blue (lowest) to red (highest). (c) and (d) show DLS histograms corresponding to (a) and (b), respectively. (e) and (f) show DLS histograms of the PSI suspension prior to sorting (200 nm to 10 lm) and an [S] channel fraction (150 nm to 550 nm), respectively, measured using a cuvette-based instrument for comparison with (a)–(d), confirming the differences in the size distribution.

This article reports the further development and optimization of a microfluidic device for sorting nanocrystals for segregation by size using dielectrophoretic focusing with special focus on fast sorting speeds and high volume, to match the high sample consumption and flow rates required for SFX sample delivery. The fraction that was separated with the device showed a marked improvement in size homogeneity as seen in the histogram in figure 6.5, showing a size distribution between of between 150 and 550 nm reported with DLS and 125 to 300 nm measured with NTA compared to the unsorted size distribution of 150 nm to 10 µm measured with DLS. Data sets were collected on both sorted and non-sorted fractions of PSI crystals and these

were evaluated to ~4 Å, indicating no significant loss of resolution due to processing through the device.

My involvement was in isolation, purification and crystallization of PSI. I also performed optimization of on-site crystal concentration and sample delivery for SFX data collection.

6.1.5. Serial femtosecond crystallography of soluble proteins in lipidic cubic phase (Fromme et al., 2015)

(IUCrJ (2015). 2, 545–551)

Raimund Fromme, Andrii Ishchenko, Markus Metz, **Shatabdi Roy Chowdhury**, Shibom Basu, Se´bastien Boutet, Petra Fromme, Thomas A. White, Anton Barty, John C. H. Spence, Uwe Weierstall, Wei Liu and Vadim Cherezov

Abstract: Serial femtosecond crystallography (SFX) at X-ray free-electron lasers (XFELs) enables high-resolution protein structure determination using micrometre-sized crystals at room temperature with minimal effects from radiation damage. SFX requires a steady supply of microcrystals intersecting the XFEL beam at random orientations. An LCP–SFX method has recently been introduced in which microcrystals of membrane proteins are grown and delivered for SFX data collection inside a gel-like membrane-mimetic matrix, known as lipidic cubic phase (LCP), using a special LCP microextrusion injector. Here, it is demonstrated that LCP can also be used as a suitable carrier medium for microcrystals of soluble proteins, enabling a dramatic reduction in the amount of crystallized protein required for data collection compared with crystals delivered by liquid injectors. High-quality LCP–SFX data sets were collected for two soluble proteins, lysozyme and phycocyanin, using less than 0.1 mg of each protein.

Viscous gel injectors were developed for delivering sensitive GPCR microcrystals grown in LCP but since they ran at very low flow-rates (4-10 nL/min) the amount of sample required was extremely low. This publication discusses that making LCP in precipitant solution does not induce damage on soluble globular protein crystals. My contribution was in isolating, purifying and crystallizing PC while optimizing precipitate conditions in LCP. I also wrote the methods section of the manuscript that describes my contributions.

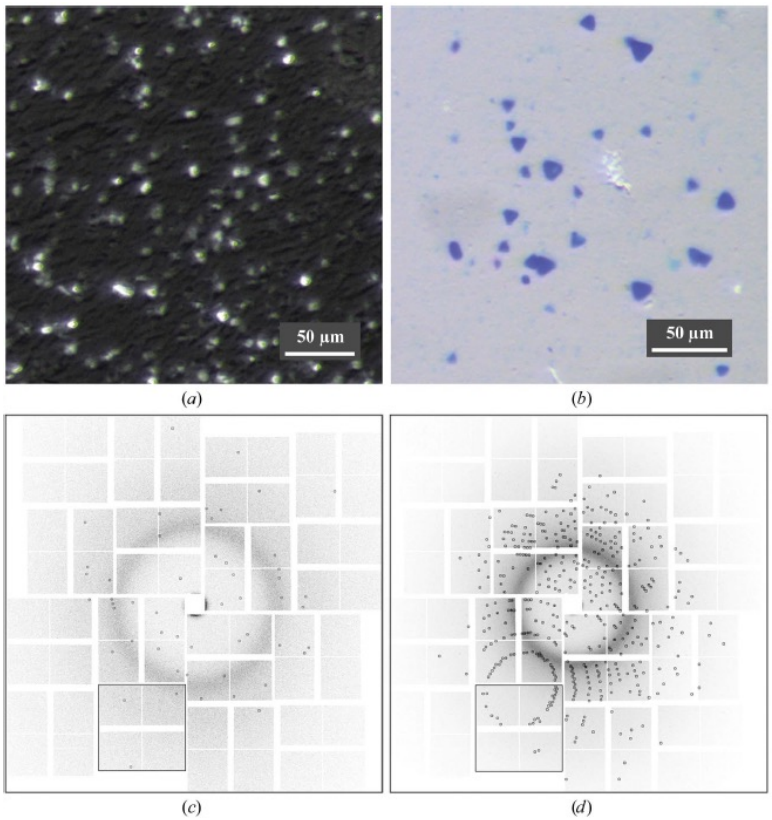

Figure 6.5: **Representative crystal images and diffraction patterns.**

(a, b) Pictures of crystals embedded in LCP for lysozyme (a) and PC (b). (c, d) Full diffraction patterns for lysozyme (c) and PC (d).

6.1.6. A novel inert crystal delivery medium for serial femtosecond crystallography (Conrad et al., 2015)

(IUCrJ (2015). 2, 421–430)

Chelsie E. Conrad, Shibom Basu, Daniel James, Dingjie Wang, Alexander Schaffer, **Shatabdi Roy-Chowdhury**, Nadia A. Zatsepin, Andrew Aquila, Jesse Coe, Cornelius Gati, Mark S. Hunter, Jason E. Koglin, Christopher Kupitz, Garrett Nelson, Ganesh Subramanian, Thomas A. White, Yun Zhao, James Zook, Se´bastien Boutet, Vadim Cherezov, John C. H. Spence, Raimund Fromme, Uwe Weierstall and Petra Fromme

Abstract: Serial femtosecond crystallography (SFX) has opened a new era in crystallography by permitting nearly damage-free, room-temperature structure determination of challenging proteins such as membrane proteins. In SFX, femtosecond

X-ray free-electron laser pulses produce diffraction snapshots from nanocrystals and microcrystals delivered in a liquid jet, which leads to high protein consumption. A slow-moving stream of agarose has been developed as a new crystal delivery medium for SFX. It has low background scattering, is compatible with both soluble and membrane proteins, and can deliver the protein crystals at a wide range of temperatures down to 4C. Using this crystalladen agarose stream, the structure of a multi-subunit complex, phycocyanin, was solved to 2.5 A ° resolution using 300 mg of microcrystals embedded into the agarose medium post-crystallization. The agarose delivery method reduces protein consumption by at least 100-fold and has the potential to be used for a diverse population of proteins, including membrane protein complexes.

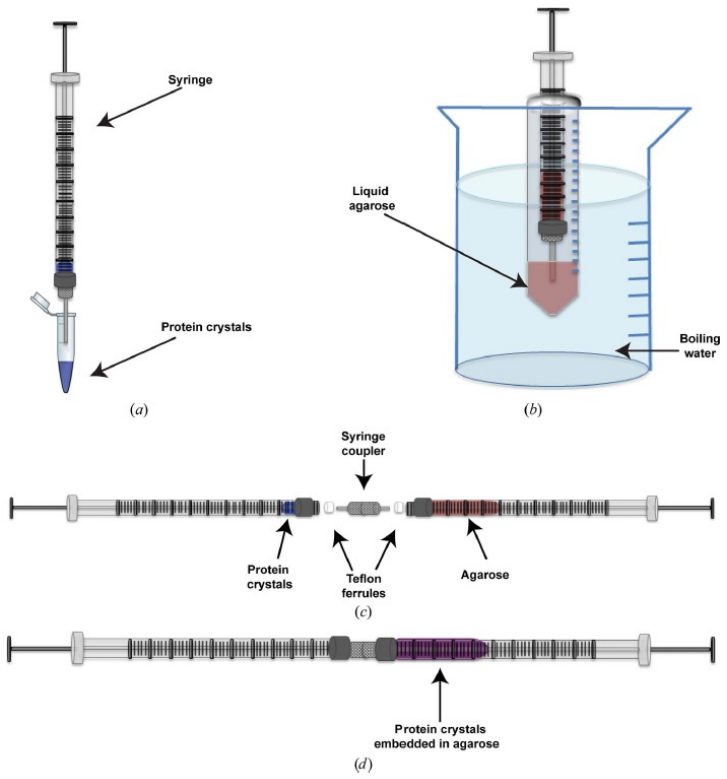

Figure 6.6: **Diagram showing how the crystals are embedded into the agarose medium.**

(a) A dense pellet of crystals is drawn up into a syringe, (b) the agarose solution (contained in a 15 ml centrifuge tube) is submerged in boiling water until the agarose dissolves, the liquid agarose is drawn up into a warmed syringe and the agarose is allowed to el and equilibrate to room temperature, (c) the protein crystals and agarose syringe are connected by a syringe coupler and (d) using the syringe coupler, the crystals are embedded throughout the agarose by moving the plungers back and forth.

The objective of this paper was to minimize sample consumption for SFX by mixing crystals in viscous medium. Low gelling agarose was tested and proven to work at XFEL and gave a lower background scattering than LCP. My contribution was in isolating, purifying and crystallizing PC while optimizing precipitate conditions for keeping crystals stable in agarose.

6.2. Method development for crystal optimization

6.2.1. Protein Crystallization in an Actuated Microfluidic Nanowell Device (Abdallah et al., 2016)

(Cryst Growth Des. 2016 ; 16(4): 2074–2082)

Bahige G. Abdallah, **Shatabdi Roy-Chowdhury**, Raimund Fromme, Petra Fromme and Alexandra Ros

Abstract: Protein crystallization is a major bottleneck of structure determination by X-ray crystallography, hampering the process by years in some cases. Numerous matrix screening trials using significant amounts of protein are often applied, while a systematic approach with phase diagram determination is prohibited for many proteins that can only be expressed in small amounts. Here, we demonstrate a microfluidic nanowell device implementing protein crystallization and phase diagram screening using nanoscale volumes of protein solution per trial. The device is made with cost-effective materials and is completely automated for efficient and economical experimentation. In the developed device, 170 trials can be realized with unique concentrations of protein and precipitant established by gradient generation and isolated by elastomeric valving for crystallization incubation. Moreover, this device can be further downscaled to smaller nanowell volumes and larger scale integration. The device was calibrated using a fluorescent dye and compared to a numerical model where concentrations of each trial can be quantified to establish crystallization phase diagrams. Using this device, we successfully crystallized lysozyme and Cphycocyanin, as visualized by compatible crystal imaging techniques such as bright-field microscopy, UV fluorescence, and second-order nonlinear imaging of chiral crystals. Concentrations yielding observed crystal formation were quantified and used to determine regions of the crystallization phase space for both proteins. Low sample consumption and compatibility with a variety of proteins and imaging techniques make this device a powerful tool for systematic crystallization studies.

For screening conditions for crystallization, a large number of parameters need to be altered. Microfluidic platforms not only provide an opportunity to tightly control

variable conditions in a versatile and economic way, but they also reduce sample consumption significantly. This article describes an automated microfluidic device that implemented batch-type crystallization condition screen using only 25 nL sample per well. The method is based on a gradient generator system that created many protein and precipitant screening conditions by splitting and recombining input solutions through an array of channels. The wells were separated by a 'doormat' valve and the material permitted protein crystallization along with the ability to visualize the droplets by brightfield microscopy, UV-fluorescence and SONICC.

The developed device exhibits >200 wells and generates 170 unique crystallization conditions (due to the outermost wells serving as a control containing only one of the components). The set-up successfully produced crystals of lysozyme using NaCl as the precipitant and microcrystals of PC were seen with PEG-3350.

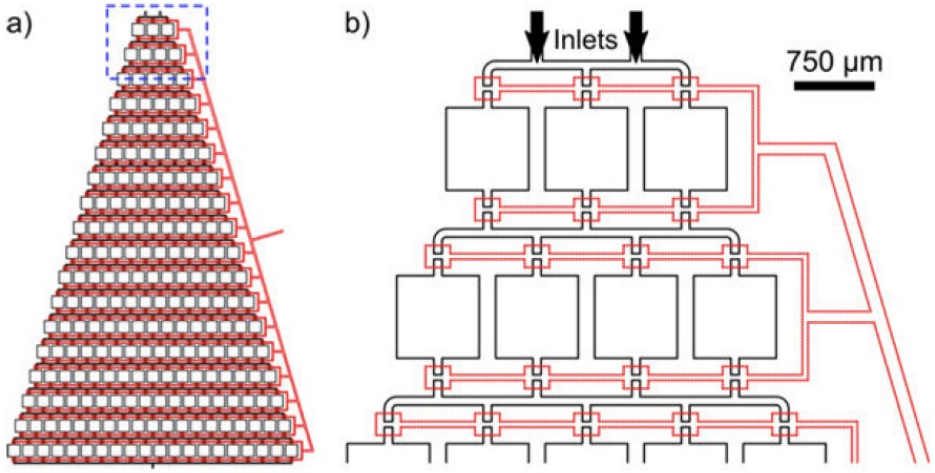

Figure 6.7: **Overview schematic of the nano-well gradient generator**

a) with incorporated "doormat" valve system (red dashes) showing 207 wells. (b) Zoom-in of the highlighted region in (a) detailing the "split and recombine" gradient generation design with incorporated valve system. Each well is isolated in the fluid layer and becomes connected by the overlapping valve region during the filling step.

My contribution in this experiment was isolation, purification, and establishing crystallization conditions for PC. I provided protein and precipitant at concentrations that were optimized for batch crystallization.

6.2.2. High Throughput Protein Nanocrystal Fractionation in a Microfluidic Sorter (Abdallah et al., 2015a)

(Anal. Chem. 2015, 87, 4159−4167)

Bahige G. Abdallah, **Shatabdi Roy-Chowdhury**, Jesse Coe, Petra Fromme, and Alexandra Ros

Abstract: Protein crystallography is transitioning into a new generation with the introduction of the X-ray free electron laser, which can be used to solve the structures of complex proteins via serial femtosecond crystallography. Sample characteristics play a critical role in successful implementation of this new technology, whereby a small, narrow protein crystal size distribution is desired to provide high quality diffraction data. To provide such a sample, we developed a microfluidic device that facilitates dielectrophoretic sorting of heterogeneous particle mixtures into various size fractions. The first generation device demonstrated great potential and success toward this endeavor; thus, in this work, we present a comprehensive optimization study to improve throughput and control over sorting outcomes. First, device geometry was designed considering a variety of criteria, and applied potentials were modeled to determine the

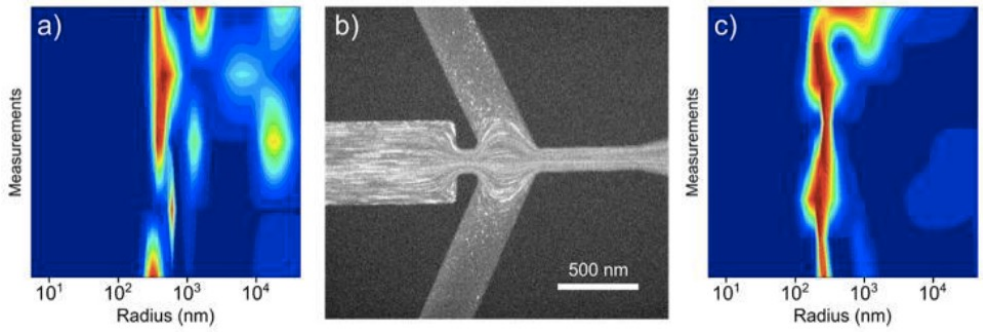

Figure 6.8: **Microfluidic sorter improves particle size distribution**

a) DLS heat map illustrating the broad size distribution (200 nm-20 μm) of bulk PSI suspension. b) Fluorescence microscopy image of crystals being sorted where large crystals are focused and small micrometer sized crystals are deflected and c) depicts DLS map of submicrometer fraction that depicts the effect of sorting.

scheme achieving the largest sorting efficiency for isolating nanoparticles from microparticles. Further, to investigate sorting efficiency within the nanoparticle regime, critical geometrical dimensions and input parameters were optimized to achieve high sorting efficiencies. Experiments revealed fractionation of nanobeads from microbeads in the optimized device with high sorting efficiencies, and protein crystals were sorted into submicrometer size fractions as desired for future serial femtosecond crystallography experiments.

This article reports on the development, characterization and testing of a novel microfluidic device designed to sort nanocrystals. The importance of size homogeneity and interesting properties of discrete crystals have been explained in previous chapters. The device described here aims to allow optimization of the homogeneity of the nanocrystal size post-crystallogenesis through a fractionation technique. The method used for crystal size segregation is based upon dielectrophoretic separation, utilizing inhomogeneities in an induced electric field within microfluidic channels that creates a flow profile that is sensitive to the size of the particle.

The modelled separation of nanocrystals was validated, showing sorting efficiencies of 91.6% and 93.8% for particle sizes of 500 nm and 2.5 μm respectively, as characterized by DLS and NTA. My contribution to this research was production of PSI nanocrystal sample as well as size characterization using DLS and NTA. I also contributed to the experiments conducted together with other authors and helped in editing the manuscript.

6.2.3. Microcrystallization techniques for serial femtosecond crystallography using photosystem II from Thermosynechococcus elongatus as a model system (C. Kupitz et al., 2014)

(Phil. Trans. R. Soc. B 369: 20130316)

Christopher Kupitz, Ingo Grotjohann, Chelsie E. Conrad, **Shatabdi Roy-Chowdhury**, Raimund Fromme and Petra Fromme

Abstract: Serial femtosecond crystallography (SFX) is a new emerging method, where X-ray diffraction data are collected from a fully hydrated stream of nano- or microcrystals of biomolecules in their mother liquor using high-energy, X-ray free-electron lasers. The success of SFX experiments strongly depends on the ability to grow large amounts of well-ordered nano/microcrystals of homogeneous size distribution. While methods to grow large single crystals have been extensively explored in the past, method developments to grow nano/ microcrystals in sufficient amounts for SFX experiments are still in their infancy. Here, we describe and compare three methods (batch, free interface diffusion (FID) and FID centrifugation) for growth of nano/microcrystals for time-resolved SFX experiments using the large membrane protein complex photosystem II as a model system.

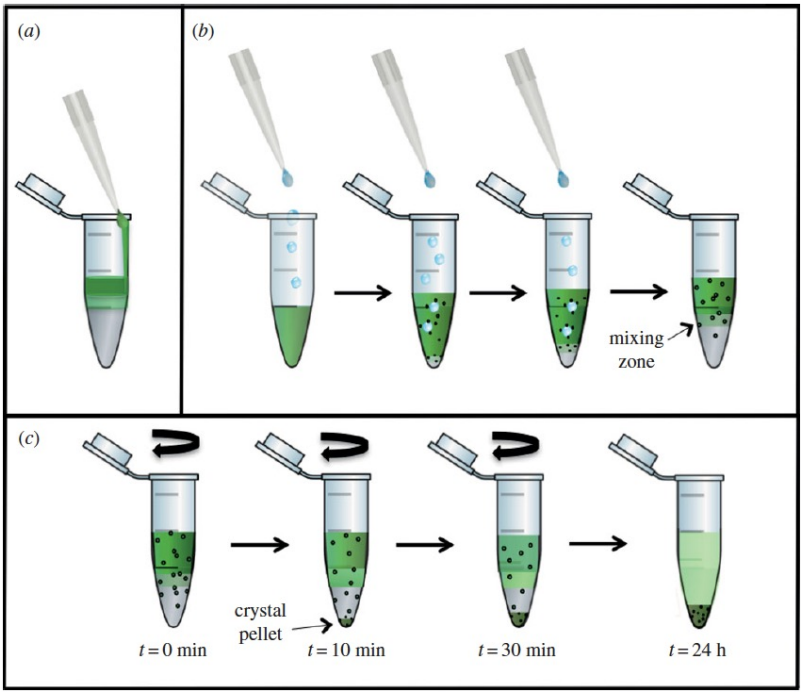

Figure 6.9: : **Schematic of the set-up for crystallization experiments**

with FID (a,b) and FID centrifugation (c). (a) Experimental set-up in which the protein solution is carefully layered on top of the precipitant solution, where only few crystals form at the interface. (b) In the inverse set-up the precipitant solution is added dropwise to the protein solution, inducing increased transient nucleation at the drop–protein interface. (c) The experiment shown in (b) is continued by centrifugation. The nuclei formed in the protein solution are accelerated by centrifugation towards the interface zone, where they grow into nano- or microcrystals. When they reach a specific size they sediment into the precipitant zone, where they stop growing. Thereby nano- or microcrystals with a very narrow size distribution can be achieved.

This article summarizes various methods available for growth of microcrystals for SFX. Batch method has been described in chapter 3, but free-interface diffusion (FID) has also worked well for 1-5 μm sized crystals. Using PSII as a model protein, many crystallization conditions were explored and some of them produced microcrystals.

My contribution here was isolation, purification and crystallization of PSII. I mainly contributed in established conditions for FID by centrifugation and wrote that section of the manuscript.

6.3. Time-resolved studies at X-ray free electron sources

6.3.1. Structural enzymology using X-ray free electron lasers (Kupitz et al., 2017)

(Struct. Dyn. 4, 044003 (2017))

Christopher Kupitz, Jose L. Olmos, Jr., Mark Holl, Lee Tremblay, Kanupriya Pande, Suraj Pandey, Dominik Oberth€ur, Mark Hunter, Mengning Liang, Andrew Aquila, Jason Tenboer, George Calvey, Andrea Katz, Yujie Chen, Max O. Wiedorn, Juraj Knoska, Alke Meents, Valerio Majriani, Tyler Norwood, Ishwor Poudyal, Thomas Grant, Mitchell D. Miller, Weijun Xu, Aleksandra Tolstikova, Andrew Morgan, Markus Metz, Jose M. Martin-Garcia, James D. Zook, **Shatabdi Roy-Chowdhury**, Jesse Coe, Nirupa Nagaratnam, Domingo Meza, Raimund Fromme, Shibom Basu, Matthias Frank, Thomas White, Anton Barty, Sasa Bajt, Oleksandr Yefanov, Henry N. Chapman, Nadia Zatsepin, Garrett Nelson, Uwe Weierstall, John Spence, Peter Schwander, Lois Pollack, Petra Fromme, Abbas Ourmazd, George N. Phillips, Jr., and Marius Schmidt

Abstract: Mix-and-inject serial crystallography (MISC) is a technique designed to image enzyme catalyzed reactions in which small protein crystals are mixed with a substrate just prior to being probed by an X-ray pulse. This approach offers several advantages over flow cell studies. It provides (i) room temperature structures at near atomic resolution, (ii) time resolution ranging from microseconds to seconds, and (iii) convenient reaction initiation. It outruns radiation damage by using femtosecond X-ray pulses allowing damage and chemistry to be separated. Here, we demonstrate that MISC is feasible at an X-ray free electron laser by studying the reaction of M. tuberculosis ß-lactamase microcrystals with ceftriaxone antibiotic solution. Electron density maps of the apo-ß lactamase and of the ceftriaxone bound form were obtained at 2.8A ° & 2.4A ° resolution, respectively. These

results pave the way to study cyclic and non-cyclic reactions and represent a new field of time-resolved structural dynamics for numerous substrate-triggered biological reactions.

This publication describes results from mix-and-inject TR-SFX on β-lactamase (BlaC) from *Mycobacterium tuberculosis* in both its apo form and in complex with the antibiotic ceftriaxone. This marks one of the first published diffusive mixing TR-SFX experiments.

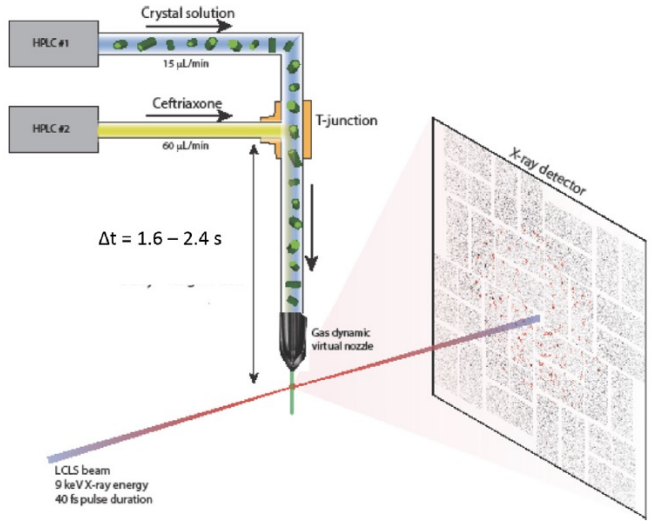

Figure 6.10: **Data collection schematic showing the T-junction set-up.**

This was used for a mixing time of about 2 s. The T-junction was placed outside of the nozzle rod in our experiment but could also be engineered to fit inside closer to the interaction region or shorter mixing times.

The tuberculosis causing bacteria *M. tuberculosis* is resistant to treatment with antibiotics due to the evolution of its BlaC protein which uses a serine residue to open the β-lactam ring via nucleophilic attack, rendering the antibiotic inactive. In order to combat this medicinally, clarity on the mechanism of this inactivation is needed and so visualization of the structures along the reaction timeline was desired. A T-junction was used to mix crystals with a 2-3 µm thickness with a solution of Ceftriaxone using a 15 µL/min flow rate of crystal slurry and a 60 µL/min with a time delay of ~2 sec, leading to steady state data collection (turnover rate had been measured to be 49 +/- 17/min). Structures of the apo (2.8 Å) and substrate bound (2.4 Å) enzyme were achieved from collection of 12,853 and 22,646 indexed diffraction patterns respectively. Difference

electron density maps exhibit strong evidence of successful diffusion into the binding pocket by Ceftriaxone. This provides a path forward for uncovering unknown intermediates at higher temporal resolution in the push for mechanistic understanding.

My contributions to this work included sample characterization and handling, establishing conditions for injection of crystal suspension and I took the lead in sample loading and delivery.

6.3.2. The room temperature crystal structure of a bacterial phytochrome determined by serial femtosecond crystallography (Edlund et al., 2016)

(Scientific Reports 6:35279 (2016))

Petra Edlund, Heikki Takala, Elin Claesson, Léocadie Henry, Robert Dods, Heli Lehtivuori, Matthijs Panman, Kanupriya Pande, Thomas White, Takanori Nakane, Oskar Berntsson, Emil Gustavsson, Petra Båth, Vaibhav Modi, **Shatabdi Roy-Chowdhury**, James Zook, Peter Berntsen, Suraj Pandey, Ishwor Poudyal, Jason Tenboer, Christopher Kupitz, Anton Barty, Petra Fromme, Jake D. Koralek, Tomoyuki Tanaka, John Spence, Mengning Liang, Mark S. Hunter, Sebastien Boutet, Eriko Nango, Keith Moffat, Gerrit Groenhof, Janne Ihalainen, Emina A. Stojković, Marius Schmidt & Sebastian Westenhoff

Abstract: Phytochromes are a family of photoreceptors that control light responses of plants, fungi and bacteria. A sequence of structural changes, which is not yet fully understood, leads to activation of an output domain. Time-resolved serial femtosecond crystallography (SFX) can potentially shine light on these conformational changes. Here we report the room temperature crystal structure of the chromophorebinding domains of the Deinococcus radiodurans phytochrome at 2.1 Å resolution. The structure was obtained by serial femtosecond X-ray crystallography from microcrystals at an X-ray free electron laser. We find overall good agreement compared to a crystal structure at 1.35 Å resolution derived from conventional crystallography at cryogenic temperatures, which we also report here. The thioether linkage between chromophore and protein is subject to positional ambiguity at the synchrotron, but is fully resolved with SFX. The study paves the way for time-resolved structural investigations of the phytochrome photocycle with time-resolved SFX.

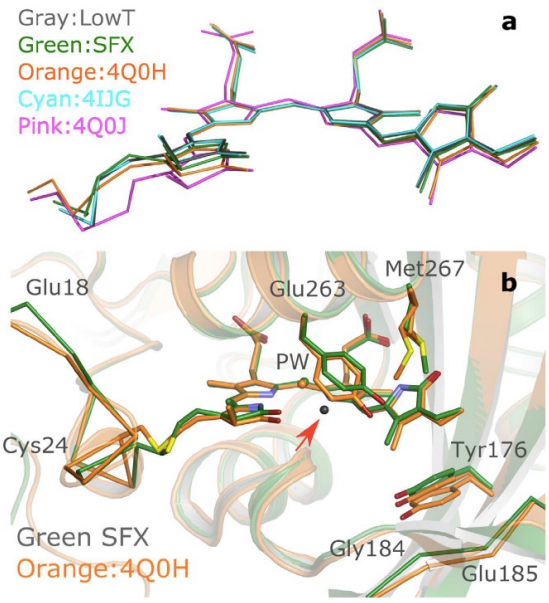

Figure 6.11: **Comparison of Cryo and SFX structures to earlier published PAS-GAF structures.**

a) Comparison of the biliverdin conformation and cystein24 thioether linkage of Cryo and SFX structures with previously reported structures. (b) Comparison of the SFX structure and 4Q0H[9] PAS-GAF-structures reveals differences in the D- and A-ring orientation, the thioether linkage and the positions of Tyr263, Met267, Tyr173 and the residues 17–25 and 184–186. The grey water (marked by red arrow) is only observable in the Cryo structure

Phytochromes indirectly control light-dependent metabolic pathways in various organisms. This article compares structures of in a new crystal form of the wild-type phytochrome PAS-GAF domains from *D. radiodurans* solved using cryogenic conditions (1.35 A) and at XFELs SACLA (2.5 A) and LCLS (2.2 A). Apart from a few differences, the chromophore shows identical conformation in all structures, as confirmed using composite omit maps.

I took a lead role in sample loading and sample delivery in limited light conditions at LCLS. I also helped the lead authors in finding ideal conditions for crystal crushing and optimized crystal density and size for delivery by GDVN.

6.3.3. Femtosecond structural dynamics drives the trans/cis isomerization in photoactive yellow protein (Pande et al., 2016)

(Science VOL 352 ISSUE 6286 2016)

Kanupriya Pande, Christopher D. M. Hutchison, Gerrit Groenhof, Andy Aquila, Josef S. Robinson, Jason Tenboer, Shibom Basu, Sébastien Boutet, Daniel P. DePonte, Mengning Liang, Thomas A. White, Nadia A. Zatsepin, Oleksandr Yefanov, Dmitry Morozov, Dominik Oberthuer, Cornelius Gati, Ganesh Subramanian, Daniel James, Yun Zhao, Jake Koralek, Jennifer Brayshaw, Christopher Kupitz, Chelsie Conrad, **Shatabdi Roy-Chowdhury**, Jesse D. Coe, Markus Metz, Paulraj Lourdu Xavier, Thomas D. Grant, Jason E. Koglin, Gihan Ketawala, Raimund Fromme, Vukica Šrajer, Robert Henning, John C. H. Spence, Abbas Ourmazd, Peter Schwander, Uwe Weierstall, Matthias Frank, Petra Fromme, Anton Barty, Henry N. Chapman, Keith Moffat, Jasper J. van Thor, Marius Schmidt

Abstract: A variety of organisms have evolved mechanisms to detect and respond to light, in which the response is mediated by protein structural changes after photon absorption. The initial step is often the photoisomerization of a conjugated chromophore. Isomerization occurs on ultrafast time scales and is substantially influenced by the chromophore environment. Here we identify structural changes associated with the earliest steps in the trans-to-cis isomerization of the chromophore in photoactive yellow protein. Femtosecond hard x-ray pulses emitted by the Linac Coherent Light Source were used to conduct time-resolved serial femtosecond crystallography on photoactive yellow protein microcrystals over a time range from 100 femtoseconds to 3 picoseconds to determine the structural dynamics of the photoisomerization reaction.

This article presents further research on PYP using TR-SFX, pushing temporal limits to visualize the trans/cis isomerization occurring on the femtosecond timescale. Further study based on results obtained and reported in Tenboer, Basu et al. (2014), section 6.3.5., TR-SFX was performed on PYP with time points including dark and 200 ns controls, 3 ps, and sub-ps time points spanning from 100-1000 fs. The sub-ps data sets represent the shortest and most highly resolved time points ever obtained using crystallography.

All sub ps pulses were measured using estimated 300 fs and 600 fs time delays and data were binned post collection by their time stamps. A 200 ns time delay was used as a positive control to compare with previously measured 1 μs data (Pande, Hutchinson et al. 2015) in order to quantify initiation yield from the pump laser. This successfully showed a consistent ratio of pR_1 and pR_2 states expected at this point along the reaction timeline, with a calculated reaction initiation of 12.6%. This value is lower than the previous 40% reported in Tenboer, Basu et al. (2014) due to the need for a fs pump vs. a ns pump. Whereas ns pulses allow for secondary initiations to occur to molecules that have backreacted to the ground state post initial excitation, fs pulses are faster than the

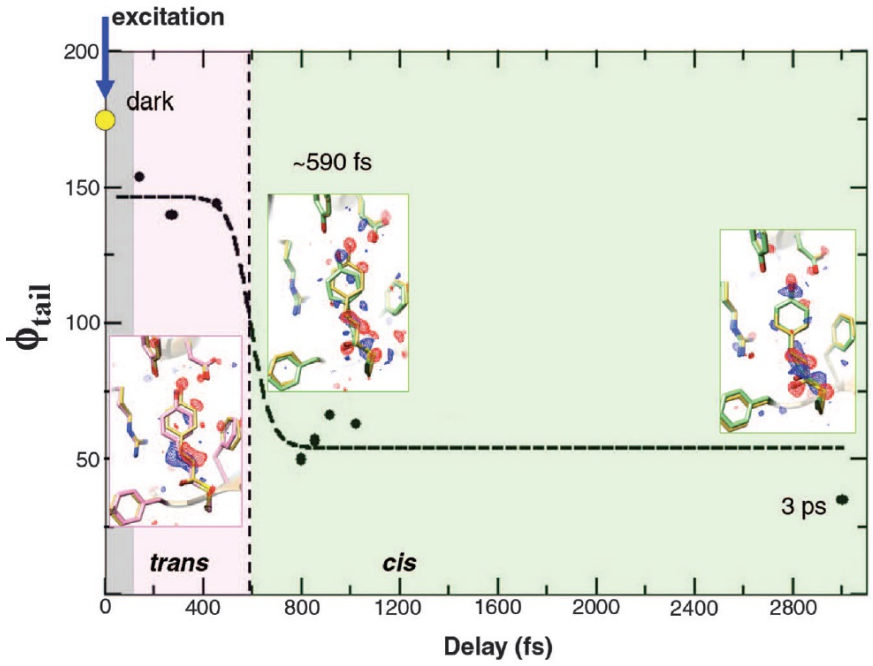

Figure 6.12: **Chromophore tail torsional angle dynamics.**

Pink: twisted trans on excited state PES; light green: cis on ground state PES. Torsional angle f_{tail} (solid spheres) is from structural refinement at various delays. Gray region: not time-resolved. Dashed line: fit with eq. S2, with a transition time of about 590 fs. Insets: structures of PYP_{fast} (pink), PYP_{slow}, and PYP_{3ps} (light green), and dark-state structure PYP_{ref} in yellow. Difference electron density is shown in red (–3s) and blue (3s).

time scale for an initially excited molecule to revert to the ground state, precluding the chance for a second excitation event.

Through a theoretical and spectroscopically supported conical intersection of excited state and ground state potential energy surfaces, the 550 fs observed timing of the isomerization of the chromophore is in good agreement with previous studies on the photoactivated dynamics of PYP. My contributions to this project included crystallization and characterization prior to and during beamtime as well as taking a lead role in sample loading and delivery during the experiment.

6.3.4. Crystal structure of rhodopsin bound to arrestin by femtosecond X-ray laser (Kang et al., 2015)

(Nature 523 (561-567) 2015)

Yanyong Kang, X. Edward Zhou, Xiang Gao, Yuanzheng He, Wei Liu, Andrii Ishchenko, Anton Barty, Thomas A. White, Oleksandr Yefanov, Gye Won Han, Qingping Xu, Parker W. de Waal, Jiyuan Ke, M. H. Eileen Tan, Chenghai Zhang, Arne Moeller, Graham M. West, Bruce D. Pascal, Ned Van Eps, Lydia N. Caro, Sergey A. Vishnivetskiy, Regina J. Lee, Kelly M. Suino-Powell, Xin Gu, Kuntal Pal, Jinming Ma, Xiaoyong Zhi, Se´bastien Boutet, Garth J. Williams, Marc Messerschmidt, Cornelius Gati, Nadia A. Zatsepin, Dingjie Wang, Daniel James, Shibom Basu, **Shatabdi Roy-Chowdhury**, Chelsie E. Conrad, Jesse Coe, Haiguang Liu, Stella Lisova, Christopher Kupitz, Ingo Grotjohann, Raimund Fromme, Yi Jiang, Minjia Tan, Huaiyu Yang, Jun Li, MeitianWang, Zhong Zheng, Dianfan Li, Nicole Howe, Yingming Zhao, Jo¨rg Standfuss, Kay Diederichs, Yuhui Dong, Clinton S. Potter, Bridget Carragher, Martin Caffrey, Hualiang Jiang, Henry N. Chapman, John C. H. Spence, Petra Fromme, Uwe Weierstall, Oliver P. Ernst, Vsevolod Katritch, Vsevolod V. Gurevich, Patrick R. Griffin, Wayne L. Hubbell, Raymond C. Stevens, Vadim Cherezov, Karsten Melcher & H. Eric Xu

Abstract: G-protein-coupled receptors (GPCRs) signal primarily through G-proteins or arrestins. Arrestin binding to GPCRs blocks G-protein interaction and redirects signaling to numerous G-protein-independent pathways. Here we report the crystal structure of a constitutively active form of human rhodopsin bound to a pre-activated form of the mouse visual arrestin, determined by serial femtosecond X-ray laser crystallography. Together with extensive biochemical and mutagenesis data, the structure reveals an overall architecture of the rhodopsin–arrestin assembly in which rhodopsin uses distinct structural elements, including transmembrane helix 7 and helix 8, to recruit arrestin. Correspondingly, arrestin adopts the pre-activated conformation, with a 206 rotation between the amino and carboxy domains, which opens up a cleft in arrestin to accommodate a short helix formed by the second intracellular loop of rhodopsin. This

structure provides a basis for understanding GPCR-mediated arrestin-biased signaling and demonstrates the power of X-ray lasers for advancing the frontiers of structural biology.

This article reports a breakthrough in structural biology of GPCRs with the rhodopsin-arrestin complex representing the first structure of any GPCR bound to arrestin. This work provided the first detailed structural insights into the molecular basis behind signaling in the largest family of cell surface receptors. It has a huge impact and is also of significant pharmacological interest as currently one third of all clinical drugs are targeted to GPCRs. In addition, the publication also includes a variety of biophysical techniques that were combined to provide proof that the structure represents the functionally active complex in a conformation similar to the native complex in the living cell.

The combination of the structure and the biophysical and functional studies provided a deep insight into intracellular signaling in arrestin pathways. With these results, evidence for the mechanisms behind both arrestin recruitment and activation was revealed. As rhodopsin serves as a model for many GPCRs, these findings represent a significant advance within the field with significant implications for the future of many pharmaceuticals.

My contributions towards this project consisted of characterization of nanocrystals, including on site analysis at LCLS, testing and preparing sample delivery injectors and loading sample for sample delivery.

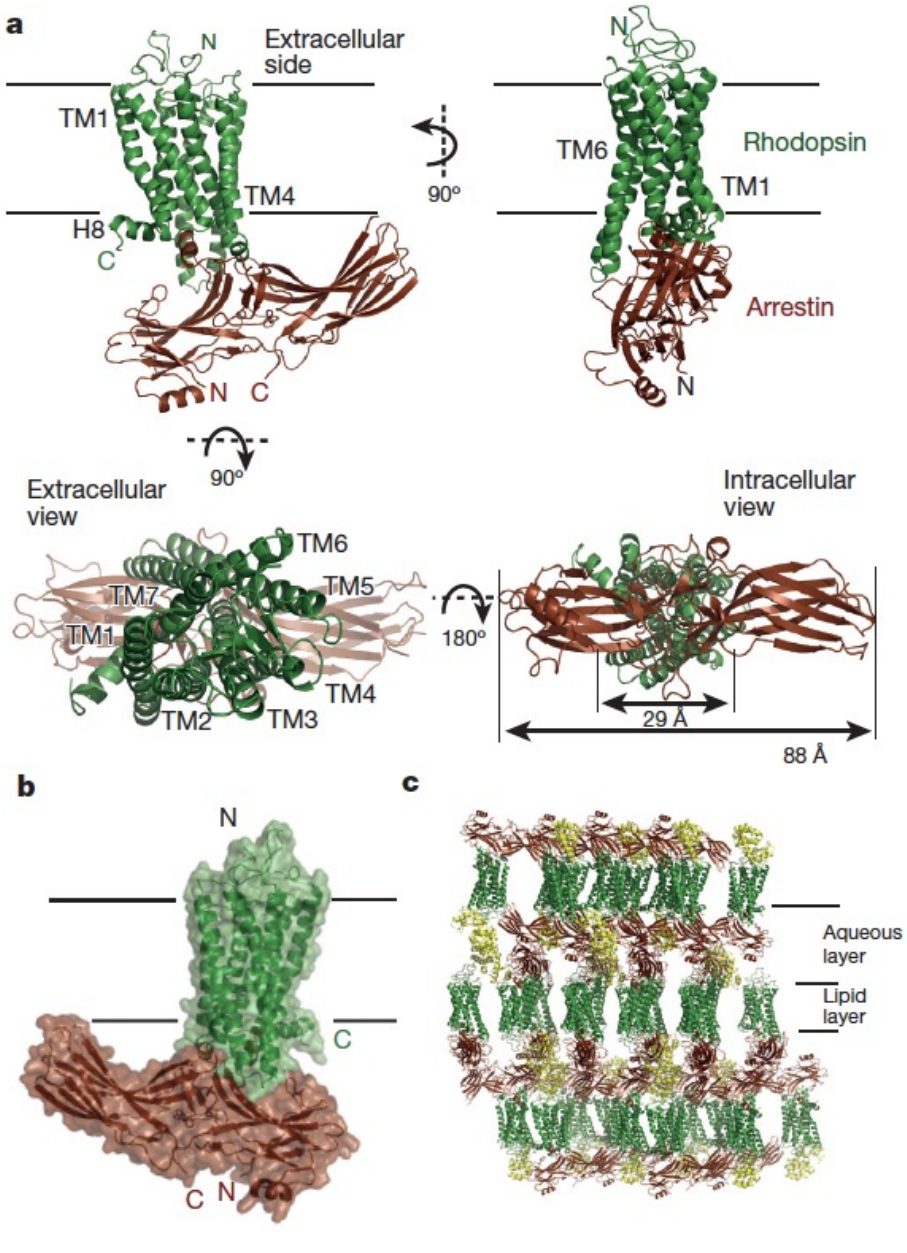

Figure 6.13: **The structure of the rhodopsin–arrestin complex**

a, The structure of the rhodopsin–arrestin complex in four orientations. The relative dimensions of rhodopsin and arrestin are shown in the intracellular view. TM1–TM7 indicates rhodopsin transmembrane helices 1–7; H8 is intracellular helix 8. b, An overall view of the rhodopsin–arrestin complex shown with transparent solid surface. T4 lysozyme (T4L) is omitted from this view. c, Crystal packing diagram of the rhodopsin–arrestin complex with T4L as yellow ribbon model.

6.3.5. Time-resolved serial crystallography captures high-resolution intermediates of photoactive yellow protein (Tenboer et al., 2014)

(Science VOL 346 ISSUE 6214 2014)

Jason Tenboer, Shibom Basu, Nadia Zatsepin, Kanupriya Pande, Despina Milathianaki, Matthias Frank, Mark Hunter, Sébastien Boutet, Garth J. Williams, Jason E. Koglin, Dominik Oberthuer, Michael Heymann, Christopher Kupitz, Chelsie Conrad, Jesse Coe, **Shatabdi Roy-Chowdhury**, Uwe Weierstall, Daniel James, Dingjie Wang, Thomas Grant, Anton Barty, Oleksandr Yefanov, Jennifer Scales, Cornelius Gati, Carolin Seuring, Vukica Srajer, Robert Henning, Peter Schwander, Raimund Fromme, Abbas Ourmazd, Keith Moffat, Jasper J. Van Thor, John C. H. Spence, Petra Fromme, Henry N. Chapman, Marius Schmidt

Abstract: Serial femtosecond crystallography using ultrashort pulses from x-ray free electron lasers (XFELs) enables studies of the light-triggered dynamics of biomolecules.We usedmicrocrystals of photoactive yellow protein (a bacterial blue light photoreceptor) as a model system and obtained high-resolution, time-resolved difference electron density maps of excellent quality with strong features; these allowed the determination of structures of reaction intermediates to a resolution of 1.6 angstroms. Our results open the way to the study of reversible and nonreversible biological reactions on time scales as short as femtoseconds under conditions that maximize the extent of reaction initiation throughout the crystal.

In these experiments, pump-probe TR-SFX was performed on the photoactive yellow protein (PYP), marking the first high resolution TR-SFX structures reported at 1.6 Å at time points of 10 ns and 1 μs in addition to the dark state. This allowed for a proof of principle to be made for pump-probe TR-SFX as the I_T, I_{CT}, pR_1 and pR_2 states of the PYP photocycle represented within these time points have been previously elucidated using the Laue method at 32 ns and 1 μs photoactivation time delays respectively.

Figure 6.14 shows a comparison of the structures obtained from the dark, ns and μs time points from both XFEL and Laue data. In addition to validation of previous results, new structural changes were found after refinement of the 1 μs TR-SFX time point as the higher % populations obtained from microcrystal set-up allowed much stronger features in the difference electron density maps, lending to more readily interpretable data.

My contributions toward this project were development of initial crystallization conditions, sample characterization, handling and taking a lead role in sample loading for delivery by GDVN.

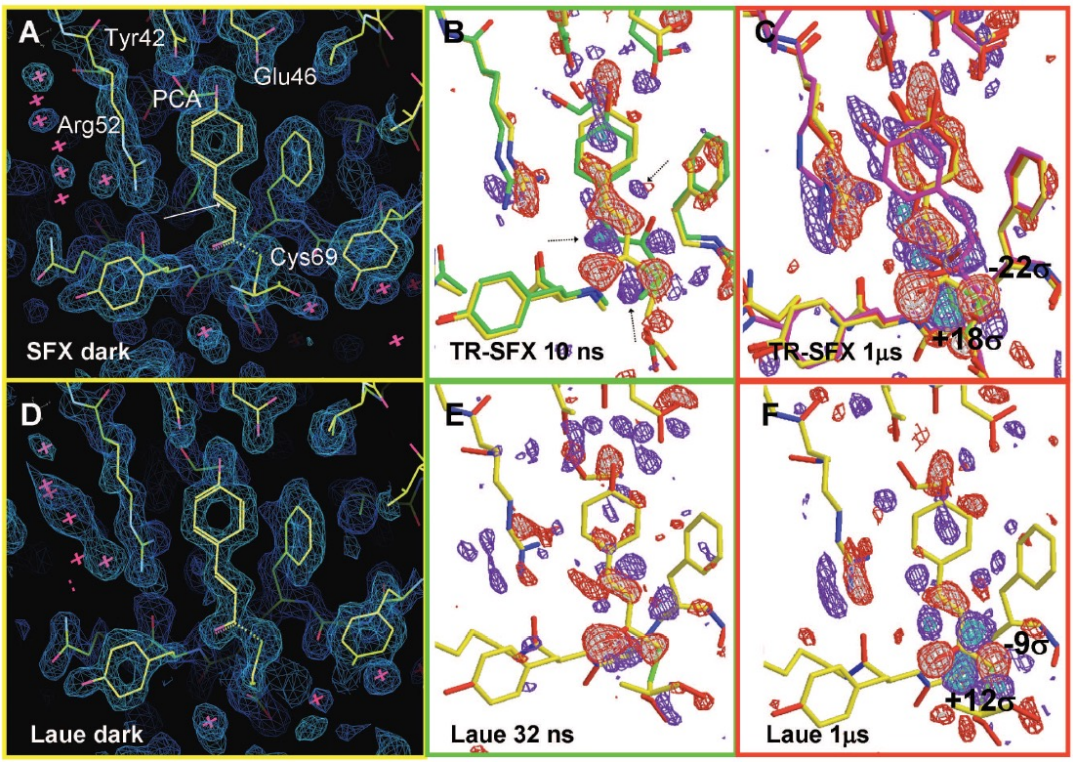

Figure 6.14: **Comparison of electron density and DED maps in the chromophore**

The dark state is shown in yellow in all maps. (A and D) Electron density maps for the PYP dark state obtained with TR-SFX and Laue, respectively (contour level 1.1s, 1.6 Å resolution).The PCA chromophore and nearby residues are marked in (A). Arrow: Double bond in the chromophore about which isomerization occurs. (B) TR-SFX DED map at 10 ns. (C) TR-SFX DED map at 1 ms. Pink and red structures: structures of pR_1 and pR_2 intermediates, respectively. (E) Laue 32-ns DED map correlates best to the TR-SFX 10-ns map. (F) Laue 1-ms DED map.

6.3.6. Serial time-resolved crystallography of photosystem II using a femtosecond X-ray laser (Kupitz et al., 2014)

(Nature 513 (261-265) 2014)

Christopher Kupitz, Shibom Basu, Ingo Grotjohann, Raimund Fromme, Nadia A. Zatsepin, Kimberly N. Rendek, Mark S. Hunter, Robert L. Shoeman, Thomas A. White, Dingjie Wang, Daniel James, Jay-How Yang, Danielle E. Cobb, Brenda Reeder, Raymond G. Sierra, Haiguang Liu, Anton Barty, Andrew L. Aquila, Daniel Deponte, Richard A. Kirian, Sadia Bari, Jesse J. Bergkamp, Kenneth R. Beyerlein, Michael J. Bogan, Carl

Caleman, Tzu-Chiao Chao, Chelsie E. Conrad, Katherine M. Davis, Holger Fleckenstein, Lorenzo Galli, Stefan P. Hau-Riege, Stephan Kassemeyer, Hartawan Laksmono, Mengning Liang, Lukas Lomb, Stefano Marchesini, Andrew V. Martin, Marc Messerschmidt, Despina Milathianaki, Karol Nass, Alexandra Ros, **Shatabdi Roy-Chowdhury**, Kevin Schmidt, Marvin Seibert, Jan Steinbrener, Francesco Stellato, Lifen Yan, Chunhong Yoon, Thomas A. Moore, Ana L. Moore, Yulia Pushkar, Garth J.Williams, Se´bastien Boutet, R. Bruce Doak, Uwe Weierstall, Matthias Frank, Henry N. Chapman, John C. H. Spence & Petra Fromme

Abstract: Photosynthesis, a process catalysed by plants, algae and cyanobacteria converts sunlight to energy thus sustaining all higher life on Earth. Two large membrane protein complexes, photosystem I and II (PSI and PSII), act in series to catalyse the light-driven reactions in photosynthesis.PSII catalyses the light-driven water splitting process, which maintains the Earth's oxygenic atmosphere1. In this process, the oxygen-evolving complex (OEC) of PSII cycles through five states, S0 to S4, in which four electrons are sequentially extracted from the OEC in four light-driven charge-separation events. Here we describe time resolved experiments on PSII nano/microcrystals from Thermosynechococcus elongatus performed with the recently developed technique of serial femtosecond crystallography. Structures have been determined fromPSII in the dark S1 state and after double laser excitation (putative S3 state) at 5 and 5.5A˚ resolution, respectively. The results provide evidence that PSII undergoes significant conformational changes at the electron acceptor side and at the Mn4CaO5 core of the OEC. These include an elongation of the metal cluster, accompanied by changes in the protein environment,which could allow for binding of the second substrate water molecule between themo-redistant protruding Mn(referred to as the 'dangler'Mn) and the Mn3CaOx cubane in the S2 to S3 transition, as predicted by spectroscopic and computational studies. This work shows the great potential for time-resolved serial femtosecond crystallography for investigation of catalytic processes in biomolecules.

This article discusses changes in OEC upon 2-flash light excitation. This work has been described in Chapter 2 & 3. My contribution was in isolating, purifying and crystallizing PSII for characterization via EPR. I also edited the main text & supplementary document for submission.

6.4. Review article

6.4.1. Serial femtosecond crystallography: A revolution in structural biology (Martin-Garcia et al., 2016)

(Archives of Biochemistry and Biophysics 602 (2016) 32e47)

Jose M. Martin-Garcia, Chelsie E. Conrad, Jesse Coe, **Shatabdi Roy-Chowdhury** and Petra Fromme

Abstract: Macromolecular crystallography at synchrotron sources has proven to be the most influential method within structural biology, producing thousands of structures since its inception. While its utility has been instrumental in progressing our knowledge of structures of molecules, it suffers from limitations such as the need for large, well-diffracting crystals, and radiation damage that can hamper native structural determination. The recent advent of X-ray free electron lasers (XFELs) and their implementation in the emerging field of serial femtosecond crystallography (SFX) has given rise to a remarkable expansion upon existing crystallographic constraints, allowing structural biologists access to previously restricted scientific territory. SFX relies on exceptionally brilliant, micro-focused X-ray pulses, which are femtoseconds in duration, to probe nano/micrometer sized crystals in a serial fashion. This results in data sets comprised of individual snapshots, each capturing Bragg diffraction of single crystals in random orientations prior to their subsequent destruction. Thus structural elucidation while avoiding radiation damage, even at room temperature, can now be achieved. This emerging field has cultivated new methods for nanocrystallogenesis, sample delivery, and data processing. Opportunities and challenges within SFX are reviewed herein.

This article discusses various aspects involved in SFX at XFELs and highlights the success stories. I contributed in writing sections of the nano-crystallization and TR-SFX sections. Additionally, I did overall editing and incorporated referee comments in the manuscript before re-submission.

REFERENCES

Abdallah, B.G., Roy-Chowdhury, S., Coe, J., Fromme, P., Ros, A., 2015a. High Throughput Protein Nanocrystal Fractionation in a Microfluidic Sorter. Analytical Chemistry 87, 4159–4167. https://doi.org/10.1021/acs.analchem.5b00589

Abdallah, B.G., Roy-Chowdhury, S., Fromme, R., Fromme, P., Ros, A., 2016. Protein Crystallization in an Actuated Microfluidic Nanowell Device. Crystal Growth & Design 16, 2074–2082. https://doi.org/10.1021/acs.cgd.5b01748

Abdallah, B.G., Zatsepin, N.A., Roy-Chowdhury, S., Coe, J., Conrad, C.E., Dörner, K., Sierra, R.G., Stevenson, H.P., Camacho-Alanis, F., Grant, T.D., Nelson, G., James, D., Calero, G., Wachter, R.M., Spence, J.C.H., Weierstall, U., Fromme, P., Ros, A., 2015b. Microfluidic sorting of protein nanocrystals by size for X-ray free-electron laser diffraction. Structural Dynamics 2, 041719. https://doi.org/10.1063/1.4928688

Awel, S., Kirian, R.A., Wiedorn, M.O., Beyerlein, K.R., Roth, N., Horke, D.A., Oberthür, D., Knoska, J., Mariani, V., Morgan, A., Adriano, L., Tolstikova, A., Xavier, P.L., Yefanov, O., Aquila, A., Barty, A., Roy-Chowdhury, S., Hunter, M.S., James, D., Robinson, J.S., Weierstall, U., Rode, A.V., Bajt, S., Küpper, J., Chapman, H.N., 2018. Femtosecond X-ray diffraction from an aerosolized beam of protein nanocrystals. Journal of Applied Crystallography 51, 133–139. https://doi.org/10.1107/S1600576717018131

Ayyer, K., Yefanov, O.M., Oberthür, D., Roy-Chowdhury, S., Galli, L., Mariani, V., Basu, S., Coe, J., Conrad, C.E., Fromme, R., Schaffer, A., Dörner, K., James, D., Kupitz, C., Metz, M., Nelson, G., Xavier, P.L., Beyerlein, K.R., Schmidt, M., Sarrou, I., Spence, J.C.H., Weierstall, U., White, T.A., Yang, J.-H., Zhao, Y., Liang, M., Aquila, A., Hunter, M.S., Robinson, J.S., Koglin, J.E., Boutet, S., Fromme, P., Barty, A., Chapman, H.N., 2016. Macromolecular diffractive imaging using imperfect crystals. Nature 530, 202–206. https://doi.org/10.1038/nature16949

Conrad, C.E., Basu, S., James, D., Wang, D., Schaffer, A., Roy-Chowdhury, S., Zatsepin, N.A., Aquila, A., Coe, J., Gati, C., Hunter, M.S., Koglin, J.E., Kupitz, C., Nelson, G., Subramanian, G., White, T.A., Zhao, Y., Zook, J., Boutet, S., Cherezov, V., Spence, J.C.H., Fromme, R., Weierstall, U., Fromme, P., 2015. A novel inert crystal delivery medium for serial femtosecond crystallography. IUCrJ 2, 421–430. https://doi.org/10.1107/S2052252515009811

Edlund, P., Takala, H., Claesson, E., Henry, L., Dods, R., Lehtivuori, H., Panman, M., Pande, K., White, T., Nakane, T., Berntsson, O., Gustavsson, E., Båth, P., Modi, V., Roy-Chowdhury, S., Zook, J., Berntsen, P., Pandey, S., Poudyal, I., Tenboer, J., Kupitz, C., Barty, A., Fromme, P., Koralek, J.D., Tanaka, T., Spence, J., Liang, M., Hunter, M.S., Boutet, S., Nango, E., Moffat, K., Groenhof, G., Ihalainen, J.,

Stojković, E.A., Schmidt, M., Westenhoff, S., 2016. The room temperature crystal structure of a bacterial phytochrome determined by serial femtosecond crystallography. Scientific Reports 6. https://doi.org/10.1038/srep35279

Fromme, R., Ishchenko, A., Metz, M., Chowdhury, S.R., Basu, S., Boutet, S., Fromme, P., White, T.A., Barty, A., Spence, J.C.H., Weierstall, U., Liu, W., Cherezov, V., 2015. Serial femtosecond crystallography of soluble proteins in lipidic cubic phase. IUCrJ 2, 545–551. https://doi.org/10.1107/S2052252515013160

Kang, Y., Zhou, X.E., Gao, X., He, Y., Liu, W., Ishchenko, A., Barty, A., White, T.A., Yefanov, O., Han, G.W., Xu, Q., de Waal, P.W., Ke, J., Tan, M.H.E., Zhang, C., Moeller, A., West, G.M., Pascal, B.D., Van Eps, N., Caro, L.N., Vishnivetskiy, S.A., Lee, R.J., Suino-Powell, K.M., Gu, X., Pal, K., Ma, J., Zhi, X., Boutet, S., Williams, G.J., Messerschmidt, M., Gati, C., Zatsepin, N.A., Wang, D., James, D., Basu, S., Roy-Chowdhury, S., Conrad, C.E., Coe, J., Liu, H., Lisova, S., Kupitz, C., Grotjohann, I., Fromme, R., Jiang, Y., Tan, M., Yang, H., Li, J., Wang, M., Zheng, Z., Li, D., Howe, N., Zhao, Y., Standfuss, J., Diederichs, K., Dong, Y., Potter, C.S., Carragher, B., Caffrey, M., Jiang, H., Chapman, H.N., Spence, J.C.H., Fromme, P., Weierstall, U., Ernst, O.P., Katritch, V., Gurevich, V.V., Griffin, P.R., Hubbell, W.L., Stevens, R.C., Cherezov, V., Melcher, K., Xu, H.E., 2015. Crystal structure of rhodopsin bound to arrestin by femtosecond X-ray laser. Nature 523, 561–567. https://doi.org/10.1038/nature14656

Kupitz, Christopher, Basu, S., Grotjohann, I., Fromme, R., Zatsepin, N.A., Rendek, K.N., Hunter, M.S., Shoeman, R.L., White, T.A., Wang, D., James, D., Yang, J.-H., Cobb, D.E., Reeder, B., Sierra, R.G., Liu, H., Barty, A., Aquila, A.L., Deponte, D., Kirian, R.A., Bari, S., Bergkamp, J.J., Beyerlein, K.R., Bogan, M.J., Caleman, C., Chao, T.-C., Conrad, C.E., Davis, K.M., Fleckenstein, H., Galli, L., Hau-Riege, S.P., Kassemeyer, S., Laksmono, H., Liang, M., Lomb, L., Marchesini, S., Martin, A.V., Messerschmidt, M., Milathianaki, D., Nass, K., Ros, A., Roy-Chowdhury, S., Schmidt, K., Seibert, M., Steinbrener, J., Stellato, F., Yan, L., Yoon, C., Moore, T.A., Moore, A.L., Pushkar, Y., Williams, G.J., Boutet, S., Doak, R.B., Weierstall, U., Frank, M., Chapman, H.N., Spence, J.C.H., Fromme, P., 2014. Serial time-resolved crystallography of photosystem II using a femtosecond X-ray laser. Nature 513, 261–265. https://doi.org/10.1038/nature13453

Kupitz, C., Grotjohann, I., Conrad, C.E., Roy-Chowdhury, S., Fromme, R., Fromme, P., 2014. Microcrystallization techniques for serial femtosecond crystallography using photosystem II from Thermosynechococcus elongatus as a model system. Philosophical Transactions of the Royal Society B: Biological Sciences 369, 20130316–20130316. https://doi.org/10.1098/rstb.2013.0316

Kupitz, C., Olmos, J.L., Holl, M., Tremblay, L., Pande, K., Pandey, S., Oberthür, D., Hunter, M., Liang, M., Aquila, A., Tenboer, J., Calvey, G., Katz, A., Chen, Y.,

Wiedorn, M.O., Knoska, J., Meents, A., Majriani, V., Norwood, T., Poudyal, I., Grant, T., Miller, M.D., Xu, W., Tolstikova, A., Morgan, A., Metz, M., Martin-Garcia, J.M., Zook, J.D., Roy-Chowdhury, S., Coe, J., Nagaratnam, N., Meza, D., Fromme, R., Basu, S., Frank, M., White, T., Barty, A., Bajt, S., Yefanov, O., Chapman, H.N., Zatsepin, N., Nelson, G., Weierstall, U., Spence, J., Schwander, P., Pollack, L., Fromme, P., Ourmazd, A., Phillips, G.N., Schmidt, M., 2017. Structural enzymology using X-ray free electron lasers. Structural Dynamics 4, 044003. https://doi.org/10.1063/1.4972069

Martin-Garcia, J.M., Conrad, C.E., Coe, J., Roy-Chowdhury, S., Fromme, P., 2016. Serial femtosecond crystallography: A revolution in structural biology. Archives of Biochemistry and Biophysics 602, 32–47. https://doi.org/10.1016/j.abb.2016.03.036

Martin-Garcia, J.M., Conrad, C.E., Nelson, G., Stander, N., Zatsepin, N.A., Zook, J., Zhu, L., Geiger, J., Chun, E., Kissick, D., Hilgart, M.C., Ogata, C., Ishchenko, A., Nagaratnam, N., Roy-Chowdhury, S., Coe, J., Subramanian, G., Schaffer, A., James, D., Ketwala, G., Venugopalan, N., Xu, S., Corcoran, S., Ferguson, D., Weierstall, U., Spence, J.C.H., Cherezov, V., Fromme, P., Fischetti, R.F., Liu, W., 2017. Serial millisecond crystallography of membrane and soluble protein microcrystals using synchrotron radiation. IUCrJ 4, 439–454. https://doi.org/10.1107/S205225251700570X

Pande, K., Hutchison, C.D.M., Groenhof, G., Aquila, A., Robinson, J.S., Tenboer, J., Basu, S., Boutet, S., DePonte, D.P., Liang, M., White, T.A., Zatsepin, N.A., Yefanov, O., Morozov, D., Oberthuer, D., Gati, C., Subramanian, G., James, D., Zhao, Y., Koralek, J., Brayshaw, J., Kupitz, C., Conrad, C., Roy-Chowdhury, S., Coe, J.D., Metz, M., Xavier, P.L., Grant, T.D., Koglin, J.E., Ketawala, G., Fromme, R., rajer, V., Henning, R., Spence, J.C.H., Ourmazd, A., Schwander, P., Weierstall, U., Frank, M., Fromme, P., Barty, A., Chapman, H.N., Moffat, K., van Thor, J.J., Schmidt, M., 2016. Femtosecond structural dynamics drives the trans/cis isomerization in photoactive yellow protein. Science 352, 725–729. https://doi.org/10.1126/science.aad5081

Tenboer, J., Basu, S., Zatsepin, N., Pande, K., Milathianaki, D., Frank, M., Hunter, M., Boutet, S., Williams, G.J., Koglin, J.E., Oberthuer, D., Heymann, M., Kupitz, C., Conrad, C., Coe, J., Roy-Chowdhury, S., Weierstall, U., James, D., Wang, D., Grant, T., Barty, A., Yefanov, O., Scales, J., Gati, C., Seuring, C., Srajer, V., Henning, R., Schwander, P., Fromme, R., Ourmazd, A., Moffat, K., Van Thor, J.J., Spence, J.C.H., Fromme, P., Chapman, H.N., Schmidt, M., 2014. Time-resolved serial crystallography captures high-resolution intermediates of photoactive yellow protein. Science 346, 1242–1246. https://doi.org/10.1126/science.1259357

Aebi, U., Pollard, T.D., 1987. A glow discharge unit to render electron microscope grids and other surfaces hydrophilic. Journal of Electron Microscopy Technique 7, 29–33. https://doi.org/10.1002/jemt.1060070104

Chapman, H.N., Fromme, P., Barty, A., White, T.A., Kirian, R.A., Aquila, A., Hunter, M.S., Schulz, J., DePonte, D.P., Weierstall, U., Doak, R.B., Maia, F.R.N.C., Martin, A.V., Schlichting, I., Lomb, L., Coppola, N., Shoeman, R.L., Epp, S.W., Hartmann, R., Rolles, D., Rudenko, A., Foucar, L., Kimmel, N., Weidenspointner, G., Holl, P., Liang, M., Barthelmess, M., Caleman, C., Boutet, S., Bogan, M.J., Krzywinski, J., Bostedt, C., Bajt, S., Gumprecht, L., Rudek, B., Erk, B., Schmidt, C., Hömke, A., Reich, C., Pietschner, D., Strüder, L., Hauser, G., Gorke, H., Ullrich, J., Herrmann, S., Schaller, G., Schopper, F., Soltau, H., Kühnel, K.-U., Messerschmidt, M., Bozek, J.D., Hau-Riege, S.P., Frank, M., Hampton, C.Y., Sierra, R.G., Starodub, D., Williams, G.J., Hajdu, J., Timneanu, N., Seibert, M.M., Andreasson, J., Rocker, A., Jönsson, O., Svenda, M., Stern, S., Nass, K., Andritschke, R., Schröter, C.-D., Krasniqi, F., Bott, M., Schmidt, K.E., Wang, X., Grotjohann, I., Holton, J.M., Barends, T.R.M., Neutze, R., Marchesini, S., Fromme, R., Schorb, S., Rupp, D., Adolph, M., Gorkhover, T., Andersson, I., Hirsemann, H., Potdevin, G., Graafsma, H., Nilsson, B., Spence, J.C.H., 2011. Femtosecond X-ray protein nanocrystallography. Nature 470, 73–77. https://doi.org/10.1038/nature09750

Cheng, Y., Grigorieff, N., Penczek, P.A., Walz, T., 2015. A Primer to Single-Particle Cryo-Electron Microscopy. Cell 161, 438–449. https://doi.org/10.1016/j.cell.2015.03.050

Frank, J., 2009. Single-particle reconstruction of biological macromolecules in electron microscopy – 30 years. Quarterly Reviews of Biophysics 42, 139. https://doi.org/10.1017/S0033583509990059

Glaeser, R.M., 2008. Retrospective: Radiation damage and its associated "Information Limitations." Journal of Structural Biology 163, 271–276. https://doi.org/10.1016/j.jsb.2008.06.001

Henderson, R., 2013. Avoiding the pitfalls of single particle cryo-electron microscopy: Einstein from noise. Proceedings of the National Academy of Sciences 110, 18037–18041. https://doi.org/10.1073/pnas.1314449110

Hunter, M.S., Fromme, P., 2011. Toward structure determination using membrane–protein nanocrystals and microcrystals. Methods 55, 387–404. https://doi.org/10.1016/j.ymeth.2011.12.006

Li, X., Zheng, S., Agard, D.A., Cheng, Y., 2015. Asynchronous data acquisition and on-the-fly analysis of dose fractionated cryoEM images by UCSFImage. Journal of Structural Biology 192, 174–178. https://doi.org/10.1016/j.jsb.2015.09.003

Mastronarde, D.N., 2005. Automated electron microscope tomography using robust prediction of specimen movements. Journal of Structural Biology 152, 36–51. https://doi.org/10.1016/j.jsb.2005.07.007

Milazzo, A.-C., Cheng, A., Moeller, A., Lyumkis, D., Jacovetty, E., Polukas, J., Ellisman, M.H., Xuong, N.-H., Carragher, B., Potter, C.S., 2011. Initial evaluation of a direct detection device detector for single particle cryo-electron microscopy. Journal of Structural Biology 176, 404–408. https://doi.org/10.1016/j.jsb.2011.09.002

Ohi, M., Li, Y., Cheng, Y., Walz, T., 2004. Negative staining and image classification — powerful tools in modern electron microscopy. Biological Procedures Online 6, 23–34. https://doi.org/10.1251/bpo70

Pantelic, R.S., Meyer, J.C., Kaiser, U., Baumeister, W., Plitzko, J.M., 2010. Graphene oxide: A substrate for optimizing preparations of frozen-hydrated samples. Journal of Structural Biology 170, 152–156. https://doi.org/10.1016/j.jsb.2009.12.020

Punjani, A., Rubinstein, J.L., Fleet, D.J., Brubaker, M.A., 2017. cryoSPARC: algorithms for rapid unsupervised cryo-EM structure determination. Nature Methods 14, 290–296. https://doi.org/10.1038/nmeth.4169

Rohou, A., Grigorieff, N., 2015. CTFFIND4: Fast and accurate defocus estimation from electron micrographs. Journal of Structural Biology 192, 216–221. https://doi.org/10.1016/j.jsb.2015.08.008

Scheres, S.H.W., 2012. RELION: Implementation of a Bayesian approach to cryo-EM structure determination. Journal of Structural Biology 180, 519–530. https://doi.org/10.1016/j.jsb.2012.09.006

Adams, P.D., Grosse-Kunstleve, R.W., Hung, L.-W., Ioerger, T.R., McCoy, A.J., Moriarty, N.W., Read, R.J., Sacchettini, J.C., Sauter, N.K., Terwilliger, T.C., 2002. *PHENIX* : building new software for automated crystallographic structure determination. Acta Crystallographica Section D Biological Crystallography 58, 1948–1954. https://doi.org/10.1107/S0907444902016657

Arkhipova, V., Guskov, A., Slotboom, D.-J., 2017. Analysis of the quality of crystallographic data and the limitations of structural models. The Journal of General Physiology 149, 1091–1103. https://doi.org/10.1085/jgp.201711852

Bergfors, T., 2003. Seeds to crystals. Journal of Structural Biology 142, 66–76. https://doi.org/10.1016/S1047-8477(03)00039-X

Brettel, K., 1997. Electron transfer and arrangement of the redox cofactors in photosystem I. Biochimica et Biophysica Acta (BBA) - Bioenergetics 1318, 322–373. https://doi.org/10.1016/S0005-2728(96)00112-0

Chapman, H.N., Fromme, P., Barty, A., White, T.A., Kirian, R.A., Aquila, A., Hunter, M.S., Schulz, J., DePonte, D.P., Weierstall, U., Doak, R.B., Maia, F.R.N.C., Martin, A.V., Schlichting, I., Lomb, L., Coppola, N., Shoeman, R.L., Epp, S.W., Hartmann, R., Rolles, D., Rudenko, A., Foucar, L., Kimmel, N., Weidenspointner, G., Holl, P., Liang, M., Barthelmess, M., Caleman, C., Boutet, S., Bogan, M.J., Krzywinski, J., Bostedt, C., Bajt, S., Gumprecht, L., Rudek, B., Erk, B., Schmidt,

C., Hömke, A., Reich, C., Pietschner, D., Strüder, L., Hauser, G., Gorke, H., Ullrich, J., Herrmann, S., Schaller, G., Schopper, F., Soltau, H., Kühnel, K.-U., Messerschmidt, M., Bozek, J.D., Hau-Riege, S.P., Frank, M., Hampton, C.Y., Sierra, R.G., Starodub, D., Williams, G.J., Hajdu, J., Timneanu, N., Seibert, M.M., Andreasson, J., Rocker, A., Jönsson, O., Svenda, M., Stern, S., Nass, K., Andritschke, R., Schröter, C.-D., Krasniqi, F., Bott, M., Schmidt, K.E., Wang, X., Grotjohann, I., Holton, J.M., Barends, T.R.M., Neutze, R., Marchesini, S., Fromme, R., Schorb, S., Rupp, D., Adolph, M., Gorkhover, T., Andersson, I., Hirsemann, H., Potdevin, G., Graafsma, H., Nilsson, B., Spence, J.C.H., 2011. Femtosecond X-ray protein nanocrystallography. Nature 470, 73–77. https://doi.org/10.1038/nature09750

Dall'Osto, L., Lico, C., Alric, J., Giuliano, G., Havaux, M., Bassi, R., 2006. Lutein is needed for efficient chlorophyll triplet quenching in the major LHCII antenna complex of higher plants and effective photoprotection in vivo under strong light. BMC Plant Biology 20.

Domonkos, I., 2004. Phosphatidylglycerol Is Essential for Oligomerization of Photosystem I Reaction Center. PLANT PHYSIOLOGY 134, 1471–1478. https://doi.org/10.1104/pp.103.037754

Fischer, N., 1998. The PsaC subunit of photosystem I provides an essential lysine residue for fast electron transfer to ferredoxin. The EMBO Journal 17, 849–858. https://doi.org/10.1093/emboj/17.4.849

Foadi, J., Aller, P., Alguel, Y., Cameron, A., Axford, D., Owen, R.L., Armour, W., Waterman, D.G., Iwata, S., Evans, G., 2013. Clustering procedures for the optimal selection of data sets from multiple crystals in macromolecular crystallography. Acta Crystallographica Section D Biological Crystallography 69, 1617–1632. https://doi.org/10.1107/S0907444913012274

Fromme, P., Jordan, P., Krauß, N., 2001. Structure of photosystem I. Biochimica et Biophysica Acta (BBA) - Bioenergetics 1507, 5–31. https://doi.org/10.1016/S0005-2728(01)00195-5

Fromme, P., Witt, H.T., 1998. Improved isolation and crystallization of photosystem I for structural analysis. Biochimica et Biophysica Acta (BBA) - Bioenergetics 1365, 175–184. https://doi.org/10.1016/S0005-2728(98)00059-0

Grotjohann, I., Fromme, P., 2005. Structure of cyanobacterial Photosystem I. Photosynthesis Research 85, 51–72. https://doi.org/10.1007/s11120-005-1440-4

Guergova-Kuras, M., Boudreaux, B., Joliot, A., Joliot, P., Redding, K., 2001. Evidence for two active branches for electron transfer in photosystem I. Proceedings of the National Academy of Sciences 98, 4437–4442. https://doi.org/10.1073/pnas.081078898

Jordan, P., Fromme, P., Witt, H.T., Klukas, O., Saenger, W., Krauû, N., 2001. Three-dimensional structure of cyanobacterial photosystem I at 2.5 AÊ resolution 411, 9.

Kabsch, W., 2010. *XDS*. Acta Crystallographica Section D Biological Crystallography 66, 125–132. https://doi.org/10.1107/S0907444909047337

Klukas, O., Schubert, W.-D., Jordan, P., Krauß, N., Fromme, P., Witt, H.T., Saenger, W., 1999. Photosystem I, an Improved Model of the Stromal Subunits PsaC, PsaD, and PsaE. Journal of Biological Chemistry 274, 7351–7360. https://doi.org/10.1074/jbc.274.11.7351

Konrad, A., Trost, A.-L., Skandary, S., Hussels, M., Meixner, A.J., Karapetyan, N.V., Brecht, M., 2014. Manipulating the excitation transfer in Photosystem I using a Fabry–Perot metal resonator with optical subwavelength dimensions. Phys. Chem. Chem. Phys. 16, 6175–6181. https://doi.org/10.1039/C3CP55195D

Kubota-Kawai, H., Mutoh, R., Shinmura, K., Sétif, P., Nowaczyk, M.M., Rögner, M., Ikegami, T., Tanaka, H., Kurisu, G., 2018. X-ray structure of an asymmetrical trimeric ferredoxin–photosystem I complex. Nature Plants 4, 218–224. https://doi.org/10.1038/s41477-018-0130-0

Li, M., Semchonok, D.A., Boekema, E.J., Bruce, B.D., 2014. Characterization and Evolution of Tetrameric Photosystem I from the Thermophilic Cyanobacterium *Chroococcidiopsis* sp TS-821. The Plant Cell 26, 1230–1245. https://doi.org/10.1105/tpc.113.120782

Malavath, T., Caspy, I., Netzer-El, S.Y., Klaiman, D., Nelson, N., 2018. Structure and function of wild-type and subunit-depleted photosystem I in Synechocystis. Biochimica et Biophysica Acta (BBA) - Bioenergetics. https://doi.org/10.1016/j.bbabio.2018.02.002

Mazor, Y., Borovikova, A., Nelson, N., 2015. The structure of plant photosystem I super-complex at 2.8 Å resolution. eLife 4. https://doi.org/10.7554/eLife.07433

Muller, M.G., Slavov, C., Luthra, R., Redding, K.E., Holzwarth, A.R., 2010. Independent initiation of primary electron transfer in the two branches of the photosystem I reaction center. Proceedings of the National Academy of Sciences 107, 4123–4128. https://doi.org/10.1073/pnas.0905407107

Porra, R.J., Thompson, W.A., Kriedemann, P.E., 1989. Determination of accurate extinction coefficients and simultaneous equations for assaying chlorophylls a and b extracted with four different solvents: verification of the concentration of chlorophyll standards by atomic absorption spectroscopy. Biochimica et Biophysica Acta (BBA) - Bioenergetics 975, 384–394. https://doi.org/10.1016/S0005-2728(89)80347-0

Şener, M.K., Jolley, C., Ben-Shem, A., Fromme, P., Nelson, N., Croce, R., Schulten, K., 2005. Comparison of the Light-Harvesting Networks of Plant and Cyanobacterial

Photosystem I. Biophysical Journal 89, 1630–1642. https://doi.org/10.1529/biophysj.105.066464

Şener, M.K., Park, S., Lu, D., Damjanović, A., Ritz, T., Fromme, P., Schulten, K., 2004. Excitation migration in trimeric cyanobacterial photosystem I. The Journal of Chemical Physics 120, 11183–11195. https://doi.org/10.1063/1.1739400

Wang, Y., Mao, L., Hu, X., n.d. Insight into the Structural Role of Carotenoids in the Photosystem I: A Quantum Chemical Analysis. Biophysical Journal 15.

Watanabe, M., Kubota, H., Wada, H., Narikawa, R., Ikeuchi, M., 2011. Novel Supercomplex Organization of Photosystem I in Anabaena and Cyanophora paradoxa. Plant and Cell Physiology 52, 162–168. https://doi.org/10.1093/pcp/pcq183

Winn, M.D., Ballard, C.C., Cowtan, K.D., Dodson, E.J., Emsley, P., Evans, P.R., Keegan, R.M., Krissinel, E.B., Leslie, A.G.W., McCoy, A., McNicholas, S.J., Murshudov, G.N., Pannu, N.S., Potterton, E.A., Powell, H.R., Read, R.J., Vagin, A., Wilson, K.S., 2011. Overview of the *CCP* 4 suite and current developments. Acta Crystallographica Section D Biological Crystallography 67, 235–242. https://doi.org/10.1107/S0907444910045749

Ananyev, G.M., Dismukes, G.C., 1996a. Assembly of the Tetra-Mn Site of Photosynthetic Water Oxidation by Photoactivation: Mn Stoichiometry and Detection of a New Intermediate †. Biochemistry (Mosc.) 35, 4102–4109. https://doi.org/10.1021/bi952667h

Ananyev, G.M., Dismukes, G.C., 1996b. High-Resolution Kinetic Studies of the Reassembly of the Tetra-Manganese Cluster of Photosynthetic Water Oxidation: Proton Equilibrium, Cations, and Electrostatics †. Biochemistry (Mosc.) 35, 14608–14617. https://doi.org/10.1021/bi960894t

Ayyer, K., Yefanov, O.M., Oberthür, D., Roy-Chowdhury, S., Galli, L., Mariani, V., Basu, S., Coe, J., Conrad, C.E., Fromme, R., Schaffer, A., Dörner, K., James, D., Kupitz, C., Metz, M., Nelson, G., Xavier, P.L., Beyerlein, K.R., Schmidt, M., Sarrou, I., Spence, J.C.H., Weierstall, U., White, T.A., Yang, J.-H., Zhao, Y., Liang, M., Aquila, A., Hunter, M.S., Robinson, J.S., Koglin, J.E., Boutet, S., Fromme, P., Barty, A., Chapman, H.N., 2016. Macromolecular diffractive imaging using imperfect crystals. Nature 530, 202–206. https://doi.org/10.1038/nature16949

Barty, A., Kirian, R.A., Maia, F.R.N.C., Hantke, M., Yoon, C.H., White, T.A., Chapman, H., 2014. *Cheetah* : software for high-throughput reduction and analysis of serial femtosecond X-ray diffraction data. J. Appl. Crystallogr. 47, 1118–1131. https://doi.org/10.1107/S1600576714007626

Borie, B., n.d. X-Ray Diffraction in Crystals, Imperfect Crystals, and Amorphous Bodies. 2.

Chapman, H.N., Barty, A., Marchesini, S., Noy, A., Hau-Riege, S.P., Cui, C., Howells, M.R., Rosen, R., He, H., Spence, J.C.H., Weierstall, U., Beetz, T., Jacobsen, C., Shapiro, D., 2006. High-resolution ab initio three-dimensional x-ray diffraction microscopy. J. Opt. Soc. Am. A 23, 1179. https://doi.org/10.1364/JOSAA.23.001179

Chapman, H.N., Fromme, P., 2017. Structure determination based on continuous diffraction from macromolecular crystals. Curr. Opin. Struct. Biol. 45, 170–177. https://doi.org/10.1016/j.sbi.2017.07.008

DePonte, D.P., Weierstall, U., Schmidt, K., Warner, J., Starodub, D., Spence, J.C.H., Doak, R.B., 2008. Gas dynamic virtual nozzle for generation of microscopic droplet streams. J. Phys. Appl. Phys. 41, 195505. https://doi.org/10.1088/0022-3727/41/19/195505

Dods, R., Båth, P., Arnlund, D., Beyerlein, K.R., Nelson, G., Liang, M., Harimoorthy, R., Berntsen, P., Malmerberg, E., Johansson, L., Andersson, R., Bosman, R., Carbajo, S., Claesson, E., Conrad, C.E., Dahl, P., Hammarin, G., Hunter, M.S., Li, C., Lisova, S., Milathianaki, D., Robinson, J., Safari, C., Sharma, A., Williams, G., Wickstrand, C., Yefanov, O., Davidsson, J., DePonte, D.P., Barty, A., Brändén, G., Neutze, R., 2017. From Macrocrystals to Microcrystals: A Strategy for Membrane Protein Serial Crystallography. Structure 25, 1461-1468.e2. https://doi.org/10.1016/j.str.2017.07.002

Elser, V., 2003. Random projections and the optimization of an algorithm for phase retrieval. J. Phys. Math. Gen. 36, 2995–3007. https://doi.org/10.1088/0305-4470/36/12/309

Fischer, N., Neumann, P., Konevega, A.L., Bock, L.V., Ficner, R., Rodnina, M.V., Stark, H., 2015. Structure of the E. coli ribosome–EF-Tu complex at <3 Å resolution by Cs-corrected cryo-EM. Nature 520, 567–570. https://doi.org/10.1038/nature14275

Grundmeier, A., Dau, H., 2012. Structural models of the manganese complex of photosystem II and mechanistic implications. Biochim. Biophys. Acta BBA - Bioenerg. 1817, 88–105. https://doi.org/10.1016/j.bbabio.2011.07.004

Han, G., Ho, F.M., Havelius, K.G.V., Morvaridi, S.F., Mamedov, F., Styring, S., 2008. Direct quantification of the four individual S states in Photosystem II using EPR spectroscopy. Biochim. Biophys. Acta BBA - Bioenerg. 1777, 496–503. https://doi.org/10.1016/j.bbabio.2008.03.007

Hart, P., 2012 The Comell-SLAC Pixel Array Detector at LCLS 4.

Kato, Y., Akita, F., Nakajima, Y., Suga, M., Umena, Y., Shen, J.-R., Noguchi, T., 2018. Fourier Transform Infrared Analysis of the S-State Cycle of Water Oxidation in the Microcrystals of Photosystem II. J. Phys. Chem. Lett. 9, 2121–2126. https://doi.org/10.1021/acs.jpclett.8b00638

Kuan, D., Duff, S., Posarac, D., Bi, X., 2015. Growth optimization of *Synechococcus elongatus* PCC7942 in lab flasks and a 2-D photobioreactor. Can. J. Chem. Eng. 93, 640–647. https://doi.org/10.1002/cjce.22154

Kupitz, Christopher, Basu, S., Grotjohann, I., Fromme, R., Zatsepin, N.A., Rendek, K.N., Hunter, M.S., Shoeman, R.L., White, T.A., Wang, D., James, D., Yang, J.-H., Cobb, D.E., Reeder, B., Sierra, R.G., Liu, H., Barty, A., Aquila, A.L., Deponte, D., Kirian, R.A., Bari, S., Bergkamp, J.J., Beyerlein, K.R., Bogan, M.J., Caleman, C., Chao, T.-C., Conrad, C.E., Davis, K.M., Fleckenstein, H., Galli, L., Hau-Riege, S.P., Kassemeyer, S., Laksmono, H., Liang, M., Lomb, L., Marchesini, S., Martin, A.V., Messerschmidt, M., Milathianaki, D., Nass, K., Ros, A., Roy-Chowdhury, S., Schmidt, K., Seibert, M., Steinbrener, J., Stellato, F., Yan, L., Yoon, C., Moore, T.A., Moore, A.L., Pushkar, Y., Williams, G.J., Boutet, S., Doak, R.B., Weierstall, U., Frank, M., Chapman, H.N., Spence, J.C.H., Fromme, P., 2014. Serial time-resolved crystallography of photosystem II using a femtosecond X-ray laser. Nature 513, 261–265. https://doi.org/10.1038/nature13453

Kupitz, C., Grotjohann, I., Conrad, C.E., Roy-Chowdhury, S., Fromme, R., Fromme, P., 2014. Microcrystallization techniques for serial femtosecond crystallography using photosystem II from Thermosynechococcus elongatus as a model system. Philos. Trans. R. Soc. B Biol. Sci. 369, 20130316–20130316. https://doi.org/10.1098/rstb.2013.0316

Lomb, L., Steinbrener, J., Bari, S., Beisel, D., Berndt, D., Kieser, C., Lukat, M., Neef, N., Shoeman, R.L., 2012. An anti-settling sample delivery instrument for serial femtosecond crystallography. J. Appl. Crystallogr. 45, 674–678. https://doi.org/10.1107/S0021889812024557

Miao, J., Charalambous, P., Kirz, J., Sayre, D., 1999. Extending the methodology of X-ray crystallography to allow imaging of micrometre-sized non-crystalline specimens. Nature 400, 342–344. https://doi.org/10.1038/22498

Murata, N., Takahashi, S., Nishiyama, Y., Allakhverdiev, S.I., 2007. Photoinhibition of photosystem II under environmental stress. Biochim. Biophys. Acta BBA - Bioenerg. 1767, 414–421. https://doi.org/10.1016/j.bbabio.2006.11.019

Pushkar, Y., Long, X., Glatzel, P., Brudvig, G.W., Dismukes, G.C., Collins, T.J., Yachandra, V.K., Yano, J., Bergmann, U., 2010. Direct Detection of Oxygen Ligation to the Mn4Ca Cluster of Photosystem II by X-ray Emission Spectroscopy. Angew. Chem. Int. Ed. 49, 800–803. https://doi.org/10.1002/anie.200905366

Roedig, P., Ginn, H.M., Pakendorf, T., Sutton, G., Harlos, K., Walter, T.S., Meyer, J., Fischer, P., Duman, R., Vartiainen, I., Reime, B., Warmer, M., Brewster, A.S., Young, I.D., Michels-Clark, T., Sauter, N.K., Kotecha, A., Kelly, J., Rowlands, D.J., Sikorsky, M., Nelson, S., Damiani, D.S., Alonso-Mori, R., Ren, J., Fry, E.E., David, C., Stuart, D.I., Wagner, A., Meents, A., 2017. High-speed fixed-target serial virus crystallography. Nat. Methods 14, 805–810. https://doi.org/10.1038/nmeth.4335

Roedig, P., Vartiainen, I., Duman, R., Panneerselvam, S., Stübe, N., Lorbeer, O., Warmer, M., Sutton, G., Stuart, D.I., Weckert, E., David, C., Wagner, A., Meents, A., 2015. A micro-patterned silicon chip as sample holder for macromolecular crystallography experiments with minimal background scattering. Sci. Rep. 5. https://doi.org/10.1038/srep10451

Seddon, A.M., Curnow, P., Booth, P.J., 2004. Membrane proteins, lipids and detergents: not just a soap opera. Biochim. Biophys. Acta BBA - Biomembr. 1666, 105–117. https://doi.org/10.1016/j.bbamem.2004.04.011

Shapiro, D., Thibault, P., Beetz, T., Elser, V., Howells, M., Jacobsen, C., Kirz, J., Lima, E., Miao, H., Neiman, A.M., Sayre, D., 2005. Biological imaging by soft x-ray diffraction microscopy. Proc. Natl. Acad. Sci. 102, 15343–15346. https://doi.org/10.1073/pnas.0503305102

Vinyard, D.J., Zachary, C.E., Ananyev, G., Dismukes, G.C., 2013. Thermodynamically accurate modeling of the catalytic cycle of photosynthetic oxygen evolution: A mathematical solution to asymmetric Markov chains. Biochim. Biophys. Acta BBA - Bioenerg. 1827, 861–868. https://doi.org/10.1016/j.bbabio.2013.04.008

Yano, J., Kern, J., Irrgang, K.-D., Latimer, M.J., Bergmann, U., Glatzel, P., Pushkar, Y., Biesiadka, J., Loll, B., Sauer, K., Messinger, J., Zouni, A., Yachandra, V.K., 2005. X-ray damage to the Mn4Ca complex in single crystals of photosystem II: A case study for metalloprotein crystallography. Proc. Natl. Acad. Sci. 102, 12047–12052. https://doi.org/10.1073/pnas.0505207102

Adams, P.D., Grosse-Kunstleve, R.W., Hung, L.-W., Ioerger, T.R., McCoy, A.J., Moriarty, N.W., Read, R.J., Sacchettini, J.C., Sauter, N.K., Terwilliger, T.C., 2002. *PHENIX* : building new software for automated crystallographic structure determination. Acta Crystallographica Section D Biological Crystallography 58, 1948–1954. https://doi.org/10.1107/S0907444902016657

Allakhverdiev, S.I., 2005. Systematic Analysis of the Relation of Electron Transport and ATP Synthesis to the Photodamage and Repair of Photosystem II in Synechocystis. PLANT PHYSIOLOGY 137, 263–273. https://doi.org/10.1104/pp.104.054478

Aquila, A., Hunter, M.S., Doak, R.B., Kirian, R.A., Fromme, P., White, T.A., Andreasson, J., Arnlund, D., Bajt, S., Barends, T.R.M., Barthelmess, M., Bogan, M.J., Bostedt, C., Bottin, H., Bozek, J.D., Caleman, C., Coppola, N., Davidsson, J., DePonte, D.P., Elser, V., Epp, S.W., Erk, B., Fleckenstein, H., Foucar, L., Frank, M., Fromme, R., Graafsma, H., Grotjohann, I., Gumprecht, L., Hajdu, J., Hampton, C.Y., Hartmann, A., Hartmann, R., Hau-Riege, S., Hauser, G., Hirsemann, H., Holl, P., Holton, J.M., Hömke, A., Johansson, L., Kimmel, N., Kassemeyer, S., Krasniqi, F., Kühnel, K.-U., Liang, M., Lomb, L., Malmerberg, E., Marchesini, S., Martin, A.V., Maia, F.R.N.C., Messerschmidt, M., Nass, K., Reich, C., Neutze, R., Rolles, D., Rudek, B., Rudenko, A., Schlichting, I., Schmidt, C., Schmidt, K.E., Schulz, J., Seibert, M.M., Shoeman, R.L., Sierra, R., Soltau, H., Starodub, D., Stellato, F., Stern, S., Strüder, L., Timneanu, N., Ullrich, J., Wang, X., Williams, G.J., Weidenspointner, G., Weierstall, U., Wunderer, C., Barty, A., Spence,

J.C.H., Chapman, H.N., 2012. Time-resolved protein nanocrystallography using an X-ray free-electron laser. Optics Express 20, 2706. https://doi.org/10.1364/OE.20.002706

Aro, E.-M., Virgin, I., Andersson, B., 1993. Photoinhibition of Photosystem II. Inactivation, protein damage and turnover. Biochimica et Biophysica Acta (BBA) - Bioenergetics 1143, 113–134. https://doi.org/10.1016/0005-2728(93)90134-2

Barty, A., Caleman, C., Aquila, A., Timneanu, N., Lomb, L., White, T.A., Andreasson, J., Arnlund, D., Bajt, S., Barends, T.R.M., Barthelmess, M., Bogan, M.J., Bostedt, C., Bozek, J.D., Coffee, R., Coppola, N., Davidsson, J., DePonte, D.P., Doak, R.B., Ekeberg, T., Elser, V., Epp, S.W., Erk, B., Fleckenstein, H., Foucar, L., Fromme, P., Graafsma, H., Gumprecht, L., Hajdu, J., Hampton, C.Y., Hartmann, R., Hartmann, A., Hauser, G., Hirsemann, H., Holl, P., Hunter, M.S., Johansson, L., Kassemeyer, S., Kimmel, N., Kirian, R.A., Liang, M., Maia, F.R.N.C., Malmerberg, E., Marchesini, S., Martin, A.V., Nass, K., Neutze, R., Reich, C., Rolles, D., Rudek, B., Rudenko, A., Scott, H., Schlichting, I., Schulz, J., Seibert, M.M., Shoeman, R.L., Sierra, R.G., Soltau, H., Spence, J.C.H., Stellato, F., Stern, S., Strüder, L., Ullrich, J., Wang, X., Weidenspointner, G., Weierstall, U., Wunderer, C.B., Chapman, H.N., 2012. Self-terminating diffraction gates femtosecond X-ray nanocrystallography measurements. Nature Photonics 6, 35–40. https://doi.org/10.1038/nphoton.2011.297

Barty, A., Kirian, R.A., Maia, F.R.N.C., Hantke, M., Yoon, C.H., White, T.A., Chapman, H., 2014. *Cheetah* : software for high-throughput reduction and analysis of serial femtosecond X-ray diffraction data. Journal of Applied Crystallography 47, 1118–1131. https://doi.org/10.1107/S1600576714007626

Chapman, H.N., Fromme, P., Barty, A., White, T.A., Kirian, R.A., Aquila, A., Hunter, M.S., Schulz, J., DePonte, D.P., Weierstall, U., Doak, R.B., Maia, F.R.N.C., Martin, A.V., Schlichting, I., Lomb, L., Coppola, N., Shoeman, R.L., Epp, S.W., Hartmann, R., Rolles, D., Rudenko, A., Foucar, L., Kimmel, N., Weidenspointner, G., Holl, P., Liang, M., Barthelmess, M., Caleman, C., Boutet, S., Bogan, M.J., Krzywinski, J., Bostedt, C., Bajt, S., Gumprecht, L., Rudek, B., Erk, B., Schmidt, C., Hömke, A., Reich, C., Pietschner, D., Strüder, L., Hauser, G., Gorke, H., Ullrich, J., Herrmann, S., Schaller, G., Schopper, F., Soltau, H., Kühnel, K.-U., Messerschmidt, M., Bozek, J.D., Hau-Riege, S.P., Frank, M., Hampton, C.Y., Sierra, R.G., Starodub, D., Williams, G.J., Hajdu, J., Timneanu, N., Seibert, M.M., Andreasson, J., Rocker, A., Jönsson, O., Svenda, M., Stern, S., Nass, K., Andritschke, R., Schröter, C.-D., Krasniqi, F., Bott, M., Schmidt, K.E., Wang, X., Grotjohann, I., Holton, J.M., Barends, T.R.M., Neutze, R., Marchesini, S., Fromme, R., Schorb, S., Rupp, D., Adolph, M., Gorkhover, T., Andersson, I., Hirsemann, H., Potdevin, G., Graafsma, H., Nilsson, B., Spence, J.C.H., 2011. Femtosecond X-ray protein nanocrystallography. Nature 470, 73–77. https://doi.org/10.1038/nature09750

Dau, H., Zaharieva, I., Haumann, M., 2012. Recent developments in research on water oxidation by photosystem II. Current Opinion in Chemical Biology 16, 3–10. https://doi.org/10.1016/j.cbpa.2012.02.011

de Wijn, R., van Gorkom, H.J., 2001. Kinetics of Electron Transfer from Q_A to Q_B in Photosystem II †. Biochemistry 40, 11912–11922. https://doi.org/10.1021/bi010852r

Debus, R.J., 2014. Evidence from FTIR Difference Spectroscopy That D1-Asp61 Influences the Water Reactions of the Oxygen-Evolving Mn_4CaO_5 Cluster of Photosystem II. Biochemistry 53, 2941–2955. https://doi.org/10.1021/bi500309f

Dekker, J.P., Grondelle, R.V., n.d. Primary charge separation in Photosystem II 14.

DePonte, D.P., Weierstall, U., Schmidt, K., Warner, J., Starodub, D., Spence, J.C.H., Doak, R.B., 2008. Gas dynamic virtual nozzle for generation of microscopic droplet streams. Journal of Physics D: Applied Physics 41, 195505. https://doi.org/10.1088/0022-3727/41/19/195505

Dilbeck, P.L., Bao, H., Neveu, C.L., Burnap, R.L., 2013. Perturbing the Water Cavity Surrounding the Manganese Cluster by Mutating the Residue D1-Valine 185 Has a Strong Effect on the Water Oxidation Mechanism of Photosystem II. Biochemistry 52, 6824–6833. https://doi.org/10.1021/bi400930g

Ferreira, K.N., Iverson, T.M., Maghlaoui, K., Barber, J., Iwata, S., 2004. Architecture of the Photosynthetic Oxygen-Evolving Center 303, 9.

Haupert, L.M., Simpson, G.J., 2011. Screening of protein crystallization trials by second order nonlinear optical imaging of chiral crystals (SONICC). Methods 55, 379–386. https://doi.org/10.1016/j.ymeth.2011.11.003

Isobe, H., Shoji, M., Yamanaka, S., Umena, Y., Kawakami, K., Kamiya, N., Shen, J.-R., Yamaguchi, K., 2012. Theoretical illumination of water-inserted structures of the CaMn4O5 cluster in the S2 and S3 states of oxygen-evolving complex of photosystem II: full geometry optimizations by B3LYP hybrid density functional. Dalton Transactions 41, 13727. https://doi.org/10.1039/c2dt31420g

Kamiya, N., Shen, J.-R., 2003. Crystal structure of oxygen-evolving photosystem II from Thermosynechococcus vulcanus at 3.7-A resolution. Proceedings of the National Academy of Sciences 100, 98–103. https://doi.org/10.1073/pnas.0135651100

Kanady, J.S., Tsui, E.Y., Day, M.W., Agapie, T., 2011. A Synthetic Model of the Mn3Ca Subsite of the Oxygen-Evolving Complex in Photosystem II. Science 333, 733–736. https://doi.org/10.1126/science.1206036

Kern, J., Alonso-Mori, R., Tran, R., Hattne, J., Gildea, R.J., Echols, N., Glockner, C., Hellmich, J., Laksmono, H., Sierra, R.G., Lassalle-Kaiser, B., Koroidov, S., Lampe, A., Han, G., Gul, S., DiFiore, D., Milathianaki, D., Fry, A.R., Miahnahri, A., Schafer, D.W., Messerschmidt, M., Seibert, M.M., Koglin, J.E., Sokaras, D., Weng, T.-C., Sellberg, J., Latimer, M.J., Grosse-Kunstleve, R.W., Zwart, P.H., White, W.E., Glatzel, P., Adams, P.D., Bogan, M.J., Williams, G.J., Boutet, S., Messinger, J., Zouni, A., Sauter, N.K., Yachandra, V.K., Bergmann, U., Yano, J., 2013. Simultaneous Femtosecond X-ray Spectroscopy and Diffraction of

Photosystem II at Room Temperature. Science 340, 491–495. https://doi.org/10.1126/science.1234273

Kern, J., Tran, R., Alonso-Mori, R., Koroidov, S., Echols, N., Hattne, J., Ibrahim, M., Gul, S., Laksmono, H., Sierra, R.G., Gildea, R.J., Han, G., Hellmich, J., Lassalle-Kaiser, B., Chatterjee, R., Brewster, A.S., Stan, C.A., Glöckner, C., Lampe, A., DiFiore, D., Milathianaki, D., Fry, A.R., Seibert, M.M., Koglin, J.E., Gallo, E., Uhlig, J., Sokaras, D., Weng, T.-C., Zwart, P.H., Skinner, D.E., Bogan, M.J., Messerschmidt, M., Glatzel, P., Williams, G.J., Boutet, S., Adams, P.D., Zouni, A., Messinger, J., Sauter, N.K., Bergmann, U., Yano, J., Yachandra, V.K., 2014. Taking snapshots of photosynthetic water oxidation using femtosecond X-ray diffraction and spectroscopy. Nature Communications 5. https://doi.org/10.1038/ncomms5371

Kupitz, Christopher, Basu, S., Grotjohann, I., Fromme, R., Zatsepin, N.A., Rendek, K.N., Hunter, M.S., Shoeman, R.L., White, T.A., Wang, D., James, D., Yang, J.-H., Cobb, D.E., Reeder, B., Sierra, R.G., Liu, H., Barty, A., Aquila, A.L., Deponte, D., Kirian, R.A., Bari, S., Bergkamp, J.J., Beyerlein, K.R., Bogan, M.J., Caleman, C., Chao, T.-C., Conrad, C.E., Davis, K.M., Fleckenstein, H., Galli, L., Hau-Riege, S.P., Kassemeyer, S., Laksmono, H., Liang, M., Lomb, L., Marchesini, S., Martin, A.V., Messerschmidt, M., Milathianaki, D., Nass, K., Ros, A., Roy-Chowdhury, S., Schmidt, K., Seibert, M., Steinbrener, J., Stellato, F., Yan, L., Yoon, C., Moore, T.A., Moore, A.L., Pushkar, Y., Williams, G.J., Boutet, S., Doak, R.B., Weierstall, U., Frank, M., Chapman, H.N., Spence, J.C.H., Fromme, P., 2014. Serial time-resolved crystallography of photosystem II using a femtosecond X-ray laser. Nature 513, 261–265. https://doi.org/10.1038/nature13453

Kupitz, C., Grotjohann, I., Conrad, C.E., Roy-Chowdhury, S., Fromme, R., Fromme, P., 2014. Microcrystallization techniques for serial femtosecond crystallography using photosystem II from Thermosynechococcus elongatus as a model system. Philosophical Transactions of the Royal Society B: Biological Sciences 369, 20130316–20130316. https://doi.org/10.1098/rstb.2013.0316

Loll, B., Kern, J., Saenger, W., Zouni, A., Biesiadka, J., 2005. Towards complete cofactor arrangement in the 3.0 Å resolution structure of photosystem II. Nature 438, 1040–1044. https://doi.org/10.1038/nature04224

McPHERSON, A., 1990. Current approaches to macromolecular crystallization. European Journal of Biochemistry 189, 1–23. https://doi.org/10.1111/j.1432-1033.1990.tb15454.x

Mukherjee, S., Stull, J.A., Yano, J., Stamatatos, T.C., Pringouri, K., Stich, T.A., Abboud, K.A., Britt, R.D., Yachandra, V.K., Christou, G., 2012. Synthetic model of the asymmetric [Mn3CaO4] cubane core of the oxygen-evolving complex of photosystem II. Proceedings of the National Academy of Sciences 109, 2257–2262. https://doi.org/10.1073/pnas.1115290109

Neutze, R., Moffat, K., 2012. Time-resolved structural studies at synchrotrons and X-ray free electron lasers: opportunities and challenges. Current Opinion in Structural Biology 22, 651–659. https://doi.org/10.1016/j.sbi.2012.08.006

Neutze, R., Wouts, R., Hajdu, J., 2000. Potential for biomolecular imaging with femtosecond X-ray pulses 406, 6.

Ng, J.D., Gavira, J.A., Garcı´a-Ruı´z, J.M., 2003. Protein crystallization by capillary counterdiffusion for applied crystallographic structure determination. Journal of Structural Biology 142, 218–231. https://doi.org/10.1016/S1047-8477(03)00052-2

Patzlaff, J.S., Barry, B.A., 1996. Pigment Quantitation and Analysis by HPLC Reverse Phase Chromatography: A Characterization of Antenna Size in Oxygen-Evolving Photosystem II Preparations from Cyanobacteria and Plants †. Biochemistry 35, 7802–7811. https://doi.org/10.1021/bi960056z

Pokhrel, R., Brudvig, G.W., 2014. Oxygen-evolving complex of photosystem II: correlating structure with spectroscopy. Physical Chemistry Chemical Physics 16, 11812. https://doi.org/10.1039/c4cp00493k

Pushkar, Y., Yano, J., Sauer, K., Boussac, A., Yachandra, V.K., 2008. Structural changes in the Mn4Ca cluster and the mechanism of photosynthetic water splitting. Proceedings of the National Academy of Sciences 105, 1879–1884. https://doi.org/10.1073/pnas.0707092105

Rajagopal, S., Anderson, S., Srajer, V., Schmidt, M., Pahl, R., Moffat, K., 2005. A Structural Pathway for Signaling in the E46Q Mutant of Photoactive Yellow Protein. Structure 13, 55–63. https://doi.org/10.1016/j.str.2004.10.016

Renger, G., 2012. Mechanism of light induced water splitting in Photosystem II of oxygen evolving photosynthetic organisms. Biochimica et Biophysica Acta (BBA) - Bioenergetics 1817, 1164–1176. https://doi.org/10.1016/j.bbabio.2012.02.005

Sierra, R.G., Laksmono, H., Kern, J., Tran, R., Hattne, J., Alonso-Mori, R., Lassalle-Kaiser, B., Glöckner, C., Hellmich, J., Schafer, D.W., Echols, N., Gildea, R.J., Grosse-Kunstleve, R.W., Sellberg, J., McQueen, T.A., Fry, A.R., Messerschmidt, M.M., Miahnahri, A., Seibert, M.M., Hampton, C.Y., Starodub, D., Loh, N.D., Sokaras, D., Weng, T.-C., Zwart, P.H., Glatzel, P., Milathianaki, D., White, W.E., Adams, P.D., Williams, G.J., Boutet, S., Zouni, A., Messinger, J., Sauter, N.K., Bergmann, U., Yano, J., Yachandra, V.K., Bogan, M.J., 2012. Nanoflow electrospinning serial femtosecond crystallography. Acta Crystallographica Section D Biological Crystallography 68, 1584–1587. https://doi.org/10.1107/S0907444912038152

Spence, J.C.H., Weierstall, U., Chapman, H.N., 2012. X-ray lasers for structural and dynamic biology. Reports on Progress in Physics 75, 102601. https://doi.org/10.1088/0034-4885/75/10/102601

Šrajer, V., Ren, Z., Teng, T.-Y., Schmidt, M., Ursby, T., Bourgeois, D., Pradervand, C., Schildkamp, W., Wulff, M., Moffat, K., 2001. Protein Conformational Relaxation and Ligand Migration in Myoglobin: A Nanosecond to Millisecond Molecular

Movie from Time-Resolved Laue X-ray Diffraction †. Biochemistry 40, 13802–13815. https://doi.org/10.1021/bi010715u

Suga, M., Akita, F., Hirata, K., Ueno, G., Murakami, H., Nakajima, Y., Shimizu, T., Yamashita, K., Yamamoto, M., Ago, H., Shen, J.-R., 2015. Native structure of photosystem II at 1.95 Å resolution viewed by femtosecond X-ray pulses. Nature 517, 99–103. https://doi.org/10.1038/nature13991

Tenboer, J., Basu, S., Zatsepin, N., Pande, K., Milathianaki, D., Frank, M., Hunter, M., Boutet, S., Williams, G.J., Koglin, J.E., Oberthuer, D., Heymann, M., Kupitz, C., Conrad, C., Coe, J., Roy-Chowdhury, S., Weierstall, U., James, D., Wang, D., Grant, T., Barty, A., Yefanov, O., Scales, J., Gati, C., Seuring, C., Srajer, V., Henning, R., Schwander, P., Fromme, R., Ourmazd, A., Moffat, K., Van Thor, J.J., Spence, J.C.H., Fromme, P., Chapman, H.N., Schmidt, M., 2014. Time-resolved serial crystallography captures high-resolution intermediates of photoactive yellow protein. Science 346, 1242–1246. https://doi.org/10.1126/science.1259357

Umena, Y., Kawakami, K., Shen, J.-R., Kamiya, N., 2011. Crystal structure of oxygen-evolving photosystem II at a resolution of 1.9 Å. Nature 473, 55–60. https://doi.org/10.1038/nature09913

Wampler, R.D., Begue, N.J., Simpson, G.J., 2008. Molecular Design Strategies for Optimizing the Nonlinear Optical Properties of Chiral Crystals. Crystal Growth & Design 8, 2589–2594. https://doi.org/10.1021/cg700732n

Weierstall, U., James, D., Wang, C., White, T.A., Wang, D., Liu, W., Spence, J.C.H., Bruce Doak, R., Nelson, G., Fromme, P., Fromme, R., Grotjohann, I., Kupitz, C., Zatsepin, N.A., Liu, H., Basu, S., Wacker, D., Won Han, G., Katritch, V., Boutet, S., Messerschmidt, M., Williams, G.J., Koglin, J.E., Marvin Seibert, M., Klinker, M., Gati, C., Shoeman, R.L., Barty, A., Chapman, H.N., Kirian, R.A., Beyerlein, K.R., Stevens, R.C., Li, D., Shah, S.T.A., Howe, N., Caffrey, M., Cherezov, V., 2014. Lipidic cubic phase injector facilitates membrane protein serial femtosecond crystallography. Nature Communications 5. https://doi.org/10.1038/ncomms4309

White, T.A., Kirian, R.A., Martin, A.V., Aquila, A., Nass, K., Barty, A., Chapman, H.N., 2012. *CrystFEL* : a software suite for snapshot serial crystallography. Journal of Applied Crystallography 45, 335–341. https://doi.org/10.1107/S0021889812002312

Yamaguchi, K., Isobe, H., Yamanaka, S., Saito, T., Kanda, K., Shoji, M., Umena, Y., Kawakami, K., Shen, J.-R., Kamiya, N., Okumura, M., 2013. Full geometry optimizations of the mixed-valence $CaMn_4O_4X(H_2O)_4$ (X=OH or O) cluster in OEC of PS II: Degree of symmetry breaking of the labile Mn-X-Mn bond revealed by several hybrid DFT calculations. International Journal of Quantum Chemistry 113, 525–541. https://doi.org/10.1002/qua.24117

Yano, J., Kern, J., Irrgang, K.-D., Latimer, M.J., Bergmann, U., Glatzel, P., Pushkar, Y., Biesiadka, J., Loll, B., Sauer, K., Messinger, J., Zouni, A., Yachandra, V.K., 2005.

X-ray damage to the Mn4Ca complex in single crystals of photosystem II: A case study for metalloprotein crystallography. Proceedings of the National Academy of Sciences 102, 12047–12052. https://doi.org/10.1073/pnas.0505207102

Yano, J., Yachandra, V.K., 2007. Oxidation state changes of the Mn4Ca cluster in Photosystem II. Photosynthesis Research 92, 289–303. https://doi.org/10.1007/s11120-007-9153-5

Bai, X., McMullan, G., Scheres, S.H.., 2015. How cryo-EM is revolutionizing structural biology. Trends in Biochemical Sciences 40, 49–57. https://doi.org/10.1016/j.tibs.2014.10.005

Bragg, W.L., 1913. The Structure of Some Crystals as Indicated by Their Diffraction of X-rays. Proceedings of the Royal Society A: Mathematical, Physical and Engineering Sciences 89, 248–277. https://doi.org/10.1098/rspa.1913.0083

Buban, J.P., Ramasse, Q., Gipson, B., Browning, N.D., Stahlberg, H., 2010. High-resolution low-dose scanning transmission electron microscopy. Journal of Electron Microscopy 59, 103–112. https://doi.org/10.1093/jmicro/dfp052

Caffrey, M., Li, D., Howe, N., Shah, S.T.A., 2014. “Hit and run” serial femtosecond crystallography of a membrane kinase in the lipid cubic phase. Philosophical Transactions of the Royal Society B: Biological Sciences 369, 20130621–20130621. https://doi.org/10.1098/rstb.2013.0621

CALLAWAY, E., n.d. Molecular-imaging pioneers scoop Nobel 1.

Campbell, M.G., Cheng, A., Brilot, A.F., Moeller, A., Lyumkis, D., Veesler, D., Pan, J., Harrison, S.C., Potter, C.S., Carragher, B., Grigorieff, N., 2012. Movies of Ice-Embedded Particles Enhance Resolution in Electron Cryo-Microscopy. Structure 20, 1823–1828. https://doi.org/10.1016/j.str.2012.08.026

Chapman, H.N., Fromme, P., Barty, A., White, T.A., Kirian, R.A., Aquila, A., Hunter, M.S., Schulz, J., DePonte, D.P., Weierstall, U., Doak, R.B., Maia, F.R.N.C., Martin, A.V., Schlichting, I., Lomb, L., Coppola, N., Shoeman, R.L., Epp, S.W., Hartmann, R., Rolles, D., Rudenko, A., Foucar, L., Kimmel, N., Weidenspointner, G., Holl, P., Liang, M., Barthelmess, M., Caleman, C., Boutet, S., Bogan, M.J., Krzywinski, J., Bostedt, C., Bajt, S., Gumprecht, L., Rudek, B., Erk, B., Schmidt, C., Hömke, A., Reich, C., Pietschner, D., Strüder, L., Hauser, G., Gorke, H., Ullrich, J., Herrmann, S., Schaller, G., Schopper, F., Soltau, H., Kühnel, K.-U., Messerschmidt, M., Bozek, J.D., Hau-Riege, S.P., Frank, M., Hampton, C.Y., Sierra, R.G., Starodub, D., Williams, G.J., Hajdu, J., Timneanu, N., Seibert, M.M., Andreasson, J., Rocker, A., Jönsson, O., Svenda, M., Stern, S., Nass, K., Andritschke, R., Schröter, C.-D., Krasniqi, F., Bott, M., Schmidt, K.E., Wang, X., Grotjohann, I., Holton, J.M., Barends, T.R.M., Neutze, R., Marchesini, S., Fromme, R., Schorb, S., Rupp, D., Adolph, M., Gorkhover, T., Andersson, I., Hirsemann, H., Potdevin, G., Graafsma, H., Nilsson, B., Spence, J.C.H., 2011. Femtosecond X-ray protein nanocrystallography. Nature 470, 73–77. https://doi.org/10.1038/nature09750

Conrad, C.E., Basu, S., James, D., Wang, D., Schaffer, A., Roy-Chowdhury, S., Zatsepin, N.A., Aquila, A., Coe, J., Gati, C., Hunter, M.S., Koglin, J.E., Kupitz, C., Nelson, G., Subramanian, G., White, T.A., Zhao, Y., Zook, J., Boutet, S., Cherezov, V., Spence, J.C.H., Fromme, R., Weierstall, U., Fromme, P., 2015. A novel inert crystal delivery medium for serial femtosecond crystallography. IUCrJ 2, 421–430. https://doi.org/10.1107/S2052252515009811

DePonte, D.P., Weierstall, U., Schmidt, K., Warner, J., Starodub, D., Spence, J.C.H., Doak, R.B., 2008. Gas dynamic virtual nozzle for generation of microscopic droplet streams. Journal of Physics D: Applied Physics 41, 195505. https://doi.org/10.1088/0022-3727/41/19/195505

Dobro, M.J., Melanson, L.A., Jensen, G.J., McDowall, A.W., 2010. Plunge Freezing for Electron Cryomicroscopy, in: Methods in Enzymology. Elsevier, pp. 63–82. https://doi.org/10.1016/S0076-6879(10)81003-1

Egelman, E.H., 2016. The Current Revolution in Cryo-EM. Biophysical Journal 110, 1008–1012. https://doi.org/10.1016/j.bpj.2016.02.001

Eng, P.J., Newville, M., Rivers, M.L., Sutton, S.R., 1998. Dynamically figured Kirkpatrick Baez x-ray microfocusing optics, in: McNulty, I. (Ed.), . pp. 145–156. https://doi.org/10.1117/12.330342

Fromme, R., Ishchenko, A., Metz, M., Chowdhury, S.R., Basu, S., Boutet, S., Fromme, P., White, T.A., Barty, A., Spence, J.C.H., Weierstall, U., Liu, W., Cherezov, V., 2015. Serial femtosecond crystallography of soluble proteins in lipidic cubic phase. IUCrJ 2, 545–551. https://doi.org/10.1107/S2052252515013160

Fuller, F.D., Gul, S., Chatterjee, R., Burgie, E.S., Young, I.D., Lebrette, H., Srinivas, V., Brewster, A.S., Michels-Clark, T., Clinger, J.A., Andi, B., Ibrahim, M., Pastor, E., de Lichtenberg, C., Hussein, R., Pollock, C.J., Zhang, M., Stan, C.A., Kroll, T., Fransson, T., Weninger, C., Kubin, M., Aller, P., Lassalle, L., Bräuer, P., Miller, M.D., Amin, M., Koroidov, S., Roessler, C.G., Allaire, M., Sierra, R.G., Docker, P.T., Glownia, J.M., Nelson, S., Koglin, J.E., Zhu, D., Chollet, M., Song, S., Lemke, H., Liang, M., Sokaras, D., Alonso-Mori, R., Zouni, A., Messinger, J., Bergmann, U., Boal, A.K., Bollinger, J.M., Krebs, C., Högbom, M., Phillips, G.N., Vierstra, R.D., Sauter, N.K., Orville, A.M., Kern, J., Yachandra, V.K., Yano, J., 2017. Drop-on-demand sample delivery for studying biocatalysts in action at X-ray free-electron lasers. Nature Methods 14, 443–449. https://doi.org/10.1038/nmeth.4195

Garman, E.F., 2010. Radiation damage in macromolecular crystallography: what is it and why should we care? Acta Crystallographica Section D Biological Crystallography 66, 339–351. https://doi.org/10.1107/S0907444910008656

Grigorieff, N., 2013. Direct detection pays off for electron cryo-microscopy. eLife 2. https://doi.org/10.7554/eLife.00573

Henderson, R., 1995. The potential and limitations of neutrons, electrons and X-rays for atomic resolution microscopy of unstained biological molecules. Quarterly Reviews of Biophysics 28, 171. https://doi.org/10.1017/S003358350000305X

Hirata, K., Shinzawa-Itoh, K., Yano, N., Takemura, S., Kato, K., Hatanaka, M., Muramoto, K., Kawahara, T., Tsukihara, T., Yamashita, E., Tono, K., Ueno, G., Hikima, T., Murakami, H., Inubushi, Y., Yabashi, M., Ishikawa, T., Yamamoto, M., Ogura, T., Sugimoto, H., Shen, J.-R., Yoshikawa, S., Ago, H., 2014. Determination of damage-free crystal structure of an X-ray–sensitive protein using an XFEL. Nature Methods 11, 734–736. https://doi.org/10.1038/nmeth.2962

Holton, J.M., 2009. A beginner's guide to radiation damage. Journal of Synchrotron Radiation 16, 133–142. https://doi.org/10.1107/S0909049509004361

Holton, J.M., Frankel, K.A., 2010. The minimum crystal size needed for a complete diffraction data set. Acta Crystallographica Section D Biological Crystallography 66, 393–408. https://doi.org/10.1107/S0907444910007262

Jordan, P., Fromme, P., Witt, H.T., Klukas, O., Saenger, W., Krauû, N., 2001. Three-dimensional structure of cyanobacterial photosystem I at 2.5 AÊ resolution 411, 9.

Kupitz, C., Grotjohann, I., Conrad, C.E., Roy-Chowdhury, S., Fromme, R., Fromme, P., 2014. Microcrystallization techniques for serial femtosecond crystallography using photosystem II from Thermosynechococcus elongatus as a model system. Philosophical Transactions of the Royal Society B: Biological Sciences 369, 20130316–20130316. https://doi.org/10.1098/rstb.2013.0316

Kupitz, C., Olmos, J.L., Holl, M., Tremblay, L., Pande, K., Pandey, S., Oberthür, D., Hunter, M., Liang, M., Aquila, A., Tenboer, J., Calvey, G., Katz, A., Chen, Y., Wiedorn, M.O., Knoska, J., Meents, A., Majriani, V., Norwood, T., Poudyal, I., Grant, T., Miller, M.D., Xu, W., Tolstikova, A., Morgan, A., Metz, M., Martin-Garcia, J.M., Zook, J.D., Roy-Chowdhury, S., Coe, J., Nagaratnam, N., Meza, D., Fromme, R., Basu, S., Frank, M., White, T., Barty, A., Bajt, S., Yefanov, O., Chapman, H.N., Zatsepin, N., Nelson, G., Weierstall, U., Spence, J., Schwander, P., Pollack, L., Fromme, P., Ourmazd, A., Phillips, G.N., Schmidt, M., 2017. Structural enzymology using X-ray free electron lasers. Structural Dynamics 4, 044003. https://doi.org/10.1063/1.4972069

Li, X., Mooney, P., Zheng, S., Booth, C.R., Braunfeld, M.B., Gubbens, S., Agard, D.A., Cheng, Y., 2013. Electron counting and beam-induced motion correction enable near-atomic-resolution single-particle cryo-EM. Nature Methods 10, 584–590. https://doi.org/10.1038/nmeth.2472

Li, X., Zheng, S., Agard, D.A., Cheng, Y., 2015. Asynchronous data acquisition and on-the-fly analysis of dose fractionated cryoEM images by UCSFImage. Journal of Structural Biology 192, 174–178. https://doi.org/10.1016/j.jsb.2015.09.003

Liu, W., Wacker, D., Gati, C., Han, G.W., James, D., Wang, D., Nelson, G., Weierstall, U., Katritch, V., Barty, A., Zatsepin, N.A., Li, D., Messerschmidt, M., Boutet, S., Williams, G.J., Koglin, J.E., Seibert, M.M., Wang, C., Shah, S.T.A., Basu, S., Fromme, R., Kupitz, C., Rendek, K.N., Grotjohann, I., Fromme, P., Kirian, R.A., Beyerlein, K.R., White, T.A., Chapman, H.N., Caffrey, M., Spence, J.C.H., Stevens, R.C., Cherezov, V., 2013. Serial Femtosecond Crystallography of G Protein-Coupled Receptors. Science 342, 1521–1524. https://doi.org/10.1126/science.1244142

Loll, B., Kern, J., Saenger, W., Zouni, A., Biesiadka, J., 2005. Towards complete cofactor arrangement in the 3.0 Å resolution structure of photosystem II. Nature 438, 1040–1044. https://doi.org/10.1038/nature04224

Lu, P., Bai, X., Ma, D., Xie, T., Yan, C., Sun, L., Yang, G., Zhao, Y., Zhou, R., Scheres, S.H.W., Shi, Y., 2014. Three-dimensional structure of human γ-secretase. Nature 512, 166–170. https://doi.org/10.1038/nature13567

Lučić, V., Förster, F., Baumeister, W., 2005. STRUCTURAL STUDIES BY ELECTRON TOMOGRAPHY: From Cells to Molecules. Annual Review of Biochemistry 74, 833–865. https://doi.org/10.1146/annurev.biochem.73.011303.074112

Martin-Garcia, J.M., Conrad, C.E., Nelson, G., Stander, N., Zatsepin, N.A., Zook, J., Zhu, L., Geiger, J., Chun, E., Kissick, D., Hilgart, M.C., Ogata, C., Ishchenko, A., Nagaratnam, N., Roy-Chowdhury, S., Coe, J., Subramanian, G., Schaffer, A., James, D., Ketwala, G., Venugopalan, N., Xu, S., Corcoran, S., Ferguson, D., Weierstall, U., Spence, J.C.H., Cherezov, V., Fromme, P., Fischetti, R.F., Liu, W., 2017. Serial millisecond crystallography of membrane and soluble protein microcrystals using synchrotron radiation. IUCrJ 4, 439–454. https://doi.org/10.1107/S205225251700570X

Mastronarde, D.N., 2005. Automated electron microscope tomography using robust prediction of specimen movements. Journal of Structural Biology 152, 36–51. https://doi.org/10.1016/j.jsb.2005.07.007

Meents, A., Gutmann, S., Wagner, A., Schulze-Briese, C., 2010. Origin and temperature dependence of radiation damage in biological samples at cryogenic temperatures. Proceedings of the National Academy of Sciences 107, 1094–1099. https://doi.org/10.1073/pnas.0905481107

Moffat, K., n.d. Time-Resolved Crystallography 9.

Mueller, C., Marx, A., Epp, S.W., Zhong, Y., Kuo, A., Balo, A.R., Soman, J., Schotte, F., Lemke, H.T., Owen, R.L., Pai, E.F., Pearson, A.R., Olson, J.S., Anfinrud, P.A., Ernst, O.P., Dwayne Miller, R.J., 2015. Fixed target matrix for femtosecond time-resolved and in situ serial micro-crystallography. Structural Dynamics 2, 054302. https://doi.org/10.1063/1.4928706

Nave, C., 1998. A Description of Imperfections in Protein Crystals. Acta Crystallographica Section D Biological Crystallography 54, 848–853. https://doi.org/10.1107/S0907444998001875

Neutze, R., Hajdu, J., 1997. Femtosecond time resolution in x-ray diffraction experiments. Proceedings of the National Academy of Sciences 94, 5651–5655. https://doi.org/10.1073/pnas.94.11.5651

Neutze, R., Wouts, R., Hajdu, J., 2000. Potential for biomolecular imaging with femtosecond X-ray pulses 406, 6.

Ng, J.D., Gavira, J.A., Garcı´a-Ruı´z, J.M., 2003. Protein crystallization by capillary counterdiffusion for applied crystallographic structure determination. Journal of Structural Biology 142, 218–231. https://doi.org/10.1016/S1047-8477(03)00052-2

Orlova, E.V., Saibil, H.R., 2011. Structural Analysis of Macromolecular Assemblies by Electron Microscopy. Chemical Reviews 111, 7710–7748. https://doi.org/10.1021/cr100353t

Pande, K., Hutchison, C.D.M., Groenhof, G., Aquila, A., Robinson, J.S., Tenboer, J., Basu, S., Boutet, S., DePonte, D.P., Liang, M., White, T.A., Zatsepin, N.A., Yefanov, O., Morozov, D., Oberthuer, D., Gati, C., Subramanian, G., James, D., Zhao, Y., Koralek, J., Brayshaw, J., Kupitz, C., Conrad, C., Roy-Chowdhury, S., Coe, J.D., Metz, M., Xavier, P.L., Grant, T.D., Koglin, J.E., Ketawala, G., Fromme, R., rajer, V., Henning, R., Spence, J.C.H., Ourmazd, A., Schwander, P., Weierstall, U., Frank, M., Fromme, P., Barty, A., Chapman, H.N., Moffat, K., van Thor, J.J., Schmidt, M., 2016. Femtosecond structural dynamics drives the trans/cis isomerization in photoactive yellow protein. Science 352, 725–729. https://doi.org/10.1126/science.aad5081

Rodriguez, J.A., Eisenberg, D.S., Gonen, T., 2017. Taking the measure of MicroED. Current Opinion in Structural Biology 46, 79–86. https://doi.org/10.1016/j.sbi.2017.06.004

Roedig, P., Vartiainen, I., Duman, R., Panneerselvam, S., Stübe, N., Lorbeer, O., Warmer, M., Sutton, G., Stuart, D.I., Weckert, E., David, C., Wagner, A., Meents, A., 2015. A micro-patterned silicon chip as sample holder for macromolecular crystallography experiments with minimal background scattering. Scientific Reports 5. https://doi.org/10.1038/srep10451

Scheres, S.H.W., 2012. RELION: Implementation of a Bayesian approach to cryo-EM structure determination. Journal of Structural Biology 180, 519–530. https://doi.org/10.1016/j.jsb.2012.09.006

Schlichting, I., 2015. Serial femtosecond crystallography: the first five years. IUCrJ 2, 246–255. https://doi.org/10.1107/S205225251402702X

Schmidt, M., 2013. Mix and Inject: Reaction Initiation by Diffusion for Time-Resolved Macromolecular Crystallography. Advances in Condensed Matter Physics 2013, 1–10. https://doi.org/10.1155/2013/167276

Schotte, F., Cho, H.S., Kaila, V.R.I., Kamikubo, H., Dashdorj, N., Henry, E.R., Graber, T.J., Henning, R., Wulff, M., Hummer, G., Kataoka, M., Anfinrud, P.A., 2012. Watching a signaling protein function in real time via 100-ps time-resolved Laue crystallography. Proceedings of the National Academy of Sciences 109, 19256–19261. https://doi.org/10.1073/pnas.1210938109

Sigworth, F.J., 2016. Principles of cryo-EM single-particle image processing. Microscopy 65, 57–67. https://doi.org/10.1093/jmicro/dfv370

Singh, D., Berntsen, K., Baakman, C., Vriend, G., Lahiri, T., 2018. A Critical Note on Symmetry Contact Artifacts and the Evaluation of the Quality of Homology Models. Symmetry 10, 25. https://doi.org/10.3390/sym10010025

Sugahara, M., Song, C., Suzuki, M., Masuda, T., Inoue, S., Nakane, T., Yumoto, F., Nango, E., Tanaka, R., Tono, K., Joti, Y., Kameshima, T., Hatsui, T., Yabashi, M., Nureki, O., Numata, K., Iwata, S., 2016. Oil-free hyaluronic acid matrix for serial femtosecond crystallography. Scientific Reports 6. https://doi.org/10.1038/srep24484

Suloway, C., Pulokas, J., Fellmann, D., Cheng, A., Guerra, F., Quispe, J., Stagg, S., Potter, C.S., Carragher, B., 2005. Automated molecular microscopy: The new Leginon system. Journal of Structural Biology 151, 41–60. https://doi.org/10.1016/j.jsb.2005.03.010

Weierstall, U., James, D., Wang, C., White, T.A., Wang, D., Liu, W., Spence, J.C.H., Bruce Doak, R., Nelson, G., Fromme, P., Fromme, R., Grotjohann, I., Kupitz, C., Zatsepin, N.A., Liu, H., Basu, S., Wacker, D., Won Han, G., Katritch, V., Boutet, S., Messerschmidt, M., Williams, G.J., Koglin, J.E., Marvin Seibert, M., Klinker, M., Gati, C., Shoeman, R.L., Barty, A., Chapman, H.N., Kirian, R.A., Beyerlein, K.R., Stevens, R.C., Li, D., Shah, S.T.A., Howe, N., Caffrey, M., Cherezov, V., 2014. Lipidic cubic phase injector facilitates membrane protein serial femtosecond crystallography. Nature Communications 5. https://doi.org/10.1038/ncomms4309

Wu, S., Armache, J.-P., Cheng, Y., 2016. Single-particle cryo-EM data acquisition by using direct electron detection camera. Microscopy 65, 35–41. https://doi.org/10.1093/jmicro/dfv355

APPENDIX A

BUFFER RECIPE FOR GROWING CYANOBACTERIAL CELL CULTURES

Modified BG-11 recipe:

10X solutions were prepared with (per liter)

1.5 g of $NaNO_3$,

0.075 g of $MgSO_4.7H_2O$,

0.036 g of $CaCl_2.2H_2O$,

0.04 g of K_2HPO_4,

0.02 g of Na_2CO_3,

6 mg of $C_6H_8O_7.H_2O$,

6 mg of $C_6H_{11}FeNO_7$,

1 mg of $Na_2EDTA.2H_2O$.

Micronutrients play an essential role in metabolism (Rueter et.al., 1987) and are essential for long-term sustained cell growth.

10x trace metal solution contained (per liter)

2.86 g of H_3BO_3,

1.81g of $MnCl_2.4H_2O$,

0.222 g of $ZnSO_4.7H_2O$,

0.39 g of $Na_2MoO_4.2H_2O$,

0.079 g of $CuSO_4.5H_2O$

0.0492 g of $Co(NO_3)_2.6H_2O$.

$FeCl_3$ solution: 0.2905 g $FeCl_3$ filled to 1 L with millipure water.

NTA-medium recipe:

For 10X solutions, in 1L of water, dissolve

1 g of Nitriloacetic acid (NTA)

0.6 g of $CaCl_2.6(H_2O)$

1 g of $MgSO_4.H_2O$

1.03 g of KNO_3

6.89 g of $NaNO_3$

1.1 g of Na_2HPO_4

Add 5 mL of Micronutrient solution

Add 10 mL FeCl3

Dissolve all components and make up the buffer to pH=8.2 (some NTA would crash or conjugate with Fe but that's ok!)

T. elongatus cells were grown in media prepared freshly. pH was adjusted to 8.2 and then the volume was adjusted with purified distilled water.

APPENDIX B

PERMISSION RECEIVED FROM ELSEVIER FOR USING PREVIOUSLY PUBLISHED MATERIAL

B: Permission from Elsevier for Chapter 2

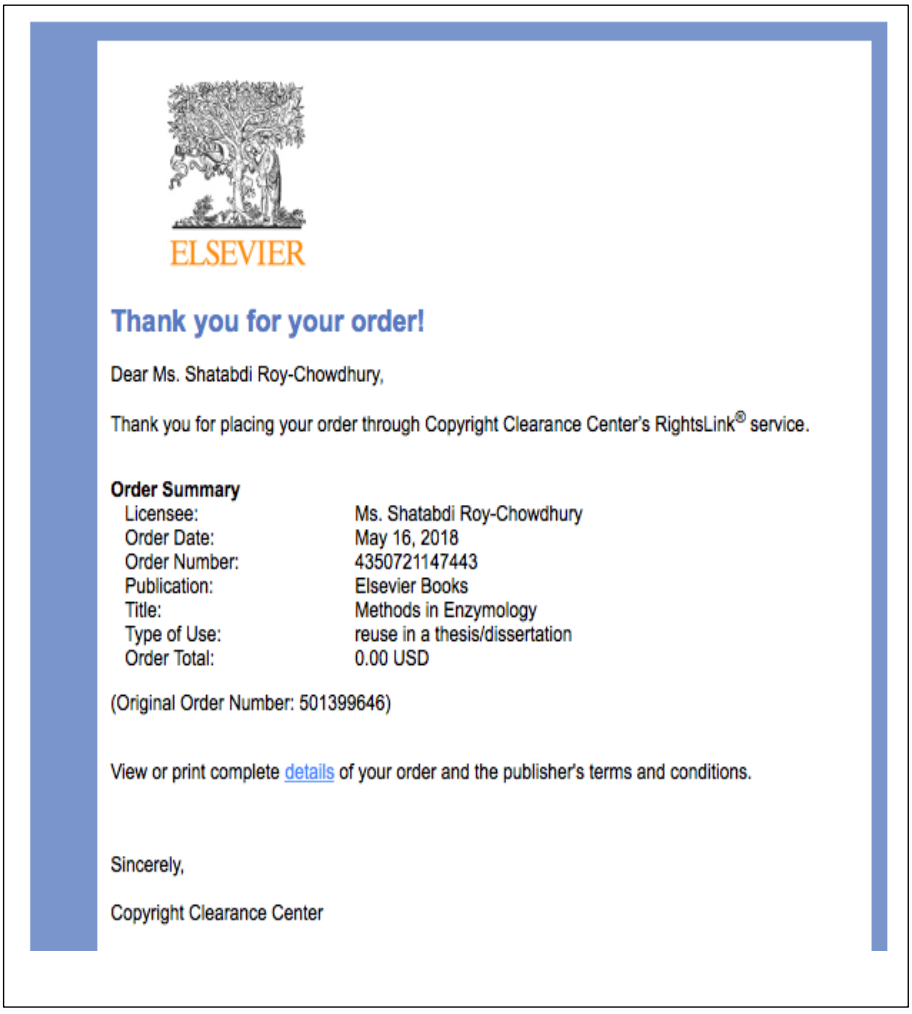

ELSEVIER

Thank you for your order!

Dear Ms. Shatabdi Roy-Chowdhury,

Thank you for placing your order through Copyright Clearance Center's RightsLink® service.

Order Summary

Licensee:	Ms. Shatabdi Roy-Chowdhury
Order Date:	May 16, 2018
Order Number:	4350721147443
Publication:	Elsevier Books
Title:	Methods in Enzymology
Type of Use:	reuse in a thesis/dissertation
Order Total:	0.00 USD

(Original Order Number: 501399646)

View or print complete details of your order and the publisher's terms and conditions.

Sincerely,

Copyright Clearance Center